

N63-18407

Report 1

## FLUX SWITCHING IN MULTIPATH CORES

Prepared for:

JET PROPULSION LABORATORY  
4800 OAK GROVE DRIVE  
PASADENA, CALIFORNIA

CONTRACT 950095  
UNDER NASw-6

By: D. Nitzan

STANFORD RESEARCH INSTITUTE

MENLO PARK, CALIFORNIA



### OTS PRICE

XEROX

\$

MICROFILM

\$

~~XXXXXXXXXX~~



STANFORD RESEARCH

MENLO PARK

SRI

November 1961

Report 1

## FLUX SWITCHING IN MULTIPATH CORES

Prepared for:

JET PROPULSION LABORATORY  
4800 OAK GROVE DRIVE  
PASADENA, CALIFORNIA

CONTRACT 950095  
UNDER NASw-6

By: D. Nitzan

SRI Project No. 3696

Approved:

*W. B. Adams for*  
J. R. ANDERSON, MANAGER COMPUTER TECHNIQUES LABORATORY

*J. D. Roe*  
J. D. ROE, DIRECTOR ENGINEERING SCIENCES DIVISION

Copy No. **21**

CR-50,058



## ABSTRACT

---

A multipath ferrite core is divided into legs whose properties constitute the flux-switching characteristics of the core. Flux switching due to rotation of magnetization and domain growth is divided into elastic and inelastic components. The switching characteristics of each individual leg are expressed in terms of the static  $\phi$ - $F$  loop, elastic parameter  $\epsilon$  and inelastic parameters  $\rho$  and  $F_0$ . Based on these parameters, each leg is represented by an electrical-circuit analogue. The assembly of these analogues, according to the physical layout of the individual legs, represents the electrical-circuit analogue of the multipath core. These analogues facilitate the computation of  $\dot{\phi}$ ,  $\phi$  and  $F$  in each leg during switching time. Other means to express flux switching are described. These include a ring-element model that assumes slow switching and  $\phi$ - $F$  curves that represent the net change in  $\phi$  due to a given  $F$  pulse.

Continuous-output flux, which results from setting a multipath core followed by switching the set flux back and forth around a minor aperture, is plotted versus the SET MMF, with the minor-aperture DRIVE MMF as a parameter. All-magnetic discrete flux-transfer schemes are classified into two categories, nonresistance type and resistance type. A circuit representing each type is described, and bistable operation is explained in terms of flux gain and a drive-current range map.

Various switching effects, caused by the geometry of a multipath core in conjunction with an external MMF, are discussed. These effects include flux division due to path ratio of two legs in parallel, pole distribution left behind after the removal of a drive on an outside leg, and excessive setting and unsetting due to hard drive on an outside leg. Multipath-core shaping is shown to affect soft thresholds existing in partially demagnetized states, read-out voltage amplitude, and flux clipping necessary for proper flux-gain characteristic.

Flux patterns in a multipath core are described simply by an arrow model. In analogy to domain wall theory, a more detailed model in terms of "zone boundaries" is proposed, and zone patterns for different flux states are suggested. Analyses of flux patterns based on solving Laplace's equation that have appeared in the literature are described and evaluated.

A literature survey in the last section covers sources referred to in the first four sections of the report, as well as supplementary sources.

# CONTENTS

ABSTRACT . . . . .	iii
LIST OF ILLUSTRATIONS . . . . .	ix
LIST OF SYMBOLS . . . . .	xv
ACKNOWLEDGMENTS . . . . .	xxiii
PREFACE . . . . .	xxv
 I FLUX-SWITCHING CHARACTERISTICS . . . . .	 1
A. Toroidal Equivalence of a Multipath Core . . . . .	1
1. The Need for Toroidal Equivalence . . . . .	1
2. Leg Model . . . . .	3
3. Restrictions on Leg Model . . . . .	3
4. Erroneous Toroidal Model . . . . .	4
B. Static Loops . . . . .	4
1. Interpretation of $B$ in Polycrystalline Ferrite . . . . .	5
2. $B(H)$ and Domain Growth . . . . .	7
3. $\phi$ - $F$ Loop of Toroid . . . . .	8
4. $\phi$ - $F$ Loops of a Multipath Core . . . . .	11
C. Mechanism of Flux Switching . . . . .	11
1. Elastic Switching From Quiescent State . . . . .	13
2. Nature of Inelastic Switching . . . . .	14
3. Combined Change in $B$ . . . . .	15
4. $dB/dt$ . . . . .	17
D. Elastic Switching Models . . . . .	17
1. Elastic Permeability . . . . .	18
2. Calculated $\Delta\phi_e$ in Saturation . . . . .	21
3. Switching Inductance . . . . .	23
4. Average Switching Inductance . . . . .	24
5. Switching Inductance in a Multipath Core . . . . .	25
E. Inelastic Switching Models . . . . .	25
1. Measurement Problems . . . . .	25
2. $\phi_p$ Versus $F$ and $\phi$ . . . . .	25
3. Dynamic Threshold MMF . . . . .	26
4. Switching Resistance . . . . .	28
5. Average Switching Resistance . . . . .	30
6. Switching Resistance in a Multipath Core . . . . .	31
F. Electrical-Circuit Analogue . . . . .	31
1. Summary of Switching Models . . . . .	32
2. Electrical-Circuit Analogue for a Leg . . . . .	34
3. Electrical-Circuit Analogue for a Multipath Core . . . . .	35
4. Computation . . . . .	

## CONTENTS

G.	Ring-Element Model . . . . .	36
1.	Static State . . . . .	36
2.	Dynamic State . . . . .	40
3.	Calculated $\dot{\phi}_p(t)$ . . . . .	42
4.	Application to a Multipath Core . . . . .	44
H.	$\phi$ - $F$ Curves . . . . .	45
1.	Introduction . . . . .	45
2.	Automatic Plotting of $\phi$ - $F$ Curves . . . . .	45
3.	Typical $\phi$ - $F$ Curves . . . . .	46
4.	Soft Threshold . . . . .	48
5.	Evaluation of Core Characteristics . . . . .	50
6.	$\phi$ - $F$ Curves of a Cracked Core . . . . .	50
I.	Conclusions . . . . .	53
II	FLUX TRANSFER . . . . .	55
A.	Setting Characteristics . . . . .	55
1.	Asymmetrical Read-Out . . . . .	55
2.	Symmetrical Read-Out . . . . .	58
3.	Other Setting Characteristics . . . . .	59
B.	All-Magnetic Flux Transfer . . . . .	59
1.	All-Magnetic Schemes . . . . .	59
2.	Nonresistance Flux-Transfer Schemes . . . . .	61
3.	Resistance Flux-Transfer Schemes . . . . .	64
4.	Flux Gain . . . . .	67
5.	Range Map . . . . .	70
6.	Comparison Between Nonresistance and Resistance Flux-Transfer Schemes . . . . .	72
C.	Conclusions . . . . .	74
III	GEOMETRY EFFECTS . . . . .	75
A.	Effect of Path-Length Ratio on Flux Division . . . . .	75
1.	Flux Division in a Laddie . . . . .	75
2.	Initial Explanation of $\dot{\phi}$ Waveforms . . . . .	76
3.	Revised Explanation of $\dot{\phi}$ Waveforms . . . . .	77
4.	More Data on Flux Division . . . . .	80
5.	Effects on Multihole-Structure Operation . . . . .	82
6.	Measures Against Undesired Flux Division . . . . .	82
B.	Drive on Leg 4 . . . . .	85
1.	Degrees of Freedom of Switched Flux . . . . .	85
2.	Negative Drive on Leg 4 of a Cleared Core . . . . .	86
3.	Positive Drive on Leg 4 of a Cleared Core . . . . .	89
4.	Negative Drive on Leg 4 of a Set Core . . . . .	94
C.	Multipath-Core Shaping . . . . .	99
1.	Effect of Shaping on Soft Threshold . . . . .	100
2.	Effect of Shaping on Read-Out . . . . .	102
3.	Minor-Aperture Flux Clipping . . . . .	106
4.	Effect of Flux Leakage . . . . .	108
D.	Legs in Series and Parallel . . . . .	109
1.	Legs in Series . . . . .	109
2.	Legs in Parallel . . . . .	112
E.	Conclusions . . . . .	114



## CONTENTS

IV	FLUX PATTERNS . . . . .	115
A.	Arrow Model . . . . .	115
1.	Rules . . . . .	115
2.	Application . . . . .	117
3.	Evaluation . . . . .	119
B.	Zone Configurations . . . . .	119
1.	Zone Boundary . . . . .	120
2.	Zone Pattern of a Set Core . . . . .	120
3.	Zone Pattern of a Cleared Core . . . . .	124
4.	Zone Pattern of an Unshaped Core . . . . .	126
C.	Analysis of Flux Patterns . . . . .	128
1.	Effect of Poles on $H$ Equalization . . . . .	128
2.	Calculation of Flux Leakage . . . . .	129
3.	Analysis of Flux Pattern in a Multipath Core . . . . .	134
D.	Conclusions . . . . .	136
V	LITERATURE SURVEY . . . . .	139
A.	References . . . . .	139
B.	Bibliography . . . . .	155
C.	Literature Classification . . . . .	173
1.	Subject Classification . . . . .	173
2.	Alphabetical Order of Authors' Names . . . . .	176
APPENDIX A	GEOMETRICAL PROPERTIES OF A LEG . . . . .	181
APPENDIX B	CALCULATION OF $\Delta\phi_{\epsilon_s}$ . . . . .	185
APPENDIX C	CALCULATION OF $\dot{\phi}_\rho$ , $\bar{\rho}$ AND $\rho_{\phi,av}$ . . . . .	189
APPENDIX D	ANALYSIS OF SETTING CHARACTERISTICS . . . . .	195
INDEX	. . . . .	207



## ILLUSTRATIONS

---

Fig. 1	Division of a Multipath Core Into Legs . . . . .	2
Fig. 2	Equivalent Toroid and Leg . . . . .	2
Fig. 3	Division of a Multipath Core Into Two Toroids . . . . .	4
Fig. 4	Static $B$ - $H$ Loops . . . . .	4
Fig. 5	Shape and Orientation of Domains in a Ferrite Particle . . . . .	5
Fig. 6	$B$ - $H$ Characteristic of a Ferrite Particle . . . . .	6
Fig. 7	Schematic Plot of Energy of Ellipsoidal Domain vs. Cross-Sectional Radius . . . . .	6
Fig. 8	Toroidal Core . . . . .	7
Fig. 9	Static $\phi$ - $F$ Loop . . . . .	8
Fig. 10	Division of a Three-Leg Core Into Legs . . . . .	8
Fig. 11	Static $\phi$ - $F$ Loops of Legs $m$ , 3 and 4 . . . . .	10
Fig. 12	Mechanism of Elastic-Flux Switching . . . . .	11
Fig. 13	Elastic Changes in $B$ . . . . .	12
Fig. 14	Inelastic Change in $B$ . . . . .	14
Fig. 15	Effect of $\Delta B$ History on $\Delta B_e$ . . . . .	15
Fig. 16	$\Delta B_e$ and $\Delta B_p$ During Fall Time of $H$ . . . . .	15
Fig. 17	Typical $\dot{B}$ Waveshape ( $\Delta B < 2B_r$ ) . . . . .	17
Fig. 18	Variation of $\mu_e$ With $B$ and $H$ . . . . .	18
Fig. 19	A Leg . . . . .	18
Fig. 20	$\Delta \phi_e$ in Negative Saturation Caused by Applied $F$ . . . . .	20
Fig. 21	Hyperbolic Model for $B(H)$ in Negative Saturation . . . . .	20
Fig. 22	Hyperbolic Model for $\mu_e$ in Negative Saturation . . . . .	20
Fig. 23	Hyperbolic Model for $\Delta \phi_e$ of a Leg in Negative Saturation . . . . .	21
Fig. 24	Three Regions in a Toroid . . . . .	22
Fig. 25	$\dot{\phi}_e$ (Generated by $F$ ) vs. $\phi$ and Prepulse Duration . . . . .	22
Fig. 26	Hyperbolic Model of $\epsilon$ vs. $F$ in Negative Saturation . . . . .	23
Fig. 27	Measured $\epsilon$ vs. $F$ in Negative Saturation for Multipath-Core Legs. . . . .	24
Fig. 28	Creation of Poles in Ellipsoidal Domains . . . . .	26
Fig. 29	Determination of $\rho(t)$ and $\rho(\phi)$ from $\dot{\phi}_p(t)$ and $(F-F_0)(t)$ . . . . .	27
Fig. 30	$\dot{\phi}(t)$ Calculated from a Parabolic Model for $\rho$ . . . . .	28
Fig. 31	Evaluation of $\rho_p$ From Measured $\dot{\phi}_p$ vs. $F$ . . . . .	29

# ILLUSTRATIONS

Fig. 32	$1/\tau$ vs. $H$ . . . . .	29
Fig. 33	Experimental $\rho_1$ , $\rho_3$ , and $\rho_4$ vs. $\phi/\phi_r$ of a Multipath Core . . . . .	31
Fig. 34	Equivalent Electrical Circuits of a Magnetic Leg . . . . .	33
Fig. 35	Electrical-Circuit Analogue for a Leg . . . . .	33
Fig. 36	Functions of Rectifiers and Relays in Leg Analogue . . . . .	34
Fig. 37	Three-Leg Core Analogue . . . . .	35
Fig. 38	Idealized Static $B$ - $F$ Loops . . . . .	38
Fig. 39	Calculated Static $\phi$ - $F$ Loop . . . . .	38
Fig. 40	$\tau$ vs. $r$ in a Toroid . . . . .	41
Fig. 41	$r'$ and $r''$ vs. $t$ for Constant $F$ . . . . .	41
Fig. 42	$B$ vs. $r$ and $t$ in a Toroid Cross Section . . . . .	41
Fig. 43	$r'$ and $r''$ vs. $t$ for Constant- $F$ Pulse Train . . . . .	43
Fig. 44	$r'$ and $r''$ vs. $t$ for $F = kt$ . . . . .	43
Fig. 45	$\dot{\phi}_\rho$ vs. $t$ for Constant $F$ . . . . .	44
Fig. 46	$\dot{\phi}_\rho$ vs. $t$ for $F = kt$ . . . . .	44
Fig. 47	Calculated $\phi$ - $F$ Loops of Multipath-Core Links . . . . .	44
Fig. 48	Variation of $\phi$ and $F$ Corresponding to One Point in a $\phi$ - $F$ Curve . . . . .	46
Fig. 49	Automatically-Plotted $\phi$ - $F$ Curve . . . . .	47
Fig. 50	$\phi$ - $F$ Curves with $T$ as a Parameter . . . . .	47
Fig. 51	$\phi$ - $F$ Curves with $T_{ps}$ and $T$ as Parameters . . . . .	48
Fig. 52	$\phi$ - $F$ Curve Test for a Multipath Core . . . . .	49
Fig. 53	$\phi$ - $F$ Curves of a Multipath Core with $T_{ps}$ and $T$ as Parameters . . . . .	50
Fig. 54	Static Characteristic of a Cracked Toroid . . . . .	51
Fig. 55	$\phi$ - $F$ Curve of a Cracked Toroid . . . . .	52
Fig. 56	$\phi$ - $F$ Curve of a Cracked Multipath Core . . . . .	53
Fig. 57	Setting-Characteristics Test . . . . .	56
Fig. 58	Asymmetrical Setting Characteristics . . . . .	57
Fig. 59	Symmetrical Setting Characteristics . . . . .	58
Fig. 60	Symmetrical Setting Characteristics ( $F_s$ and $F_D$ Simultaneous for Several Cycles) . . . . .	60
Fig. 61	A Nonresistance Flux-Transfer Scheme . . . . .	61
Fig. 62	Alternative Wiring for a Nonresistance Scheme . . . . .	63
Fig. 63	A Resistance Flux-Transfer Scheme . . . . .	64
Fig. 64	Quiescent Condition of a Resistance Scheme . . . . .	66
Fig. 65	Variation of $F$ and $\phi$ in Each Leg During ADVANCE and PRIME Periods of a Resistance Scheme . . . . .	68
Fig. 66	Bistable Flux-Transfer Characteristic . . . . .	69
Fig. 67	Obtaining Bistable Flux-Transfer Characteristic by Turns Ratio and Flux Clipping . . . . .	69

# ILLUSTRATIONS

Fig. 68	Stability Regions of Flux-Transfer Characteristics . . . . .	71
Fig. 69	Effect of Varying $I_{sup}$ on $G$ and $\Delta\phi_T$ . . . . .	71
Fig. 70	$G$ and $\Delta\phi_T$ vs. $I_A$ Due to Unsetting Effect . . . . .	73
Fig. 71	Two Types of Range Maps for a Resistance Flux-Transfer Scheme . . . . .	73
Fig. 72	Flux Division in a Laddic . . . . .	75
Fig. 73	Waveforms of $\dot{\phi}_2$ and $\dot{\phi}_3$ , Fig. 72(a) . . . . .	76
Fig. 74	Simplified Electrical-Circuit Analogue for Fig. 72(a) . . . . .	78
Fig. 75	Flux Switching in Laddic Legs, Fig. 72 . . . . .	79
Fig. 76	Flux Division in a Circular Multipath Core . . . . .	80
Fig. 77	Flux Division in a Circular Multipath Core, Fig. 76(b) . . . . .	81
Fig. 78	Effect of Slope of Ramp $F$ Drive on Flux Division . . . . .	82
Fig. 79	Continuous-Structure Shift Register . . . . .	83
Fig. 80	A Scanner . . . . .	83
Fig. 81	Methods of Minimizing Flux Division . . . . .	85
Fig. 82	Negative Drive on Leg 4 of a Cleared Core . . . . .	86
Fig. 83	Flux Switching in the Core of Fig. 82 . . . . .	87
Fig. 84	Setting a Cleared Core via Leg 4 . . . . .	90
Fig. 85	Flux Switching in the Core of Fig. 84 Using High Drive . . . . .	90
Fig. 86	Pole Distribution in a Stressed State Following Hard Leg-4 Setting . . . . .	91
Fig. 87	Low-Drive Setting of the Core in Fig. 84 . . . . .	92
Fig. 88	Full Supersetting Effect via Leg 1 . . . . .	93
Fig. 89	$\Delta\phi_3$ and $\Delta\phi_4$ due to Leg-1 Supersetting Effect . . . . .	94
Fig. 90	Effect of Extreme Winding Position in a Set Core . . . . .	95
Fig. 91	Various Winding Positions . . . . .	96
Fig. 92	Negative Drive on Leg 4 of a Set Core . . . . .	97
Fig. 93	Flux Switching in the Core of Fig. 92 . . . . .	97
Fig. 94	Unsetting Effect in a Laddic . . . . .	99
Fig. 95	Hard CLEAR Drive on a Two-Leg Core . . . . .	100
Fig. 96	Clearing a Three-Leg Circular Core . . . . .	101
Fig. 97	Alternative Methods of Shaping a Circular Multipath Core . . . . .	102
Fig. 98	Flux-State Read-Out . . . . .	103
Fig. 99	Alternative Drives for Read-Out . . . . .	104
Fig. 100	Static CLEAR State When $w_4 > w_3 = 1/2 w_m$ . . . . .	104
Fig. 101	Effect of Extra Leg Width on CLEAR-State Read-Out . . . . .	105
Fig. 102	Setting a Receiver via Leg 1 . . . . .	107
Fig. 103	Leg-2 Flux Clipping in Fig. 102(a) . . . . .	107
Fig. 104	Shaping Legs 1 and 2 for Flux Clipping . . . . .	108

# ILLUSTRATIONS

Fig. 105	Round and Rectangular Cores . . . . .	109
Fig. 106	Field Distribution Determined from a Wire-Mesh Analogue . . . . .	109
Fig. 107	Equivalent Leg for Two Legs in Series . . . . .	110
Fig. 108	Equivalent Leg for Two Legs in Parallel . . . . .	113
Fig. 109	Arrow-Model Scaling . . . . .	115
Fig. 110	Arrow-Model Polarity . . . . .	116
Fig. 111	Different Flux Closures . . . . .	117
Fig. 112	Flux Pattern in a Set Core . . . . .	118
Fig. 113	Erroneous Description of Flux Switching . . . . .	118
Fig. 114	Mushy Regions . . . . .	119
Fig. 115	Zone Boundary in a Bulk Ferrite . . . . .	120
Fig. 116	A Shaped Multipath Core . . . . .	121
Fig. 117	Zone Boundaries for a Core Set via Leg 3 . . . . .	121
Fig. 118	Magnetization Vectors Across a Boundary . . . . .	122
Fig. 119	Zone Boundaries for a Core Set via Leg 4 . . . . .	123
Fig. 120	Possible Zone Boundaries for a Cleared Core . . . . .	124
Fig. 121	Possible Domains Near Crystal Surface . . . . .	125
Fig. 122	Alternative Zone Boundaries in a CLEAR State . . . . .	126
Fig. 123	Zone Pattern for a CLEAR State . . . . .	126
Fig. 124	Zone Pattern for a Set Core . . . . .	126
Fig. 125	Zone Pattern for a Partially Set and Primed Core . . . . .	127
Fig. 126	$\Delta\phi_0$ vs. Increasing and Decreasing $F_D$ . . . . .	128
Fig. 127	Effect of Poles on $H$ Distribution . . . . .	128
Fig. 128	Direct Current $I$ Inside a Tube . . . . .	129
Fig. 129	Direct Current $I$ Outside a Tube . . . . .	133
Fig. 130	Direct Current $I$ Inside and Outside a Tube . . . . .	133
Fig. 131	Calculated Leakage Flux . . . . .	133
Fig. 132	Assumed $B$ vs. $H$ . . . . .	134
Fig. 133	A Multipath Core of Constant $\mu$ Driven by Direct Current . . . . .	135
Fig. 134	High- $\mu$ Thin Band and Pole Distribution . . . . .	135
Fig. 135	Computed Magnetic Field in a Tube . . . . .	137
Fig. 136	BIAX Memory Element . . . . .	162
Fig. 137	Flux Switching in a BIAX Memory Element by Zone Growth . . . . .	163
Fig. A-1	Constant-Width Leg . . . . .	183
Fig. D-1	Setting Characteristic Windings . . . . .	197
Fig. D-2	Switching Paths Corresponding to Various $F_D$ Values . . . . .	198

# ILLUSTRATIONS

Fig. D-3	Flux Switching in Legs 3 and 4 for $F_D = F_{Df}$ vs. $\Delta\phi_D$ . . . . .	200
Fig. D-4	Flux Switching for $F_D = F_{Dm} + 3/4 F_{Df}$ and $\Delta\phi_s = 7/2 \phi_r$ . . . . .	200
Fig. D-5	Calculated Asymmetrical Setting Characteristics . . . . .	202
Fig. D-6	Flux Switching in Legs 3 and 4 for $F_D = F_p = 3/5 F_{Df}$ . . . . .	203
Fig. D-7	Flux Switching in Legs 3 and 4 for $2\phi_r + \Delta\phi_s < \Delta\phi_D^* < 4\phi_r$ . . . . .	204
Fig. D-8	Flux Switching when $\Delta\phi_D'' > \Delta\phi_s$ : . . . . .	205
Fig. D-9.	Calculated Symmetrical Setting Characteristics . . . . .	206





## LIST OF SYMBOLS

<u>Symbol</u>	<u>Definition</u>	<u>Reference</u>
$A$	Cross-sectional area of a leg	Fig. 19
$\Delta A$	Cross-sectional area of a small ferrite particle	p. 4
$\delta A$	Area of a domain cross section in the plane of $\Delta A$	p. 4
$a$	Parameter in the hyperbolic model for $B(H)$	Eq. (28)
$B$	Flux density	
$B_r$	Maximum residual $B$	Fig. 4
$B_s$	Intrinsic flux density of a saturated material	p. 5
$\Delta B$	Over-all change in $B$	Eq. (20)
$\Delta B_e$	Elastic $\Delta B$	p. 14
$\Delta B_p$	Inelastic $\Delta B$	p. 14
$\dot{B}$	Time rate of change of $B$	Eq. (21)
$\dot{B}_A$	$\dot{B}$ due to domain growth	Eq. (21a)
$\dot{B}_{air}$	$\dot{B}$ due to air flux	Eq. (21c)
$\dot{B}_e$	Elastic $\dot{B}$	Eq. (22)
$\dot{B}_{eA}$	$\dot{B}_e$ due to domain growth	p. 16
$\dot{B}_{e\theta}$	$\dot{B}_e$ due to rotation of magnetization	p. 16
$\dot{B}_\theta$	$\dot{B}$ due to rotation of magnetization	Eq. (21b)
$\dot{B}_p$	Inelastic $\dot{B}$	Eq. (23)
$\dot{B}_{pA}$	$\dot{B}_p$ due to domain growth	p. 16
$\dot{B}_{p\theta}$	$\dot{B}_p$ due to rotation of magnetization	p. 16

# SYMBOLS

<u>Symbol</u>	<u>Definition</u>	<u>Reference</u>
$C_\ell$	Capacitance of coupling loop	p. 59
$d$	MMF of a static $\phi$ - $F$ loop	Fig. 9
$d^{av}$	Average $d$ of a linearized static $\phi$ - $F$ loop	Fig. 9; Eq. (17)
$d_{eff}$	Effective $d$ of a cracked core	Eq. (70a)
$d_{jk}$	$d$ of a leg equivalent to Legs $j$ and $k$ in series	e.g. Eq. (96)
$d^{max}$	Maximum $d$ of a linearized static $\phi$ - $F$ loop	Fig. 9
$d^{min}$	Minimum $d$ of a linearized static $\phi$ - $F$ loop	Fig. 9
$d^{sat}$	Saturation $d$	Fig. 9
$d^{th}$	Threshold $d$	Fig. 9
$F$	MMF	
$F_0$	Dynamic MMF threshold	Eq. (38)
$F_{0jk}$	$F_0$ of Legs $j$ and $k$ in series	e.g. Eq. (97)
$F_{0j  k}$	$F_0$ of Legs $j$ and $k$ in parallel	e.g. Eq. (102)
$F_A$	$F$ at lower knee of $\phi$ - $F$ curve	Fig. 49
$F_a$	$F$ across a crack in a toroid	Fig. 54
$F_{A,34}$	$F_A$ of a minor aperture	Fig. 52(b)
$F_{A,M}$	$F_A$ of a major aperture	Fig. 52(b)
$F_B$	$F$ at upper knee of $\phi$ - $F$ curve	Fig. 49
$F_{B,34}$	$F_B$ of a minor aperture	Fig. 52(b)
$F_{B,M}$	$F_B$ of a major aperture	Fig. 52(b)
$F_C$	CLEAR MMF	p. 55
$F_D$	DRIVE MMF	p. 55
$F_{ex}$	Excess MMF over a threshold value	e.g. Eq. (70)
$F_i^{max}$	$d^{sat}$ of the inner ring of a toroid	p. 37

# SYMBOLS

<u>Symbol</u>	<u>Definition</u>	<u>Reference</u>
$F_i^{\min}$	$d^{\text{th}}$ of the inner ring of a toroid	p. 37
$F_o^{\max}$	$d^{\text{sat}}$ of the outer ring of a toroid	p. 37
$F_o^{\min}$	$d^{\text{th}}$ of the outer ring of a toroid	p. 37
$F_p$	PRIME MMF	p. 55
$F_{ps}$	$F$ of a preset pulse	p. 48
$F_s$	SET MMF	p. 55
$G$	Flux gain	Eq. (80); Fig. 66
$g$	Ratio of outer to inner radius	p. 37
$H$	Magnetic field intensity	
$H_0$	Dynamic $H$ field threshold	Eq. (46); Fig. 32
$H_c$	Coercive $H$	Fig. 4
$H^{\max}$	Maximum $H$ of an idealized $B$ - $H$ loop	Fig. 4(b)
$H^{\min}$	Minimum $H$ of an idealized $B$ - $H$ loop	Fig. 4(b)
$H_r$	Normal component of $H$	Eq. (111)
$H_{\text{sat}}$	Saturation $H$	Fig. 4(a)
$H_{\text{th}}$	Threshold $H$	Fig. 4(a)
$H_\theta$	Tangential component of $H$	Eq. (110)
$h$	Height of a core or a leg	Fig. 8; Fig. 19
$I$	Current	
$I_A$	ADVANCE current	p. 61
$I'_A$	ADVANCE current in an alternative nonresistance-type scheme	p. 63
$I_A^{\max}$	Maximum $I_A$ sustaining bistable operation	e.g. Eq. (74)
$I_A^{\min}$	Minimum $I_A$ sustaining bistable operation	Fig. 71
$I_{AB}$	Component of $I_A$ in the receiver side of a nonresistance-type coupling loop	p. 62

# SYMBOLS

Symbol	Definition	Reference
$I_{AT}$	Component of $I_A$ in the transmitter side of a nonresistance-type coupling loop	p. 62
$I_C$	CLEAR current	p. 61
$I_D$	DRIVE current	p. 55
$I_P$	PRIME current	p. 55; p. 64
$I_P^{\max}$	Maximum $I_P$ sustaining bistable operation	Fig. 71
$I_P^{\min}$	Minimum $I_P$ sustaining bistable operation	Fig. 71
$I_s$	SET current	p. 55
$I_{sup}$	Supply current, e.g. $I_A$ or $I_P$	p. 70
$i_\ell$	Coupling-loop current	p. 63
$i_{\ell b}$	Backward $i_\ell$ in a resistance-type flux-transfer scheme	Fig. 63(a)
$k$	Number of legs prevented from switching	p. 86
$L_\ell$	Inductance of a coupling loop	p. 59
$l$	Length of a leg	Fig. 19
$l^{av}$	Average $l$	p. 30
$l_i$	$l$ of the short edge	Fig. 19
$l^{\max}$	$l_o$ of a circular leg	p. 9
$l^{\min}$	$l_i$ of a circular leg	p. 9
$l_o$	$l$ of the long edge	Fig. 19
$M$	External MMF	e.g. Fig. 37
$M_s$	Saturation magnetization	p. 5
$m$	Ratio of $H^{\max}$ to $H^{\min}$	p. 37
$N$	Number of turns	
$N_A$	$N$ of ADVANCE winding	Fig. 62
$N_b$	$N$ of PRIME winding in the major aperture	Fig. 63(a)

# SYMBOLS

<u>Symbol</u>	<u>Definition</u>	<u>Reference</u>
$N_C$	$N$ of CLEAR winding	Fig. 61(a)
$N_D$	$N$ of DRIVE winding	p. 55
$N_P$	$N$ of PRIME winding in the minor aperture	Fig. 63(a)
$N_R$	$N$ of a receiver input winding	Figs. 61; 62; 63(a)
$N_s$	$N$ of SET winding	p. 55
$N_T$	$N$ of a transmitter output winding	Figs. 61; 62; 63(a)
$N_x$	$N$ of ADVANCE winding in the minor aperture	Fig. 63(a)
$n$	Index of half cycle	p. 67
$n$	Number of legs of a junction	Eq. (88)
$n$	Index for a term in Fourier series	p. 130
$R^{av}$	Average radius of a circular main leg	Fig. 10
$R_i$	Inside radius of a circular main leg	Fig. 10
$R_\ell$	Resistance of a coupling loop	p. 59
$R_o$	Outside radius of a circular main leg	Fig. 10
$r$	Radius	
$r^{av}$	Average radius of a toroid	Fig. 8
$r_i$	Inside radius of a toroid	Fig. 8
$r^{min}$	Radius of a domain for which energy diagram has a minimum	Fig. 7
$r_o$	Outside radius of a toroid	Fig. 8
$r_{th}$	Radius of a domain for which energy diagram has a maximum slope	Fig. 7
$r'$	Inside radius of a high- $\mu$ region	Fig. 24
$r''$	Outside radius of a high- $\mu$ region	Fig. 24
$S_v$	Switching coefficient	Eq. (46)
$T$	Time length of MMF pulse	p. 46

# SYMBOLS

<u>Symbol</u>	<u>Definition</u>	<u>Reference</u>
$T_p$	$T$ of a preset pulse	p. 48
$t$	Time	
$t_p$	Peaking time of $\dot{\phi}_p$	Figs. 29 and 30; Eq. (42)
$V$	Magnetic scalar potential	p. 129
$V_{r_o i}$	$V$ due to $\sigma_{r_o}$ inside a circle of radius $r_o$	Eq. (114)
$V_{r_o o}$	$V$ due to $\sigma_{r_o}$ outside a circle of radius $r_o$	Eq. (115)
$V_{Ci}$	$V$ due to Current $I$ inside circle of convergence	Eq. (112)
$V_{Co}$	$V$ due to Current $I$ outside circle of convergence	Eq. (113)
$w$	Width of a leg	Fig. 19
$\alpha$	Angle formed by leg cross sections	Fig. 19
$\beta$	Angle between intersections of minor and major average paths and center of major aperture	Fig. 10
$\delta$	Angle between intersections of minor and major average paths and center of minor aperture	Fig. 10
$\epsilon$	Coefficient of elastic switching	Eq. (33)
$\epsilon_s$	$\epsilon$ in saturation	Eq. (34)
$\epsilon_{s0}$	$\epsilon_s$ at $F = 0$	Eq. (35)
$\bar{\epsilon}_s$	Average $\epsilon_s$	Eq. (36)
$\epsilon_{jk}$	$\epsilon$ of a leg equivalent to Legs $j$ and $k$ in series	e.g. Eq. (99)
$\epsilon_{j  k}$	$\epsilon$ of a leg equivalent to Legs $j$ and $k$ in parallel	e.g. Eq. (104)
$\theta$	Angle between magnetization vector and $H$	Fig. 5
$\theta$	A cylindrical coordinate	Fig. 128
$\mu_0$	Permeability of vacuum (air)	Eq. (2)
$\mu_s$	$\mu_\epsilon$ in saturation	Eq. (29)

SYMBOLS

<u>Symbol</u>	<u>Definition</u>	<u>Reference</u>
$\mu_e$	Differential elastic permeability	Eq. (24)
$\rho$	Coefficient of inelastic switching	Eq. (38)
$\bar{\rho}$	Time-averaged $\rho$	Eq. (43)
$\rho_{jk}$	$\rho$ of a leg equivalent to Legs $j$ and $k$ in series	e.g. Eq. (98)
$\rho_{j\parallel k}$	$\rho$ of a leg equivalent to Legs $j$ and $k$ in parallel	e.g. Eq. (103)
$\rho_p$	Peak $\rho$	Eq. (39)
$\rho_{\phi, av}$	Flux-averaged $\rho$	Eq. (44)
$\sigma$	Pole density	p. 130
$\sigma_{r_o}$	$\sigma$ on tube outer surface of radius $r_o$	p. 130
$\sigma_{r_i}$	$\sigma$ on tube inner surface of radius $r_i$	p. 130
$\sigma_{r_o n}$	$n$ th term of $\sigma_{r_o}$ expressed by Fourier series	p. 130
$\sigma_{r_i n}$	$n$ th term of $\sigma_{r_i}$ expressed by Fourier series	p. 131
$\tau$	Switching time	p. 30; p. 40
$\tau_f$	Fall time	p. 91
$\tau_i$	Time for complete switching of innermost ring	p. 40
$\tau_p$	Priming time	p. 65
$\phi$	Flux	
$\phi_{ps}$	$\phi$ reached by a preset pulse	p. 48
$\phi_r$	Maximum level of residual $\phi$	Fig. 9
$\phi_{r0}$	Initial flux level above which the parabolic model for $\rho$ is a good fit	Fig. 30
$\phi_{rj\parallel k}$	$\phi_r$ of a leg equivalent to Legs $j$ and $k$ in parallel	e.g. Eq. (101)
$\Delta\phi$	Change of $\phi$	
$\Delta\phi_C$	Clipped $\Delta\phi$	p. 70

# SYMBOLS

<u>Symbol</u>	<u>Definition</u>	<u>Reference</u>
$\Delta \phi_o$	Output $\Delta \phi$	p. 55
$\Delta \phi_R$	Received $\Delta \phi$	p. 67
$\Delta \phi_{res}$	Residual $\Delta \phi$	p. 45
$\Delta \phi_T$	Transmitted $\Delta \phi$	p. 67
$\Delta \phi_e$	Elastic $\Delta \phi$	p. 19
$\Delta \phi_{e_s}$	$\Delta \phi_e$ in saturation	Eq. (30)
$\dot{\phi}$	Time rate of change of $\phi$	
$\overline{\dot{\phi}}$	Average $\dot{\phi}$	p. 30
$\dot{\phi}_p$	Peak $\dot{\phi}_p$	Eq. (41)
$\dot{\phi}_e$	Elastic $\dot{\phi}$	Eq. (32)
$\dot{\phi}_p$	Inelastic $\dot{\phi}$	Eq. (38)
$\mathcal{R}$	Reluctance	p. 76



## ACKNOWLEDGMENTS

---

The criticism and contribution of Dr. D. R. Bennion and Mr. V. W. Hesterman have been most valuable, and are gratefully acknowledged.

The author also wishes to thank AMP Inc. for permission to include in this report unpublished material which has resulted from a project sponsored by AMP Inc.



## PREFACE

---

Multipath ferrite cores have been in application for more than six years. The main attractive feature of these devices is their ability to buffer between input and output circuitry, in addition to storage and nondestructive read-out characteristics. In this way, semiconductor elements may be eliminated and a higher reliability obtained.

During these years a vast amount of effort has been exerted in improving the switching properties of multipath cores (and at the same time reducing their cost) by developing better manufacturing techniques. The field of multipath-core circuitry is progressing very fast. New circuits have been invented and old ones improved. Some all-magnetic circuits (using multipath cores and wire only) for digital application have been in production for some time.

The theory of flux switching in multipath ferrite cores is complex. In addition to the complexity of the material properties, there is also the geometry factor, as a result of which more degrees of freedom are introduced. The subject of switching in multipath cores is covered in several literature sources. These sources include, among others, papers and reports based on work supported at Stanford Research Institute by Burroughs Corporation, Paoli, Pennsylvania; Office of Naval Research, Washington, D.C.; Wright Air Development Division, Wright-Patterson Air Force Base, Ohio; Air Force Cambridge Research Laboratories, Bedford, Massachusetts; and AMP, Incorporated, Harrisburg, Pennsylvania.

The objective of this report is to evaluate and organize the material published to date on flux switching in multipath cores that is scattered throughout the literature and at SRI.

A literature search has ended up with about a hundred and fifty sources which are directly or indirectly associated with multipath cores. The majority of these papers deal mostly with the application of a multipath core in logic and memory circuits. Unfortunately, the literature

on flux switching in multipath cores for its own sake has been found to be very meager, and in some papers erroneous hypotheses or conclusions have been made. In this report we have tried to organize this material and show where and why misleading statements have been made.

Initially, the intention was to write only an informal report on a literature survey. However, as soon as writing of the report was started, it was realized that a large amount of material that had been accumulated at SRI needed further work in order to present it more formally. Much of this material resulted from a project supported by AMP, Incorporated, Harrisburg, Pennsylvania. While the material was being written for this report, new ideas came about and further research was done. Many of these ideas have not, as yet, been verified experimentally; to do so is left for the remaining part of this project.

## I FLUX-SWITCHING CHARACTERISTICS

In this section we divide a multipath core into "legs," each of which may have the properties of a simple toroid. The dependence of basic switching properties of ferrite cores (toroids and multipath cores) on core material and geometry is discussed and expressed mathematically. The switching properties are then represented by electrical-circuit analogues. The dependence of  $\phi$  on  $F$  and the effect of the "history" of  $\phi$  and  $F$  on succeeding flux switching are discussed.

### A. TOROIDAL EQUIVALENCE OF A MULTIPATH CORE

#### 1. THE NEED FOR TOROIDAL EQUIVALENCE

Ever since Transfluxors were first described,<sup>1\*</sup> an effort has been made to represent multipath cores by sets of toroidal cores or their equivalents. Three of the factors for such an equivalence are as follows:

- (1) The more complex structure of a multipath core is broken into simple elements.<sup>2,3</sup> The difference among different multipath cores then amounts to the different arrays of such elements. Each of these elements has switching properties similar to those of a toroid.
- (2) A large amount of literature on the properties of toroidal cores is available. This information may be applied directly to each portion of a multipath core that can be represented by a toroid.<sup>3</sup>
- (3) Some advantageous properties of a multipath core that are not common to a single toroid may be realized by synthesizing an equivalent multipath core using toroids and coupling loops only.<sup>4</sup> This arrangement may be used both in practical circuits<sup>5</sup> and to simulate a multipath core for the purpose of measuring MMF along a portion of the core.

#### 2. LEG MODEL

Let us start by introducing the concept of a leg model. A multipath core may be divided into legs.<sup>2,3</sup> Figure 1 shows such a division for

---

\* References are listed in Sec. V, pp. 139-154.

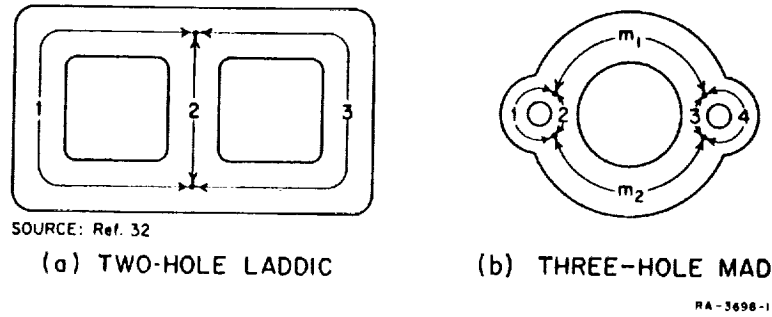


FIG. 1 DIVISION OF A MULTIPATH CORE INTO LEGS

for two types of multipath cores. In Fig. 1(a) a Laddic is divided into three legs; in Fig. 1(b) a three-hole MAD is divided into six legs. Each leg has the same switching characteristics as a toroid of the same material, cross section, and path length.

To justify this statement, refer to Fig. 2. A toroid and a leg are made of identical magnetic material, and have the same cross section and mean length. The ends of the leg are shunted by a material of infinite permeability. Assuming that the initial magnetic state of the toroid and the leg are the same, and neglecting the slight difference in pole distribution, as Current  $I$  is applied, the magnetic field intensities in the leg and along the mean path of the toroid are the same. This is so because  $F = \oint H dl = 0$  along the shunting material whose permeability is infinite. The individual small particles in the leg material cannot "know" how the magnetic path is closed, and for a given  $H$ , every particle has a unique  $B$ . Over all, since the toroid and the leg have the same  $H$  and the same cross-section, the flux in one is equal to the flux in the

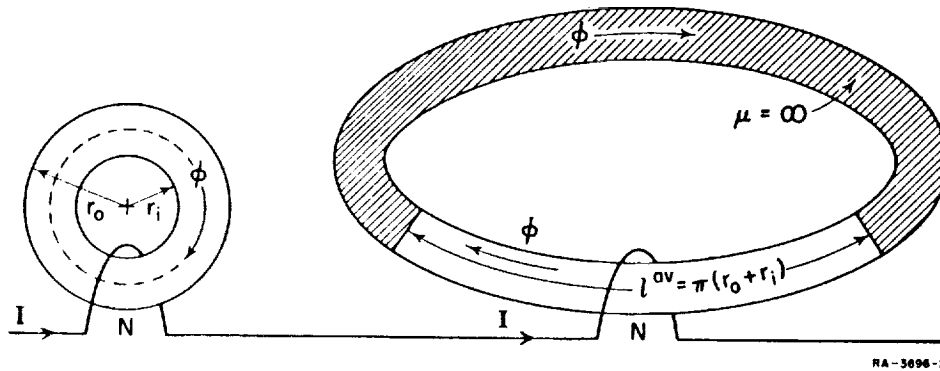


FIG. 2 EQUIVALENT TOROID AND LEG

other. Finally, since the toroid and the leg have the same relations between  $\phi$  and  $F$ , they may be considered magnetically equivalent.

### 3. RESTRICTIONS ON LEG MODEL

There are still two more points in connection with the leg model which deserve comment:

- (1) The physical boundaries of a leg are not accurately defined in some geometrical configurations. For example, legs are less clearly defined in Fig. 1(b) than in Fig. 1(a). In such configurations, the accuracy of the leg model is lower.
- (2) Although each leg in a multipath core has its own  $\phi$ - $F$  characteristics, the  $F$  and  $\phi$  of each leg are not independent of the  $F$  and  $\phi$  of the other legs. This restriction, however, is no different from that on an equivalent circuit composed of toroids. Simultaneous equations relating the various  $F$  and  $\phi$  have to be solved in both cases. We shall elaborate on this topic in Part F.

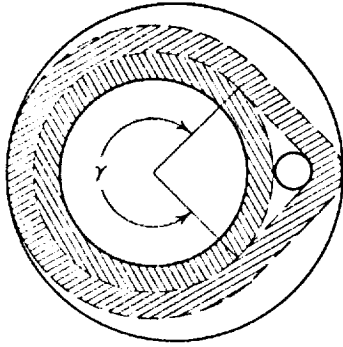
Despite these drawbacks, the leg model has been of great help in the magnetics work at SRI, both in understanding the qualitative nature of complex phenomena and in quantitatively evaluating simpler cases. With machine computation, leg models may be very useful for obtaining quantitative solutions for complex problems.

The problem of switching properties of a multipath core is, therefore, reduced initially to the problem of switching properties of a single leg. We shall now discuss the effects of material and geometry on the switching characteristics of a leg.

### 4. ERRONEOUS TOROIDAL MODEL

Before we proceed to analyze the behavior of a leg, let us briefly discuss another type of toroidal equivalence of multiaperture core which has appeared in the literature,<sup>6,7</sup> but which is not valid.

In Refs. 6 and 7, a multipath core is divided into two separate and independent toroids, as shown in Fig. 3. If such a division were physically made, switching around the minor aperture would then be impossible except for air flux. Hence, this type of division is invalid. Another way to show the fallacy of this model is to consider small particles in the material of the partial ring of angle  $\gamma$  (Fig. 3) around the major



SOURCE: Ref. 6

RA-3696-3

FIG. 3 DIVISION OF A MULTIPATH CORE INTO TWO TOROIDS

aperture. The individual particle there "does not know" whether it belongs to a toroid or a multipath core, whether the flux by the minor aperture closes in the inner path or the outer path. The only thing that can be determined about any particle is the relation between  $H$  and  $B$ . Hence, the aggregate of all small particles within the ring sector of angle  $\gamma$  should be treated as a whole leg, rather than as portions of two separate, independent toroids. We shall return later in this report to some erroneous applications based on this model.

## B. STATIC LOOPS

### 1. INTERPRETATION OF $B$ IN POLYCRYSTALLINE FERRITE

The static properties of polycrystalline ferrite are described by a  $B$ - $H$  loop, Fig. 4. A physical interpretation of  $B$  as an average quantity over a small region of material is suggested as follows.

In polycrystalline ferrite, domains are nucleated and grow in ellipsoidal or cylindrical form under the influence of  $H$ .<sup>8</sup> Consider a small ferrite particle of cross section  $\Delta A$ , Fig. 5(a), which contains several domains whose areas may be different in size. Let the area of the  $j$ th domain be denoted by  $\delta A_j$ , so that

$$\sum_j \delta A_j = \Delta A \quad (1)$$

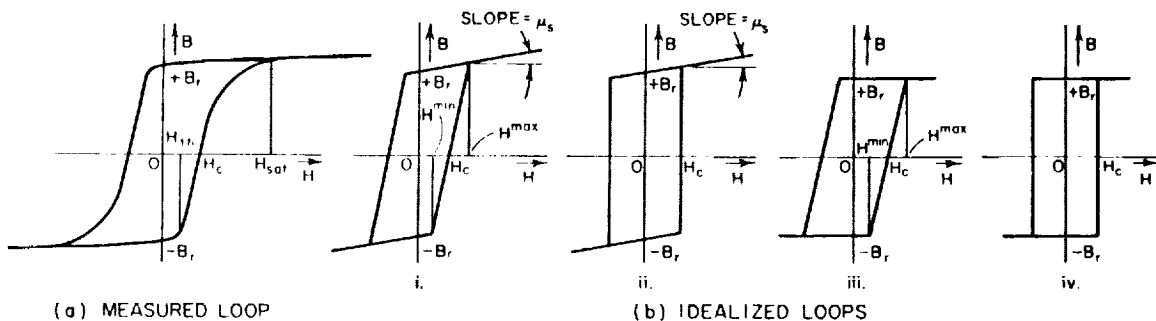
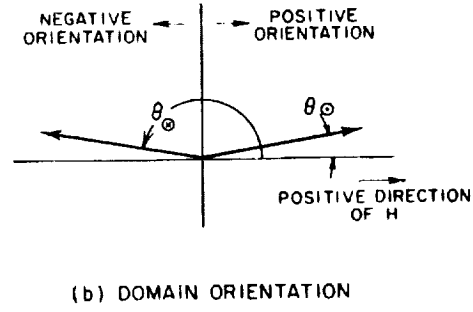
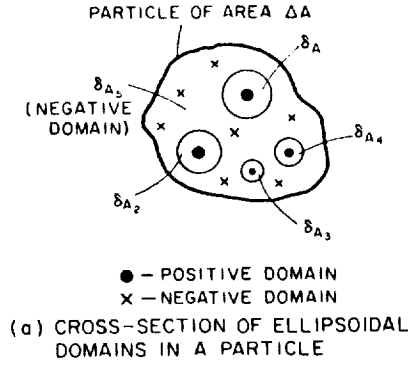


FIG. 4 STATIC  $B$ - $H$  LOOPS

RA 3696 4





RA-3696-5

FIG. 5 SHAPE AND ORIENTATION OF DOMAINS IN A FERRITE PARTICLE

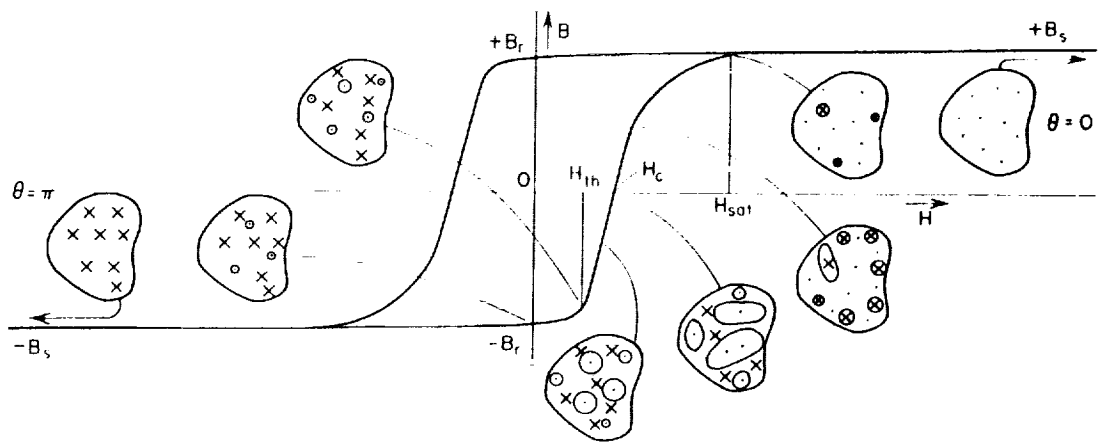
Note that the direction of magnetization in each domain is not necessarily exactly parallel or antiparallel to  $H$ . Let us denote the deviation of the magnetization of the  $j$ th domain from the direction of  $H$  (referred to as positive direction) by an angle,  $\theta_j$ . If  $0 \leq \theta_j < \pi/2$ , the domain is regarded as "positive," and if  $\pi/2 < \theta_j \leq \pi$ , the domain is regarded as "negative." Let  $B_s = \mu_0 M_s$ , where  $M_s$  is the saturation magnetization of the material. Summing over all the positive and negative domains in  $\Delta A$ , the  $B$  of the particle is,

$$B = B_s \frac{\sum_j \delta A_j \cos \theta_j}{\Delta A} + \mu_0 H \quad (2)$$

in which  $\mu_0 H$  is commonly known as the air-flux density.

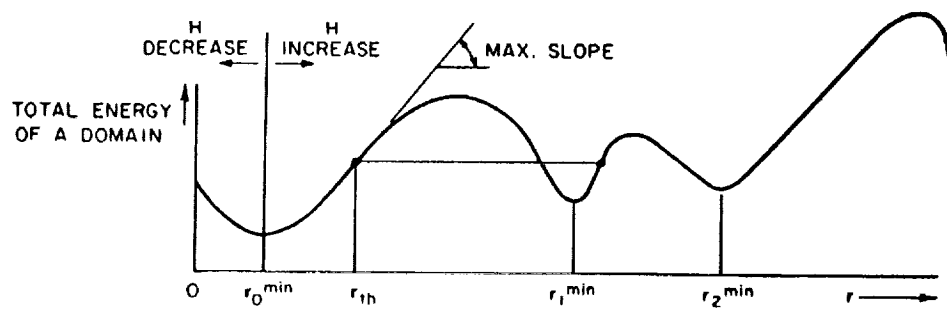
## 2. $B(H)$ AND DOMAIN GROWTH

Consider Fig. 6, and let  $H$  be highly negative. The particle, then, acts as a single negative domain whose  $\theta = \pi$ . Following Eq. (2),  $B = -B_s + \mu_0 H$ . Now let  $H$  be released. As  $H \rightarrow 0$ ,  $\theta$  decreases (rotation of magnetization in a domain) and a few small positive domains may nucleate around inclusions, crystal boundaries, voids and imperfections. The particle is now at its remanent state  $B = -B_r$ . According to the schematic static wall-energy diagram of Fig. 7, in this state a cylindrical,  $j$ th, positive domain rests at its point of minimum energy, so that its radius is equal



RA 1696 6

FIG. 6 B-H CHARACTERISTIC OF A FERRITE PARTICLE



RA-5698-7

FIG. 7 SCHEMATIC PLOT OF ENERGY OF ELLIPSOIDAL DOMAIN vs. CROSS-SECTIONAL RADIUS

to  $r_0^{\min}$ . Now let  $H$  increase slowly in the positive direction. The radius of the domain increases in accordance with its energy-versus-radius curve, Fig. 7. At  $H = H_{th}$  the maximum slope of the energy curve is reached,  $r = r_{th}$ , and the domain would "spill over" the energy hill to a new energy valley and stay at  $r > r_1^{\min}$ . [If  $H$  is now released,  $r$  drops back to  $r_1^{\min}$  and, following Eq. (2),  $B > -B_r$ .] Note that the knee of the  $B$ - $H$  loop is not sharp because of the variations in  $H_{th}$  among domains throughout the material. As  $H$  increases further, the cylindrical positive domains expand and new ones may be nucleated. As  $H$  approaches  $H_c$ , a few of them will collide, forming larger domains, Fig. 6. Most of the domains collide at  $H = H_c$ , but some may collide at values of  $H$  above or below  $H_c$ . By now,  $\sum_j \delta A_j \cos \theta_j = 0$ , hence  $B = \mu_0 H \approx 0$ . Collisions of cylindrical positive domains will result in development of more-or-less-cylindrical negative domains.<sup>9</sup> As  $H$  increases beyond  $H_c$ , the radii of these negative domains decrease, and at positive saturation, they disappear.

It should be emphasized that Fig. 7 represents only a static energy diagram, not a dynamic energy diagram corresponding to a finite domain-wall velocity, and as such can only be used to describe small displacements of  $r$  around minimum values  $r_j^{\min}$ .

### 3. $\phi$ - $F$ LOOP OF TOROID

So far we have discussed the  $B$ - $H$  loop of ferrite material. In practice, the  $\phi$ - $F$  loop rather than  $B$ - $H$  loop is measured. Consider a toroidal core, Fig. 8. Its (static)  $\phi$ - $F$  loop, Fig. 9, depends on the material property ( $B$ - $H$  loop) and geometry ( $r_o$ ,  $r_i$ ,  $h$ ):

$$d^{th} = 2\pi r_i H_{th} \quad (3)$$

$$d^{sat} = 2\pi r_o H_{sat} \quad (4)$$

$$\phi_r = B_r A = B_r h(r_o - r_i) \quad (5)$$

The  $\phi$ - $F$  loop in Fig. 9 is piecewise linearized around the curved knees by dotted lines whose intersections define  $d^{\min}$  and  $d^{\max}$ . To simplify analysis and design,  $d^{\min}$  and  $d^{\max}$ , rather than  $d^{th}$  and  $d^{sat}$ , are most commonly used.

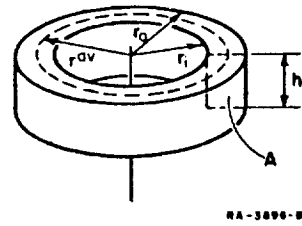


FIG. 8 TOROIDAL CORE

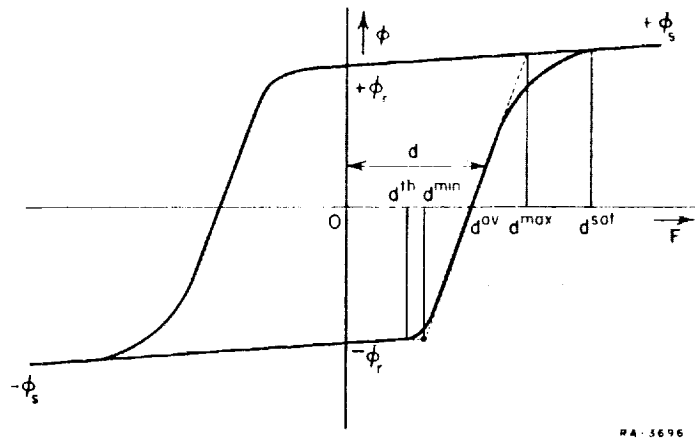
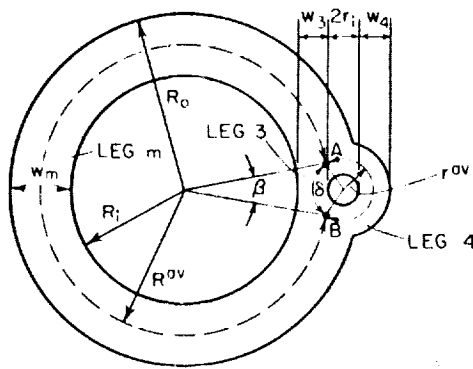


FIG. 9 STATIC  $\phi$ -F LOOP

#### 4. $\phi$ -F LOOPS OF A MULTIPATH CORE

Consider, for example, the multipath core in Fig. 10. First we divide it into three legs: legs  $m$ , 3, and 4. Such a division should be considered as an approximation and is made according to the following steps:

- (1) The average paths around the two apertures are determined. Around the major aperture,  $R^{av} = \frac{1}{2}(R_o + R_i)$ ; around the minor aperture,  $r^{av} = r_i + \frac{1}{4}(w_3 + w_4)$ .



- (2) The two intersection points, A and B, of the two average paths form angles  $\beta$  and  $\delta$  with the centers of the major and minor apertures.

- (3) Points A and B define Legs  $m$ , 3, and 4, as shown in Fig. 10. The minimum, maximum, and average lengths of these legs are evaluated as follows:

FIG. 10 DIVISION OF A THREE-LEG CORE INTO LEGS

(a)  $l^{\min}$  is determined by the inner ring of switching:

$$l_m^{\min} = 2\pi R_i \left(1 - \frac{\beta}{2\pi}\right) \quad (6)$$

$$l_3^{\min} = 2\pi r_i \frac{\delta}{2\pi} \quad (7)$$

$$l_4^{\min} = 2\pi r_i \left(1 - \frac{\delta}{2\pi}\right) \quad (8)$$

(b)  $l^{\max}$  is determined by the outer ring of switching:

$$l_m^{\max} = 2\pi R_o \left(1 - \frac{\beta}{2\pi}\right) \quad (9)$$

$$l_3^{\max} = \pi(2r_i + w_3 + w_4) \frac{\delta}{2\pi} \quad (10)$$

$$l_4^{\max} = \pi(2r_i + w_3 + w_4) \left(1 - \frac{\delta}{2\pi}\right) \quad (11)$$

(c)  $l^{\Delta v}$  is determined from  $l^{\min}$  and  $l^{\max}$ :

$$l_m^{\Delta v} = \pi(R_i + R_o) \left(1 - \frac{\beta}{2\pi}\right) \quad (12)$$

$$l_3^{\Delta v} = \pi \frac{4r_i + w_3 + w_4}{2} \frac{\delta}{2\pi} \quad (13)$$

$$l_4^{\Delta v} = \pi \frac{4r_i + w_3 + w_4}{2} \left(1 - \frac{\delta}{2\pi}\right) \quad (14)$$

Assuming that the  $B$ - $H$  loop is ideal, as in Fig. 4(b)i, we may now compute and plot the  $\phi$ - $F$  loops of Legs  $m$ , 3, and 4. For any leg, in general,

$$d^{\text{th}} = l^{\min} \cdot H^{\min} \quad (15)$$

and

$$d^{\text{sat}} = l^{\max} \cdot H^{\max} \quad (16)$$

Since  $d^{\min}$  and  $d^{\max}$  are defined as the values of  $F$  obtained by extrapolating the linear portion of the  $\phi$ - $F$  loop to  $\phi = -\phi_r$  and  $\phi = +\phi_r$ , as shown in Fig. 9, an average value of  $d$  is then defined as

$$d^{\text{av}} = \frac{d^{\min} + d^{\max}}{2} \quad (17)$$

For the sake of simplification, a  $\phi$ - $F$  loop may be approximated by a parallelogram defined by  $d^{\min}$  and  $d^{\max}$ . For the case where  $w_3 = w_4 = \frac{1}{2}(R_o - R_i)$  (Fig. 10), the linearized  $\phi$ - $F$  loops of the three legs are shown in Fig. 11.

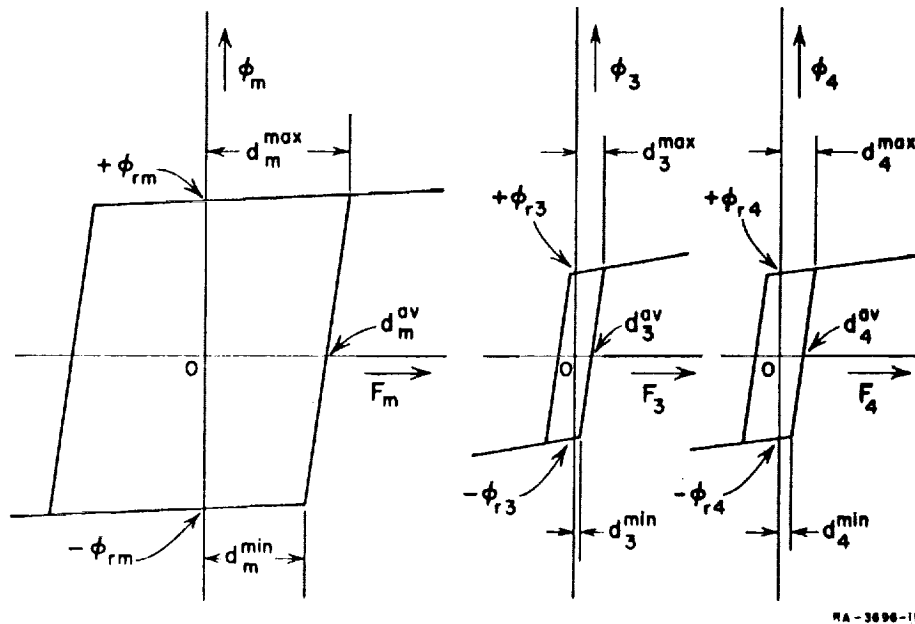


FIG. 11 STATIC  $\phi$ - $F$  LOOPS OF LEGS  $m$ , 3 AND 4

Note that  $H^{\min}$  and  $H^{\max}$  may be determined from testing the multipath core as if it were a toroid.

Determination of the  $\phi$ - $F$  loop of a three-leg MAD was given as an illustration. The process with multipath cores of other geometry is similar.

### C. MECHANISM OF FLUX SWITCHING

In this part an attempt is made to describe the physical mechanism of flux switching in polycrystalline ferrite.

#### 1. ELASTIC SWITCHING FROM QUIESCENT STATE

Consider a ferrite particle, of cross-sectional area  $\Delta A$ , which is in the quiescent state  $B = -B_r$ . In general, there will be a few small positive domains in  $\Delta A$ . Let us look at one of these domains in relation to its (schematic) static energy curve, shown in Fig. 12. The cross section of this domain, as well as  $\Delta A$ , lie in the  $y$ - $z$  plane. Initially the domain radius is  $r_0^{\min}$  and its saturation flux density,  $B_s$ , points at an angle  $\theta_0^{\min}$  away from the  $x$  axis. A positive change in  $H$ ,  $\Delta H_a$ , which is smaller than  $H_{th}$ , is applied along the  $x$  axis. This causes  $B$  to change for two reasons:

- (1) Growth of domain area from  $\pi r_0^{\min 2}$  to  $\pi(r_0^{\min} + \Delta r)^2$
- (2) Rotation of  $B_s$  by a negative angle  $\Delta\theta$ .

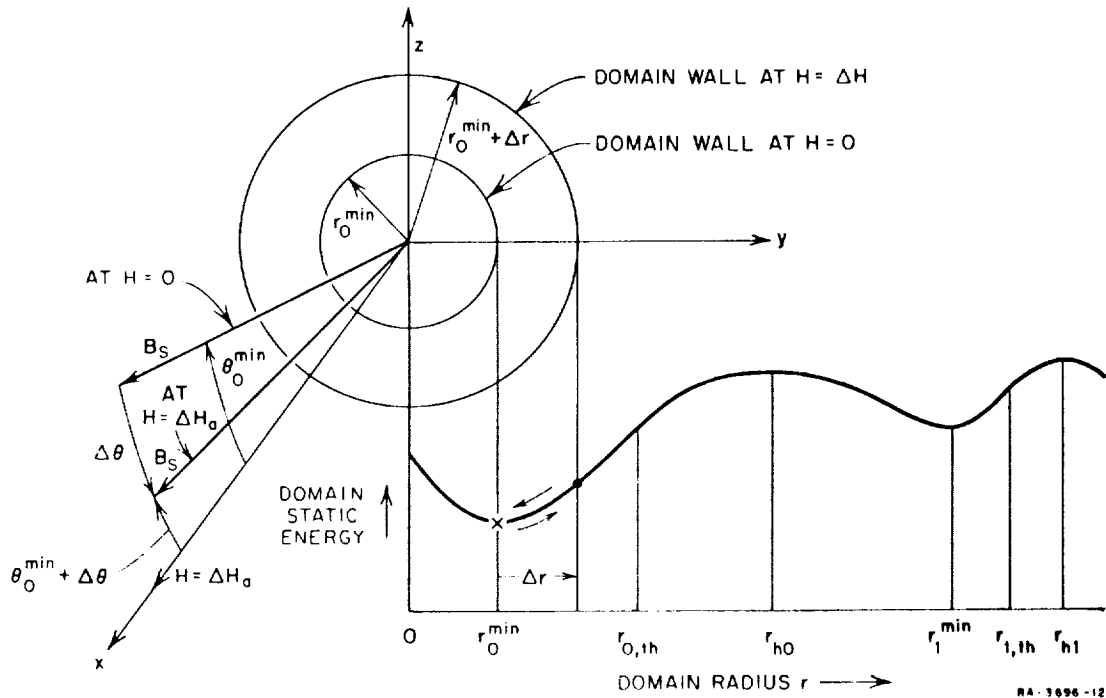


FIG. 12 MECHANISM OF ELASTIC-FLUX SWITCHING

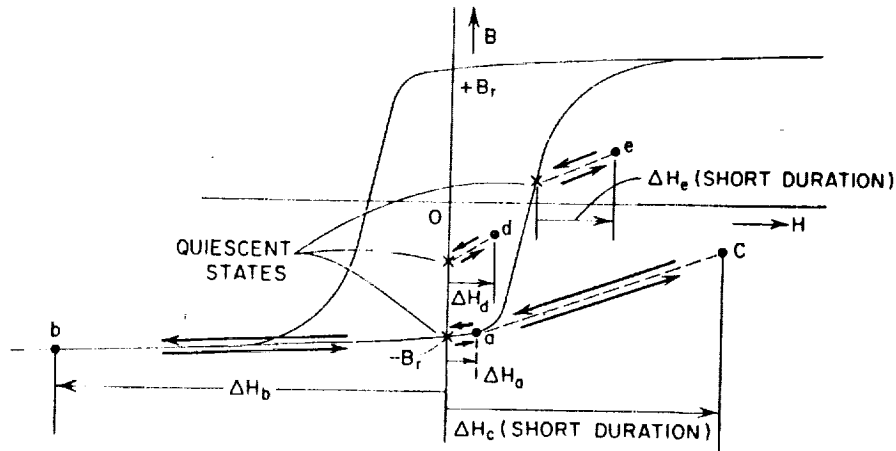
Using Eq. (2), the change in flux density due to all positive domains is

$$\Delta B^{(+)} = \frac{B_s}{\Delta A} \pi \sum_{\text{positive domains}} [(r_{0j}^{\min} + \Delta r_j)^2 \cos(\theta_{0j}^{\min} + \Delta \theta_j) - r_{0j}^{\min 2} \cos \theta_{0j}^{\min}] \quad (18)$$

At the same time there may be some rotation of magnetization in the negative domain(s), which contributes  $\Delta B^{(-)}$  to  $\Delta B$ . Including the air flux density, the over-all change in  $B$  is

$$\Delta B = \Delta B^{(+)} + \Delta B^{(-)} + \mu_0 \Delta H_a \quad (19)$$

This change in  $B$  is shown in Fig. 13 (Point a).



NA-3696-13

FIG. 13 ELASTIC CHANGES IN B

The domain in Fig. 12 stays in this state ( $r = r_0^{\min} + \Delta r$ ;  $\theta = \theta_0^{\min} + \Delta \theta$ ) as long as  $H$  is not changed. When  $\Delta H_a$  is removed, the domain returns to its original state ( $r = r_0^{\min}$ ;  $\theta = \theta_0^{\min}$ ). Similarly, all the other positive and negative domains, as well as air flux, return to their initial state. In other words, when  $\Delta H_a$  is removed, there is a change in  $B$  equal to that of Eq. (19), but opposite in sign (see Fig. 13). We see that the net change in  $B$ , caused by the application and removal of  $\Delta H_a$ , is zero. Therefore, the change in  $B$  due to  $\Delta H_a$ , Eq. (19), is elastic (reversible) in nature.



If, instead of a positive  $\Delta H$ , a negative  $\Delta H$ ,  $\Delta H_b$  is applied, the particle will be pushed into negative saturation. The positive domain in Fig. 12 will shrink and its magnetization will rotate in a direction toward the negative  $\Delta H_b$ . In fact, the rotation may even change the polarity of this domain, or the domain may shrink to nothing by wall motion. Changes of this sort amount to annihilation of a number of positive domains. Additional contribution to  $\Delta B$  comes from rotation of magnetization in the negative domain(s) in a direction to align the domain with  $\Delta H_b$ . Again, the over-all (negative) change in  $B$  is elastic because, when  $\Delta H_b$  is removed,  $B$  changes by the same amount in the positive direction. Since  $\Delta H_b$  pushes the particle into (negative) saturation,  $\Delta B$  is completely elastic, regardless of the magnitude of  $\Delta H_b$ .

Let us consider once more a positive  $\Delta H$ ,  $\Delta H_c$ , applied to the particle in the quiescent, remanent state  $B = -B_r$ . This time, however, let  $\Delta H_c$  be a high triangular pulse of very short duration  $T$  (see Fig. 13). Referring back to Fig. 12, one can see that the domain starts growing; however, since  $T$  is so short, the domain will not have the chance to grow beyond its first hill. On the other hand, since rotation of magnetization is much faster than domain wall motion, the magnetization will tend to align itself with the direction of  $\Delta H_c$ . In the same manner, all the other positive domains will align themselves with  $\Delta H_c$ , and new (positive) domains will nucleate, resulting in a positive contribution to  $\Delta B$ . Additional contribution to  $\Delta B$  comes from magnetization rotation of the negative domain(s) and  $\mu_0 \Delta H_c$ . The total  $\Delta B$  is essentially elastic because positive domains do not expand beyond their first energy hills, and as  $\Delta H_c$  drops to zero, almost all the domains return to their original size and orientation.

Elastic changes in  $B$  may also start from other quiescent states inside the static  $B$ - $H$  loop or on its boundary, provided that  $\Delta H$  or its duration is limited. Elastic excursions of this type, caused by  $\Delta H_d$  and  $\Delta H_e$ , are illustrated in Fig. 13.

## 2. NATURE OF INELASTIC SWITCHING

Let a particle be at negative remanent state,  $B = -B_r$ . A positive  $\Delta H$ , this time larger than  $H_{th}$ , is applied. The radius of the domain in Fig. 12 exceeds  $r_{h0}$ , so that the domain sweeps over the first energy hill and may go beyond other hills. Once the domain wall is beyond the first hill, if  $\Delta H$  is removed, the net  $\Delta B$  due to the application and

removal of  $\Delta H$  is positive. This is so because the succeeding valleys of minimum energy, which may trap the wall, correspond to radii equal to or larger than  $r_1^{\min}$ . The change in  $B$  in this case is regarded as inelastic (irreversible).

Domains continue to grow as long as  $H$  is beyond their threshold values, because energy hills no longer obstruct them. Therefore, in-

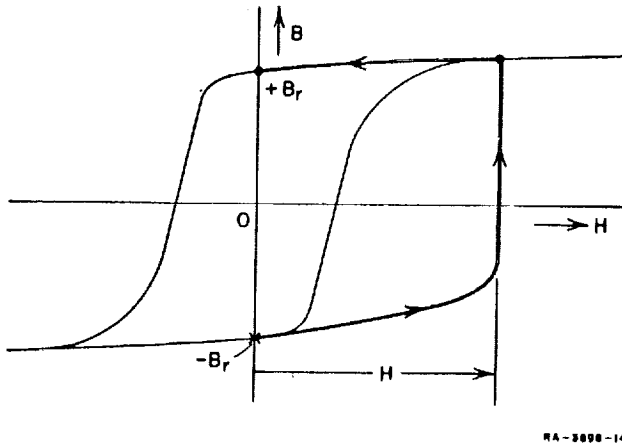


FIG. 14 INELASTIC CHANGE IN  $B$

elastic switching does not depend on the rate of change of  $H$ , but rather on the magnitude of  $H$ . In fact, the more  $H$  exceeds its threshold value (the value determined by the slope of the nearest hill), the faster is the domain wall motion. Figure 14, for example, shows the  $B$ - $H$  path followed as  $B$  changes inelastically under an  $H$  pulse of trapezoidal shape.

### 3. COMBINED CHANGE IN $B$

An inelastic change of a domain is preceded by an elastic change of its size and orientation. Similar changes occur with other positive domains, including the newly created ones. When all the domains in the particle are considered, it is possible for some domains to be beyond their first hills, while others have not yet reached theirs. In terms of the elastic change in  $B$ ,  $\Delta B_e$ , and the inelastic change in  $B$ ,  $\Delta B_p$ , the over-all change in  $B$  is

$$\Delta B = \Delta B_e + \Delta B_p \quad (20)$$

Now consider the case in which domains are growing under the influence of a positive  $H$  (say,  $H$  constant) when  $H$  is suddenly reduced to zero. This change in  $H$  causes magnetization to rotate (a negative contribution to  $\Delta B$ ), and domains to shrink or continue to expand in order to reach their nearest minimum-energy radii. (Due to variation in static energy, domain walls slow down when their radii fall between  $r_j^{\min}$  and  $r_{hj}$ , Fig. 12, and increase speed when their radii fall between  $r_{hj}$  and  $r_{j+1}^{\min}$ . As a result, more domains are expected to shrink than to expand, causing a small negative contribution to  $\Delta B$ .)

When  $B$  is not close to  $-B_r$ , the effects of shrinkage and expansion of domains tend to cancel. This argument suggests that for the same  $B$  and  $\Delta H$ , the  $\Delta B_e$  following elastic and inelastic change in  $B$ , Path a, Fig. 15, is likely to be smaller than the corresponding  $\Delta B_e$  following a purely elastic change in  $B$ , Path b, Fig. 15.

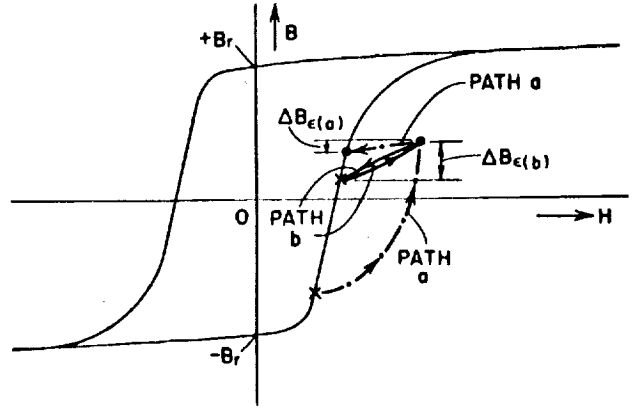


FIG. 15 EFFECT OF  $\Delta B$  HISTORY ON  $\Delta B_e$

Note that the terms *elastic* and *inelastic* refer to changes in  $B$ , while they are taking place. The contribution of an average domain that has passed beyond its first energy hill is limited to a contribution to future  $\Delta B_e$ , which will be determined by the relative position of the domain radius in the energy curve when, at some later instant,  $H$  falls below its threshold value. In other words,  $\Delta B_e$  is determined during a fast fall of  $H$  to a value inside or on the static loop. If  $H$  falls slowly, both negative  $\Delta B_e$  (mainly due to rotation) and positive  $\Delta B_p$  are present, and  $\Delta B$  follows Eq. (20). Figure 16 shows the different paths followed by the operating point in the  $B$ - $H$  plane for a short and a long fall time of  $H$ . In the former case there is not enough time for domain

walls to move during the fall time; therefore the resulting  $\Delta B_p$  is smaller than in the latter case.

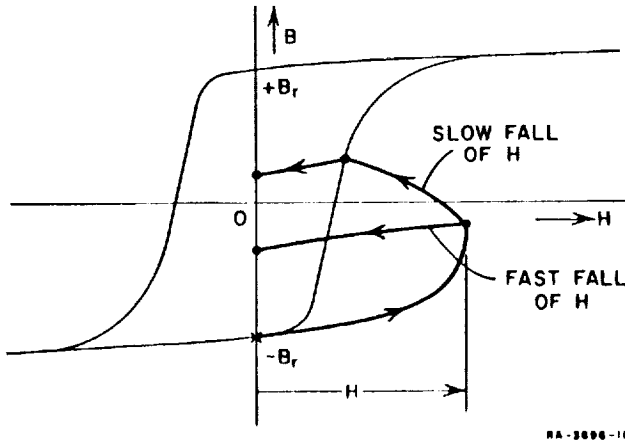


FIG. 16  $\Delta B_e$  AND  $\Delta B_p$  DURING FALL TIME OF  $H$

#### 4. $dB/dt$

Equation (2) holds in both static and dynamic conditions. Differentiating this equation with respect to time, we get

$$\dot{B} = \dot{B}_A + \dot{B}_\theta + \dot{B}_{\text{irr}} \quad (21)$$

in which

$$\dot{B}_A = \frac{B_s}{\Delta A} \sum_j \cos \theta_j \frac{d}{dt} \delta A_j, \quad (21a)$$

$$\dot{B}_\theta = -\frac{B_s}{\Delta A} \sum_j \delta A_j \sin \theta_j \frac{d\theta_j}{dt}, \quad (21b)$$

and

$$\dot{B}_{air} = \mu_0 \frac{dH}{dt}. \quad (21c)$$

The term  $\dot{B}_A$  in Eq. (21a) is generated by domain wall motion; the term  $\dot{B}_\theta$  in Eq. (21b) comes from rotation of magnetization; and the last term,  $\dot{B}_{air}$  in Eq. (21c), is due to change in air flux.

The expressions of  $\dot{B}$ , Eq. (21), may be used to describe elastic  $\dot{B}$ ,  $\dot{B}_e$ , and inelastic  $\dot{B}$ ,  $\dot{B}_\rho$ . Adding the elastic components of these expressions, we obtain

$$\dot{B}_e = \dot{B}_{eA} + \dot{B}_{e\theta} + \dot{B}_{air}. \quad (22)$$

From our previous discussion, it will be recalled that the signs of  $\dot{B}_{e\theta}$  and  $\dot{B}_{air}$  are always the same as that of  $\dot{H}$ . The sign of  $\dot{B}_{eA}$  is also the same as that of  $\dot{H}$ , especially if  $B$  changes by a small amount near a quiescent state. Therefore, the sign of  $\dot{B}_e$  can be assumed always to follow that of  $\dot{H}$ . Since the contribution from each domain to the term  $\dot{B}_{eA}$  is proportional to the domain circumference, and the contribution to the term  $\dot{B}_{e\theta}$  is proportional to the domain area, both terms will increase when domains are large. Hence,  $\dot{B}_e$ , as a function of  $B$ , is expected to reach a peak around  $B = 0$ .

Adding the inelastic components of  $\dot{B}_A$  and  $\dot{B}_\theta$ , Eq. (21), we obtain

$$\dot{B}_\rho = \dot{B}_{\rho A} + \dot{B}_{\rho\theta}. \quad (23)$$

There is no direct connection between the sign of  $\dot{B}_\rho$  and the sign of  $\dot{H}$ .  $\dot{B}_\rho$  is only affected by the excess of  $H$  over some threshold.

Provided  $\dot{B}_\rho$  is not too low,  $\dot{B}_\rho(B)$  will reach a peak around  $B = 0$  for two reasons:

- (1) The contribution of each domain to  $\dot{B}_{\rho A}$  is proportional to domain circumference and around  $B = 0$  the total domain-wall length is likely to be large.
- (2) During domain collisions, sharp corners of the combined domains smooth out in order to reduce wall area, and thus minimize their energy ("surface tension").

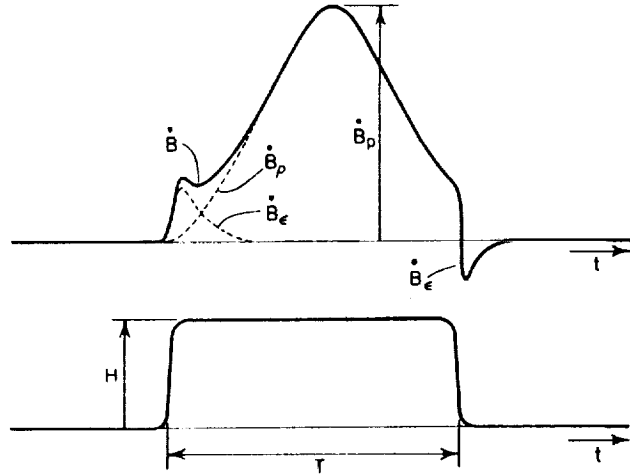
A typical waveshape of  $\dot{B}$ , generated by a constant  $\dot{H}$ , is shown in Fig. 17. It has been reported<sup>10</sup> that  $\dot{B}_e$  lags behind  $\dot{H}$ . Further investigation is needed to determine the nature of this relaxation process. The division of  $\dot{B}$  into  $\dot{B}_e$  and  $\dot{B}_\rho$ , following the application of  $\dot{H}$ , is explained in Part E-1.

#### D. ELASTIC SWITCHING MODELS

##### 1. ELASTIC PERMEABILITY

The characteristic of elastic switching  $\Delta B_e$  due to  $\Delta H$  may be described in terms of the differential elastic permeability

$$\mu_e = \frac{d\Delta B_e}{dH} \quad (24)$$



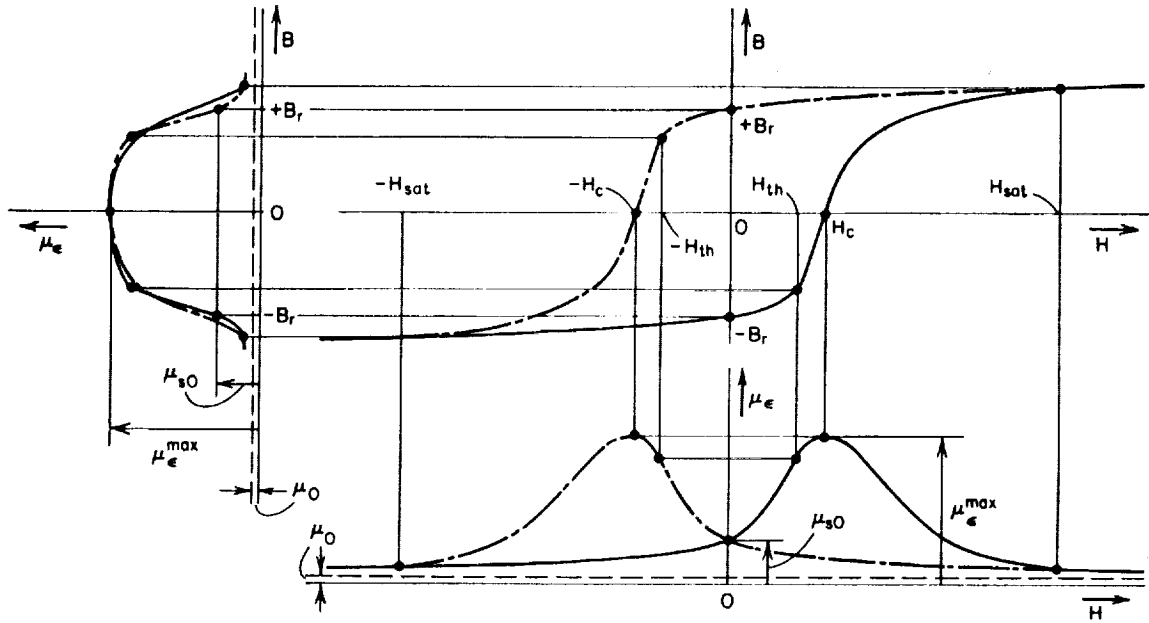
RA-3696-17

FIG. 17 TYPICAL  $\dot{B}$  WAVESHAPE ( $\Delta B < 2 B_r$ )

In positive and negative saturation,  $\Delta B_e(H)$  follows the static  $B-H$  loop, shown in Fig. 4. Denoting  $\mu_e$  in saturation by  $\mu_s$ ,  $\mu_s = dB/dH$ . In the region  $-B_r \leq B \leq +B_r$ ,

$$\mu_e = \frac{d(\Delta B - \Delta B_\rho)}{dH} \quad (25)$$

The physical mechanism of elastic switching, discussed previously, calls for  $\mu_e$  to be approximately symmetrical with respect to  $B$ , peaking near  $B = 0$ . Figure 18 shows the variations of  $\mu_e$  with  $B$  and  $H$ , constructed in conjunction with the  $B-H$  loop.



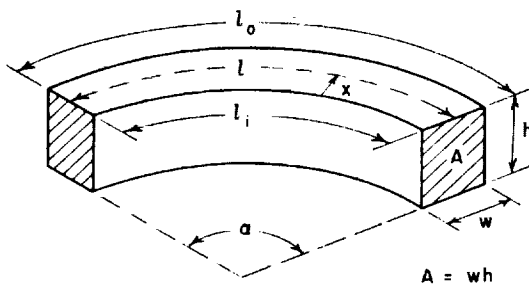
RA-5696-18

FIG. 18 VARIATION OF  $\mu_e$  WITH B AND H

## 2. CALCULATED $\Delta\phi_e$ IN SATURATION

Consider a leg, Fig. 19, of constant width  $w$ , height  $h$ , angle  $\alpha$ , length of inner edge  $l_i$ , and length of outer edge  $l_o$ . The cross-hatched sections at the ends of the leg are perpendicular to the inner and outer edges. Let  $l$  be the length of a path whose (radial) distance from the inner edge is  $x$ . It is shown in Appendix A that

$$l = l_i + \alpha x = l_i + \frac{l_o - l_i}{w} x \quad (26)$$



RA 5696-19

FIG. 19 A LEG

This relation holds for any shape of constant-width leg in a multipath core, including a toroid. (In the case of a toroid,  $\alpha = 2\pi$ ,  $w = r_o - r_i$ ,  $l_i = 2\pi r_i$ , and  $l_o = 2\pi r_o$ .) The elastic change of flux,  $\Delta\phi_e$ , can be calculated from these geometry properties and  $\mu_e$ .

Assume that the leg is initially at negative remanent state  $\phi = -\phi_r$ ,

Fig. 20. Negative constant  $F$  is applied, pushing the leg elastically into negative saturation. Assuming that  $\mu_s$  is constant [Loop (b) in Fig. 4], it is shown in Appendix B that the resulting elastic flux change in saturation, denoted by  $\Delta\phi_{\epsilon_s}$ , is

$$\Delta\phi_{\epsilon_s} = F\mu_s h \frac{w}{l_o - l_i} \ln \frac{l_o}{l_i} \quad (27)$$

For the case of a toroid,  $(l_o - l_i)/w$  is replaced by  $2\pi$ , and  $l_o/l_i$  by  $r_o/r_i$ . This agrees with the  $\Delta\phi_{\epsilon_s}$  calculated for a toroid on p. 22 of Ref. 11.

A better approximation for  $\mu_s$  may be obtained by describing the material component of  $B(H)$ , denoted by  $B_m(H)$ , by a hyperbola, Fig. 21. Adding the linear air component,  $B_{air}$ , changes the total  $B$  in negative saturation to

$$B = -B_r + (B_s - B_r) \frac{H}{a - H} + \mu_0 H \quad (28)$$

where  $a$  is a model parameter.

Following Eq. (24), the hyperbolic model for  $\mu_s$  is

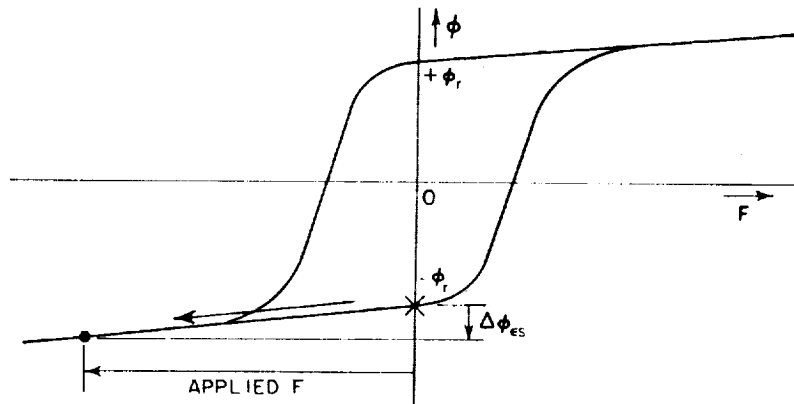
$$\mu_s = (B_s - B_r) \frac{a}{(a - H)^2} + \mu_0 \quad (29)$$

A plot of  $\mu_s$  versus  $H$  is shown in Fig. 22. This model is applied in Appendix B to calculate  $\Delta\phi_{\epsilon}$  of a saturated leg as a function of  $F$ . The result is

$$\Delta\phi_{\epsilon_s} = Fh \frac{w}{l_o - l_i} \left( \frac{B_s - B_r}{a} \ln \frac{F - al_o}{F - al_i} + \mu_0 \ln \frac{l_o}{l_i} \right) \quad (30)$$

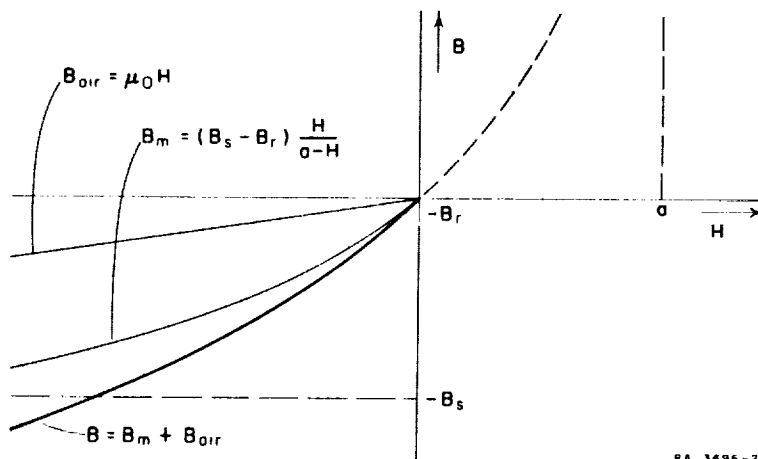
A plot of  $\Delta\phi_{\epsilon_s}$  versus  $F$  is shown in Fig. 23.

In positive saturation Eq. (30) is modified by having plus signs in front of the terms  $al_o$  and  $al_i$ .



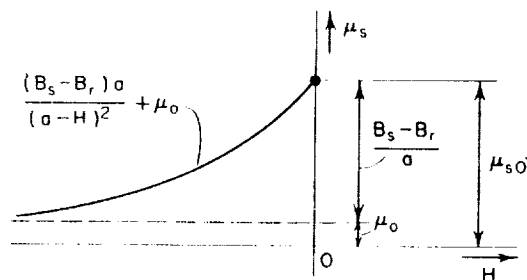
RA-3696-20

FIG. 20  $\Delta\phi_e$  IN NEGATIVE SATURATION CAUSED BY APPLIED F



RA 3696-21

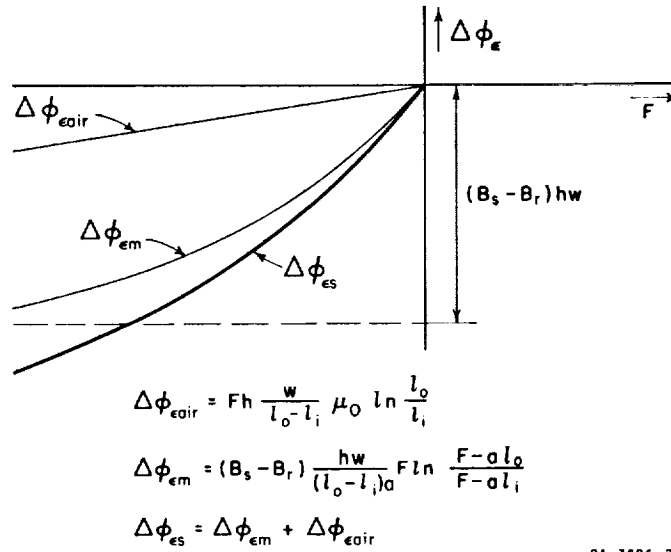
FIG. 21 HYPERBOLIC MODEL FOR  $B(H)$  IN NEGATIVE SATURATION



RA-3696-22

FIG. 22 HYPERBOLIC MODEL FOR  $\mu_e$  IN NEGATIVE SATURATION





RA-3696-23

FIG. 23 HYPERBOLIC MODEL FOR  $\Delta\phi_\epsilon$  OF A LEG IN NEGATIVE SATURATION

Calculation of  $\Delta\phi_\epsilon(F, \phi)$  in the region  $-\phi_r < \phi < \phi_r$  is much more complex. In Fig. 24, three regions are distinguished: Region I is in positive saturation; Region III is in negative saturation; and Region II is between saturations. In calculating  $\Delta\phi_\epsilon$ , the limits of integration  $r'$  and  $r''$  are functions of  $F$ .

In Ref. 12,  $\dot{\phi}_\epsilon$  is plotted versus  $\phi$  in the region  $-\phi_r \leq \phi \leq \phi_r$ . It is shown there that the "history" of  $\phi$  has an important effect on  $\dot{\phi}_\epsilon$ . For a given  $\phi$ ,  $\dot{\phi}_\epsilon$  is higher if, to get to  $\phi$  (from  $-\phi_r$ ), a prepulse of higher amplitude and shorter duration is used (see Fig. 25). An attempt is made to get a best-fit mathematical formula which describes  $\dot{\phi}_\epsilon$  as a function of  $F$  and  $\phi$ , but unfortunately, the article is both short and vague. Further investigation in this area is needed.

### 3. SWITCHING INDUCTANCE

Unlike inelastic switching, elastic switching must be generated by a change in  $H$ . The elastic component of the time-rate of change of  $B$  is, therefore, written as

$$\dot{B}_\epsilon = \frac{d \Delta B_\epsilon}{dH} \frac{dH}{dt} = \mu_\epsilon \dot{H} \quad (31)$$

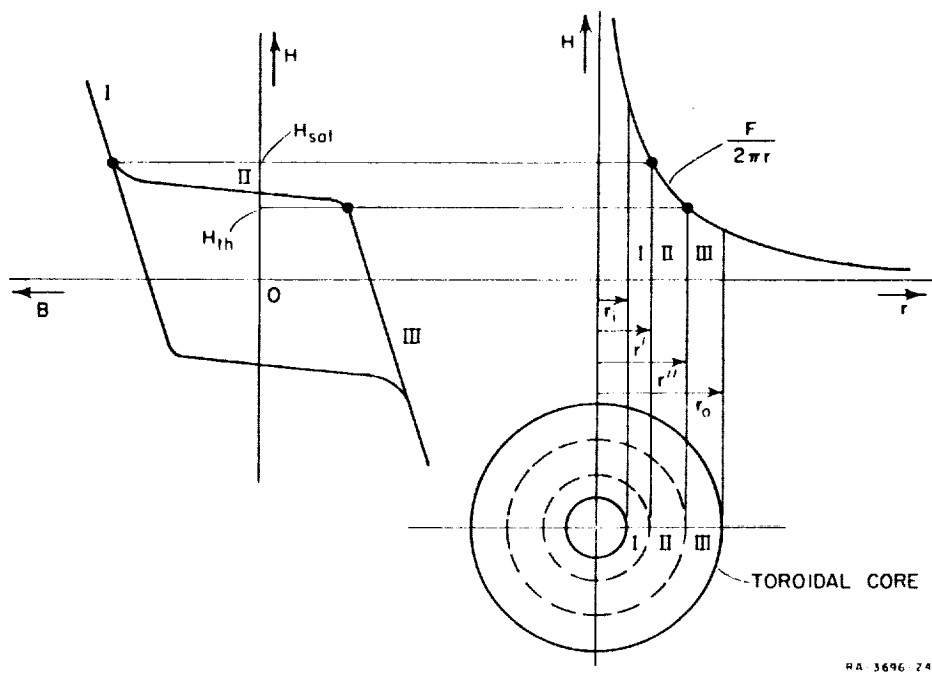


FIG. 24 THREE REGIONS IN A TOROID

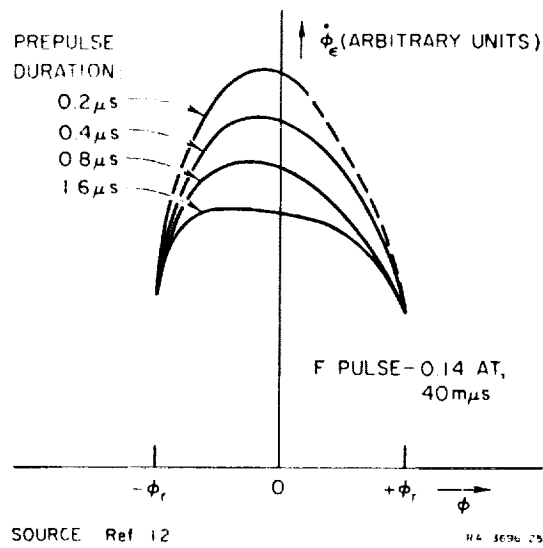


FIG. 25  $\dot{\phi}_e$  (Generated by F) vs.  $\phi$  AND PREPULSE DURATION

Similarly, considering the over-all cross section of a leg, the elastic component of  $\dot{\phi}$  may be expressed by

$$\dot{\phi}_e = \epsilon \dot{F} \quad (32)$$

where

$$\epsilon = \frac{d \Delta \phi_e}{dF} \quad (33)$$

Note that  $\epsilon$  may be regarded as switching inductance per turn squared.

Following Eq. (33), differentiating  $\Delta \phi_{e,s}$ , Eq. (30), with respect to  $F$  results in an expression for  $\epsilon$  in saturation,

$$\epsilon_s = \frac{hw}{l_o - l_i} \left\{ (B_s - B_r) \left[ \frac{(l_o - l_i)F}{(F - al_o)(F - al_i)} + \frac{1}{a} \ln \frac{F - al_o}{F - al_i} \right] + \mu_0 \ln \frac{l_o}{l_i} \right\} \quad (34)$$

For the special case of remanent state ( $F = 0$ ),  $\epsilon_s(F)$  becomes

$$\epsilon_{s,0} = \frac{hw}{l_o - l_i} \left( \frac{B_s - B_r}{a} + \mu_0 \right) \ln \frac{l_o}{l_i} \quad (35)$$

A plot of  $\epsilon_s(F)$  in negative saturation, based on Eq. (34), is shown in Fig. 26.

No model has been suggested yet for  $\epsilon(F)$  in the region  $-\phi_r < \phi < \phi_r$ . Further investigation is needed.

#### 4. AVERAGE SWITCHING INDUCTANCE

The nonlinear value of  $\epsilon_s$ , Eq. (34), is too complex for manual computation. In order to simplify the computation, a constant, average value of  $\epsilon_s$ , denoted by  $\bar{\epsilon}_s$ ,

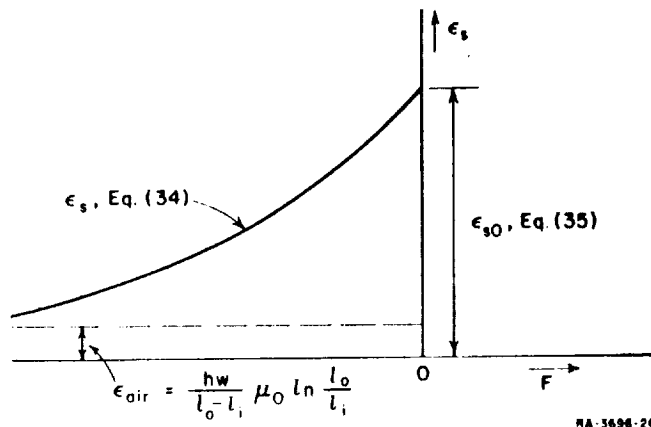


FIG. 26 HYPERBOLIC MODEL OF  $\epsilon$  vs.  $F$  IN NEGATIVE SATURATION

might be used. If  $F$  varies between  $F_1$  and  $F_2$ , a crude approximation for  $\bar{\epsilon}_s$  may be obtained by dividing  $[\Delta\phi_{\epsilon_s}(F_2) - \Delta\phi_{\epsilon_s}(F_1)]$ , Eq. (30), by  $(F_2 - F_1)$ :

$$\bar{\epsilon}_s \approx \frac{hw}{l_o - l_i} \left[ \frac{B_s - B_r}{(F_2 - F_1)a} \left( F_2 \ln \frac{F_2 - al_o}{F_2 - al_i} - F_1 \ln \frac{F_1 - al_o}{F_1 - al_i} \right) + \mu_0 \ln \frac{l_o}{l_i} \right] \quad (36)$$

## 5. SWITCHING INDUCTANCE IN A MULTIPATH CORE

Equations (34), (35), and (36) can be applied directly to each leg in a multipath core. In some cases, the values of  $l_o$  and  $l_i$  depend upon the flux-switching path. For example,  $l_o$  and  $l_i$  of Leg 3 in Fig. 10 depend on whether the flux switches around the major aperture or around the minor aperture. This additional complexity can be avoided by taking fixed average values of  $l$ , but this lowers the accuracy of the model. Plots of measured  $\epsilon_s$  of Legs  $m$ , 3, and 4 of a commercial multipath core (AMP Inc. No. 395 813-1) are shown in Fig. 27.

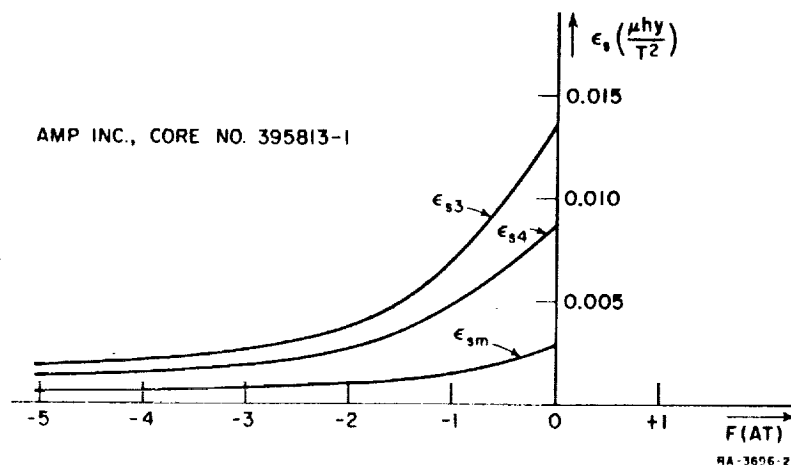


FIG. 27 MEASURED  $\epsilon$  vs.  $F$  IN NEGATIVE SATURATION FOR MULTIPATH-CORE LEGS

## E. INELASTIC SWITCHING MODELS

### 1. MEASUREMENT PROBLEMS

An attempt is made in Part C to explain the physical mechanism of inelastic switching. The objective in this part is to determine a model for this switching, but first we have to decide how to measure  $\dot{B}_\rho$ . The difficulty is that  $\dot{B}_\rho$  cannot be isolated from the total  $\dot{B}$ , where

$$\dot{B} = \dot{B}_\epsilon + \dot{B}_\rho \quad (37)$$

However, this difficulty may be circumvented by means of two considerations. First,  $\dot{B}_\epsilon$  has an appreciable magnitude only during a short interval of time, and  $\Delta B_\epsilon$  is normally much smaller than  $\Delta B_\rho$ . This leaves most of  $\dot{B}$ , except around the rise and fall of  $H$ , practically inelastic (Fig. 17). Second, we make the following test: Let an  $H$  pulse have short rise and fall times and a constant amplitude. The duration,  $T$ , of the  $H$  pulse is varied, and the resulting  $\Delta B_\epsilon$  during the fall time is plotted versus  $T$ . The waveform  $(d\Delta B_\epsilon)/dT$  versus  $T$  is then identified with the waveform of  $\dot{B}_\epsilon$  versus  $t$ . What is left over after subtracting this waveform from the original  $\dot{B}$  is assumed to be  $\dot{B}_\rho$ . In this way,  $\dot{B}$  in Fig. 17 is divided into its two components.

Because of the finite thickness of the tested core, our measurements are based on  $\dot{\phi}_\rho$  rather than on  $\dot{B}_\rho$ .

### 2. $\dot{\phi}_\rho$ VERSUS $F$ AND $\phi$

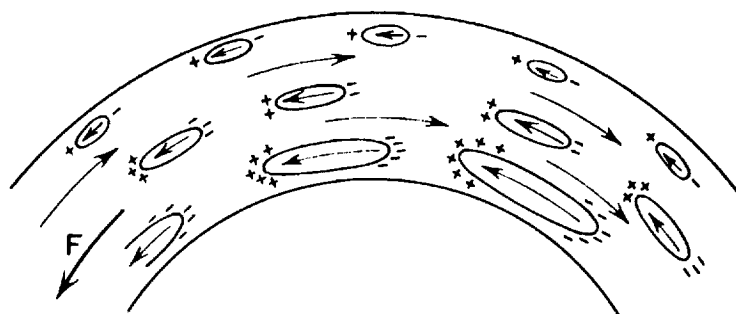
It is found experimentally that  $\dot{\phi}_\rho$  is proportional to the excess of MMF,  $F$ , over some threshold  $F_0$ , and is also a function of  $\phi$ . This relationship is described by the expression

$$\dot{\phi}_\rho = \rho(F - F_0) \quad (38)$$

where  $\rho = \rho(\phi)$  is the switching parameter having units of resistance per turn squared or, briefly, switching resistance per turn squared. Domain growth affects both  $F_0$  and  $\rho$ , but we will discuss them separately.

### 3. DYNAMIC THRESHOLD MMF

In Ref. 3,  $F_0$  is identified with the static threshold,  $d$ , and as such should increase almost linearly with  $\phi$ . This assumption is valid



RA-3696-28

FIG. 28 CREATION OF POLES IN ELLIPSOIDAL DOMAINS

only for slow switching; when  $\dot{\phi}$  is high,  $F_0$  differs from  $d$ . The exact behavior is not known, but a tentative explanation is as follows. Figure 28 shows a segment of a toroidal core, initially saturated in the clockwise (CLEAR) direction, whose flux is being reversed by  $F$  in the counterclockwise (SET) direction. If  $F > d^{sat}$  (see Fig. 9), ellipsoidal domains grow throughout the entire cross section. Following Maxwell's  $\nabla \cdot \bar{B} = 0$ , magnetic poles are created on the surface of these domains, mainly on their tips. The polarities of these poles are in a direction to help  $F$  switch the material between domain tips having poles of opposite polarity, and thus reduce the apparent external threshold.

When  $F$  is low, existing domains grow slowly, or are even immobile, and very few new domains are nucleated. In this case the operating point moves along the static loop, the inner layer switches first, and a "switching ring" expands radially. Therefore, in slow switching, the effect of creation of poles is negligible, but when  $F$  is high, the effect will be quite pronounced. This agrees with the experimental observation. Note that the poles at the tips of a domain tend to reverse the magnetization of the domain, but are too weak to do so.

In conclusion, since the variation of  $F_0$  with  $\phi$  and  $F$  is very complex, even to the point that we don't know for sure whether it increases or decreases with  $\phi$ , we shall assume that it is constant. This will also simplify the mathematics. Further investigation is needed.

#### 4. SWITCHING RESISTANCE

Switching resistance per turn squared is defined in Eq. (38). From the waveshape of  $F(t)$  and  $\phi(t)$  it is possible to determine  $\rho(t)$  and  $\rho(\phi)$

point by point. Such a graphical procedure is illustrated in Fig. 29. Similar procedures can be applied to other shapes of  $F$  such as ramp, sinusoidal, or damped sinusoidal. It is evident from Fig. 29 that  $\rho$  reaches its peak in the vicinity of  $\phi = 0$ . This is in agreement with our discussion on  $\dot{B}_\rho$ , in Part C-4.

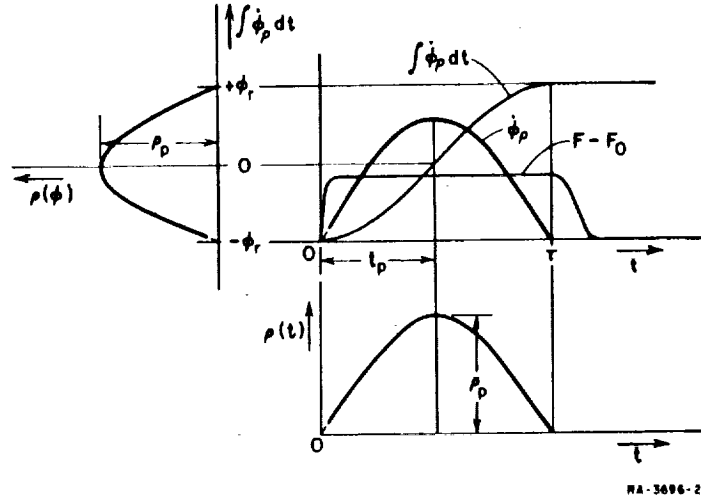


FIG. 29 DETERMINATION OF  $\rho(t)$  AND  $\rho(\phi)$  FROM  $\dot{\phi}_p(t)$  AND  $(F-F_0)(t)$

Several mathematical functions have been suggested in the literature in order to describe  $\rho(\phi)$ . An extensive comparison and evaluation of these models can be found in Ref. 10. Among these models, one of the best is the parabolic model

$$\rho = \rho_p \left[ 1 - \left( \frac{\phi}{\phi_r} \right)^2 \right] \quad (39)$$

Calculations based on this model (cf. Appendix C) result in the following. For constant  $F$ ,

$$\dot{\phi}_p = \dot{\phi}_p \operatorname{sech}^2 \left[ \frac{\dot{\phi}_p t}{\phi_r} - \tanh^{-1} \left( \frac{\phi_{r0}}{\phi_r} \right) \right] \quad (40)$$

where

$$\dot{\phi}_p = \rho_p (F - F_0) \quad (41)$$

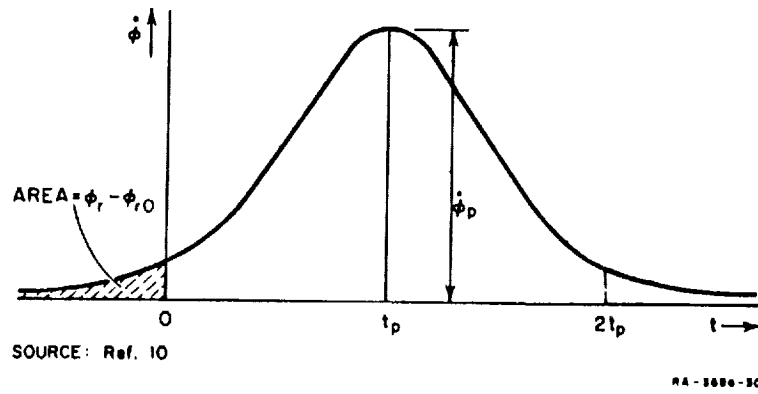


FIG. 30  $\dot{\phi}(t)$  CALCULATED FROM A PARABOLIC MODEL FOR  $\rho$

is the peak of  $\dot{\phi}_p$ , and  $\phi = -\phi_{r0}$  is the flux level above which the parabolic model is a good fit. Note that  $\phi_{r0}$  is slightly smaller than  $\phi_r$ . The function  $\dot{\phi}_p(t)$ , Eq. (40), is plotted in Fig. 30. The peaking time,  $t_p$ , is chosen in such a way that the cross-hatched area is equal to  $\phi_r - \phi_{r0}$ . As such,  $t_p$  in Fig. 30 is only an approximation for  $t_p$  in Fig. 29. It is evaluated by equating the expression in the brackets, Eq. (40), to zero:

$$t_p = \frac{\phi_r}{\rho_p (F - F_0)} \tanh^{-1} \left( \frac{\phi_{r0}}{\phi_r} \right) \quad (42)$$

Chopping the cross-hatched portion is necessary in order to avoid an infinite value for  $t_p$ . The area under the whole curve is equal to  $2\phi_r$ , hence the area under the desired (unchopped) waveshape is equal to  $\phi_r + \phi_{r0}$ .

##### 5. AVERAGE SWITCHING RESISTANCE

In order to simplify manual computation, a constant, time-averaged value of  $\rho$ , denoted by  $\bar{\rho}$ , is needed. Most of the inelastic switching occurs when  $\phi$  varies between  $-\phi_{r0}$  and  $\phi_{r0}$ . It is, therefore, justifiable to evaluate  $\bar{\rho}$  by averaging  $\rho$  during the period  $2t_p$ , Fig. 30.

It is shown in Appendix C that when the parabolic model for  $\rho$ , Eq. (39), is used,

$$\bar{\rho} = \rho_p \frac{\phi_{r0}/\phi_r}{\tanh^{-1}(\phi_{r0}/\phi_r)} \quad (43)$$



For example, for  $\phi_{r0} = 0.9 \phi_r$  (a common specification for measuring the switching time  $\tau$ ),  $\bar{\rho} = 0.61 \rho_p$ .

The  $\phi$ -averaged  $\rho$  of Eq. (39) is shown in Appendix C to be

$$\rho_{\phi, av} = \frac{2}{3} \rho_p \quad (44)$$

When the ratio  $\bar{\rho}/\rho_p = 2/3$  is inserted into Eq. (43), it is found that this corresponds to  $\phi_{r0} = 0.86 \phi_r$ .

In conclusion,  $\bar{\rho}$  is about  $0.6 \rho_p$  to  $0.66 \rho_p$ , or, choosing the average of these values,

$$\bar{\rho} \cong 0.63 \rho_p \quad (45)$$

The value of  $\rho_p$  is easily determined from the plot of measured  $\dot{\phi}_p$  versus  $F$ . A typical plot is shown in Fig. 31. Note that the assumption of constant  $\rho_p$  and constant  $F_0$  is valid for medium and high  $F$ , but is poor for low  $F$ .

A common term in the literature, describing material properties, is "switching coefficient,"  $S_w$ , which may be defined as

$$S_w = \int_0^\tau (H - H_0) dt \quad (46)$$

For constant  $F$  (Fig. 32),

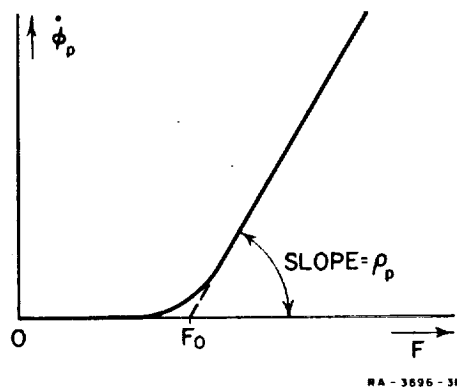


FIG. 31 EVALUATION OF  $\rho_p$  FROM MEASURED  $\dot{\phi}_p$  vs.  $F$

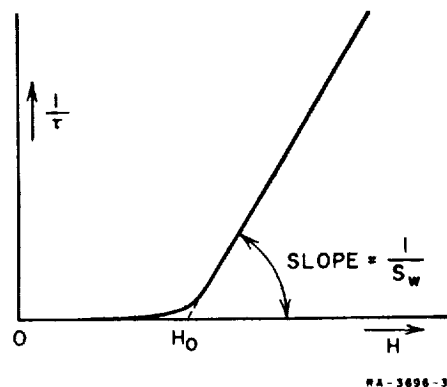


FIG. 32  $1/\tau$  vs.  $H$

$$S_{\square} = (H - H_0)\tau \approx \frac{F - F_0}{l^{\text{av}}} \tau \quad (47)$$

where

$$l^{\text{av}} = \frac{1}{2} (l_i + l_o) \quad .$$

Note that the switching time,  $\tau$ , is not a function of the amount of switched flux. For constant  $F$ ,

$$\frac{\tau}{\phi} = \frac{2\phi_r}{\tau} = \bar{\rho}(F - F_0) \quad .$$

Substituting  $\tau$  from Eq. (47), we get

$$\bar{\rho} = \frac{2\phi_r}{S_{\square} l^{\text{av}}} = \frac{2B_r}{S_{\square}} \frac{A}{l^{\text{av}}} \quad (48)$$

where  $A = hw$ .

From Eqs. (48) and (45)

$$\rho_p \approx 1.6 \frac{2B_r}{S_{\square}} \frac{A}{l^{\text{av}}} \quad (49)$$

## 6. SWITCHING RESISTANCE IN A MULTIPATH CORE

Normally the material and height  $h$  is common to all the legs of a multipath core. If we know  $\rho_p$  of one leg,  $\rho_p$  of any other leg can be determined from Eq. (49).

As an example, consider the multipath core in Fig. 10:

$$\rho_{\square p} : \rho_{3p} : \rho_{4p} = \frac{w_{\square}}{l_{\square}^{\text{av}}} : \frac{w_3}{l_3^{\text{av}}} : \frac{w_4}{l_4^{\text{av}}} = \frac{2}{l_{\square}^{\text{av}}} : \frac{1}{l_3^{\text{av}}} : \frac{1}{l_4^{\text{av}}} \quad (50)$$

A plot of measured  $\rho_{\square}$ ,  $\rho_3$  and  $\rho_4$  versus  $\phi/\phi_r$  is shown in Fig. 33 for a commercial multipath core (AMP Inc. No. 395 813-1).

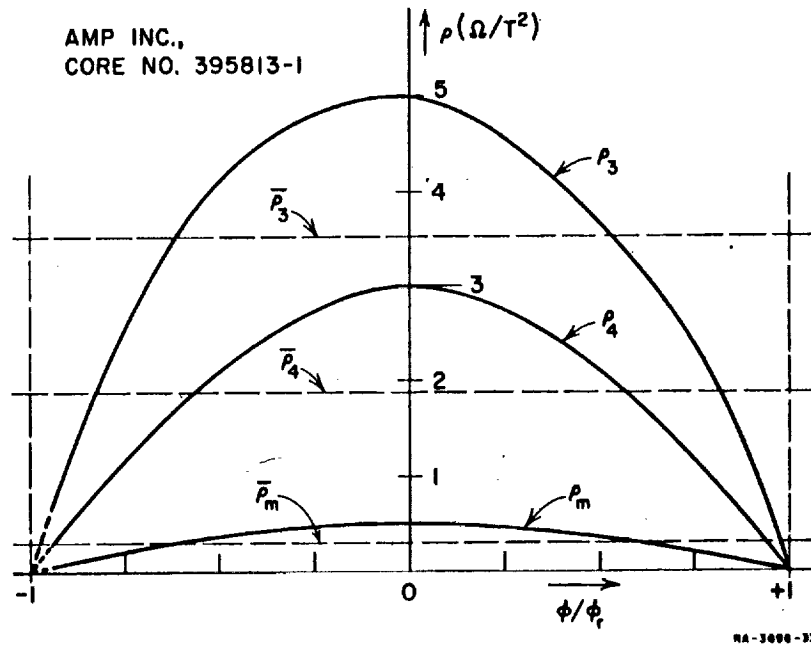


FIG. 33 EXPERIMENTAL  $\rho_m$ ,  $\rho_3$ , AND  $\rho_4$  vs.  $\phi/\phi_r$  OF A MULTIPATH CORE

## F. ELECTRICAL-CIRCUIT ANALOGUE

### 1. SUMMARY OF SWITCHING MODELS

A summary of elastic and inelastic switching models for a leg is given as follows.

Elastic flux switching is described by Eq. (32):

$$\dot{\phi}_e = \epsilon \dot{F} \quad , \quad (51)$$

where  $\epsilon$  is a function of  $F$ ,  $\phi$  and the "history" of the variations of  $\phi$  (see Part D-2). In negative saturation,  $\epsilon(F)$  is evaluated from Eq. (34), and its fixed, average value is determined from Eq. (36). (In positive saturation the sign in front of  $F$  in Eqs. (34) and (36) should be changed.) No model is known yet for  $\epsilon(F, \phi, \text{"history" of } \phi)$  when  $|\phi| < \phi_r$ .

Inelastic flux switching is described by Eq. (38) for a positive  $F$ . If  $F$  is negative, a plus sign should be in front of  $F_0$ . A general expression for  $\dot{\phi}_\rho$  is

$$\dot{\phi}_\rho = \rho(F \mp F_0) \begin{cases} (-) & \text{if } F \geq F_0 \\ (+) & \text{if } F \leq -F_0 \end{cases} \quad (52)$$

where  $\rho$  is a function of  $\phi$ . A parabolic model for  $\rho$  is given by Eqs. (39) and (49).

The total  $\dot{\phi}$  is obtained by combining Eqs. (51) and (52):

$$\dot{\phi} = \epsilon \dot{F} + \rho(F \mp F_0) \begin{cases} (-) & \text{if } F \geq F_0 \\ (+) & \text{if } F \leq -F_0 \\ \rho = 0 & \text{if } |\phi| \geq \phi_r \text{ or } |F| < F_0 \end{cases} \quad (53)$$

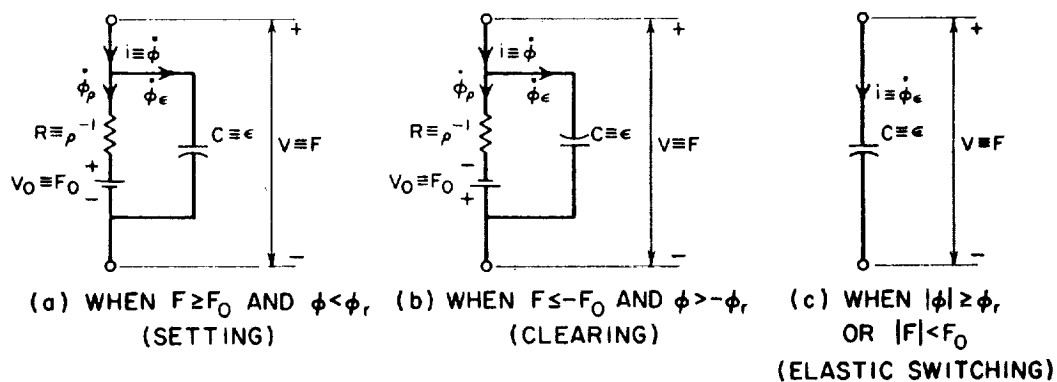
The condition that  $\rho = 0$  if  $|\phi| \geq \phi_r$  excludes inelastic flux switching in positive or negative saturation. The condition that  $\rho = 0$  if  $|F| < F_0$  excludes inelastic switching before  $F$  reaches its threshold value; this condition is only an approximation in view of the fact that  $F_0$  is an artifice, obtained by extrapolation of  $\dot{\phi}_p$  versus  $F$ , Fig. 31. For slow switching,  $F_0$  should have the value of the dc threshold MMF.

## 2. ELECTRICAL-CIRCUIT ANALOGUE FOR A LEG

It is suggested in Ref. 13 that an analogy be made between quantities associated with a magnetic leg and an electrical circuit. Accordingly,  $\phi$  is treated as "current" and  $F$  as "voltage."

The instantaneous relationship between  $\dot{\phi}$  and  $F$ , Eq. (53), is analogous to the relationship between voltage,  $V$ , and current,  $i$ , in the electrical circuits (which include nonlinear components) shown in Fig. 34. The three modes of operation, setting, clearing, and elastic switching, are expressed by the inequalities of Eq. (53) and are represented in Fig. 34 by three separate circuits, (a), (b), and (c). The positive polarities of  $\phi$  and  $F$  are shown for the sake of reference only. Note that  $\rho$  appears as "conductance" in these equivalent circuits.

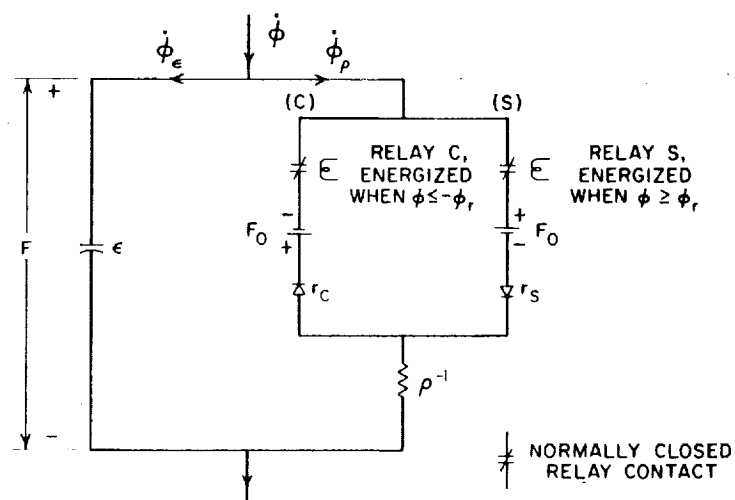
The need for three separate equivalent circuits in Fig. 34 stems from the restricting conditions of  $F$  and  $\phi$ . By adding ideal rectifiers and ideal relay contacts, these three circuits may be combined into a single circuit.<sup>3</sup> Such an arrangement is shown in Fig. 35. The (S) and (C) branches correspond to setting ( $\dot{\phi}_p > 0$ ) and clearing ( $\dot{\phi}_p < 0$ ) modes of operation. The normally closed contact of Relay S opens when  $\phi \geq \phi_r$  and the contact of Relay C opens when  $\phi \leq -\phi_r$ . (The arrangement for sensing  $\phi$  and energizing the relay coils is not shown.) In this way  $\dot{\phi}_p = 0$  when the leg is saturated. The function of the ideal rectifiers



SOURCE: Ref. 13

RA-3696-34

FIG. 34 EQUIVALENT ELECTRICAL CIRCUITS OF A MAGNETIC LEG



RA-3696-35

FIG. 35 ELECTRICAL-CIRCUIT ANALOGUE FOR A LEG

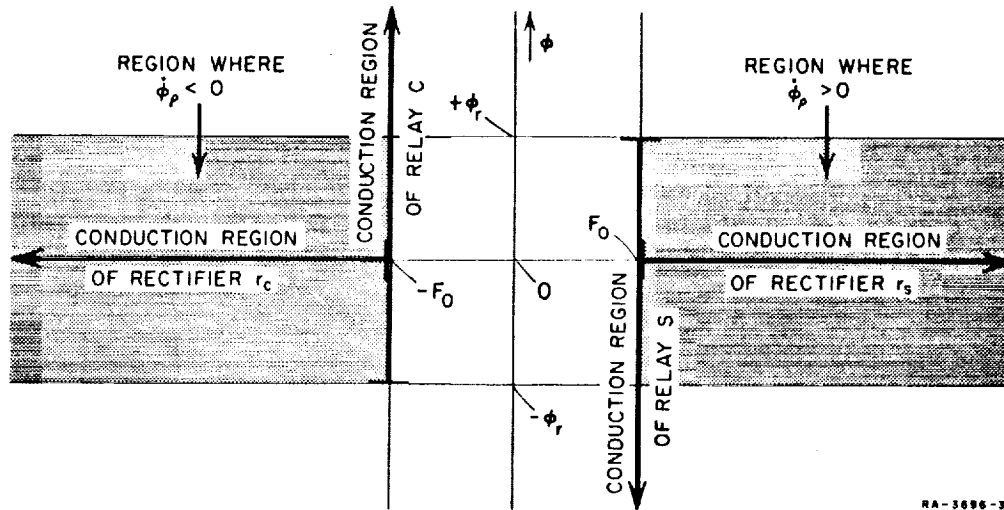


FIG. 36 FUNCTIONS OF RECTIFIERS AND RELAYS IN LEG ANALOGUE

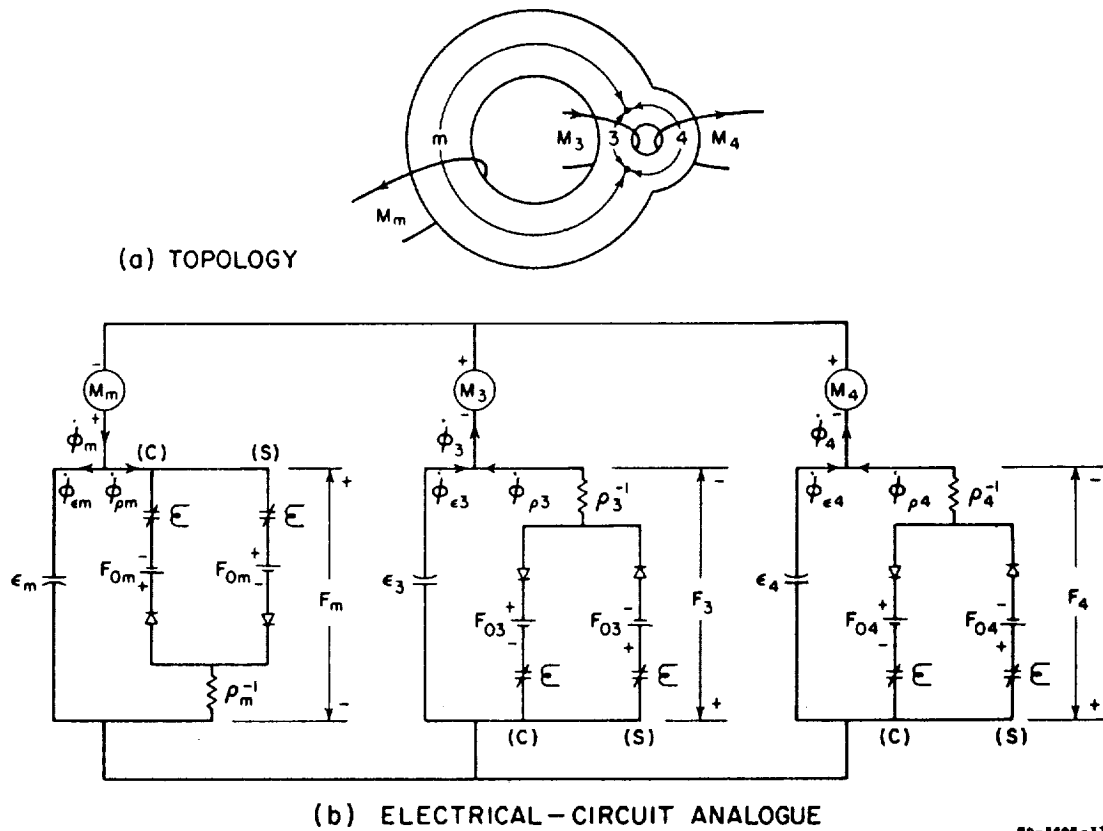
is to prevent  $F_0$  from being active when  $|F| < F_0$ , and to prevent the circulation of  $\dot{\phi}_p$  around the loop composed of the (S) and (C) branches. These functions of the relays and rectifiers are summarized graphically in Fig. 36.

### 3. ELECTRICAL-CIRCUIT ANALOGUE FOR A MULTIPATH CORE

The electrical circuit analogue for each leg in a multipath core is identical with that of Fig. 35, except that  $\epsilon$ ,  $\rho$ ,  $F_0$  and activation of the relay coils are determined by the dimensions  $w$ ,  $l_i$  and  $l_o$  of each leg. By assembling these models according to the physical layout of the legs, the electrical-circuit analogue for a multipath core is obtained. An analogue for a three-leg core is shown in Fig. 37. Positive reference of  $\dot{\phi}$  and  $F$  in each leg corresponds to the SET (counterclockwise) direction around the major aperture. The MMF generators  $M_m$ ,  $M_3$ , and  $M_4$  represent the net external MMFs acting on Legs  $m$ , 3, and 4, respectively.

Not incorporated in the electrical-circuit analogue is the requirement for flux continuity. However, if  $\phi$  is continuous initially, it is also continuous later, because the continuity of  $\dot{\phi}$  is maintained in the electrical-circuit analogue.

An extension to an electrical-circuit analogue for the multipath core in Fig. 1(b) may be achieved by the use of a grounded  $\pi$  network. In



RB-5696-37

FIG. 37 THREE-LEG CORE ANALOGUE

this network, Analogue  $m$  (composed of Legs  $m_1$  and  $m_2$  in series) is connected in series with parallel connection of Analogues 1 and 2 and the parallel connection of Analogues 3 and 4.

#### 4. COMPUTATION

Using electrical-circuit analogues for multipath cores may facilitate the analysis of a circuit that includes such cores.<sup>3</sup> The problem is how to handle the nonlinearity of the parameters  $\epsilon$  and  $\rho$ , and how to take into account saturation and threshold properties. These difficulties may be overcome by having a computer carry out the following procedure.

A mode of operation is defined as a period during which all the leg models remain unchanged. However, the magnitude of  $\epsilon$  and  $\rho$  will vary with time within each mode. Switching from one mode to another occurs whenever switching of active elements of at least one leg model takes place; this happens when  $F$  or  $\phi$  of a leg reaches a threshold value. Each

mode of operation is divided into small time intervals, each of which is of short duration,  $\Delta t$ . During each  $\Delta t$ , all the values of  $\epsilon$  and  $\rho$  in the circuit are assumed to be constant. In this way each time interval is described by  $n \times n$  linear differential equations, in which the  $F$ s across the legs appear as variables. When  $F$  has been solved for, the  $\dot{\phi}$  of each leg is computed by substituting the approximate  $F$  into Eq. (53). By integrating the  $\dot{\phi}_\rho$  component,  $\Delta\phi_\rho$  versus time is determined. For each leg, the values for  $\epsilon$  and  $\rho$  used at every time interval  $\Delta t$  are determined from the final values of  $\phi$  and  $F$  of the previous  $\Delta t$ . In this way the nonlinearities of  $\epsilon$  and  $\rho$  are accounted for in a piecewise fashion. This computation is based on an assumed initial  $\phi$  and  $F$  of each leg, and is repeated versus time until either  $F$  or  $\dot{\phi}_\rho$  of any leg in the circuit calls for switching to a new mode of operation. The final conditions of each mode serve as the initial conditions for the following mode. The  $n \times n$  matrices are solved versus time as before, until another mode of switching occurs. This procedure is repeated until all the  $\dot{\phi}$ s become zero, at which time flux switching has been completed.

A detailed machine computation for a shift register, which includes seven cores and ten loops, is reported in Ref. 14. The procedure and switching models are different from those outlined above, but the complexity is of the same order of magnitude.

Considerable simplification in computation may be achieved by assuming constant, average values for  $\epsilon$  and  $\rho$ . The problem then amounts to solving for variables in a linear-circuit network.

## G. RING-ELEMENT MODEL

### 1. STATIC STATE

Consider the  $B$ - $H$  loop, Fig. 4(a), of a particle. If a toroid reaches a static state by slow switching, it is very likely that all particles with the same radius  $r$  also have the same  $B$  and  $H$ . In this case, one may assign a  $B$ - $H$  loop to designate the static flux state of a ring element of height  $h$ , radius  $r$ , and thickness  $dr$ . When an MMF  $F$  is applied to the toroid, the resulting  $H$  along this ring element is

$$H = F/2\pi r \quad . \quad (54)$$



For a given value of  $F$  between  $2\pi r_i H_{th}$  and  $2\pi r_o H_{sat}$ , three physical regions are distinguished in the toroid<sup>11</sup> (see Fig. 24):

Region I— $r_i \leq r \leq r'$ , positive-saturation region

Region II— $r' < r < r''$ , high-permeability region

Region III— $r'' \leq r \leq r_o$ , negative-saturation region.

This model may be used to define four static values of  $F$ : Switching in the inner ring element can start if  $F = 2\pi r_i H_{th}$  and can be completed if  $F = 2\pi r_i H_{sat}$ ; switching in the outer ring element can start if  $F = 2\pi r_o H_{th}$  and can be completed if  $F = 2\pi r_o H_{sat}$ . In Ref. 15 these four values of  $F$  are defined in a similar way, except that an idealized  $B$ - $H$  loop [Fig. 4(b)iii] is assumed. The shape of a  $\phi$ - $F$  loop that results from this model is shown, but no calculation is given. This calculation is carried out in considerable detail in Ref. 16. A brief summary of this work follows:

The objective is to calculate the static  $\phi$ - $F$  loop, assuming first an ideal  $B$ - $H$  loop, as in Fig. 4(b)iii, and second, a ring-element model for  $H$ , as in Eq. (54). Combining the two assumptions results in a static  $B$ - $F$  loop for a ring element of radius  $r$ . Let  $F_i^{min} = 2\pi r_i H^{min}$ , and  $F_i^{max} = 2\pi r_i H^{max}$ . Then, for  $r_i \leq r \leq r_o$ ,

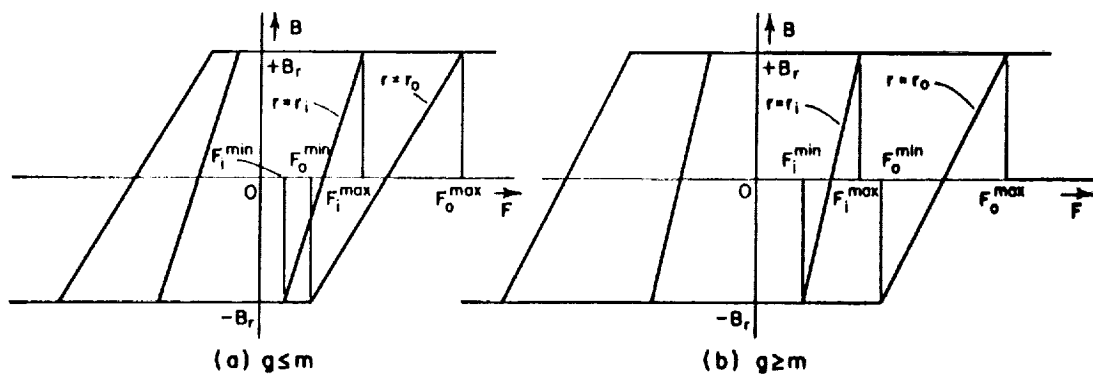
$$B = \frac{2B_r}{F_i^{max} - F_i^{min}} \left( F \frac{r_i}{r} + \frac{F_i^{max} + F_i^{min}}{2} \right) \begin{cases} (-) \text{ for } 2\pi r H^{min} \leq F \leq 2\pi r H^{max} \\ (+) \text{ for } -2\pi r H^{max} \leq F \leq -2\pi r H^{min} \end{cases} \quad (55)$$

Let  $g = r_o/r_i$  (geometry coefficient) and  $m = H^{max}/H^{min}$  (material coefficient). In constructing the  $B$ - $F$  loops for the inner and outer radii, Fig. 38, two cases are distinguished: in Case (a),  $g \leq m$ , or  $F_i^{max} \geq F_o^{min}$ , where  $F_o^{min} = 2\pi r_o H^{min} = gF_i^{min}$ ; in Case (b),  $g \geq m$ , or  $F_i^{max} \leq F_o^{min}$ .

Based on the ring model, static  $\phi$  is

$$\phi = h \int_{r_i}^{r_o} B(F, r) dr \quad (56)$$

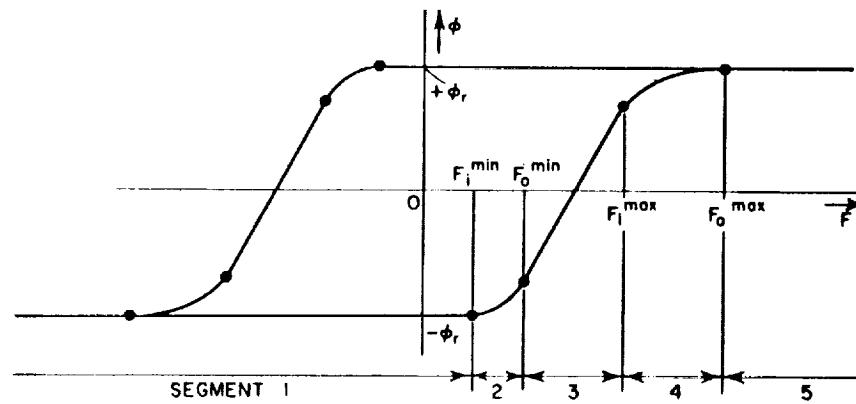
Substitution of  $B(F, r)$ , Eq. (55), into Eq. (56) yields the desired static  $\phi(F)$  loop. The result for Case (a) ( $g \leq m$ ) is divided into five segments, as shown in Fig. 39 and in the following equations:



SOURCE: Ref. 16

RA-3696-38

FIG. 38 IDEALIZED STATIC B-F LOOPS



SOURCE: Ref. 16

RA-3696-39

FIG. 39 CALCULATED STATIC  $\phi$ -F LOOP

Segment 1.  $F \leq F_i^{\min}$

$$\phi = -\phi_r = -h(r_o - r_i)B_r \quad (57)$$

Segment 2.  $F_i^{\min} \leq F \leq F_o^{\min}$

$$\phi = L_i \left[ 2F \left( \ln \frac{F}{F_i^{\min}} - 1 \right) - F_i^{\max}(g - 1) + F_i^{\min}(g + 1) \right] \quad (58)$$

where

$$L_i = hr_i \frac{B_r}{F_i^{\max} - F_i^{\min}} \quad (59)$$

Segment 3.  $F_o^{\min} \leq F \leq F_i^{\max}$

$$\phi = L_i [2F \ln g - (F_i^{\max} + F_i^{\min})(g - 1)] \quad (60)$$

Segment 4.  $F_i^{\max} \leq F \leq F_o^{\max}$

$$\phi = L_i \left[ 2F \left( 1 + \ln \frac{gF_i^{\max}}{F} \right) - F_i^{\max}(g + 1) - F_i^{\min}(g - 1) \right] \quad (61)$$

Segment 5.  $F_o^{\max} \leq F$

$$\phi = +\phi_r = h(r_o - r_i)B_r \quad (62)$$

Note that only Segments 2 and 4 are nonlinear. Similar calculation can be carried out for Case (b) ( $g \geq m$ ).

A more general treatment of this derivation is given in Ref. 9. It is shown there that Segment 3 is described by a linear relation between  $\phi$  and  $F$  for any function  $B(H)$  in Case (b) ( $g \geq m$ ), and for a linear function  $B(H)$  in Case (a) ( $g \leq m$ ). It is concluded from these rules that if the  $B-H$  loop is nonlinear, the  $\phi-F$  loop may still have a linear portion. In fact, the higher  $r_o/r_i$  is, the larger is the linear portion of the  $\phi-F$  loop.

## 2. DYNAMIC STATE

The ring-element model may also be used in the analysis of dynamic slow switching. In Ref. 11, this model is simplified by assuming that  $H_{th} \approx H_{sat} \approx H_c$ . At first glance (see Fig. 24), one might think that under this assumption Region II would reduce to a mere domain wall. However, this is not true for a dynamic state; it is only true for a static state reached with  $H$  monotonically increasing or constant. This is so because Region II,  $r' < r < r''$ , is defined as the region where  $B_r > B > -B_r$ , and it takes time to switch from  $-B_r$  to  $B_r$ .

Suppose that a toroid is initially in negative saturation, and a constant  $F$  is applied. Throughout the toroid cross section,  $H$  varies with  $r$  according to Eq. (54). Switching is, therefore, fastest in the innermost ring, and the smaller the radius of any ring element is, the shorter will be the switching time,  $\tau$ . Substituting Eq. (54) into Eq. (47) results in the hyperbolic function

$$\tau = \frac{S_w}{\frac{F}{2\pi r} - H_0} \quad (63)$$

A plot of  $\tau(r)$  is shown in Fig. 40 for  $r_i \leq r \leq r''$ , assuming that  $F < 2\pi r_i H_0$ . In Ref. 11,  $r$  and  $\tau$  are identified with  $r'$  and  $t$  in order to show the variation of Region II with time (see Fig. 41). Thus,

$$r' = \frac{Ft}{2\pi(S_w + H_0 t)} \quad (64)$$

and

$$r'' = \frac{F}{2\pi H_0} \quad (65)$$

Note that since  $F$  is a constant,  $r''$  is invariant with time. Note also that  $r' = r_i$  until the innermost ring is completely switched. Variation of  $B$  with  $r$  and  $t$  is shown schematically in Fig. 42. The innermost ring is only partially switched at  $t = t_1$ , and is completely switched at  $t = \tau_i$ . For  $t \geq \tau_i$ ,  $r'$  is obtained from Eq. (64).

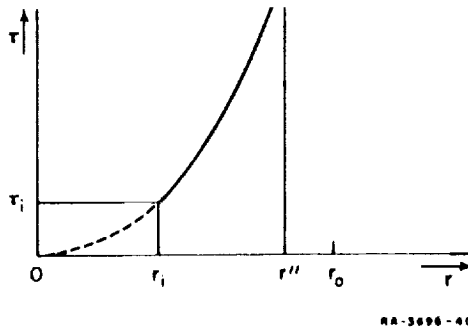
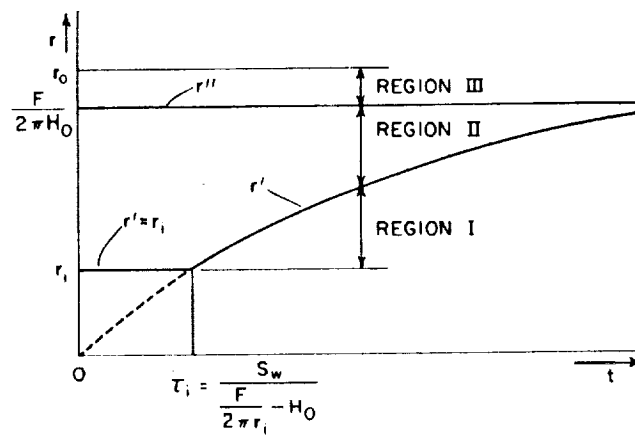
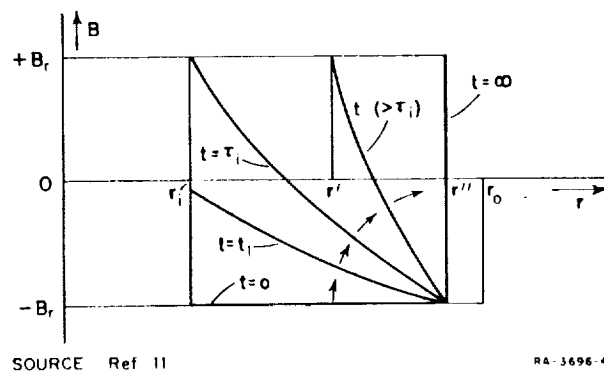


FIG. 40  $\tau$  vs.  $r$  IN A TOROID



SOURCE: Ref. 11

FIG. 41  $r'$  AND  $r''$  vs.  $t$  FOR CONSTANT  $F$



SOURCE: Ref. 11

FIG. 42  $B$  vs.  $r$  AND  $t$  IN A TOROID CROSS SECTION

A plot of  $r'$  and  $r''$  versus time is shown in Fig. 43 for a train of constant- $F$  pulses. Between pulses,  $r''$  remains unchanged because the  $B$  of a ring element in the material between  $r'$  and  $r''$  is static. In Ref. 11,  $r''$  is shown dropping to  $r_i$  between pulses, when  $F = 0$ . This mistake apparently stems from misinterpretation of Eq. (65), which is valid only when the pulse is on.

A more general expression for  $r'$  is<sup>11</sup>

$$r' = \frac{\int_0^t F dt'}{2\pi(S_w + H_0 t)} \quad (66)$$

For a ramp function  $F = kt$ , Eqs. (65) and (66) result in the plot of Fig. 44. Switching starts at  $r = r_i$  at  $t = \tau_{i,th}$  and ends at  $r = r_o$  at  $t = \tau_o$ .

### 3. CALCULATED $\dot{\phi}_\rho(t)$

In order to calculate  $\dot{\phi}_\rho(t)$  from the ring model, it is first assumed<sup>17,11</sup> that  $\dot{B}$  is independent of  $B$ . This assumption is equivalent to approximating  $\rho(\phi)$  by  $\bar{\rho}$ . Hence,  $\dot{B}$  of a ring element of radius  $r$  is

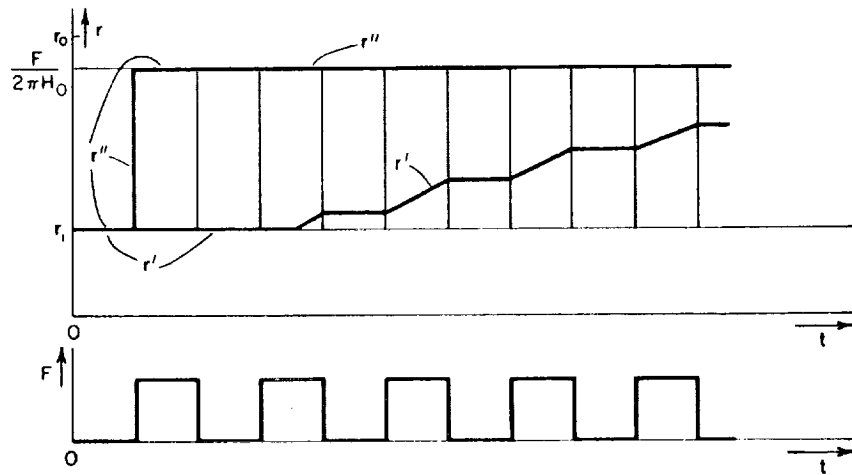
$$\dot{B}_\rho \cong \frac{2B_r}{\tau} \quad (67)$$

For a constant  $F$ , substituting Eq. (63) into Eq. (67) and integrating from  $r = r_i$  to  $r = r_o$  results in

$$\dot{\phi}_\rho = \frac{2B_r h}{S_w} \left[ \frac{F}{2\pi} \ln \frac{r''}{r'} - H_0(r'' - r') \right] \quad (68)$$

where  $r'(t)$  is as plotted in Fig. 41, following Eq. (64), and  $r''$  is given in Eq. (65). Calculated  $\dot{\phi}_\rho$ , Eq. (68), is compared<sup>11</sup> with experimental  $\dot{\phi}_\rho$  in Fig. 45. Note that the calculated  $\dot{\phi}_\rho$  is constant during  $0 \leq t \leq \tau_i$ , since  $r' = r_i$  is constant during this period. In this period, the agreement between calculated and experimental  $\dot{\phi}_\rho$  is obviously poor.

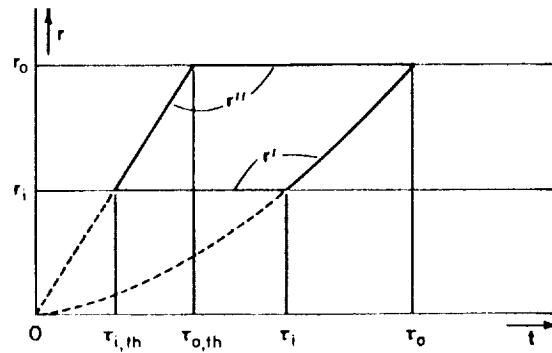
When repeated for a ramp function  $F = kt$ , calculated  $\dot{\phi}(t)$  is shown in Ref. 11 to have a shape closer to the experimentally observed waveform (Fig. 46).



MODIFIED FROM Ref. 11

RA-3696-43

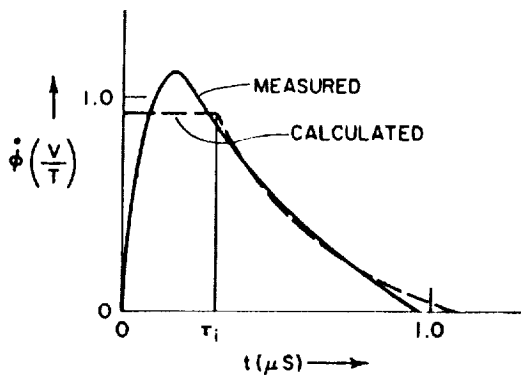
FIG. 43  $r'$  AND  $r''$  vs.  $t$  FOR CONSTANT-F PULSE TRAIN



SOURCE: Ref. 11

RA-3696-44

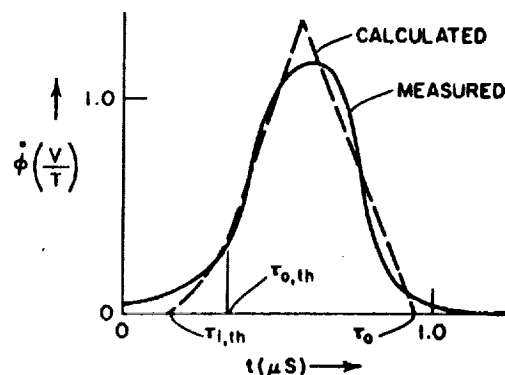
FIG. 44  $r'$  AND  $r''$  vs.  $t$  FOR  $F=kt$



SOURCE: Ref. 11

NA-3898-46

FIG. 45  $\dot{\phi}_p$  vs.  $t$  FOR CONSTANT  $F$



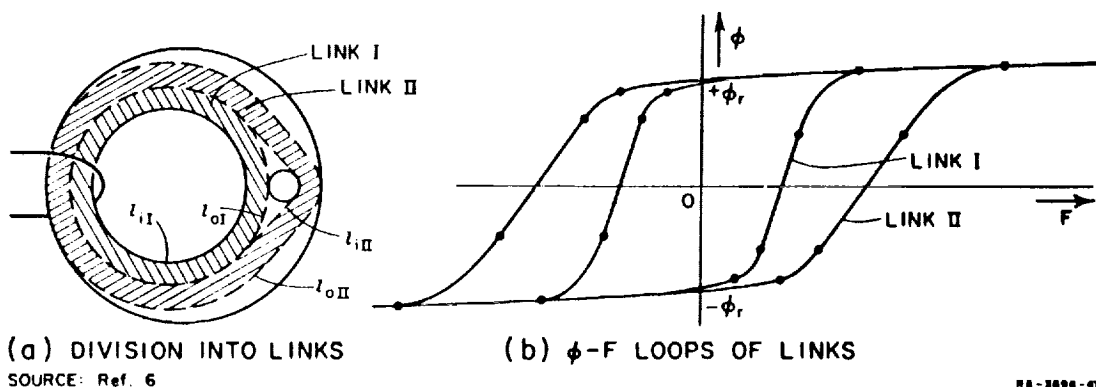
SOURCE: Ref. 11

NA-3898-46

FIG. 46  $\dot{\phi}_p$  vs.  $t$  FOR  $F=kt$

#### 4. APPLICATION TO A MULTIPATH CORE

In Ref. 6, a multipath core is divided into two links, as shown in Fig. 47(a). Each link of inside length  $l_i$  and outside length  $l_o$  is treated as a separate toroid, with its own separate static  $\phi$ - $F$  loop [see Fig. 47(b)]. Since Link II is not exactly circular, it is represented by a circular link of equal corresponding  $l_i$  and  $l_o$ . This approach is valid as long as one deals with static loops that have been obtained by slow switching caused by  $NI$  applied in the major aperture. Therefore, when setting of the main leg is done very slowly, it is sound to determine from Fig. 47 what portion of the flux in the main leg is divided into Link II, which is the outer leg. Furthermore, in order to prevent any



(a) DIVISION INTO LINKS  
SOURCE: Ref. 6

(b)  $\phi$ - $F$  LOOPS OF LINKS

NA-3898-47

FIG. 47 CALCULATED  $\phi$ - $F$  LOOPS OF MULTIPATH-CORE LINKS



flux change in the outer leg and yet complete switching in the inner link, the condition

$$\frac{H^{\max}}{H^{\min}} = m \leq \frac{l_{III}}{l_{OI}} \quad (69)$$

must be satisfied. In Ref. 6, however, no restriction is made with regard to the switching speed. It is stated there that Inequality (69) must be satisfied in order to secure a reliable decoupling between individual magnetic circuit components. This conclusion is invalid when switching is not slow. As a matter of fact, when a HOLD MMF is applied on the outer leg, decoupling can be obtained without satisfying Inequality (69), even when switching is slow. This is another argument against the conclusion in Ref. 6.

A reduction of a multipath core during setting time into an equivalent toroid is also suggested on pp. 127-128 of Ref. 11. However, it is recognized there that such an equivalence is valid only under low drive, i.e., slow switching.

## H. $\phi$ -F CURVES

### 1. INTRODUCTION

In Parts E and G, models are proposed for  $\dot{\phi}_p(t)$  versus  $F$ . In most circuits that involve magnetic cores, operation is characterized by the stored residual flux,  $\Delta\phi_{res}$ , at the end of switching time  $\tau$ , rather than by instantaneous  $\dot{\phi}$  during  $\tau$ . Circuits of this nature include magnetic amplifiers, memory arrays, shift registers and a large number of logic circuits. Evaluation of  $\Delta\phi_{res}$  versus  $F$  is, therefore, important.

In some references<sup>15,17</sup> the curve  $\Delta\phi_{res}$  versus  $F$  is referred to as the " $\phi$ -F curve," and this term will be used here. (In Ref. 11 it is called "S Curve.") The term  $\phi$ -F curve should not be confused with the term  $\phi$ -F loop, which refers to the static variation of  $\phi$  with  $F$ .

### 2. AUTOMATIC PLOTTING OF $\phi$ -F CURVES

Automatic plotting of  $\phi$ -F curves is described in Ref. 17. A drive pulse,  $I$ , of duration  $T$ , is applied to  $N$  turns of a tested core, which is initially in negative saturation, and to a delay line in series with the

$x$ -axis of an oscilloscope. The resulting  $\phi$  is integrated, and  $\Delta\phi$  feeds the  $y$ -axis of the oscilloscope. Just after  $F$  drops to zero, a strobing pulse turns on the beam of the oscilloscope for a short time. A bright spot appears on the oscilloscope screen, positioned according to the coordinates  $x = F$  and  $y = \Delta\phi_{res}$ . The core is then driven back into negative saturation. Variations of  $\phi$  and  $F$  during a complete cycle are superimposed on the static  $\phi$ - $F$  loop in Fig. 48. By making the envelope of a train of drive pulses have the shape of a saw tooth, this process is repeated for varying values of  $F$ . A steady repetition of this triangular pulse train allows one to photograph the  $\phi$ - $F$  curve directly from the oscilloscope screen.

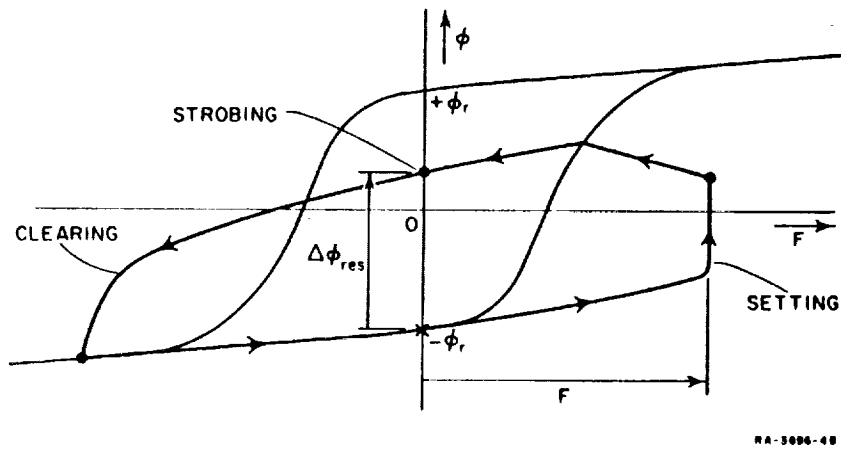


FIG. 48 VARIATION OF  $\phi$  AND  $F$  CORRESPONDING TO ONE POINT IN A  $\phi$ - $F$  CURVE

### 3. TYPICAL $\phi$ - $F$ CURVES

A typical automatically plotted  $\phi$ - $F$  curve for a toroid is shown in Fig. 49. The values of  $F$  at the knees are denoted by  $F_A$  and  $F_B$ .

It is found experimentally that a  $\phi$ - $F$  curve is affected by the pulse duration  $T$ . Figure 50(a) shows a family of measured  $\phi$ - $F$  curves, with  $T$  as a parameter.<sup>17</sup> As  $T$  decreases, there is less time available for the core to switch; hence, in order to get the same  $\Delta\phi_{res}$ , higher  $F$  is needed. This explains the fanning of the curves to the right as  $T$  decreases. In addition, as explained in Part C, in order to get inelastic flux change, domains have to move beyond their first energy hills. If  $T$  is smaller, a higher  $F$  is needed in order to overcome these hills. This explains why the value for  $F_A$  increases as  $T$  decreases.

Calculated  $\phi$ - $F$  curves, assuming that  $\dot{B} \sim (H - H_0)$ , are given in Ref. 17. A family of these curves, with  $T$  as a parameter, is shown in Fig. 50(b). The main disagreement with the measured curves is the fact that  $F_A$  is independent of  $T$ .

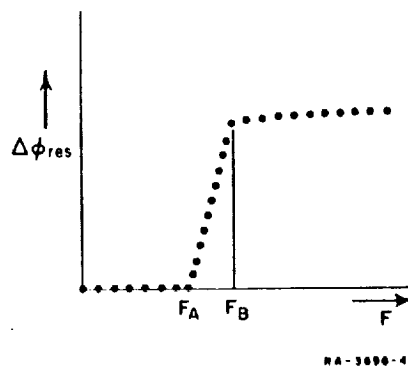


FIG. 49 AUTOMATICALLY-PLOTTED  $\phi$ - $F$  CURVE

It is interesting to compare the value of  $F_A$  with the values of  $d^{\min}$ ,  $d^{\max}$  and  $F_0$ . A curve close to a static  $\phi$ - $F$  loop is obtained under the condition of slow switching ( $T \rightarrow \infty$ ). We conclude, therefore, that  $F_A \rightarrow d^{\min}$  as  $T$  becomes very long. The correlation between  $F_A$  and  $F_0$  is not so straightforward. We have tested different cores made of three types of material (General Ceramics 5209, S4, and S6) and have found some consistent empirical proportions between  $d^{\min}$ ,  $d^{\max}$  and  $F_0$ . For GC 5209 material,  $F_0 \cong d^{\max}$ ; for GC S4 material,  $d^{\min} < F_0 < d^{\max}$  [ $F_0 \cong \frac{1}{2}(d^{\min} + d^{\max})$ ]; and for GC S6 material,  $d^{\max} < F_0$  ( $F_0 \cong 1.2 d^{\max}$  to  $1.6 d^{\max}$ ). No explanation for these results is known.

Consider a multipath core with one major aperture and a number of minor apertures, e.g., Fig. 1(b). When driven through its major aperture, the multipath core is tested as if it were a toroid. The resulting  $\phi$ - $F$  curves are similar to those of a toroid, Fig. 50(a), except for the appearance of a slight kink in the middle due to the minor apertures.

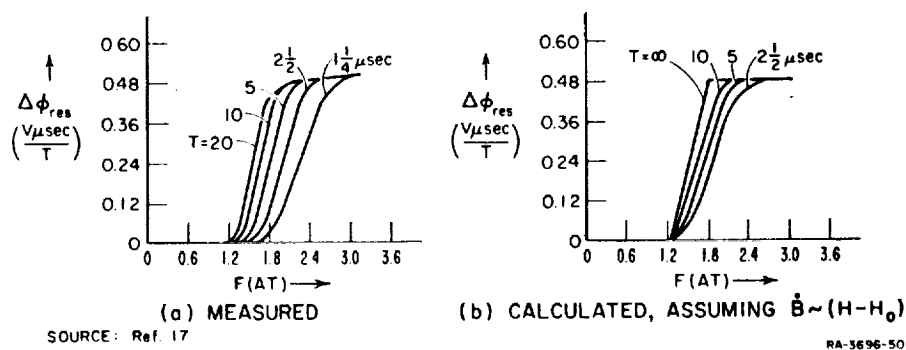
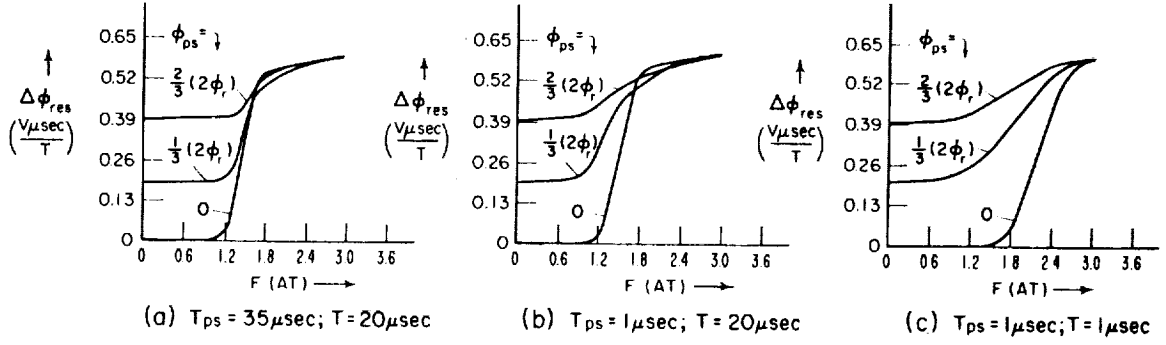


FIG. 50  $\phi$ - $F$  CURVES WITH  $T$  AS A PARAMETER

#### 4. SOFT THRESHOLD

Let us now repeat the measurement of a  $\phi$ - $F$  curve using a fixed  $T$ , except for one modification. Before the SET pulse,  $F$ , is applied, let a PRESET pulse,  $F_{ps}$ , of duration  $T_{ps}$ , bring the core to some flux level  $\phi_{ps}$ . For automatic plotting of the  $\phi$ - $F$  curves, the core is driven by a repetitive cycle of CLEAR, PRESET, and SET MMFs. The amplitude of the CLEAR and PRESET pulses are fixed for any given curve, but the amplitude of the SET pulse is variable, as before.

The resulting  $\phi$ - $F$  curves, as given in Ref. 17, are shown in Fig. 51 for three values of preset flux  $\phi_{ps}$  and three combinations of  $T_{ps}$  and  $T$ .



SOURCE: Ref. 17

RA-3696-51

FIG. 51  $\phi$ - $F$  CURVES WITH  $T_{ps}$  AND  $T$  AS PARAMETERS

From these curves we learn about the effect of  $F_{ps}$  and  $T_{ps}$ . When  $T_{ps}$  is long, flux presetting is slow and gentle, and the threshold  $F_A$  increases slightly with  $\phi_{ps}$  due to the increase in the circumference of the ring of unswitched flux (of amount  $\phi_r - \phi_{ps}$ ). On the other hand, if  $T_{ps}$  is short, the threshold  $F_A$  decreases as  $\phi_{ps}$  increases. (Note that, for a given  $T_{ps}$ , the higher  $\phi_{ps}$  is, the higher is  $F_{ps}$ .)

It is concluded, therefore, that a short and high prepulse  $F_{ps}$  reduces the threshold MMF for any following switching. The lower threshold is called "soft" and a possible physical explanation for it is as follows. If  $F_{ps} > l_o d^{\text{max}}$ , flux switches throughout the entire cross section of a leg by means of a growth of ellipsoidal domains. As shown in Fig. 28, poles are created at the tips of these domains. The polarity of these poles is such that they tend to decrease the net apparent threshold, as

explained in Part E-3. The higher  $F_{ps}$  is, the smaller is the percentage difference between the excess  $(H - H_0)$  along  $l_o$  and the excess  $(H - H_0)$  along  $l_i$ , i.e., the more uniform is the domain distribution. For a given  $\phi_{ps}$ , this amounts to a larger number of domains, and hence more poles are created and the apparent threshold value drops.

Consider now the multipath core in Fig. 1(b). The sequence of CLEAR, PRESET, and SET pulses is repeated as before (Fig. 51), except that now the PRESET pulse,  $F_{ps}$ , is applied to Leg 1 and the SET pulse,  $F$ , is applied to Leg 4, as shown in Fig. 52(a). A  $\phi$ - $F$  curve thus becomes a plot of  $\Delta\phi_{res}$  in Leg 4 versus the SET MMF. Let us examine a typical curve,

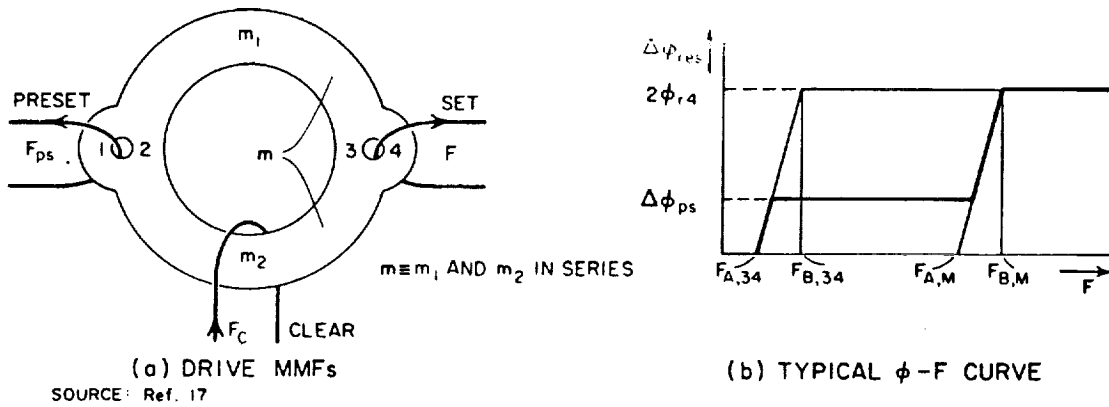
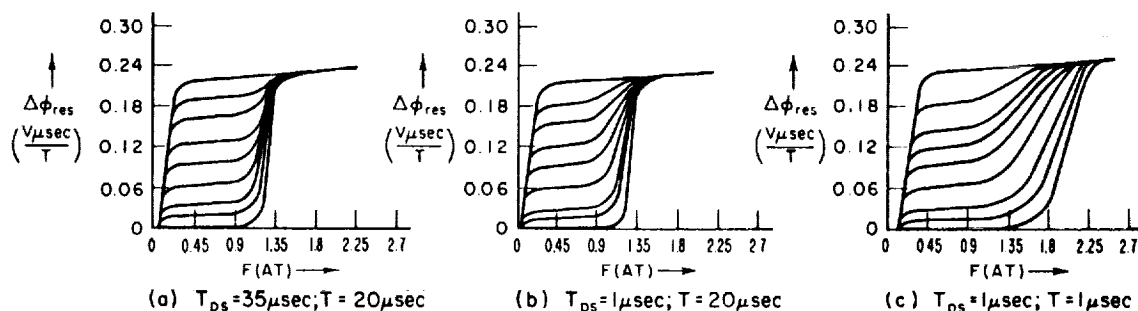


FIG. 52  $\phi$ - $F$  CURVE TEST FOR A MULTIPATH CORE

Fig. 52(b). Here, a PRESET pulse,  $F_{ps}$ , switches flux  $\Delta\phi_{ps}$  around Legs 1,  $m$ , and 3. When  $F$  is applied to Leg 4, a low threshold has to be overcome in order to switch  $\Delta\phi_{ps}$  from Leg 3 to Leg 4. Once  $\Delta\phi_{ps}$  is switched around the minor aperture,  $F$  has to increase considerably before it can switch flux around the major aperture. This accounts for the middle plateau in the curve. A further increase in  $F$  enables flux to switch around Legs 2,  $m$ , and 4 until Leg 4 is saturated, where the higher plateau is reached.

Families of measured  $\phi$ - $F$  curves, with  $T$ ,  $T_{ps}$ , and  $\phi_{ps}$  as parameters, are given in Ref. 17 and shown here in Fig. 53. A soft threshold is caused by a PRESET pulse of short duration and high amplitude, as in the case of a toroid. Similarly, a SET pulse of short duration and high amplitude increases the threshold value for any level of  $\phi_{ps}$ .



SOURCE: Ref. 17

PA 3696 53

FIG. 53  $\phi$ - $F$  CURVES OF A MULTIPATH CORE WITH  $T_{ps}$  AND  $T$  AS PARAMETERS

The effect of soft threshold on flux switching in multipath cores is very important. Unfortunately, we do not have sufficient quantitative information about the relation between factors that affect the flux state and the resulting reduction in effective threshold. More investigation should be carried out along this line.

#### 5. EVALUATION OF CORE CHARACTERISTICS

A change in the material, or the geometry of a core (or both) may manifest itself in the shape of a  $\phi$ - $F$  curve. A necessary condition for cores to be uniform is to have identical families of  $\phi$ - $F$  curves, Fig. 50(a). Information about the core characteristics may be completed by recording a family of curves of instantaneous  $\Delta\phi(t)$  versus  $F$ , with  $t$  as a parameter. Such curves may be obtained by strobing  $\Delta\phi(t)$  during the switching time of the tested core. In Ref. 9, a family of curves  $\Delta\phi(t)$  versus  $F$  with  $t$  as a parameter is redrawn as a family of curves  $\Delta\phi(t)$  versus  $t$  with  $F$  as a parameter. From these curves one may construct  $\dot{\phi}(t)$  versus  $t$  for a given  $F$ .

#### 6. $\phi$ - $F$ CURVES OF A CRACKED CORE

We shall now discuss the effect of a crack in a core on the  $\phi$ - $F$  curves. First, consider a cracked toroid, Fig. 54(a). In terms of our leg models, and ignoring fringing effects, the core is divided into two legs, Leg  $m$  (material) and Leg  $a$  (air). Their cross-sectional areas are assumed to be the same and their respective lengths are  $l_m$  and  $l_a$ .

Suppose that the core has been cleared (fully switched in the clockwise direction). In order to satisfy the requirement for continuity of flux, poles are created near the air gap. Their polarity is such that they tend to demagnetize Leg  $m$ . The directions of the arrowheads in Fig. 54(a) serve merely as positive references. In fact,  $F_a$ ,  $\phi_a$ , and  $\phi_m$  are negative in sign. We note that  $\phi_m = \phi_a$  and, since no external MMF is present,  $F_m = -F_a$ . Superposition of the straight line  $-\phi_a = \mu_0 A (-F_a) / l_a$  on the  $\phi$ - $F$  loop of Leg  $m$  yields the quiescent state  $\phi = \phi_Q$  and  $F = F_Q$ , as shown in Fig. 54(b). Note that if  $l_a$  is larger, the quiescent point,  $Q$ , may climb above the knee, along the steep side of the static loop.

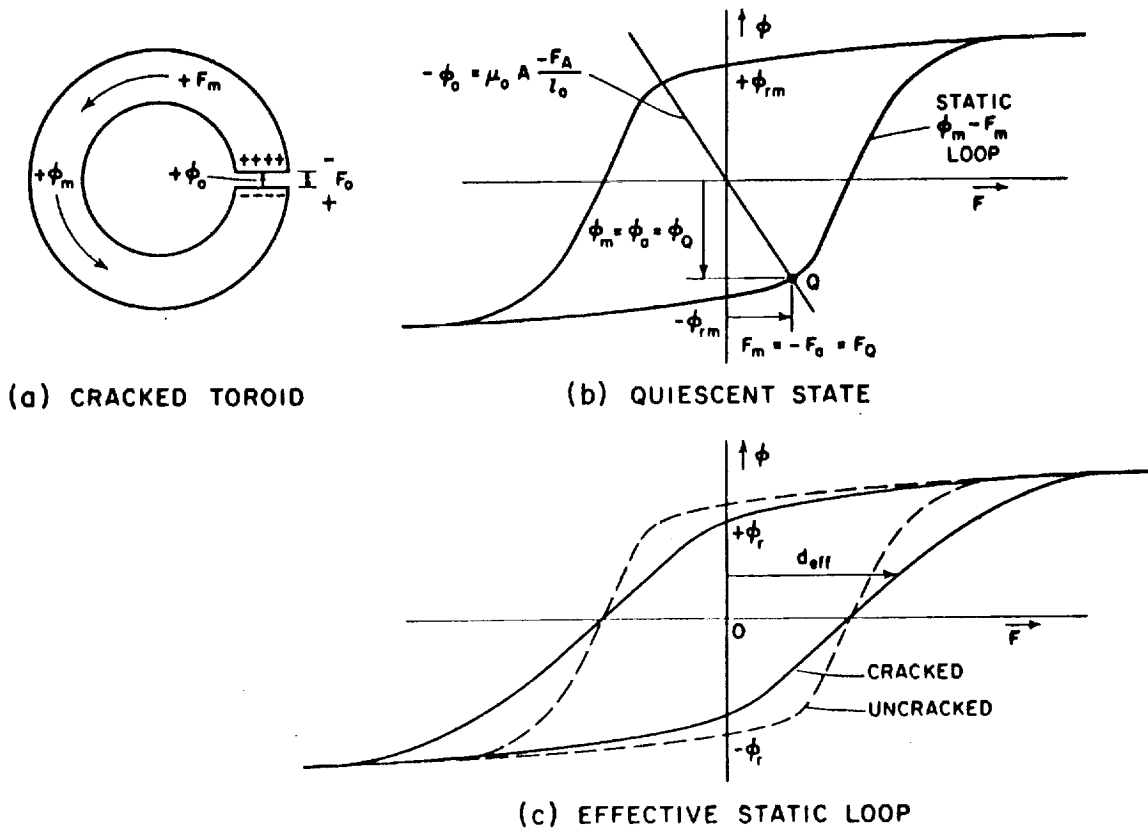


FIG. 54 STATIC CHARACTERISTIC OF A CRACKED TOROID

External positive MMF,  $F$ , is now applied to the cracked toroid, and Leg  $m$  is driven by total MMF,  $(F - F_a)$ . Note that  $F_a$  varies as the flux in Leg  $m$  changes. The excess MMF of Leg  $m$  over its static threshold is

$$F_{m,ex} = F - d_{eff} \quad (70)$$

where

$$d_{eff} = d + F_a \quad (70a)$$

Here  $d_{eff}$  is the effective static threshold as seen by  $F$ , the external MMF. In the region  $-\phi_r \leq \phi \leq 0$ ,  $-F_Q \leq F_a \leq 0$  so that  $d_{eff} < d$ , but in the region  $0 \leq \phi \leq \phi_r$ ,  $0 \leq F_a \leq F_Q$ , so  $d_{eff} > d$ . A plot of effective static loop of the cracked toroid is shown in Fig. 54(c).

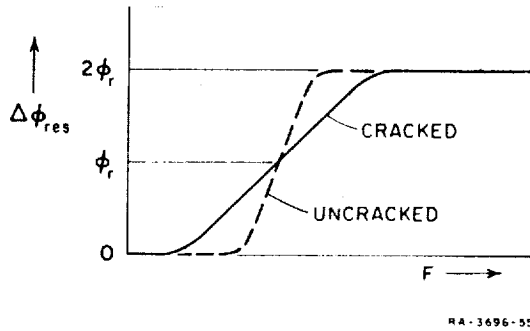


FIG. 55  $\phi$ - $F$  CURVE OF A CRACKED TOROID

A similar modification occurs with the  $\phi$ - $F$  curve. An effective  $\phi$ - $F$  curve for a cracked toroid is compared in Fig. 55 with a normal  $\phi$ - $F$  curve. The effective  $\phi$ - $F$  curve is the actual curve that will appear on the oscilloscope screen, using the automatic-plotting technique described previously.

Note that if  $F \gg d$ , the effect of the poles is smaller.

This has been verified experimentally in Ref. 18, where some calculations to predict the effect of an air gap on voltage waveshapes are given.

Now let us consider a crack in Leg 4 of a multipath core, Fig. 56(a). After the core is cleared through the major aperture, poles will be created across the crack. These poles tend to push Leg 3 further into negative saturation, but tend to set Legs  $m$  and 4. Suppose that this cracked core is driven by a SET MMF through the major aperture in order to obtain its  $\phi$ - $F$  curve. Because of the poles, flux switched in Leg  $m$  will first close through Leg 4. The  $\phi$ - $F$  curve will be modified in a way similar to that of a toroid, Fig. 55. When Leg 4 is half switched ( $\phi_4 = 0$ ), the net pole density on each side of the crack is zero; hence,



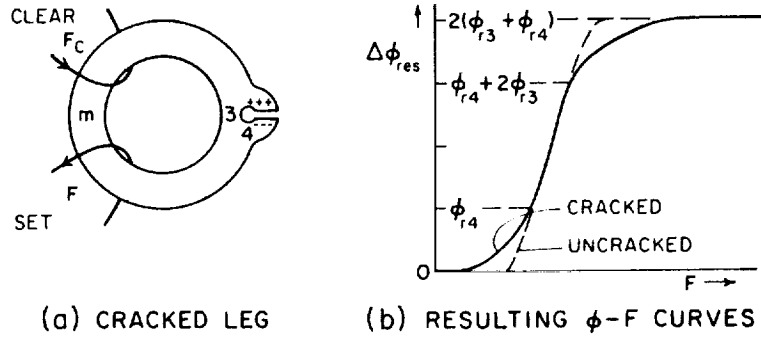


FIG. 56  $\phi$ -F CURVE OF A CRACKED MULTIPATH CORE

somewhere before  $\Delta\phi_m = \phi_{r4}$ , Leg 3 (which is shorter than Leg 4) starts to provide a closure path for the flux switched in Leg  $m$ . From then until Leg 3 saturates,  $\phi_m \approx \phi_3$  and the  $\phi$ -F curve is normal. By now  $\Delta\phi_m \approx \phi_{r4} + 2\phi_{r3}$  and the remainder of flux to be switched in Leg  $m$  has to close through Leg 4. The poles are now opposing the SET MMF and, as in the case of a toroid, the  $\phi$ -F curve is stretched. The dotted line in Fig. 56(b) corresponds to an uncracked multipath core, and is added for comparison.

The general character of the  $\phi$ -F curve in Fig. 56(b) has been verified experimentally with many cracked cores (the cracks can be seen by means of a microscope). This is another area that needs further investigation.

## I. CONCLUSIONS

The objective of this section is to establish the basic physical and mathematical models for the switching characteristics of a ferrite multipath core. To obtain these characteristics, a multipath core is divided into legs (physical paths between the core junctions), and  $n$  equations with  $n$  unknowns of an electrical-circuit analogue are solved (a computer may be needed). In this manner the problem of flux switching in a multipath core is reduced to the simpler problem of determining the switching properties of a single leg. These properties are governed by two factors, material and geometry.

In an attempt to understand the properties of a polycrystalline ferrite material, we have assumed the model of elongated ellipsoidal domains. By assuming a circular cross section for each reversed domain, we are able to portray qualitatively the energy diagram versus a domain radius due to the inhomogeneity in the material. One should recall that the energy diagram is plotted schematically only; it is not based on experimental measurements. Although such a model may be challenged (there has been no direct observation of the assumed structure), this model can be used to explain the origin of the elastic and inelastic switching caused by MMF drives of varying amplitude and duration. This, perhaps, is the strongest argument for the justification of this model.

Four independent geometry parameters affect the switching properties of a leg: the edge lengths  $l_i$  and  $l_o$ , the width  $w$ , and the height  $h$ . A toroid, viewed as a one-leg core, is a special case of a leg of  $w = (l_o - l_i)/2\pi$ ; hence, it has only three independent geometry parameters. By combining the geometry parameters and the material properties, we are able to arrive at mathematical models for elastic and inelastic switching. These models turn out to be nonlinear, and one wonders how useful they are for engineering application. If a computer is readily available, the difficulties due to the nonlinearity can be overcome. However, if manual computation is specified, average quantities may be assumed, thus eliminating the nonlinearity problem. Such a procedure is justified when  $\Delta\phi$ , not  $\phi(t)$ , is the solution looked for in the problem, because  $\Delta\phi$  involves time integration of  $\phi$ , and thus may be expressed in terms of average parameters.

A large amount of information about ferrite-core switching properties that is available in the literature may be borrowed in determining the switching properties of a leg. However, several areas need further investigation:

- (1) Relaxation of  $\phi$  after  $F$  is removed,
- (2) A model for elastic  $\phi$  between a negative and a positive saturation as a function of  $\phi$  and the duration and amplitude of an MMF prepulse,
- (3) Effects of soft state on  $F_0$ ,  $\rho$  and  $\epsilon$ ,
- (4) Switching characteristics of a multipath core with a cracked leg.

## II FLUX TRANSFER

In this section we shall examine the behavior of a multipath core in different schemes of operation. We shall concentrate on the switching characteristics of multipath cores in three main schemes. The first scheme deals with the use of a multipath core to control flux continuously. Here, a multipath core acts as a saturable reactor or as the core of a magnetic amplifier. The second and third schemes deal with flux transfer for digital computer application. These schemes are referred to as the *non-resistance* scheme and the *resistance* scheme because, in the latter, resistance is needed in the coupling loop in order to enable priming (*i.e.*, switching around the minor output aperture) to take place. Both schemes must operate so that bistable operation can be obtained. This will be explained in terms of the flux gain properties that must be achieved in order to get bistability in a range of operation.

### A. SETTING CHARACTERISTICS

#### 1. ASYMMETRICAL READ-OUT

Consider a multipath core with winding arrangement as shown in Fig. 57(a). The sequence of pulse MMFs applied to the different windings<sup>19</sup> is shown in Fig. 57(b). The MMF pulses are as follows:  
 $F_C = N_C I_C = \text{constant}$ ,  $F_s = N_s I_s$ ,  $F_p = N_p I_p = \text{constant}$ , and  $F_D = N_D I_D$ .  
First, a high CLEAR pulse,  $F_C$ , clears the multipath core. Then a SET pulse,  $F_s$ , sets the core by switching positive flux in Leg 1 and (mainly) Leg 3. The amount of the set flux may be varied by varying  $F_s$ . The SET flux in Leg 3 is now "primed," *i.e.*, switched around to Leg 4, by  $F_p$ . The amplitude and duration of  $F_p$  are large enough to prime the full flux capacity of Leg 3, but the amplitude is too small to switch flux around the major aperture. Following  $F_p$ , a DRIVE MMF,  $F_D$ , is applied and clears Leg 4 (for lack of anything better, the term DRIVE is borrowed from Ref. 19). Here, the amount of flux cleared from Leg 4 depends on the magnitude of  $F_D$ . After that,  $F_p$  and  $F_D$  are applied alternately, enabling one to sense steady-state output flux  $\Delta\phi_o$  on Leg 4 during DRIVE time. Since  $F_p \neq F_D$ , this read-out is considered asymmetrical.

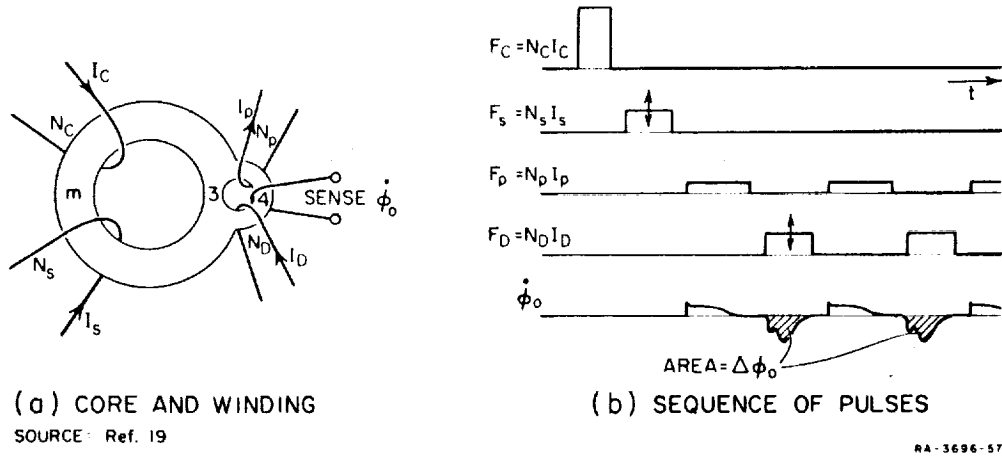


FIG. 57 SETTING-CHARACTERISTICS TEST

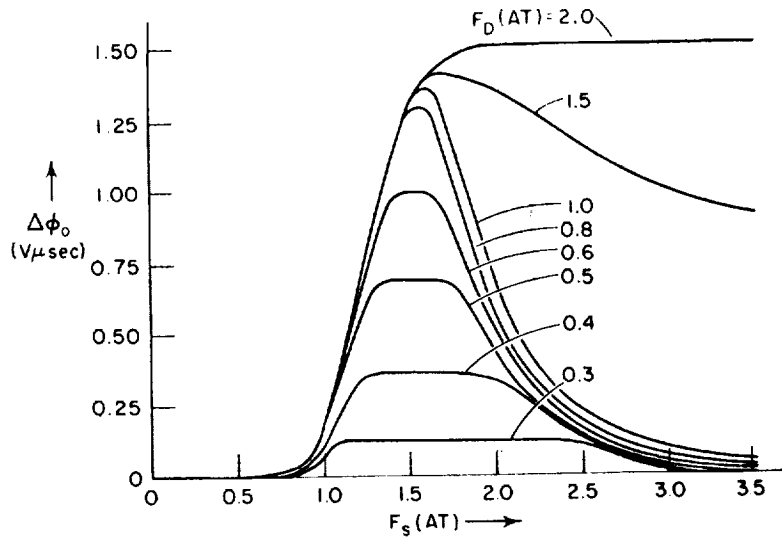
The output flux,  $\Delta\phi_o$ , depends on  $F_s$  and  $F_d$ . A plot of  $\Delta\phi_o$  versus  $F_s$  with  $F_d$  as a parameter is called *setting characteristics*. Measured characteristics, obtained from Ref. 19, are shown in Fig. 58. Because of the small magnitude of  $F_p$  and  $F_d$ , elastic  $\Delta\phi_o$  is assumed to be negligible. The shapes of these characteristics are explained as follows, considering only inelastic flux changes.

Assume that the core is in the CLEAR state. The value of  $F_p$  is fixed in the range

$$d_{34}^{\max} < F_p < d_{\#4}^{\min} \quad (71)$$

where  $d_{34}$  stands for  $d_3 + d_4$  and  $d_{\#4}$  stands for  $d_{\#} + d_4$ . Hence,  $F_p$  cannot switch flux around the major aperture. Since  $F_d$  tends to further clear the cleared core, it cannot switch flux either. It is, therefore, concluded that  $\Delta\phi_o = 0$  if  $F_s \leq d_{\#3}^{\min}$ , which explains why  $F_s$  has to be above  $\sim 0.8 AT$  before output flux can result.

Consider the case of a fixed  $F_d$  which is below the value needed to switch a fully set Leg 4 ( $F_d < 1.0 AT$ ). As  $F_s$  increases above  $d_{\#3}^{\min}$ , an amount of flux  $\Delta\phi_{s,3}$  is set into Leg 3 (and later primed into Leg 4) so that  $\Delta\phi_o$  increases. At some value of  $F_s$ , the amount of flux primed into Leg 4 is beyond the flux capacity that  $F_d$  is able to switch back, and  $\Delta\phi_o$  flattens out. This explains the plateau of  $\Delta\phi_o$ . As  $F_s$  is increased beyond the value needed to fully set Leg 3, Leg 4 is partially set by  $F_s$ ,



SOURCE: Ref. 19

RA-3696-58

FIG. 58 ASYMMETRICAL SETTING CHARACTERISTICS

say by an amount  $\Delta\phi_{s4}$ . When  $F_p$  is next applied, only  $2\phi_{r4} - \Delta\phi_{s4}$  is primed so that Leg 3 remains partially set. As a result, less amount of flux is available for switching, but this amount is still too large to be switched completely by  $F_D$ . At some value of  $F_s$ , this amount of flux matches the maximum amount that  $F_D$  is able to switch. Further increase in  $F_s$  results in a decrease in  $\Delta\phi_0$  because of the increase in  $\Delta\phi_{s4}$ . When  $F_s = d_{s4}^{max}$ , Legs 3 and 4 are fully set, and no flux can be primed, hence  $\Delta\phi_0 = 0$ . A further increase in  $F_s$  does not alter  $\Delta\phi_0$ .

If  $F_D > 1.0$  AT,  $F_D$  is large enough to switch flux around the major aperture. If  $F_s$  is below the value needed to switch flux in Leg 4,  $\Delta\phi_0$  switches around the minor aperture and is equal to  $\Delta\phi_{s3}$ , because this is all that is primed into Leg 4. For  $F_s$  above this value, part of  $\Delta\phi_0$  may result from switching around the major aperture; this calls for a higher  $\Delta\phi_0$  than is needed in the case where  $F_D < 1.0$  AT. The increase in  $\Delta\phi_0$  depends on  $F_D$ . If  $F_D$  is large enough to switch all of Leg 4 around the major aperture, the flux that can be primed,  $2\phi_{r4} - \Delta\phi_{s4}$ , has no effect, and  $\Delta\phi_0 = 2\phi_{r4}$ .

A less quantitative explanation of this sort is given in Ref. 19. Unfortunately, no analysis is presented there. An analysis of setting characteristics is given in Appendix D, but the analysis is simplified

by assuming a rectangular  $B-H$  loop, long-enough pulse duration, a ring-element model, a preference of flux to switch in a shorter path, and a very small minor aperture.

## 2. SYMMETRICAL READ-OUT

The setting-characteristics test, Fig. 57, is now repeated with one modification. The PRIME MMF,  $F_p$ , is variable and is equal in magnitude to  $F_D$ . The resulting setting characteristics, as given in Ref. 19, are shown in Fig. 59. Comparing Fig. 59 with the asymmetrical setting characteristics in Fig. 58, we notice two main differences. First, Fig. 59 shows no plateaus inside the triangular characteristic of  $F_D = 1.0$  AT; instead, the curves are triangular. Second, to the left of this triangular characteristic in Fig. 59,  $\Delta\phi_o$  is not equal to zero, but is positive and constant.

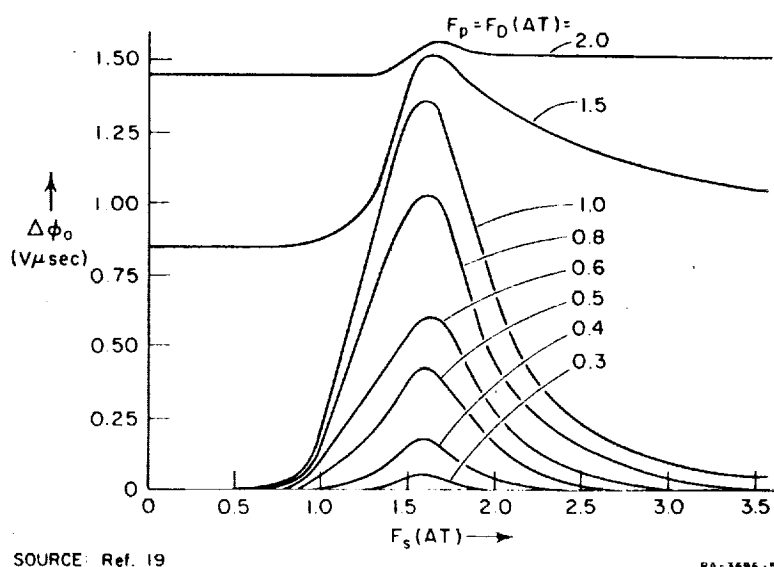


FIG. 59 SYMMETRICAL SETTING CHARACTERISTICS

The symmetrical setting characteristics are analyzed in Appendix D, and will be explained here only briefly. If  $F_s$  is small, only an inside ring of finite thickness around the major aperture is set. Since this ring is relatively far from the minor aperture, a given  $F_D$  may be able to switch only part of it. Increasing  $F_s$  increases the amount of flux that a fixed  $F_D$  can switch, which accounts for the positive slope

of the inside triangles. Beyond the peaks of the triangles,  $F_s$  sets Leg 4 as well, so that  $\Delta\phi_o$  decreases for the same reason as in the asymmetrical case.

The positive  $\Delta\phi_o$  for  $F_D = 1.5 AT$ , even if  $F_s$  is small, stems from the fact that  $F_p (=F_D)$  is now large enough to set Legs 3 and  $m$ . When  $F_D = F_p \approx 2.0 AT$ , all of Leg 3 can be set by  $F_p$ .

In Fig. 59, note that to the right of the triangular characteristics of  $F_D = 1.0 AT$  there is no difference from the asymmetrical case. This is so because Leg 3 is fully set by  $F_s$ , and  $F_p$  is large enough to prime Leg 3 in both cases.

We notice that if  $F_p (=F_D)$  is low,  $\Delta\phi_o = 0$  as  $F_s$  increases, until  $F_s$  is able to switch flux close enough to the minor aperture. This agrees with the calculated characteristics in Appendix D. On the other hand, it is claimed in another paper<sup>20</sup> that these characteristic curves (except that  $F_D$  and  $F_p$  have a sinusoidal waveform) fan out from one threshold value of  $F_s$ . It looks as though Ref. 20 is wrong at this point; in addition, the data are incomplete, since  $F_D$  is not extended far enough to get all the characteristics.

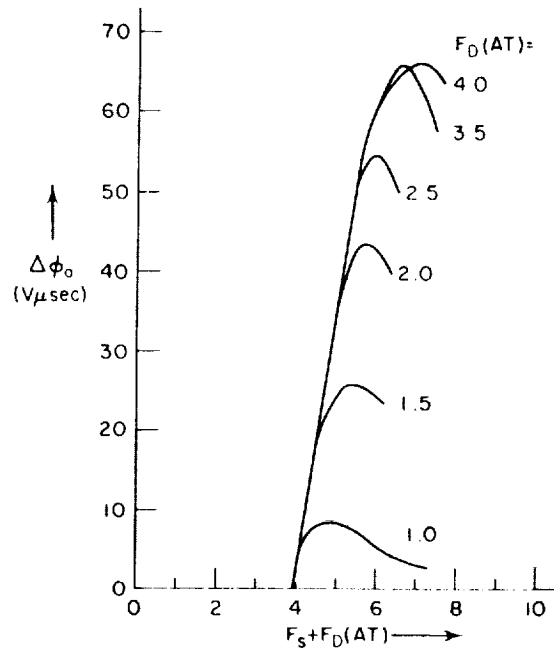
### 3. OTHER SETTING CHARACTERISTICS

Several other measured setting characteristics are presented in Ref. 20. In one case the ac  $F_D$  is ON while  $F_s$  is applied for several cycles. The resulting characteristics are replotted versus  $F_s + F_D$ , as shown in Fig. 60. This case is then repeated, except that  $F_s$  is applied during a single half-cycle, first with  $F_D$  opposing and then with  $F_D$  helping. These variations are not too important.

## B. ALL-MAGNETIC FLUX TRANSFER

### 1. ALL-MAGNETIC SCHEMES

This part deals with all-magnetic transfer of flux between multi-path cores. The term *all-magnetic* is used here to indicate that the cores are coupled by means of wire only. A coupling-loop wire is inherently composed of an ideal conductor and three impedance components: resistance,  $R_\ell$ ; inductance,  $L_\ell$ ; and capacitance,  $C_\ell$ . Any combination of these components in the coupling-loop wire may be present in an all-magnetic scheme, although some may be redundant, or even undesired. For the examples discussed in this section,  $C_\ell$  is negligible, and will be ignored.



SOURCE: Ref 20

RA 3596-60

FIG. 60 SYMMETRICAL SETTING CHARACTERISTICS  
( $F_s$  and  $F_D$  Simultaneous for Several Cycles)

The advantages of using an all-magnetic flux transfer scheme over one that incorporates semiconductor elements are primarily the following:<sup>21</sup>

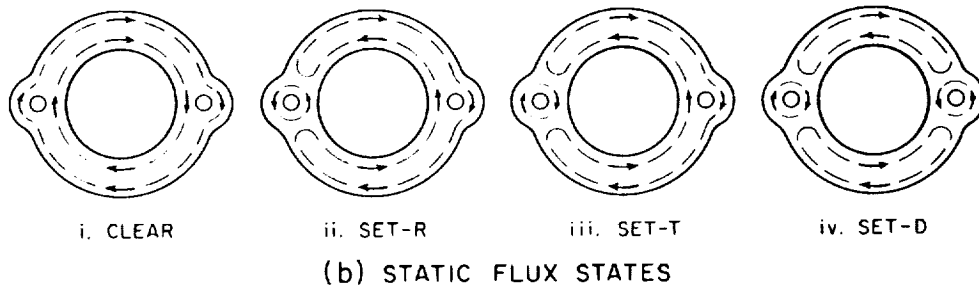
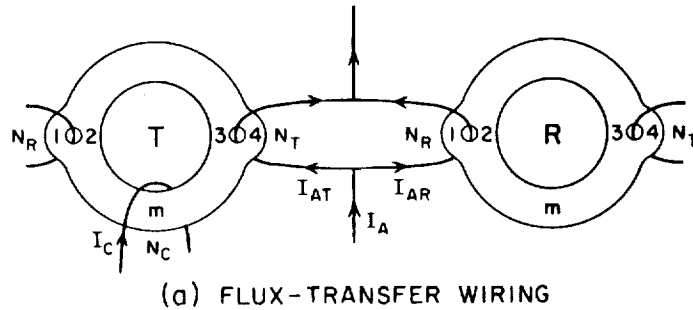
- (1) High reliability of magnetic material
- (2) Insensitivity of ferrites to radiation<sup>22</sup>, and
- (3) Possible lower cost.

In a recent survey of logic circuits using magnetic devices<sup>23</sup>, five all-magnetic schemes are listed. The magnetic devices used to realize these schemes are toroids, multipath cores and thin films. In this report only schemes using multipath cores will be considered. These schemes are classified into two categories: nonresistance and resistance. In the non-resistance schemes, any coupling-loop resistance is undesired, and hence should be minimized. In the resistance schemes,  $R_\ell$  is used as a flux sink and should be designed accordingly.



## 2. NONRESISTANCE FLUX-TRANSFER SCHEMES

Detailed descriptions of some nonresistance flux-transfer schemes can be found in Refs. 24, 25, 17, 4, and 26. We shall describe here the basic ideas of a nonresistance scheme<sup>17</sup> from the point of view of flux switching in multipath cores, rather than circuit operation.



SOURCE: Ref. 17

RA-3896-61

FIG. 61 A NONRESISTANCE FLUX-TRANSFER SCHEME

Consider two multipath cores,  $T$  (for *transmitter*) and  $R$  (for *receiver*), each with one major aperture and two minor apertures, as in Fig. 61(a). These cores are coupled by a loop of negligible impedance and driven by external MMFs which are generated by constant-current pulses  $I_A$  (ADVANCE) and  $I_C$  (CLEAR). Let four possible static flux states, CLEAR, SET- $R$ , SET- $T$  and SET- $D$ , of these cores be designated by arrowheads, as shown in Fig. 61(b). Assume that the receiver is initially in the CLEAR state, and that the transmitter is either in the CLEAR state or in the SET- $T$  state. We shall now show how a sequence of pulses  $I_A$  and  $I_C$  transfers the flux state of the transmitter to the receiver, leaving the transmitter in the CLEAR state.

As  $I_A$  is applied, it splits into two currents,  $I_{AT}$  and  $I_{AR}$ , whose magnitudes depend on the flux state of the transmitter. First, suppose that the transmitter is in the CLEAR state. If  $I_A$  is limited so that  $I_{AT}$  and  $I_{AR}$  cannot spuriously set the two cores, no change in the flux states takes place. The following CLEAR current,  $I_C$ , tends to push the transmitter further into negative saturation, so that there is still no change in the flux state of either core. Thus, the net effect of pulses  $I_A$  and  $I_C$  is the (trivial) transfer of the CLEAR flux state from the transmitter to the receiver, leaving the transmitter in the CLEAR state.

Now suppose that the transmitter is in the SET- $T$  state. Current  $I_{AT}$  is lower than in the previous case because it provides a comparatively low MMF that is needed to switch flux counterclockwise around Legs 3 and 4, thus bringing the transmitter to the SET- $D$  state. As a result, Current  $I_{AR}$ , which is equal to  $I_A - I_{AT}$ , is now large enough to switch the receiver from the CLEAR state to the SET- $R$  state. Next, Current  $I_C$  clears the transmitter and the resulting voltage  $N_T \phi_{T4}$  (subscript  $T$  is used for transmitter; subscript 4 is used for Leg 4) generates coupling-loop current which switches flux around Legs 1 and 2 of the receiver, bringing it to the SET- $T$  state. The net result is that the SET- $T$  flux state in the transmitter has been transferred into the receiver, and the transmitter is left in the CLEAR state.

Consider again the division of  $I_A$  into  $I_{AT}$  and  $I_{AR}$  in the case of the transfer of a CLEAR state. To assure that neither core will switch, the conditions

$$N_T I_{AT} \leq F_{A,M} \quad (72)$$

and

$$N_R I_{AR} \leq F_{A,M} \quad (73)$$

must be satisfied, where  $F_{A,M}$  is the threshold MMF around the major aperture via Leg 4 of the  $\phi$ - $F$  curves, Fig. 52(b). Since  $I_A = I_{AT} + I_{AR}$ , the maximum value for  $I_A$  is

$$I_A^{\max} = F_{A,M} \left( \frac{1}{N_T} + \frac{1}{N_R} \right) \quad (74)$$

Ideally,  $R_\chi$  and  $L_\chi$  should be zero, but in reality they are finite. If we require that  $I = I_A^{\max}$ , equality signs should be assumed in

Conditions (72) and (73); thus,  $N_T I_{AT} = N_R I_{AR}$ . In order to get this relation between  $I_{AT}$  and  $I_{AR}$ , the components  $R_\ell$  and  $L_\ell$  in the T and R branches should be related according to

$$\frac{R_{\ell T}}{R_{\ell R}} = \frac{L_{\ell T}}{L_{\ell R}} = \frac{N_T}{N_R} \quad (75)$$

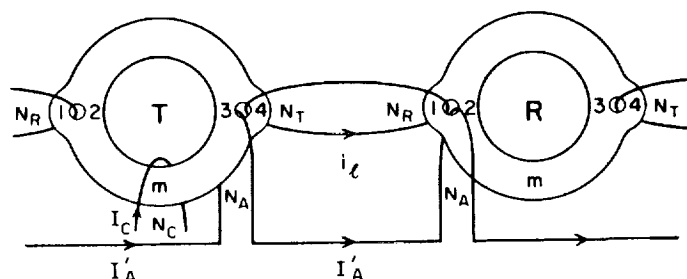
Since  $R_\ell$  and  $L_\ell$  are very small, this amounts to a difficult soldering job in tapping the main wire which carries current  $I_A$  to a small coupling loop. Such an undesired feature may be overcome by an alternative winding arrangement shown in Fig. 62. When the transmitter is in the CLEAR state, the condition

$$I'_A N_A \leq F_{A,M} \quad (76)$$

is sufficient to assure no spurious setting of either core. In this case the coupling-loop current is zero. By combining Eqs. (74) and (76) we get

$$I'_A = \frac{N_T N_R}{N_A (N_T + N_R)} I_A \quad (77)$$

If the transmitter is in the SET-T state, as  $I'_A$  is applied, flux switches around Legs 3 and 4 (bringing the transmitter to the SET-D state) and generates loop current  $i_\ell$  which, when added to  $I'_A N_A$ , switches the receiver to the SET-R state. It can be shown that, if Eq. (77) is satisfied, the wiring schemes in Figs. 61(a) and 62 are equivalent for transferring any amount of flux from the transmitter to the receiver. The wiring scheme in Fig. 62 can be more accurately controlled and is easier to manufacture.



SOURCE: Ref. 17

RA-3696-62

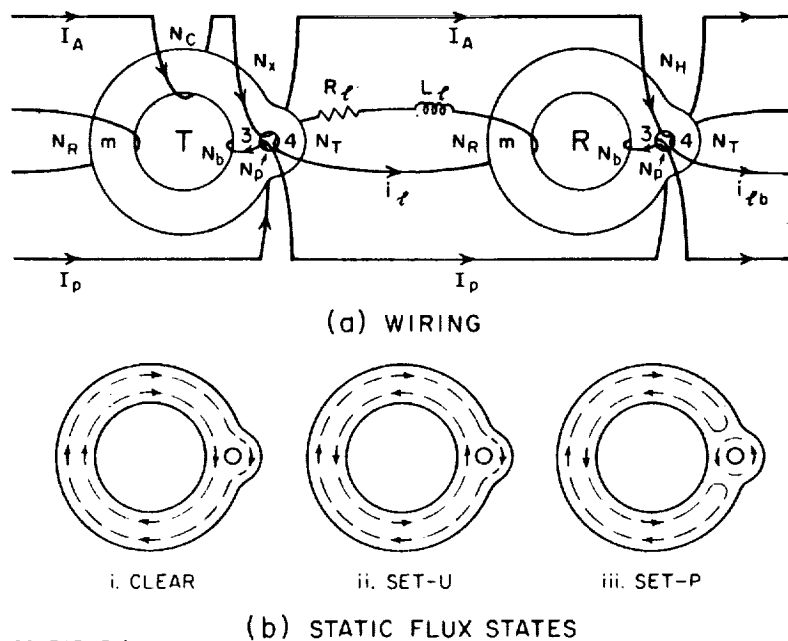
FIG. 62 ALTERNATIVE WIRING FOR A NONRESISTANCE SCHEME

### 3. RESISTANCE FLUX-TRANSFER SCHEMES

Details of some resistance flux-transfer schemes may be found in Refs. 27, 28, 11 (pp. 208-210), 2, 29, 30, and 31. The mechanism of flux transfer in a basic resistance scheme<sup>2,31</sup> is described as follows:

A source of an ADVANCE pulse-current,  $I_A$  (e.g., of a damped-sinusoidal shape), and a source of a dc PRIME current,  $I_p$  (which may alternatively have a pulse form), drive a transmitter,  $T$ , and a receiver,  $R$ , as in Fig. 63(a). A coupling loop, of resistance  $R_\ell$  and self inductance  $L_\ell$ , links the two cores. The number of turns of each winding are as indicated. Note that  $N_p$  is the total number of turns of the PRIME winding in the minor aperture.

Three possible static flux states, CLEAR, SET-U, and SET-P, are shown in Fig. 63(b). Assume that initially the receiver is in the CLEAR state and the transmitter is either in the CLEAR or the SET-P state. We shall now show that application of the ADVANCE current pulse,  $I_A$ , transfers the flux state of the transmitter to the receiver, leaving the transmitter in the CLEAR state.



SOURCE: Ref. 31

RA-369F-63

FIG. 63 A RESISTANCE FLUX-TRANSFER SCHEME

First, assume that the transmitter is in the CLEAR state. Current-pulse  $I_A$  drives it elastically into negative saturation. Coupling-loop current  $i_\ell$ , generated by  $N_T \dot{\phi}_{T4}$ , is too low to set the receiver. The net result is no change in the states of the cores.

Now suppose that the transmitter is in the SET- $P$  state. Current-pulse  $I_A$  clears the transmitter, and the loop current  $i_\ell$ , generated by mainly inelastic  $N_T \dot{\phi}_{T4}$ , is high enough to switch the receiver to the SET- $U$  state. Notice that the MMF  $N_R i_\ell$  has to overcome the threshold  $F_0$  plus the bias MMF  $N_b I_p$  before the receiver can start switching. The function of ADVANCE MMF  $N_x I_A$  is to increase  $\dot{\phi}_{T4}$  by

- (1) Overcoming the loading loop current,  $i_\ell$ , which tends to drive Leg 3 elastically into negative saturation and thus steer part of  $\Delta\phi_{T4}$  to Leg 3
- (2) Driving Leg 4 hard into negative saturation after the set flux in the transmitter is cleared.

Note that if flux switching in the transmitter is fast, there is less volt-second drop across the loop resistance. Hence, a higher  $\dot{\phi}_{T4}$  causes a higher  $i_\ell$ , so that more flux is switched in the receiver. As  $I_A$  is released, direct current  $I_p$  primes the receiver by slowly switching the set flux in Leg 3 into Leg 4. The smaller  $R_\ell$  is, the higher is the magnitude of a negative  $i_\ell$ , and hence the longer is the priming time,  $\tau_p$ . This explains the need for a finite  $R_\ell$  in the resistance flux-transfer scheme. By now the receiver is in the SET- $P$  state, and the transmitter is in the CLEAR state.

The  $N_H$  turns on Leg 4 of the receiver function to hold Leg 4 in the CLEAR state. This will prevent spurious setting of the receiver by current  $i_{\ell b}$ , Fig. 63(a), in case a CLEAR state is transferred to the receiver. The current  $i_{\ell b}$  may come from a second transmitter, coupled to the receiver under discussion, which happens to transfer a SET state to a second receiver.

Too high a PRIME current may spuriously switch a core from a CLEAR state to a SET- $P$  state. This puts an upper limit on  $I_p$  such that

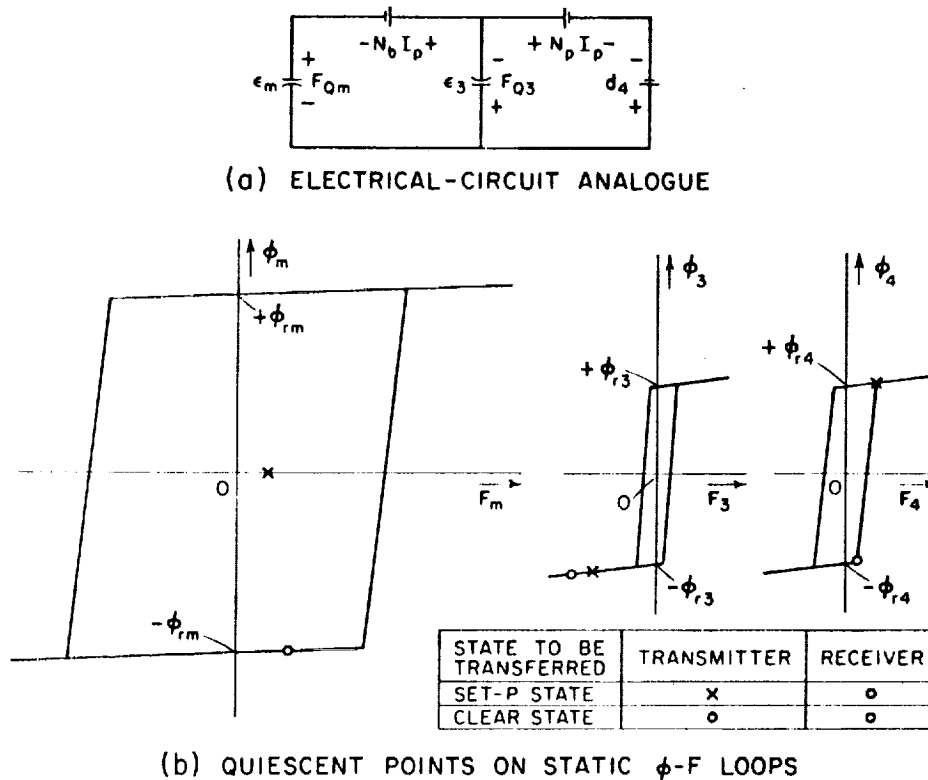
$$I_p^{\max} = \frac{d_{\pi}^{\min} + d_4^{\min}}{N_p - N_b} \quad (78)$$

On the other hand,  $I_p$  should be large enough to switch all the set flux from Leg 3 to Leg 4. This determines the lower limit for  $I_p$  as follows:

$$I_p^{\min} = \frac{d_3^{\max} + d_4^{\max}}{N_p} \quad (79)$$

A detailed analysis of the resistance flux-transfer scheme can be found in Refs. 31 and 3. It is shown in Ref. 3 that Leg 4 of the transmitter and Leg 4 of the receiver are both "clamped" to their respective static  $\phi$ - $F$  loops by a dc  $I_p$  before  $I_A$  is applied. The electrical-circuit analogue for this quiescent state is shown in Fig. 64, together with the the resulting quiescent points of each leg.

As  $I_A$  is applied, the operating points in the  $\phi$ - $F$  plane move. The motion is either wholly elastic or a combination of elastic and inelastic.



RA-3696-64

FIG. 64 QUIESCENT CONDITION OF A RESISTANCE SCHEME

Typical variations of  $F$  and  $\phi$  of each leg of the transmitter and the receiver are superimposed on its  $\phi$ - $F$  loop in Fig. 65 for the cases of transferring a CLEAR state and a SET- $P$  state. The arrows correspond to possible modes of operation (cf. Sec. I-E-4), which are designated by Roman numerals.

#### 4. FLUX GAIN

In describing nonresistance and resistance flux-transfer schemes, we have assumed so far that a core is either cleared or fully set. This, of course, is not the case, even when the cores are employed in digital systems. The following discussion applies to both nonresistance and resistance schemes.

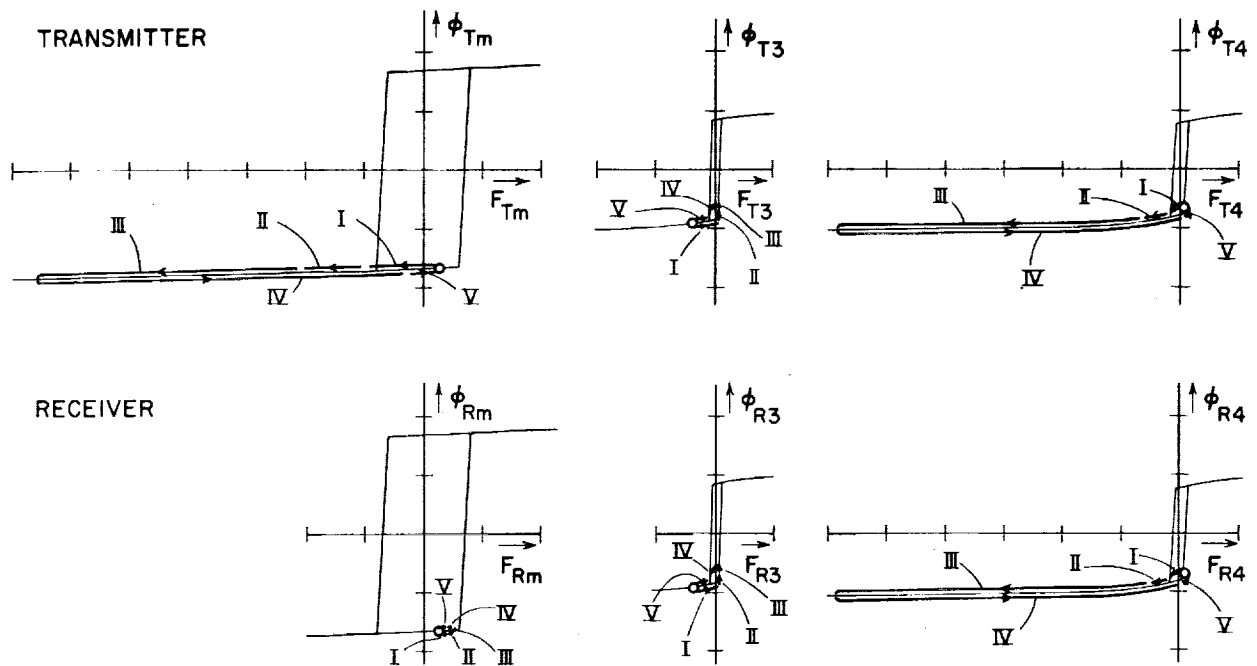
Let  $\Delta\phi_T$  be the amount of set flux in the transmitter, and let  $\Delta\phi_R$  be the amount of flux which is transferred into the receiver from the transmitter. A flux gain is defined as

$$G = \frac{\Delta\phi_R}{\Delta\phi_T} \quad (80)$$

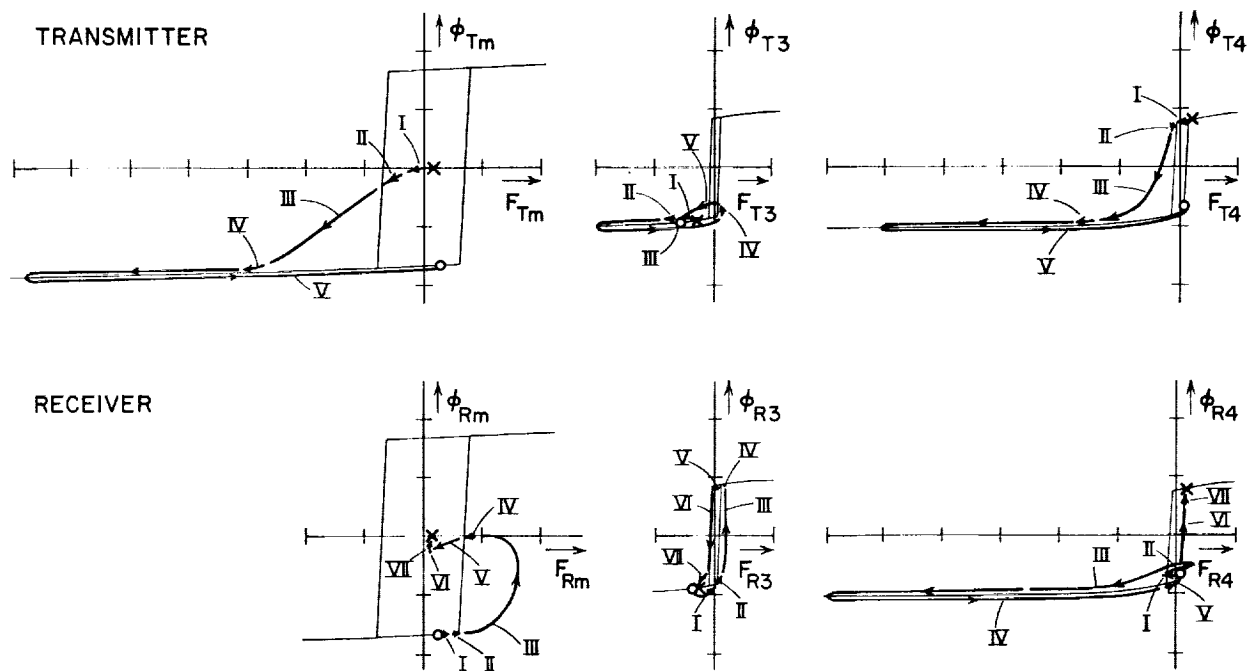
A typical plot of measured  $\Delta\phi_R$  versus  $\Delta\phi_T$  is shown in Fig. 66(a)i. The resulting curve of  $G$  versus  $\Delta\phi_T$  is shown in Fig. 66(a)ii.

Suppose that the flux-transfer process, as described so far, is repeated indefinitely every half cycle. A receiver, upon reaching the state of a transmitter during an  $n$ th half-cycle, becomes a transmitter during the next  $(n + 1)$ th half-cycle, and inversely. This is the case of a closed-loop shift register or of one that is indefinitely long. In this case, Points C and S of Fig. 66 become stable, because any small variation in  $\Delta\phi_R$  will cause a variation of the opposite polarity in the received flux during the following half cycle. The flux-transfer characteristic in Fig. 66 displays the bistability of a flux-transfer scheme: Point C corresponds to a stable CLEAR state and Point S corresponds to a stable SET state. It is concluded from Fig. 66(a) that in steady-state the core is not completely cleared or set, i.e., its stable quiescent flux level is either above  $-\phi_r$  or below  $+\phi_r$ . Note that the flux-transfer characteristic in Fig. 66(a) is experimental. Ideally, we would like it to be as shown in Fig. 66(b), where the stable flux levels are  $-\phi_r$  and  $+\phi_r$ .

A way to achieve the bistable transfer characteristic for a nonresistance scheme<sup>17</sup> is shown in Fig. 67. The wiring in Fig. 67(a) is



(a) CLEAR-STATE TRANSFER

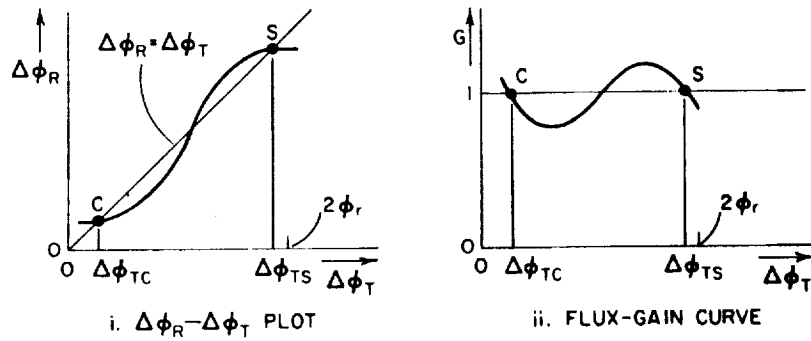


(b) SET-P STATE TRANSFER

RC-2679-9R

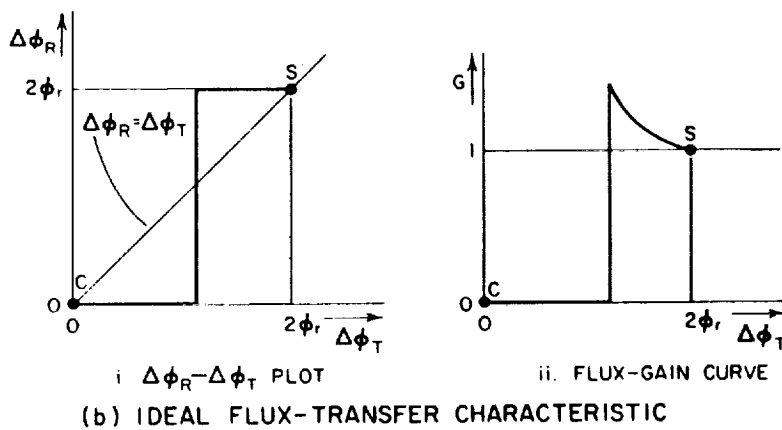
FIG. 65 VARIATION OF  $F$  AND  $\phi$  IN EACH LEG DURING ADVANCE AND PRIME PERIODS OF A RESISTANCE SCHEME





SOURCE: Ref. 17

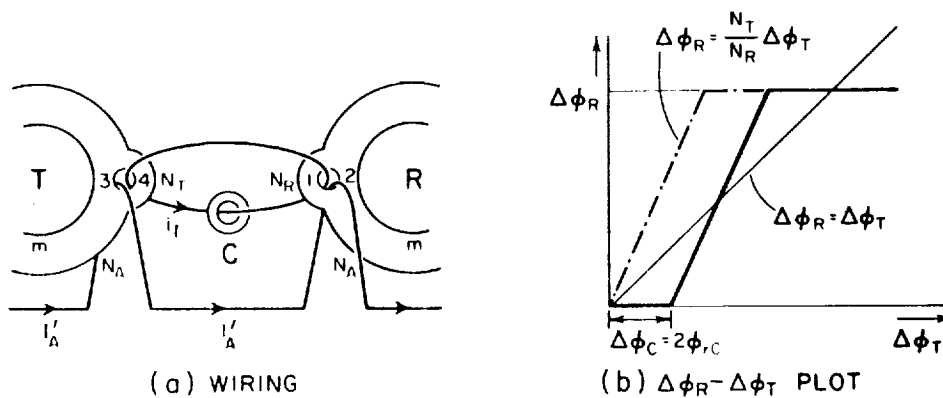
(a) EXPERIMENTAL FLUX-TRANSFER CHARACTERISTIC



(b) IDEAL FLUX-TRANSFER CHARACTERISTIC

RA-3696-65

FIG. 66 BISTABLE FLUX-TRANSFER CHARACTERISTIC



SOURCE: Ref. 17

RA-3696-66

FIG. 67 OBTAINING BISTABLE FLUX-TRANSFER CHARACTERISTIC BY TURNS RATIO AND FLUX CLIPPING

identical with the wiring of Fig. 62, except for the addition of a small toroid, C, of maximum residual flux,  $\phi_{rC}$ . Assuming that there is no flux loss in the coupling loop, if Toroid C is absent, then by the end of the ADVANCE time,  $\Delta\phi_R/\Delta\phi_T = N_T/N_R$ . By making  $N_T > N_R$ , G is made larger than one, and flux gain is achieved. Note that this relation holds as long as  $\Delta\phi_R \leq 2\phi_r$ .

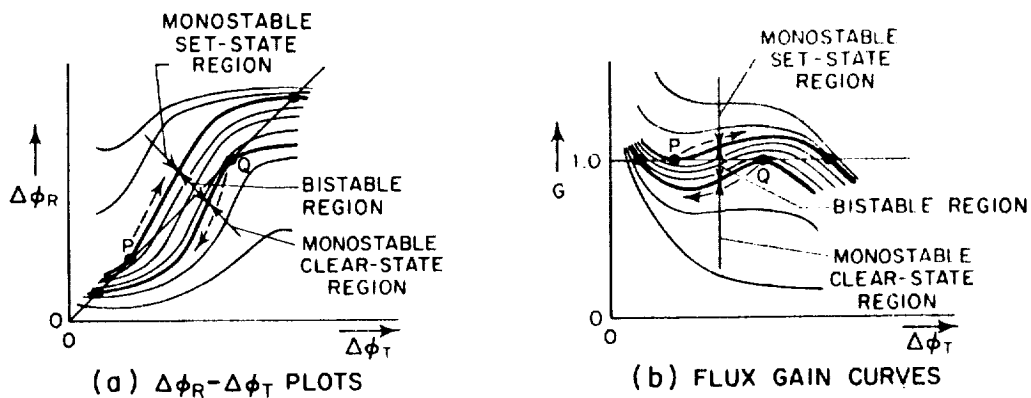
A toroid, C, in the CLEAR state is now added to the coupling loop, as shown in Fig. 67(a). By having the threshold of Toroid C much lower than that of the receiver (around the major aperture), when  $I'_A$  is applied, the toroid will switch first, and clip the amount of flux  $2\phi_{rC}$  from the transferred flux. For this reason the name *clipper* is given to Toroid C. The flux capacity of Clipper C,  $\Delta\phi_C$ , is small compared with  $\Delta\phi_R$ . The function  $\Delta\phi_R$  versus  $\Delta\phi_T$  is now obtained by shifting the straight line  $(N_T/N_R)\Delta\phi_T$ , Fig. 67(b), to the right by the amount  $\Delta\phi_C = 2\phi_{rC}$ . The resulting curve is bistable, as needed.

In Ref. 17, CLEAR drive is shown instead of ADVANCE drive in explaining how to achieve the proper flux gain relation. This CLEAR drive is there merely to show that if the flux clipper is cleared at the same time as the transmitter, basic operation is not altered. It should not be confused with the ADVANCE drive,  $I_A$ , applied to obtain the proper  $\Delta\phi_R - \Delta\phi_T$  curve.

## 5. RANGE MAP

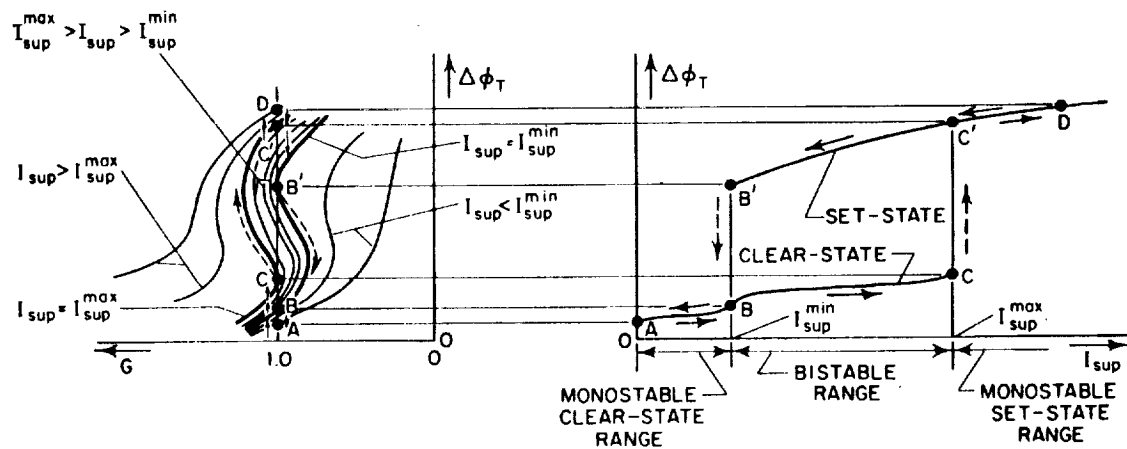
The flux-transfer characteristic, Fig. 66, corresponds to a bistable operation under a fixed set of supply currents ( $I_A$  in the nonresistance schemes and  $I_A$  and  $I_p$  in the resistance schemes). When supply current is changed, there is a change in the transfer characteristic until at some point the characteristic is tangent to a certain straight line (a 45-degree line in the  $\Delta\phi_R - \Delta\phi_T$  plot; a  $G = 1$  line in the flux-gain curve). This is illustrated in Fig. 68. Beyond the tangent point, the flux-transfer is monostable: in the  $G - \Delta\phi_T$  plane, a minimum point (Point P) corresponds to initiating a transient change in flux states from a CLEAR state to a SET state; a maximum point (Point Q) corresponds to initiating a transient change in flux states from a SET state to a CLEAR state.

A range of operation is a region of supply current in which flux transfer is bistable. Figure 69 shows a typical change in transferred flux as supply current,  $I_{sup}$ , is varied from zero to a high level and then back to zero. Supply current  $I_{sup}$  represents  $I_A$  in the nonresistance



NA 3696 67

FIG. 68 STABILITY REGIONS OF FLUX-TRANSFER CHARACTERISTICS



NA 3696-68

FIG. 69 EFFECT OF VARYING  $I_{sup}$  ON  $G$  AND  $\Delta\phi_T$

or the resistance schemes (with  $I_p$  fixed), or  $I_p$  in the resistance schemes (with  $I_A$  fixed). In each of the planes  $\Delta\phi_T - I_{sup}$  and  $G - \Delta\phi_T$ , the operating point travels along Path A-B-C-C'-D-C'-B'-B-A.

Under certain conditions, the bistable region in the resistance schemes is bound by two monostable CLEAR-state regions. This condition is caused by an unsetting effect, to be described later (see Sec. III-B-4-b). Assuming a fixed  $I_p$  and bistable operation (Point D, Fig. 70) as  $I_A$  is increased, a stable transferred SET state may drop to a CLEAR state at the boundary value of  $I_A = I_A^{max}$ , Points C' and C.

Two typical experimental range maps for a resistance scheme are compared in Fig. 71. One corresponds to monostable CLEAR-state and SET-state regions (Fig. 69), and the other corresponds to two monostable CLEAR-state regions (Fig. 70).

## 6. COMPARISON BETWEEN NONRESISTANCE AND RESISTANCE FLUX-TRANSFER SCHEMES

Before we compare the essential features of the nonresistance and resistance schemes, let us compare the different static flux states associated with each scheme, as shown in Fig. 61(b) and 63(b). There are four states in the nonresistance scheme versus three states in the resistance scheme. The absence of a second minor aperture in the resistance scheme is irrelevant, as far as the flux pattern to be compared is concerned. In fact, in present commercial resistance-type circuits, one to three dummy minor apertures do exist, but their effect on the flux pattern is insignificant. [Note that the  $N_R$  turns of the input winding to the receiver in a resistance scheme may be applied to Leg 1 as in the nonresistance scheme, Fig. 61(a). This will result in a larger amount of clipped flux.]

The CLEAR states are identical. The SET-R state is unique for the nonresistance scheme. The SET-T state has the same directions of arrowheads as the SET-U state, but has different flux-closure paths around the major and the input minor apertures. A similar distinction exists between the SET-D and SET-P states. The differences in flux closure stem from the different sequences of the applied MMFs in the two schemes.

Thorough comparison between the nonresistance and resistance schemes may be found in Ref. 31, where they are summarized in a half-page table.

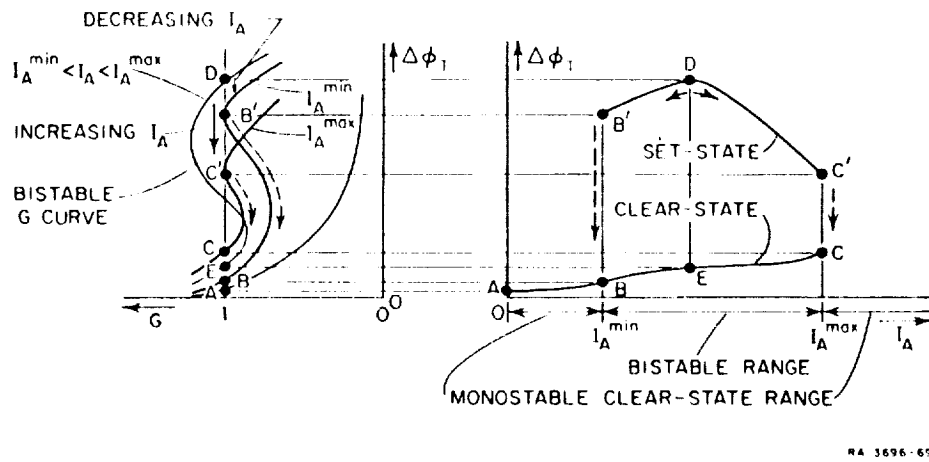


FIG. 70  $G$  AND  $\Delta\phi_T$  vs.  $I_A$  DUE TO UNSETTING EFFECT

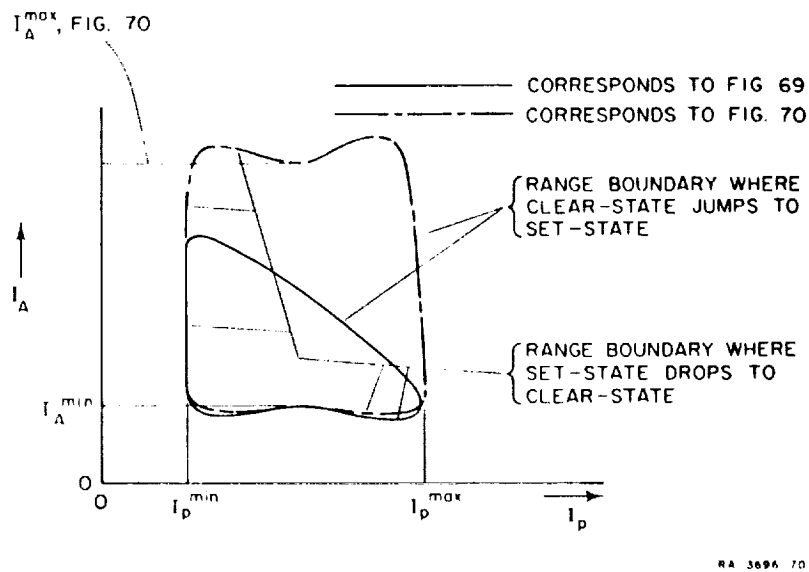


FIG. 71 TWO TYPES OF RANGE MAPS FOR A RESISTANCE FLUX-TRANSFER SCHEME

The essence of this summary is as follows: The nonresistance scheme requires four clock pulses (versus two for the resistance scheme when dc prime is used), has narrower tolerance on drive current, is faster, and consumes less energy per transfer.

### C. CONCLUSIONS

The objective in this section is to show how a multipath core can be used in different schemes in order to store a change of flux  $\Delta\phi$ , to interrogate  $\Delta\phi$ , and to transfer  $\Delta\phi$  to another load. The first scheme can be used in a control system, since  $\Delta\phi$  is continuous. A reader unfamiliar with this scheme may wish to turn to Appendix D in order to comprehend better the resulting setting characteristics. The analysis in Appendix D, based on a number of simplifying assumptions, is designed primarily to illustrate the more complex nature of flux switching in a multipath core which results from having more degrees of freedom of switching paths available.

The coverage of the nonresistance and resistance schemes for flux transfer should be regarded as a summary only. It should also be emphasized that there are other types of nonresistance and resistance schemes. Since the subject of this report is flux switching in multipath cores rather than the application of multipath cores, very little material on application has been included. For more details, other schemes, and various analyses, the reader is referred to other papers that deal with these topics (cf. pp. 174-175).

### III GEOMETRY EFFECTS

This section deals with the effects of geometry on the switching characteristics of a multipath core. The effects of leg dimensions  $l_i$ ,  $l_o$ ,  $w$ , and  $h$  (as given in Fig. 19) on switching parameters such as  $\epsilon$ ,  $\rho$ , and  $F_0$  are discussed in Secs. I-D and I-E. We want here to examine how the relations among the dimensions of the legs affect some aspects of switching behavior.

Since thickness,  $h$ , is common to all legs in most multipath cores, our discussion will concentrate on the effect of the relative path lengths and widths of legs on switching behavior.

#### A. EFFECT OF PATH-LENGTH RATIO ON FLUX DIVISION

##### 1. FLUX DIVISION IN A LADDIC

In Refs. 32 and 33, the following experiment is described. Referring to Fig. 72, it can be seen that Leg 1 of a Laddic is driven by an alternating-current pulse,  $I_1$ . The resulting  $\dot{\phi}$  in Legs 2 and 3,  $\dot{\phi}_2$  and  $\dot{\phi}_3$ , are sensed and integrated. A plot of  $\Delta\phi_2$  and  $\Delta\phi_3$  versus  $NI_1$  is shown in Fig. 72(b). When this experiment is repeated, using different leg

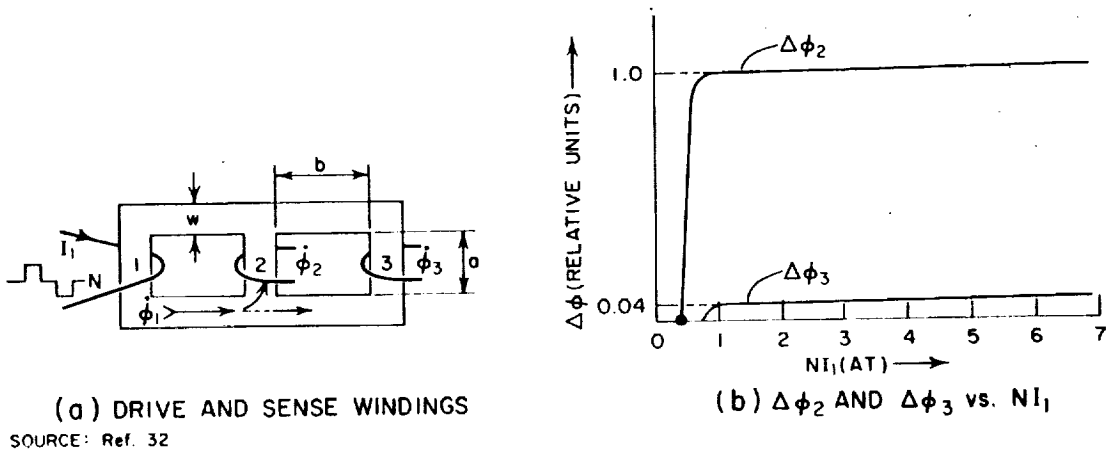


FIG. 72 FLUX DIVISION IN A LADDIC

lengths, it is found that  $\Delta\phi_2$  and  $\Delta\phi_3$  versus  $NI$  have the same shape, except that the ratio  $\Delta\phi_2/\Delta\phi_3$  depends on the ratio  $b/a$  [Dimensions  $b$  and  $a$  are defined in Fig. 72(a)]. It is reported in Ref. 32 that by varying  $b/a$  from 1 to 2 to 3.5, the resulting  $\Delta\phi_2/\Delta\phi_3$  varies from 21 to 83 to 710.

Two conclusions are drawn in Ref. 32 from the examination of the division of  $\Delta\phi_1$  into  $\Delta\phi_2$  and  $\Delta\phi_3$ . First, once Leg 1 is fully switched,  $\Delta\phi_2$  and  $\Delta\phi_3$  remain virtually constant for any increasing value of  $NI_1$ . Second, the resulting ratios  $\Delta\phi_2/\Delta\phi_3$ , which are expected to be approximately equal to the ratio of path lengths, i.e., about  $(2b + a)/a$ , are much higher than anticipated. No explanation for this phenomenon is given in either Ref. 32 or Ref. 33.

## 2. INITIAL EXPLANATION OF $\dot{\phi}$ WAVEFORMS

A further insight into the dynamic switching involved in the previous experiment is presented in Ref. 33 by recording oscillograms of  $\dot{\phi}_2$  and  $\dot{\phi}_3$  under medium and high  $NI_1$ , Fig. 73.

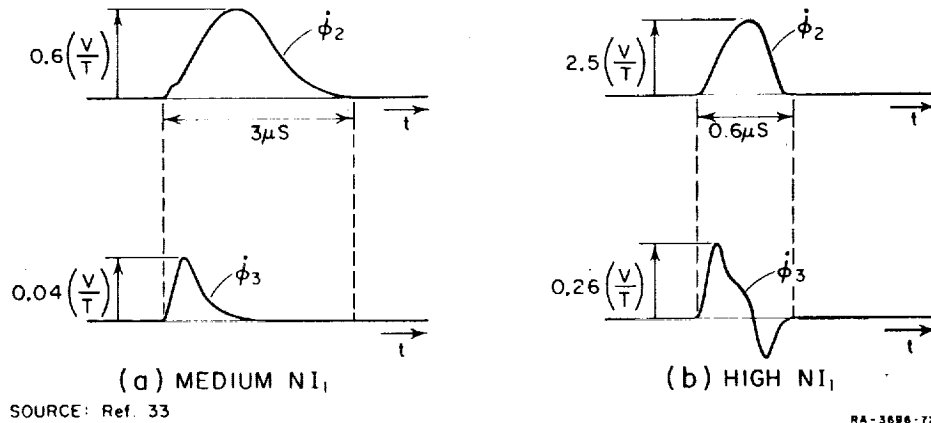


FIG. 73 WAVEFORMS OF  $\dot{\phi}_2$  AND  $\dot{\phi}_3$ , FIG. 72(a)

The waveform of  $\dot{\phi}_3$  under medium  $NI_1$  in Fig. 73(a) is high initially, then drops to zero around the time  $\dot{\phi}_2$  reaches its peak. According to Ref. 33, the explanation for this phenomenon is as follows. Let  $R_2$  and  $R_3$ , and  $\mu_2$  and  $\mu_3$  be the reluctance and incremental permeability of Legs 2 and 3, respectively. Since the cross-sectional areas of the legs are the same,



$$\frac{R_2}{R_3} = \frac{l_2 \mu_3}{l_3 \mu_2} \quad (81)$$

Initially,  $\phi_2 = -\phi_r$  and  $\phi_3 = 0$ , hence  $\mu_2 < \mu_3$  and so  $R_2/R_3$  is relatively high. Once switching is under way in Leg 2,  $R_2$  is very low and essentially "short-circuits"  $R_3$ , causing  $\phi_3$  to drop.

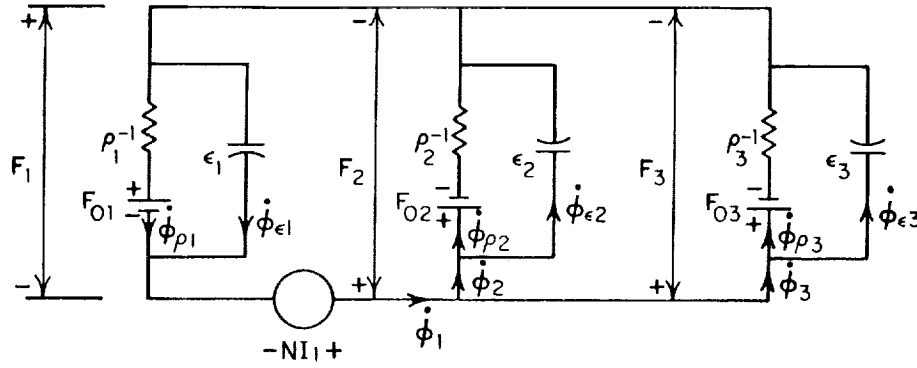
Now refer to the waveform of  $\dot{\phi}_3$  under high  $NI_1$  in Fig. 73(b). Towards the end of the switching,  $\dot{\phi}_3 < 0$ . According to Ref. 33, this can be explained by the drop of  $F_3$  along a minor loop as  $R_2$  reaches its low level.

The explanations given in Ref. 33 for the waveforms of  $\dot{\phi}_3$  in Fig. 73 are unsatisfactory for the following reasons:

- (1) The term *reluctance*,  $R = F/\phi$ , is well defined for linear material. Its use in connection with switching in nonlinear material is vague. (From the arguments given in Ref. 33 it looks as though the term reluctance is used to represent  $\rho^{-1}$ . If this is the case, then we know that  $\rho_2$  reaches a peak around  $\phi_2 = 0$ , hence, the so-called reluctance of Leg 2 should be a minimum at that point.)
- (2) It is claimed in Ref. 33 that once Leg 2 reaches its low-reluctance state,  $F_2 (=F_3)$  must drop. First, it is not clear why the value of  $F_2$  has to follow  $R_2$ , or, more precisely,  $\rho_2^{-1}$ . Second, we are going to show that in this case  $F_2$  reaches a peak when  $\rho_2^{-1}$  is a minimum.
- (3) Leg 1 is completely ignored.

### 3. REVISED EXPLANATION OF $\dot{\phi}$ WAVEFORMS

Let us now attempt to explain the oscillograms in Fig. 73, using the models developed in Sec. I. Figure 74 shows the electrical-circuit analogue for the switching laddie in Fig. 72(a). Considering only non-negative  $\phi_\rho$  in each leg, this circuit is considerably simpler than the general one in Fig. 37. The variations of the parameters of Legs 1 and 2 during the switching time are similar to the ones described in Sec. I. To evaluate these parameters, we assume that  $l_{i1} (=l_{i3}) \cong 2b + a$ ;  $l_{o1} (=l_{o3}) \cong 2b + a + 3/2 \pi w$ ;  $l_{i2} \cong a$ ; and  $l_{o2} \cong a + 1/2 \pi w$ . Since  $\Delta\phi_3$  is negligible, we may assume that the parameters of Leg 3 change very little during the switching time; and since  $\phi_3 \cong 0$ , the threshold is likely to be soft (see Sec. I-H-4) and  $\rho_3$  and  $\epsilon_3$  will be close to their peak values (see Secs. I-E-4 and I-D-1 and 2). What we do not know is



RA-3696-73

FIG. 74 SIMPLIFIED ELECTRICAL-CIRCUIT ANALOGUE FOR FIG. 72(a)

how Leg 3 is brought to the demagnetized state before switching commences. And even if we knew, our information about  $\rho$ ,  $\epsilon$ , and  $F_0$  in a "soft" state is quite limited. From the theory of ellipsoidal domains, it is likely that

$$\rho_3 < \rho_{1p} \quad , \quad F_{03} < F_{01} \quad , \quad \text{and} \quad \epsilon_3 > \epsilon_1 \quad .$$

As an approximation, let us ignore the elastic-switching parameters (the  $\epsilon$ 's). By inspection of Fig. 74.

$$\dot{\phi}_i = \rho_i (F_i - F_{0i}) \quad i = 1, 2, 3 \quad (82)$$

$$\dot{\phi}_1 = \dot{\phi}_2 + \dot{\phi}_3 \quad (83)$$

$$NI_1 = F_1 + F_2 \quad (84)$$

and

$$F_2 = F_3 \quad (85)$$

Solving these equations for  $F_3$ ,

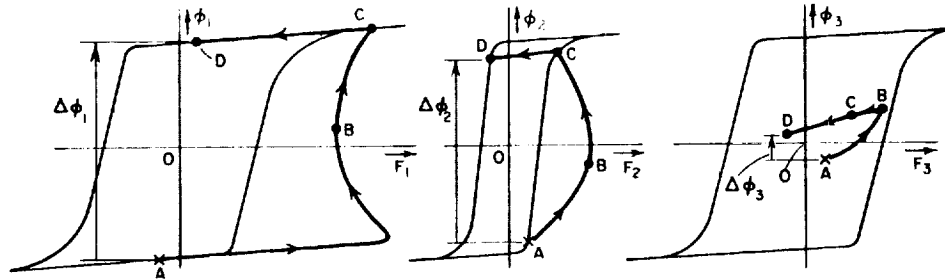
$$F_3 = F_2 = \frac{NI_1 - F_{01} + \frac{\rho_2}{\rho_1} F_{02} + \frac{\rho_3}{\rho_1} F_{03}}{1 + \frac{\rho_2}{\rho_1} + \frac{\rho_3}{\rho_1}} \quad (86)$$

Since Legs 1 and 2 switch essentially at the same rate, the term  $\rho_2/\rho_1$  is assumed to be constant:

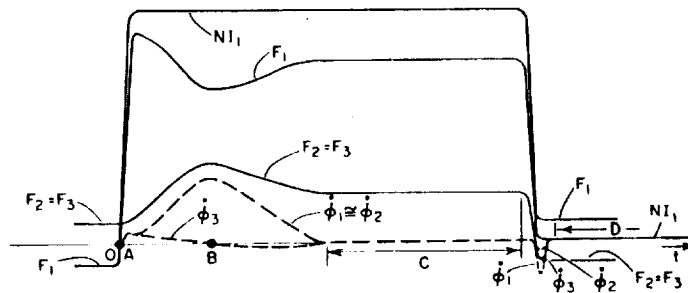
$$\frac{\rho_2}{\rho_1} = \frac{l_1^{av}}{l_2^{av}} = \frac{2b + a + (3/4)\pi w}{a + (1/4)\pi w} \quad (87)$$

On the other hand, since  $\rho_3$  is to be assumed constant and since  $\rho_1$  varies with  $\phi$  like a parabola, the term  $\rho_3/\rho_1$  is very high at the beginning and at the end of the switching time, reaching a minimum around  $\phi_1 = 0$ . Since  $\rho_2$  reaches its peak together with  $\rho_1$ , i.e., when  $\phi_1 \approx \phi_2 \approx 0$ , and since  $NI_1 > [1 + (\rho_2/\rho_1)]F_{03}$  when  $\phi_3 > 0$ , it is concluded from Eq. (86) that  $F_2$  is maximum when  $\rho_2$  reaches its peak. Since  $NI_1$  is constant,  $F_1$ , Eq. (84), must reach a minimum at this point. As stated before, this conclusion is contrary to the argument given in Ref. 33.

Based on our explanation,  $\phi$  and  $F$  of each leg vary during the period of a positive pulse  $I_1$ , as shown in Fig. 75(a). Note that when  $I_1$  falls to zero, the  $F$  values of the legs do not relax to zero. Instead, the legs are kept in a "stressed" state [Points D in Fig. 75(a)] by poles distributed at the leg junctions. The higher  $I_1$  is, the more pronounced this effect is. To understand the cause of the stress effect, refer to Point C, Fig. 75(a), where no more switching takes place, but  $I_1$  is still on. As  $I_1$  is released,  $\phi_1$  drops elastically from positive saturation. To balance  $\Delta\phi_1$ ,  $\phi_2$  or  $\phi_3$  (or both) must drop too, but since  $F_2 = F_3$ ,  $\phi_2$  and  $\phi_3$  drop together.



(a) VARIATION OF  $F$  AND  $\phi$  OF EACH LEG



(b) CONSTRUCTED WAVEFORMS

NA-3696-74

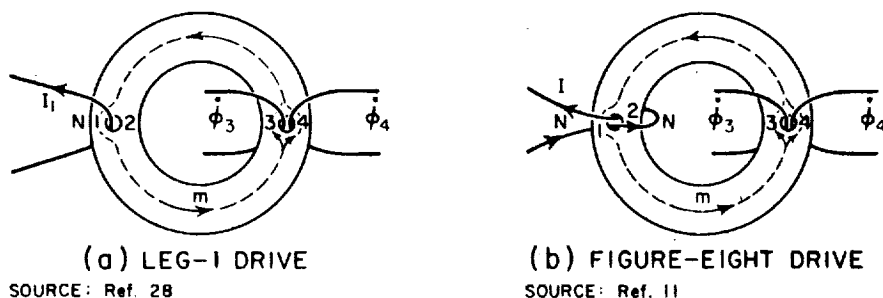
FIG. 75 FLUX SWITCHING IN LADDIC LEGS, FIG. 72

The two relations,  $\Delta\phi_1 = \Delta\phi_2 + \Delta\phi_3$  (when  $I_1$  falls) and  $F_1 = -F_2 = -F_3$  (when  $I_1 = 0$ ), determine the final static points, Points D in Fig. 75(a). During the time of the next negative pulse  $I_1$ , symmetrical variations of  $F$  and  $\phi$  take place. This determines the initial points, Points A in Fig. 75(a).

The waveforms of  $F$  and  $\dot{\phi}$  for each leg are constructed schematically in Fig. 75(b) in conjunction with the variations of  $F$  and  $\phi$  in Fig. 75(a). These agree with the oscillograms in Fig. 73, which, unfortunately, are not extended to the fall time. It would be interesting to re-run this experiment and verify our predicted waveforms.

#### 4. MORE DATA ON FLUX DIVISION

Limited information about flux division between parallel legs may also be found in Refs. 28 and 11. In both references, a ring-shaped multipath core (Fig. 76) is used for experimentation.



NA-3898-75

FIG. 76 FLUX DIVISION IN A CIRCULAR MULTIPATH CORE

In Ref. 28 the multipath core is driven via Leg 1, Fig. 76(a). In one example it is found that  $\Delta\phi_3/\Delta\phi_4 = 79/21$ . No information is given about the drive condition or the core dimensions, and no other cores are tested. A strange explanation is given for the mechanism of flux switching. Two alternatives are proposed: either a "transition band" (wide region of switching) moves radially outward from the major aperture, or two domain walls are moving outward simultaneously at different speeds, one starting from the major aperture and the other from a path encompassing both apertures. The latter explanation does not consider the possibility of simultaneous switching throughout the cross-sections of Legs 3 and 4

when  $N\dot{I}_1$  is high enough. An analysis is given in Ref. 28 for flux division. The analysis is simplified considerably by assuming constant switching resistance,  $\bar{\rho}$ . A more thorough analysis of flux division is given in Ref. 56 (cf. p. 153).

In Ref. 11 (p. 130), the multipath core is driven by a figure-eight winding on Legs 1 and 2, Fig. 76(b). A plot of inelastic  $\Delta\phi_1$ ,  $\Delta\phi_3$ , and  $\Delta\phi_4$  versus  $NI$  as given in Ref. 11, is shown in Fig. 77. Unlike  $\Delta\phi_2$  in the Laddic experiment (see Fig. 72),  $\Delta\phi_3$  reaches peak at some value of  $NI$ . As  $NI$  increases,  $\Delta\phi_4$  increases too, and since  $\Delta\phi_3 + \Delta\phi_4 = \Delta\phi_1 \approx \text{constant}$ ,  $\Delta\phi_3$  decreases.

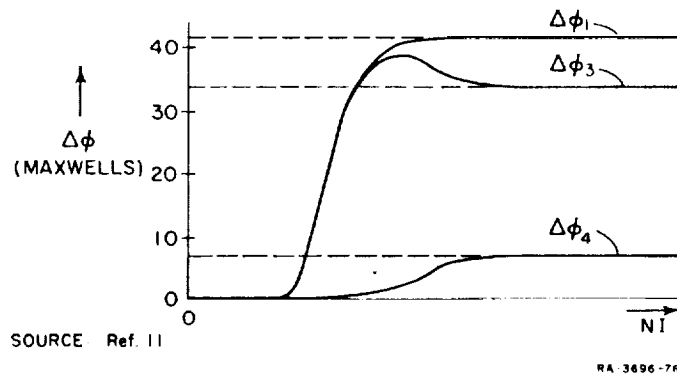
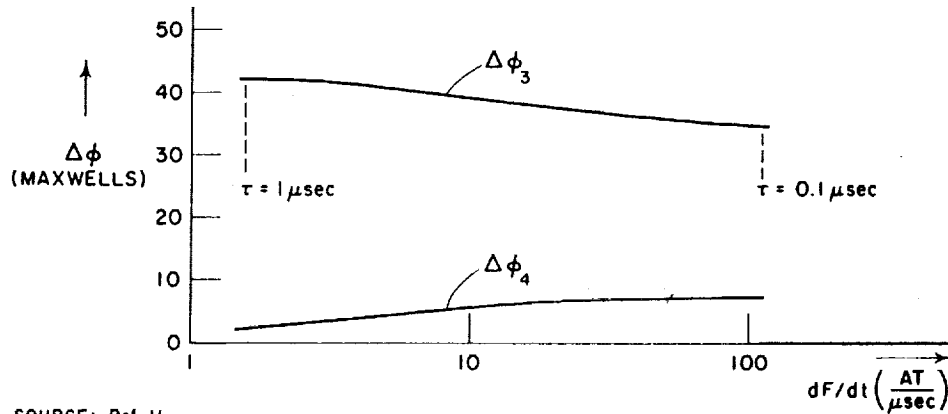


FIG. 77 FLUX DIVISION IN A CIRCULAR MULTIPATH CORE, FIG. 76(b)

The term *flux spreading* is used in Ref. 11 for flux division. It is admitted there (p. 128) that it is difficult to calculate this effect, but an attempt is made to explain the switching mechanism. Unfortunately, the explanation given makes no sense. It is based on a prior discussion according to which the switching region in the multipath core is represented by an equivalent toroid. This is the same erroneous switching model that is used in Refs. 6 and 7 (see Sec. 1-A-4).

The effect of the rise time of the drive current on flux division is presented next on pp. 129 and 131 of Ref. 11. A ramp MMF is used instead of a constant-amplitude pulse. Figure 78 shows the results. Notice that as  $dI/dt$  increases,  $\Delta\phi_4$  levels off, but  $\Delta\phi_3$  keeps on decreasing, i.e.,  $\Delta\phi_3 + \Delta\phi_4$  decreases. This fact is not mentioned in Ref. 11.



SOURCE: Ref. 11

RA-3696-77

FIG. 78 EFFECT OF SLOPE OF RAMP F DRIVE ON FLUX DIVISION

##### 5. EFFECTS ON MULTIHOLE-STRUCTURE OPERATION

The tendency of flux to switch via the shortest path is utilized to perform flux shifting in a multihole structure with no coupling loops. As an example, consider the basic idea of a continuous-structure shift register,<sup>34</sup> Fig. 79. (A similar scheme can be found on pp. 243-251 of Ref. 11.) Input current sets the inside leg, and a sequence of drive currents  $I_{A1}$ ,  $I_{A2}$ , and  $I_{A3}$  shifts the SET state from one leg to its right-hand neighbor. If a leg is in a CLEAR state,  $I_A$  has no effect. The operation of this scheme is ruined by the effect of flux division. Flux switches beyond a neighboring leg, causing the range of operation to be very poor.

In Ref. 35, a similar structure is used as a scanner, Fig. 80. A current pulse  $I_C$  clears the structure. As a ramp SET pulse,  $I_s$ , is applied, a flux-reversal zone propagates outward. This causes the voltage outputs to be displaced in time. Flux division may cause the output voltages to overlap in time; however, the use of a ramp drive reduces the flux-division effect appreciably, provided  $dI/dt$  is low (see Fig. 78). In Ref. 28, a similar structure is driven by a step current, and overlap between output voltages is appreciable.

##### 6. MEASURES AGAINST UNDESIRABLE FLUX DIVISION

In order to preserve decoupling between the input and output of a multipath core, flux division should be prevented. There are several measures by which this can be achieved.

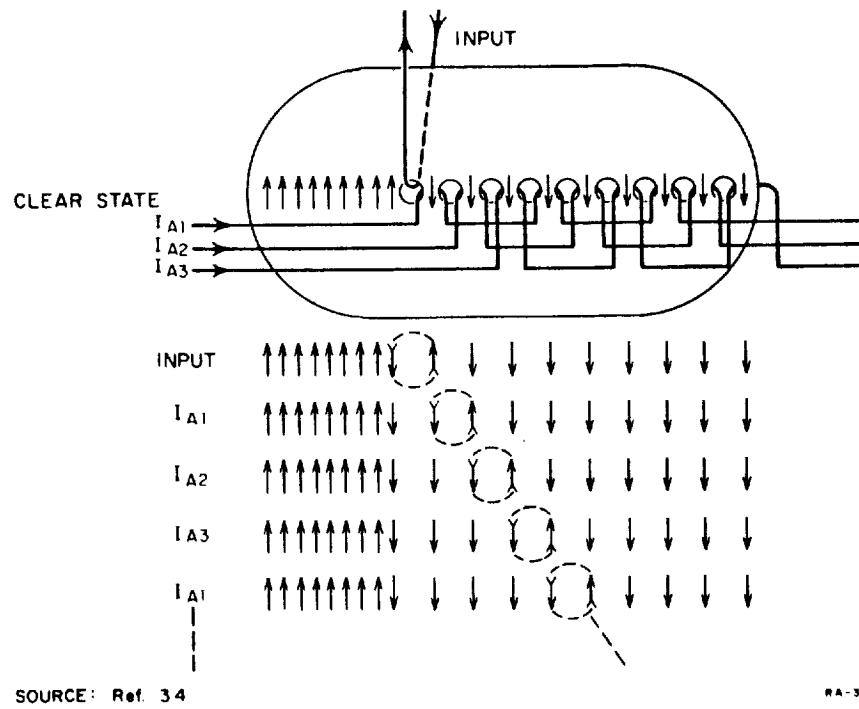


FIG. 79 CONTINUOUS-STRUCTURE SHIFT REGISTER

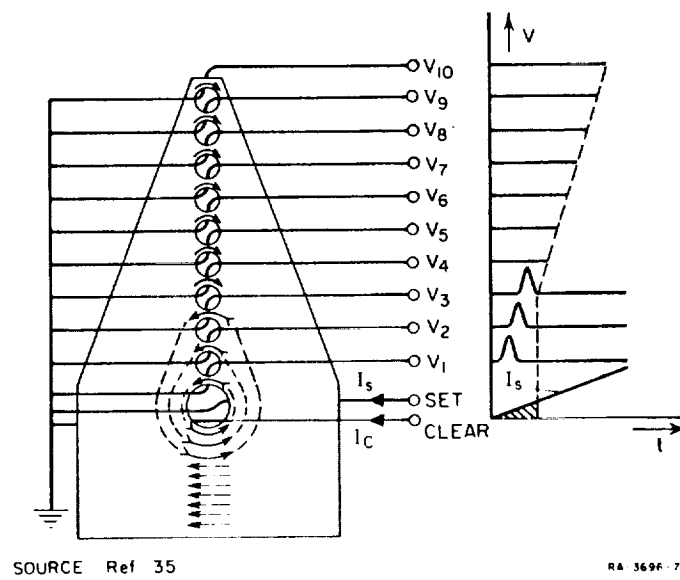


FIG. 80 A SCANNER

a. INCREASE IN PATH-LENGTH RATIO<sup>11</sup>

From our discussion on the effect of  $b/a$  on  $\Delta\phi_2/\Delta\phi_3$  in Part A-1, it is obvious that increasing the length of the output leg will lessen the undesired amount of switched flux in this leg. This method is not practical because in such applications as the nonresistance and resistance schemes, the path around the output minor aperture should be minimized. In addition, such a solution will increase the core size and increase the flux leakage in the surrounding air.

b. HOLD MMF<sup>15,11</sup>

A leg which is not supposed to switch may be acted upon by a sufficiently high external MMF to hold it in the CLEAR direction [Fig. 81(a)]. This is an effective measure, except that one has to watch out for undesired effects associated with the elastic flux generated in the held leg. (See Part B for further discussion.)

c. LOADING<sup>15,28,14,11</sup>

By loading Leg 4, any flux switched into that leg is counteracted by loop current  $i_L$  [Fig. 81(b)]. The lower  $R_L$  is, the more effective is this measure to minimize  $\phi_4$ .

d. CANCELLATION<sup>15</sup>

Linking the output loop through another minor aperture cancels the noise due to flux division [Fig. 81(c)]. This assumes that  $\dot{\phi}_4 = \dot{\phi}'_4$ . This is a clever method, but it requires the output aperture to be located symmetrically with respect to the drive current  $I_s$ , otherwise cancellation may be only partial.

e. OFFSETTING MINOR APERTURES<sup>15</sup>

By moving the minor apertures away from the center of the core, less flux links the output leg [Fig. 81(d)]. This method is impractical because it raises other serious problems, such as reduced output signal and increased noise. In addition, it is not designed for high drive current.



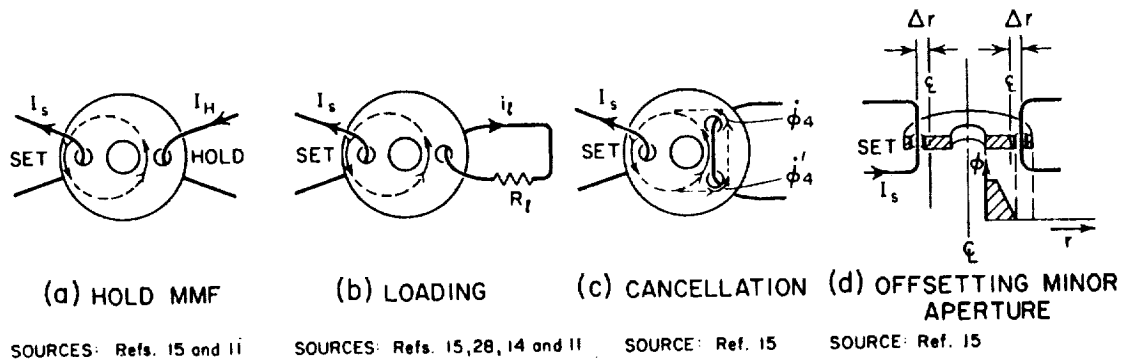


FIG. 81 METHODS OF MINIMIZING FLUX DIVISION

f. DIFFERENT MATERIAL<sup>11</sup>

By using softer material in the inside half of a core, flux is likely to spread less. This method is not too practical because of fabrication difficulties.

In conclusion, the flux-division effect in multipath cores is important and complex; we do not know enough about it. Further investigation should be continued in order to be able not only to explain the causes of this phenomenon, but also to make quantitative predictions.

B. DRIVE ON LEG 4

1. DEGREES OF FREEDOM OF SWITCHED FLUX

The basic difference between flux switching in a toroid and a multipath core stems from the difference in the number of paths through which flux can switch. If air flux is ignored, switching is constrained to one path only in a toroid. The sole constraint imposed on flux distribution in a multipath core is that at every junction of  $n$  legs

$$\sum_{j=1}^n \phi_j = 0 \quad (88)$$

Note that either one of two radial cuts in a toroid may be looked at as a junction of  $n = 2$  legs, but such a breakdown is trivial. From Eq. (88) we conclude that flux switched in any given leg has  $(n - 1)$  degrees of freedom, i.e., it may close (inelastically, elastically, or both) through

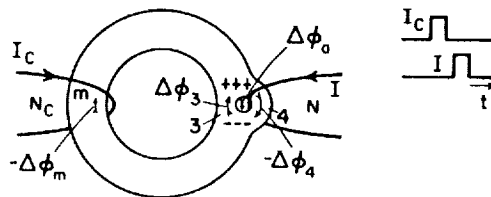
any one of the remaining  $(n - 1)$  legs. However, if  $k$  of these  $(n - 1)$  legs are prevented from switching, the number of degrees of freedom drops to  $(n - k - 1)$ .

In this section we are dealing with the case of  $n = 3$ . An MMF is applied to Leg 4, Fig. 10, and we want to examine the resulting change in the flux state, including air flux. We assume different initial states (CLEAR and SET) and vary the magnitude and polarity of the applied MMF. The effect of winding position is discussed.

## 2. NEGATIVE DRIVE ON LEG 4 OF A CLEARED CORE

### a. ELASTIC $\dot{\phi}_4$

Consider a shaped multipath core, Fig. 82, whose leg widths are  $w_3 = w_4 = (1/2)w_m$ . First, the core is driven to the CLEAR state by constant-amplitude MMF,  $N_C I_C$ . Next, a high  $NI$  drive in the CLEAR direction is applied to Leg 4, causing flux to change in each leg. Note that arrows with tails indicate changed flux. The sign of each  $\Delta\phi$  is consistent with the reference established in Sec. I-F-3, Fig. 37. The arrows shown indicate the actual direction of the switched flux.



RA-3696-01

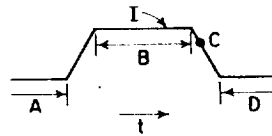
FIG. 82 NEGATIVE DRIVE ON LEG 4 OF A CLEARED CORE

The flux change in Leg 4 is purely elastic, since  $NI$  drives this leg further into negative saturation. Most of  $-\Delta\phi_4$  closes via Leg 3 because switching in Leg 3 requires only a low-value MMF for two reasons. First, cleared Leg 3 is acted upon by MMF in the SET direction, hence  $H_3$  has only to exceed a low threshold value in order to cause switching. Second, the switching path length in Leg 3 is comparatively very short.

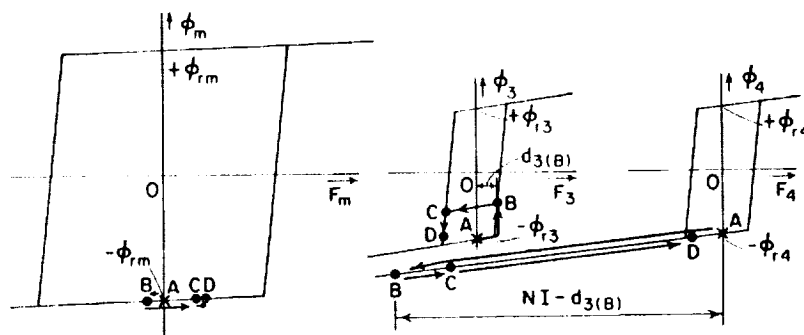
Since no MMF is applied through the major aperture,  $-F_m = F_3 \approx d_3$ , i.e., Leg  $m$  is essentially short-circuited by Leg 3. Considering, in addition, that Leg  $m$  is relatively long and that it switches elastically, it is concluded that  $-\Delta\phi_m \ll \Delta\phi_3$ , thus  $\Delta\phi_3 \approx -\Delta\phi_4$ .

Graphical representation of the flux switching in each leg is shown in Fig. 83. Initially all legs are at remanent states, Points A, due to CLEAR MMF  $N_C I_C$ . As  $NI$  is applied, Leg 4 is pushed down into negative saturation. Theoretically, if  $NI$  is indefinitely high, the resulting  $|\Delta\phi_4|$  is indefinitely large. This is primarily due to the air flux enclosed by the drive winding, including the air flux in Leg 4. Let us assume here that  $NI$  is of such a magnitude that  $|\Delta\phi_4|$  is, say, about  $\frac{1}{2}\phi_{r3}$ .

In order to allow a negative change in  $\phi_4$ ,  $\phi_3$  must increase by approximately the same amount since  $\Delta\phi_m$  is negligible. During the rise time of  $I$ , the operating point of Leg 3 moves from Point A to Point B, where  $NI$  reaches a constant value. Point B is a quiescent state, in which Leg 3 is clamped to its own  $\phi$ - $F$  loop, so that  $F_{3(B)} = d_{3(B)}$ . From this we conclude that  $-F_{4(B)} = NI - d_{3(B)}$ . Since no external MMF is applied in the



(a) WAVESHAPE OF DRIVE CURRENT



(b) VARIATIONS OF  $\phi$  AND  $F$  OF EACH LEG

PA-3896-82

FIG. 83 FLUX SWITCHING IN THE CORE OF FIG. 82

major aperture,  $F_3 = -F_4$ , hence  $F_{4(B)} = -d_{3(B)}$ . This explains the path taken by the operating point of Leg 4, and the negligible magnitude of the resulting  $\Delta\phi_4$ .

The physical mechanism that adjusts the division of  $NI$  into the proper values of  $F_3$  and  $F_4$  may be explained in terms of poles which are created at the two junctions of the three legs, as shown in Fig. 82. These poles are of such a polarity that they decrease the value of  $F_3$  to  $d_3$  (which is below the value  $F_3$  would have with the poles absent) and they help to push Leg 4 further into negative saturation. The creation of poles causes a change in air flux,  $\Delta\phi_a$ , in the direction shown in Fig. 82. Calculating  $\Delta\phi_a$  is a very complex problem. Analysis of air leakage in a toroid is simplified in Ref. 36 by reducing the problem to two dimensions, thus assuming the toroid to be a long tube. This analysis may be borrowed to calculate  $\Delta\phi_a$  around the minor aperture when the multi-path core is in the SET state, but not when it is in the CLEAR state.

The three legs remain in the quiescent state, Points B, as long as  $I$  is on. When  $I$  decreases,  $\phi_4$  increases elastically in the region of negative saturation. In order to balance  $\Delta\phi_4$ ,  $\phi_3$  decreases along a minor loop until it reaches the left side of the static loop of Leg 3, Point C. From there on  $\phi_3$  moves downward along a path close to the static loop of Leg 3, until a final state, Point D, is reached. The position of Point D is determined from the requirement for  $F_3$  and  $F_4$  to be equal and the requirement for flux continuity. Note that  $-F_4$  follows  $F_3$  and  $\Delta\phi_4$  is negligible. Physically, throughout the fall time of  $I$ , the intensity of the poles decreases but their polarity remains unchanged. When  $NI$  is falling it is the residual poles that push Leg 3 down along the path B-C-D.

#### b. STRESS EFFECT

At the terminal states, Points D, the MMF across each leg is not equal to zero, even though no external MMF is being applied. The legs stay in this state because both  $\phi_3$  and  $\phi_4$  must increase in order for  $F_3$  and  $F_4$  to be zero, but this is impossible since  $\Delta\phi_4 = \Delta\phi_a - \Delta\phi_3 \approx -\Delta\phi_3$ . Since residual MMF is left on each leg, this phenomenon is called "stress effect."<sup>37</sup> Physically, this state is sustained by poles which are created during the rise and fall times of  $I$  at the junction of the legs, Fig. 82.

Consider now the case where the drive  $NI$ , Fig. 82, is so low that Point B of leg 3, Fig. 83, is below the threshold of Leg 3. This case involves only elastic switching, so that all the legs return to their initial state, and there is no stress effect.

### 3. POSITIVE DRIVE ON LEG 4 OF A CLEARED CORE

#### a. SETTING TO A STRESSED STATE

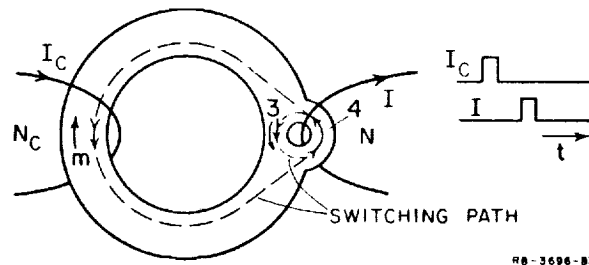
We now repeat the switching procedure in Fig. 82, except that Current  $I$  is of opposite polarity. In Fig. 84, it can be seen that first  $N_C I_C$  clears the core and then  $NI$  sets the core via Leg 4. Arrows with tails indicate switched flux; arrows without tails indicate unchanged flux.

Variations of  $F$  and  $\phi$  of each leg during setting time are superimposed on linearized  $\phi$ - $F$  loops in Fig. 85, assuming that  $I$  is high enough to fully saturate Leg 4. Initially all the legs are at their negative remanent states, Points A. During the rise time of  $I$ , Legs 4 and  $m$  are set until, at Points B, Leg 4 reaches saturation. Since  $F_3 = -F_m$ , Leg 3 is driven down into negative saturation during the setting time.

As  $I$  continues to rise, Leg 4 is driven further into positive saturation towards Point C and the resulting  $\Delta\phi_{4(B-C)}$  is purely elastic. The change in flux in Leg  $m$  is now constrained by  $\dot{\phi}_{e4}$ , hence  $\dot{\phi}_m$  becomes much smaller. As a result, the operating point of Leg  $m$  changes direction and moves towards its static loop. Since  $F_3 = -F_m$ , the drop in  $F_m$  causes the operating point of Leg 3 to be pulled upwards in negative saturation. Also, the drop in  $F_m$  increases the share of  $NI$  taken by  $F_4$ . Since

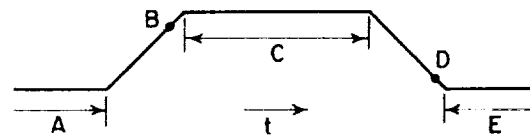
$$\dot{\phi}_m = \dot{\phi}_3 + \dot{\phi}_4, \quad (89)$$

$\Delta\phi_{m(B-C)} = \Delta\phi_{3(B-C)} + \Delta\phi_{4(B-C)}$ , where  $\Delta\phi_{3(B-C)}$  and  $\Delta\phi_{4(B-C)}$  are both positive and elastic in nature. Note, however, that  $\Delta\phi_{m(B-C)}$  is a combination of elastic and inelastic components, as discussed in Sec. I-C-3 in connection with Fig. 16. When Current  $I$  reaches its constant (highest) value, the operating point of Leg  $m$  either may still be outside its static loop (in which case it will move fast towards the loop), or it may already be climbing along the static loop. These two cases are indicated in Fig. 85 by dotted lines; the solid line corresponds to the median of these two cases, i.e.,  $I$  reaches its constant

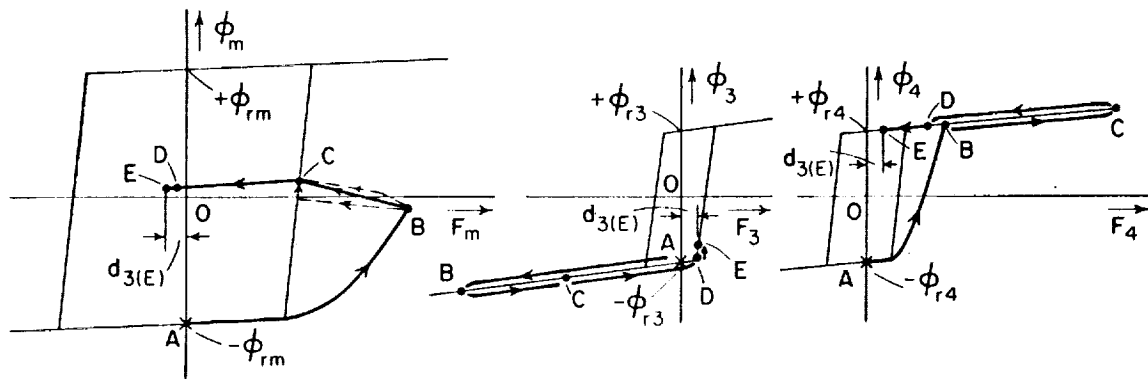


RB-3696-B3

FIG. 84 SETTING A CLEARED CORE VIA LEG 4



(a) WAVESHAPE OF DRIVE CURRENT



(b) VARIATIONS OF  $\phi$  AND  $F$  OF EACH LEG

RB-3696-B4

FIG. 85 FLUX SWITCHING IN THE CORE OF FIG. 84 USING HIGH DRIVE

value at the same time that the operating point of Leg  $m$  arrives at the static loop. The quiescent state, Point C, is identical for all cases because there is a unique solution to the values of  $F$  and of  $\phi$ , determined by the  $\phi$ - $F$  static loops. At the same time that Leg  $m$  reaches Point C along its static loop, Legs 3 and 4 reach quiescent states of their own, Points C.

Each leg remains in this state as long as Current  $I$  stays constant. When  $I$  falls, there is a change in flux in every leg. Leg  $m$  is constrained to a minor loop and Legs 3 and 4 are constrained to their static loops. An additional constraint is  $F_m = -F_3$ . Integrating Eq. (89) over the fall time  $\tau_f$  gives

$$\Delta\phi_4(\tau_f) = \Delta\phi_m(\tau_f) - \Delta\phi_3(\tau_f) \quad (90)$$

where the subscript  $(\tau_f)$  indicates a change from Point C to Point E via Point D. By inspection of Fig. 85, it can be seen that  $\Delta\phi_4(\tau_f) < 0$ ,  $\Delta\phi_m(\tau_f) < 0$ , and  $\Delta\phi_3(\tau_f) > 0$ . Hence,  $|\Delta\phi_4(\tau_f)| = |\Delta\phi_m(\tau_f)| + \Delta\phi_3(\tau_f)$ .

We now assume that  $|\Delta\phi_4(\tau_f)|$ , generated by a high  $NI$ , is large enough to cause the operating points of Legs  $m$  and 3 to cross their  $\phi$  ordinates and have their values of  $F$  change sign while  $F_4$  is still positive. When  $F_3$  reaches the threshold value  $d_3^{\min}$  (Point D), Leg 3 is essentially clamped to its static loop, causing  $-F_m$  to be clamped to  $d_3$  also. Current  $I$  keeps falling, and when it reaches zero,  $-F_m = F_4 = F_3 = d_3(E)$ .

By now the legs have reached their final static states, indicated by Points D. Here, again, the legs are left in a stressed state, since no external MMF is applied, yet in each leg,  $F \neq 0$ . The legs stay in this state because in order for  $F_3$  and  $F_4$  to drop to zero,  $\Delta\phi_3$  and  $\Delta\phi_4$  must be negative and hence  $\Delta\phi_m$  must be negative too, but this requires a further reduction in  $F_m$ , which contradicts the requirement  $-F_m = F_3 = F_4$ . The distribution of poles that sustain the stressed state is shown in Fig. 86.

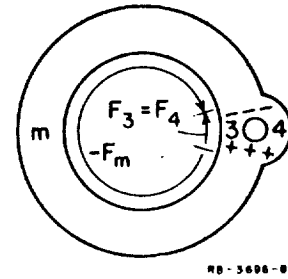


FIG. 86 POLE DISTRIBUTION IN A STRESSED STATE FOLLOWING HARD LEG-4 SETTING

The stress effect is verified indirectly by the following experiment. A cleared multipath core (AMP Inc. Core No. 395 813-1) is set via Leg 4, using  $NI = 10 F_0$ . After  $NI$  is removed, the net  $\Delta\phi_3$  is found to be about  $0.25 \phi_{r3}$ .

Suppose now that the setting of the core via Leg 4, Fig. 84, is repeated under a smaller drive, say  $NI \cong d_m^{max} + d_4^{max}$ . The variations of  $F$  and  $\phi$  for each leg are shown in Fig. 87(b). Compared with the case of high drive, the peak level of  $\phi_4$  (Point C) is now lower. Therefore, in order to satisfy the two constraints  $|\Delta\phi_{4(\tau_f)}| = |\Delta\phi_{m(\tau_f)}| + \Delta\phi_{3(\tau_f)}$  and  $-F_m = F_3 = F_4 - NI$ , the operating point of Leg 4 must drop below  $+\phi_{r4}$  and end up along the left side of the static  $\phi$ - $F$  loop as, for example, at Point E. At the same time  $F_m > 0$  and  $F_3 < 0$ . It is concluded, therefore, that the stress state caused by low  $NI$  is expressed by  $F_m = -F_3 = -F_4 = d_{4(E)}$ . The poles distribution in this case is of opposite polarity to the one of high  $NI$  drive, as is seen by comparing Figs. 87(c) and Fig. 86.

From studying the cases of high and low drives, we conclude that for a given multipath core, there is only one intermediate value

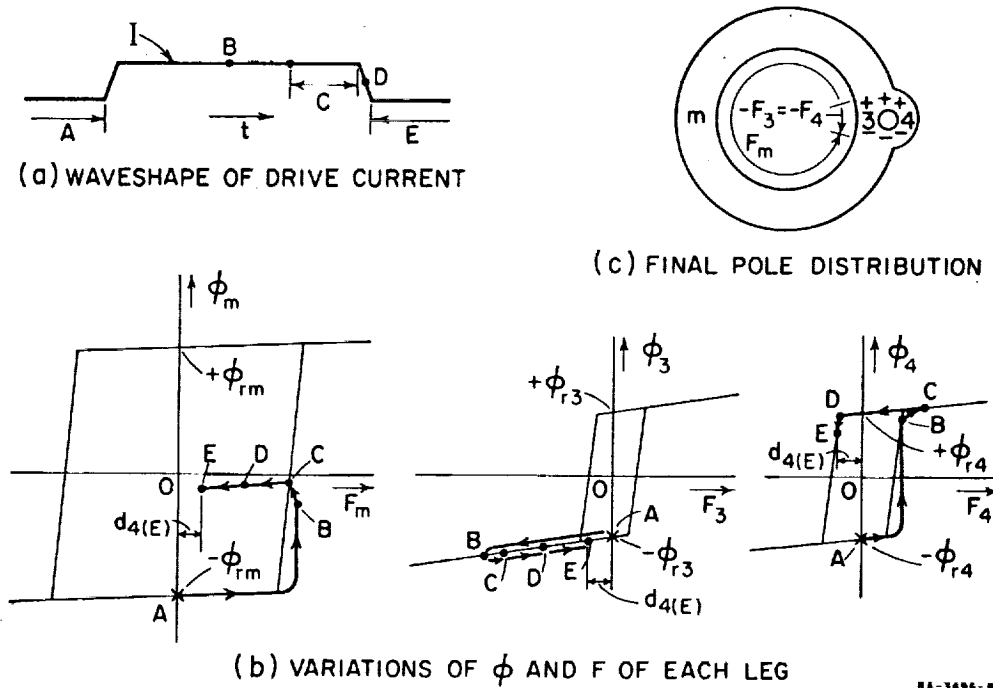


FIG. 87 LOW-DRIVE SETTING OF THE CORE IN FIG. 84



of  $NI$  for which there is no stress effect (i.e.,  $-F_m = F_3 = F_4 = 0$ ) after  $I$  is removed.

#### b. SUPERSETTING EFFECT

In comparing Figs. 85 and 87(b), we see that the net flux change  $\Delta\phi_m$  is higher if the SET MMF is higher. This difference stems from the different levels of saturated flux that Leg 4 is driven to. This phenomenon is called the *supersetting effect* because it is caused by extra setting of Leg 4 by elastic flux.

An interesting case of supersetting effect occurs when  $NI$  is so high that Point E of Leg 3, Fig. 85, is at positive saturation. In order to reach this state, the elastic flux change of Leg 4 in positive saturation is larger than the flux capacity of Leg 3, i.e.,  $\Delta\phi_{4(B-C)} \approx 2\phi_{r3} + |\Delta\phi_{3(A-B)}|$ . Note that increasing the maximum value of  $NI$  has no effect on  $\Delta\phi_{3(A-B)}$  if  $dI/dt$  is maintained constant during the rise time of  $I$ , as is evident from Fig. 85(a). After  $I$  is removed, both Leg 3 and Leg 4 are fully set. This amounts to a complete reversal of the flux of a cleared multipath core. In conclusion, the flux of a multipath core in the CLEAR state can be completely switched around not only by driving through the major aperture, but also by applying a very high MMF through the minor aperture. In further illustration of this phenomenon, consider Fig. 88. A multipath core with one major and two minor apertures

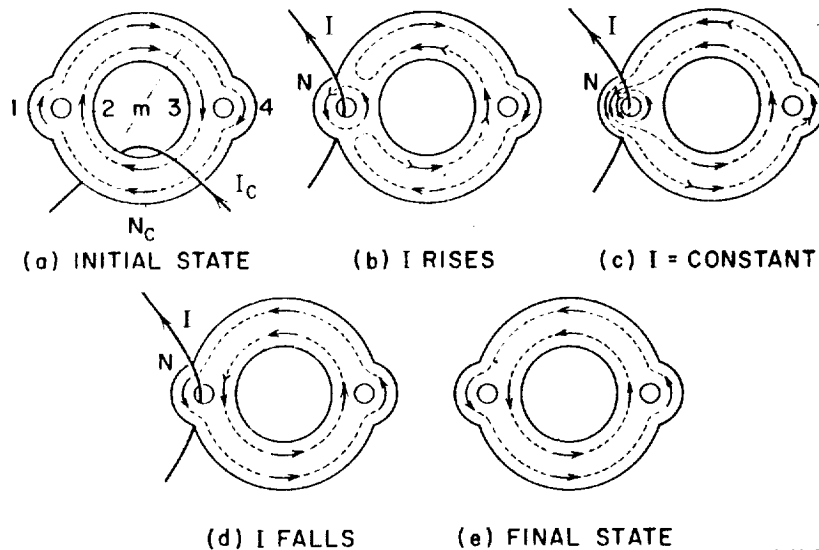


FIG. 88 FULL SUPERSETTING EFFECT VIA LEG 1

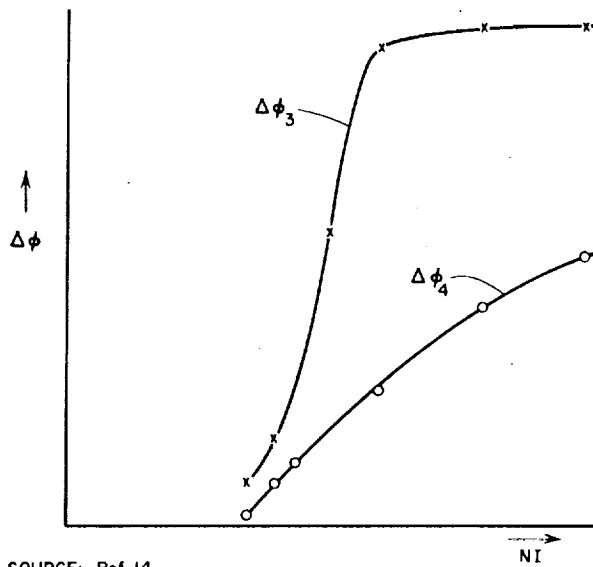


FIG. 89  $\Delta\phi_3$  AND  $\Delta\phi_4$  DUE TO LEG-1  
SUPERSETTING EFFECT

is driven first into the CLEAR state, Fig. 88(a). SET MMF  $NI$  is applied to Leg 1, and the core is set via Leg 3 during the rise time of  $I$ , Fig. 88(b). As  $I$  rises to its final value, Leg 1 is overset elastically by an amount  $2\phi_{r2}$ , causing Leg 4 to switch inelastically to the SET state, Fig. 88(c). Note that a single arrow represents  $\phi_r$  and its direction represents the polarity of  $\phi_r$ . When  $I$  is released, the flux in Leg 1 reverses elastically, closing inelastically via Leg 2, since the latter is much shorter than Leg  $m$ , Fig. 88(d). After the removal of  $I$ , a final

state of fully set core is reached, Fig. 88(e).

Consider again the case of supersetting in which Leg 4 is only partially set after  $I$  is removed. A plot of  $\Delta\phi_3$  and  $\Delta\phi_4$  versus  $NI$ , as given in Ref. 14, is sketched in Fig. 89. Note that  $\Delta\phi_3$  does not fully flatten out. This may be credited to the "wing" of the  $\phi$ - $F$  loop of Leg 3 near positive saturation. It is important not to mix flux switching in Leg 4 due to supersetting effect with that of flux division due to path-length ratio, Part A-4. This distinction is made clear on p. 95 of Ref. 14.

#### 4. NEGATIVE DRIVE ON LEG 4 OF A SET CORE

##### a. EFFECT OF WINDING POSITION

In a case where pure elastic switching is involved, the permeability is not high enough to justify ignoring the position of the current conductor. In this case, for a given current, the position of the winding affects the magnitude of  $H$ , and it is not sufficient merely to specify the number of turns in every aperture.

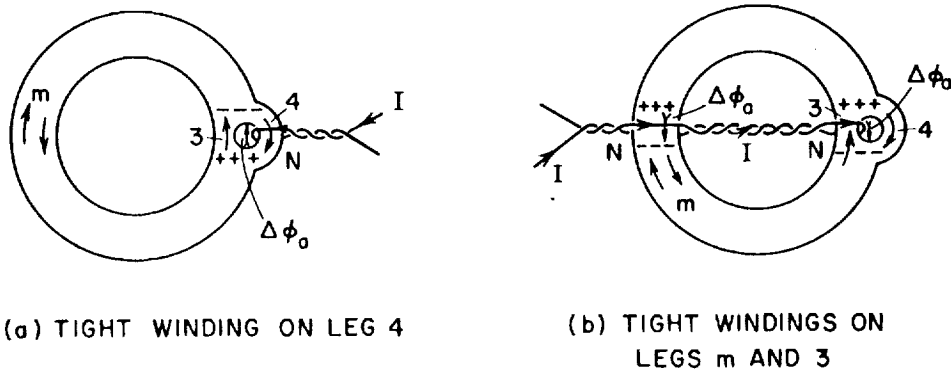
Consider a set multipath core with Leg 3 in the SET state and Leg 4 in the CLEAR state. A clockwise drive through the minor aperture generates elastic-flux switching around this aperture. Two extreme cases of winding position for such a drive are shown in Fig. 90. In both cases the windings are wound tightly around the respective legs and twisted elsewhere. Since no net current passes through the major aperture, in either case

$$-F_m = F_3 = NI - F_4 \quad (91)$$

The current conductor is closer to the material of Leg 4 in Case (a) than in Case (b). Hence,  $|H_{4(a)}| > |H_{4(b)}|$ , where subscripts (a) and (b) refer to the two cases. Since  $F_4 = \int H dl$  along Leg 4, we conclude that  $|F_{4(a)}| > |F_{4(b)}|$ . Applying this result to Eq. (91), we also conclude that  $|F_{m(b)}| = F_{3(b)} > |F_{m(a)}| = F_{3(a)}$ . In other words, the magnitude of an MMF drop across a leg is higher if the drive winding is closer to that leg.

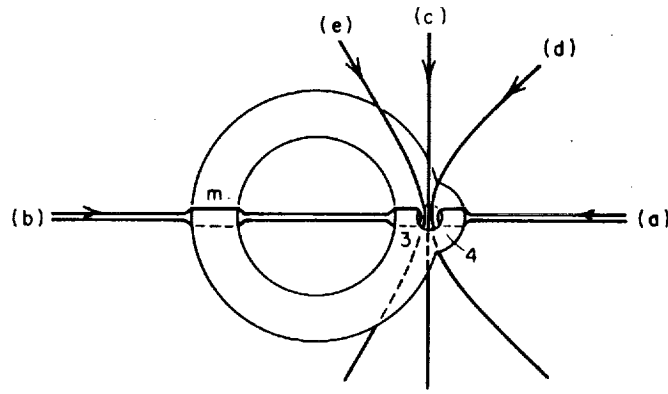
The two cases may be explained physically in terms of the effect of the winding position on pole distribution. The poles tend to distribute  $NI$  uniformly around the minor aperture, hence the polarity of the poles in Case (a) is opposite to that in Case (b). The directions of air flux in the two cases are opposite due to the polarity of the poles. As a result,  $|\Delta\phi_{e4(a)}| > |\Delta\phi_{e4(b)}|$ , and hence  $|F_{4(a)}| > |F_{4(b)}|$  and  $F_{3(a)} < F_{3(b)}$ . In addition, in Case (b) poles are also created in Leg  $m$ , as shown in Fig. 90(b).

Intermediate cases of winding position are shown schematically in Fig. 91. Cases (a) and (b) correspond to the extreme positions in



NA-3696-89

FIG. 90 EFFECT OF EXTREME WINDING POSITION IN A SET CORE



(a) AND (b) — TIGHT WINDINGS, FIG. 90  
 (c) — STRAIGHT-THROUGH WINDING  
 (d) AND (e) — LOOSE WINDINGS

NA-3696-90

FIG. 91 VARIOUS WINDING POSITIONS

Fig. 90. In Case (c), a wire is threaded straight through. This is the median of Cases (a) and (b). Case (d) corresponds to having loose windings around Leg 4 and Case (e) to having loose windings around the portion of the multipath core to the left of the minor aperture. Cases (a), (d), and (c) are the more common ones in practice. Values for  $F_4$ ,  $|F_m|$ , and  $F_3$  in Cases (d), (c) and (e) lie between the corresponding values in Cases (a) and (b). For example, a tight winding around Leg 4, Case (a), causes a smaller magnitude of  $F_m$  than a straight-through winding, Case (c).

#### b. UNSETTING EFFECT

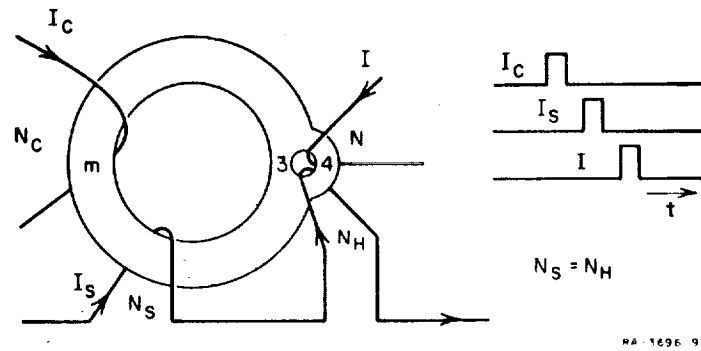
Consider the drive sequence applied to a multipath core, Fig. 92. First, the core is cleared by  $N_C I_C$ . Second, the core is set via Leg 3 by  $N_s I_s$  (flux division into Leg 4 is prevented by HOLD MMF  $N_H I_s$ ). Finally, a negative MMF,  $N I$ , is applied to the cleared Leg 4, driving it further into negative saturation. A graphical analysis of the flux switching for this case is shown in Fig. 93, starting from the CLEAR state which is reached after  $I_C$  is removed.

Variations in  $\phi$  and  $F$  of each leg during setting time, Fig. 93(b), are governed by the relations

$$F_m = N_s I_s - F_3 = (N_s - N_H) I_s - F_4 \quad (92)$$

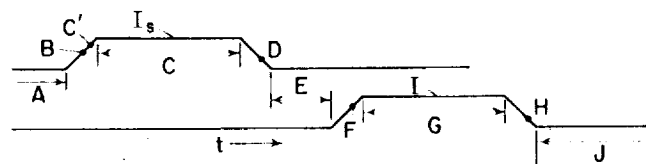
and

$$\Delta \phi_m = \Delta \phi_3 + \Delta \phi_4 \quad (93)$$

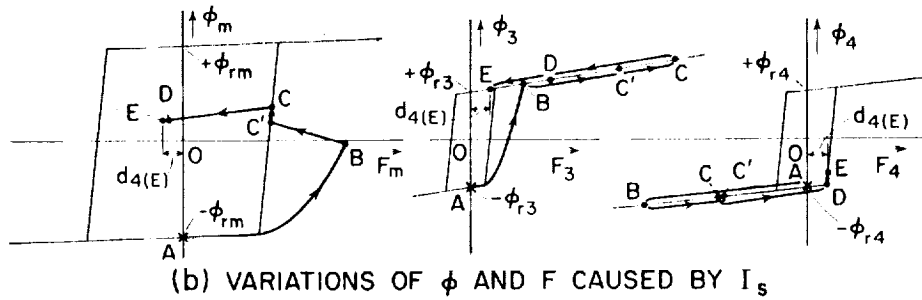


RA 1696 91

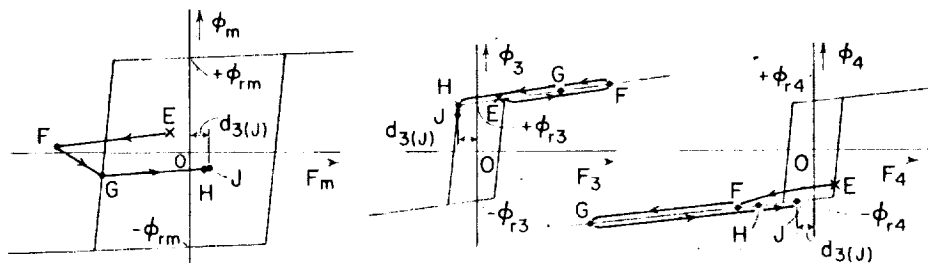
FIG. 92 NEGATIVE DRIVE ON LEG 4 OF A SET CORE



(a) WAVEFORMS OF DRIVE CURRENTS



(b) VARIATIONS OF  $\phi$  AND  $F$  CAUSED BY  $I_S$



(c) VARIATIONS OF  $\phi$  AND  $F$  CAUSED BY  $I$

FIG. 93 FLUX SWITCHING IN THE CORE OF FIG. 92

As an illustration, the plots in Fig. 93(b) are based on the assumption that  $N_s = N_H$ . Under this assumption, this case is similar to the one in Fig. 85, except that Legs 3 and 4 are interchanged. Since Leg 3 is shorter than Leg 4, driving Leg 3 into saturation by the same  $|F|$  results in a higher  $|\Delta\phi_e|$ . For this reason, Points B, C, D and E are higher in Fig. 93(b) than in Fig. 85. Note that Path B-C'-C in Fig. 93(b) is based on the assumption that Leg  $m$  reaches its static loop before Current  $I$  reaches a constant value. The decrease in  $\phi_4$  from C' to C stems from the slight increase in  $F_m$  and the equality  $F_4 = -F_m$  that results from substituting  $N_s = N_H$  into Eq. (92).

During the period between Pulses  $I_s$  and  $I$ , each leg is held in a stress state, Points E, by poles which are positive below and negative above the minor aperture, as in Fig. 86. When Current  $I$  is applied, the  $\phi$  and  $F$  of each leg vary as shown in Fig. 93(c). These are governed by Eq. (93) and the relation

$$F_m = -F_3 = -NI - F_4 \quad (94)$$

As  $I$  increases, Leg 4 is driven from Point E to negative saturation, Point F. At the same time  $\phi_m$  decreases, but since  $F_m = -F_3$ ,  $\phi_3$  increases, hence  $|\Delta\phi_{4(E-F)}| = |\Delta\phi_{m(E-F)}| + \Delta\phi_{3(E-F)}$ . Note that Leg  $m$  is initially in a soft state (Sec. I-H-4), so that less MMF is required across Leg  $m$  for a given  $\Delta\phi_m$ . This causes  $|\dot{\phi}_4|$  to increase; hence Point F of Leg 4 is located at a higher  $\phi$  level in negative saturation than if Leg  $m$  was in a hard state. From Point F until Current  $I$  reaches a constant value, Point G,  $\dot{\phi}_4$  is only elastic, hence  $|\dot{\phi}_m|$  drops off. This causes the operating point of Leg  $m$  to change direction and move to Point G on the left side of the static  $\phi$ - $F$  loop. Note that during this time the poles across the minor aperture change polarity (to plus above and minus below the aperture), and thus enable  $NI$  to be so divided that  $|F_4| > |F_m|$ . Since  $F_3 = -F_m$ ,  $\phi_3$  drops from Point F to Point G in positive saturation. Both  $\Delta\phi_{4(F-G)}$  and  $\Delta\phi_{3(F-G)}$  are negative, therefore the drop  $\Delta\phi_{m(F-G)}$  may be appreciable. In fact, if  $NI$  were very high,  $\Delta\phi_{4(F-G)}$  might bring Point G to negative saturation.

While Current  $I$  is constant, the legs stay in this quiescent state, Points G. As  $I$  falls, the flux in each leg changes elastically:  $\phi_4$  increases in negative saturation,  $\phi_m$  increases along a minor loop, and  $\phi_3$  decreases in positive saturation in such a way that  $F_3 = -F_m$ .

Since Point G of Leg 4 is far in negative saturation, the operating points of Legs  $m$  and 3 must cross their  $\phi$  ordinates before the final states, Points J, are reached. Note that the poles have the proper polarity (positive above and negative below the minor aperture) to sustain the stressed state, Points J.

It is concluded from this discussion that a negative drive on Leg 4 of a set core causes a drop in  $\phi_m$ , despite the fact that Leg 4 is initially in the CLEAR state.

This phenomenon is referred to as *unsetting effect*. If  $NI$  is high enough, a set multipath core may be completely cleared by this effect.

Referring back to Figs. 90 and 91, we have shown that tight winding on Leg 4, Case (a), results in the smallest magnitude of

$F_m$ , hence the least unsetting of Leg  $m$  is expected in this case. Maximum unsetting is obtained by using tight winding over Legs  $m$  and 3, Case (b). These conclusions have been verified experimentally.

Unsetting effect is reported also in Ref. 33 for the case of a five-leg Laddic, Fig. 94. Initially  $\phi_m = 0$  and Legs 1 and 3 are saturated upwards and Legs 2 and 4 are saturated downwards, as shown. A pulse  $NI$  is applied to Leg 2, pushing it further into negative saturation. When  $I$  is removed, it is found that the flux in every undriven leg has changed inelastically. Plotting the variations of  $\phi$  and  $F$  of each leg and consideration of the pole distribution will facilitate the explanation of these results.

### C. MULTIPATH-CORE SHAPING

The effects of relative leg lengths on switching characteristics of a multipath core are discussed in Parts A and B. We now want to include the effect of the widths of the legs on these characteristics. Regulating the relative lengths and widths of legs in order to achieve a certain switching property is what we call *core shaping*.

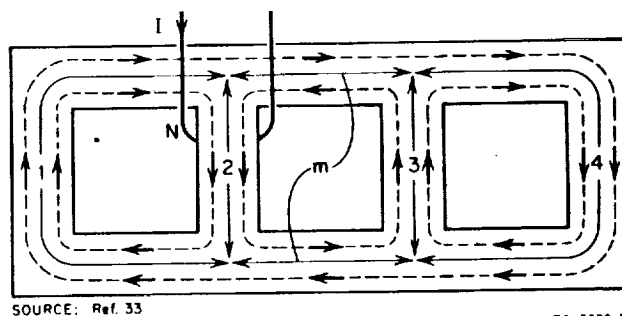


FIG. 94 UNSETTING EFFECT IN A LADDIC

# 1. EFFECT OF SHAPING ON SOFT THRESHOLD

Consider a two-leg core, Fig. 95(a), in which Leg 2 is, say, twice the width of Leg 1. The core is driven in the CLEAR direction by an MMF pulse  $N_C I_C$ . Since  $w_2 = 2w_1$ , the amount of flux in the CLEAR direction in Leg 2 depends on how hard Leg 1 is driven into negative saturation. Let us assume that  $N_C I_C$  is so high that all of Leg 2 is cleared. Consider the quiescent state (while  $I_C$  is on) as an initial condition, Points A in Fig. 95(b). The division of  $N_C I_C$  into  $F_{1(A)}$  and  $F_{2(A)}$  is self-adjusted by the poles at the leg junctions, Fig. 95(a). These poles oppose  $N_C I_C$  in Leg 2 and help  $N_C I_C$  in Leg 1. As  $I_C$  is removed,  $\phi_1$  and  $\phi_2$  rise until Points B are reached. During this switching time, the intensity of the poles decreases but the polarity stays unchanged. These poles hold Legs 1 and 2 in the stressed state, Points B, and cause a balance in flux. If the air flux leakage is negligible,  $\phi_2 \approx \phi_1$ .

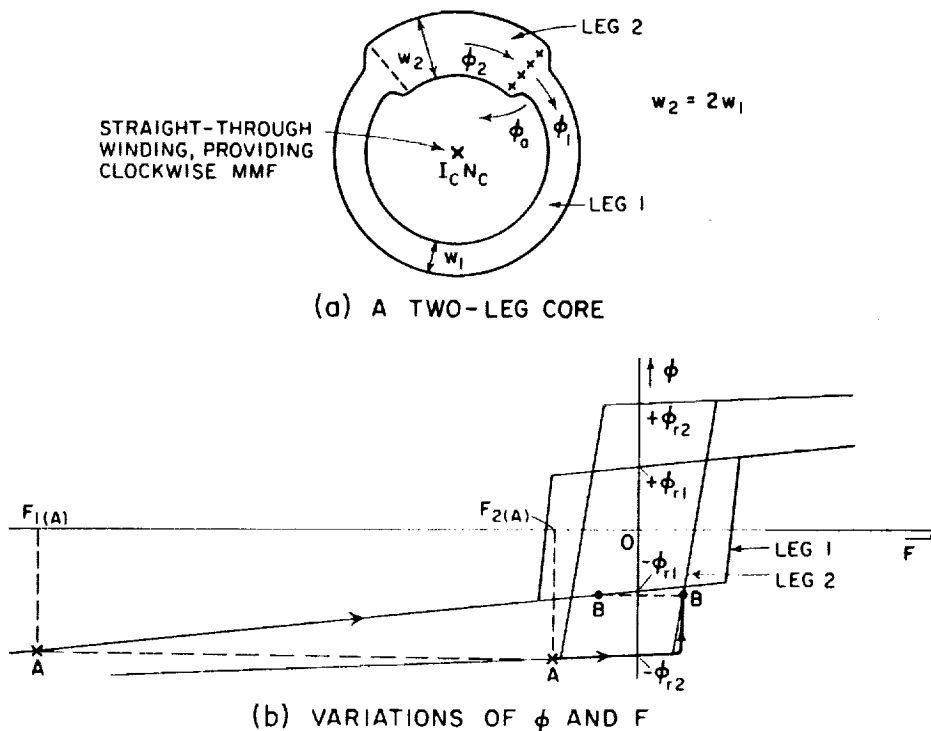


FIG. 95 HARD CLEAR DRIVE ON A TWO-LEG CORE



Let us examine the magnetic states of each leg at Points B. Leg 1 is saturated, so that it has a well-defined hard threshold. On the other hand, Leg 2 is partially demagnetized. During the fall time of  $I_C$ , especially when the fall time is short, Leg 2 may have domains of reversed magnetization scattered throughout its cross-section. As explained in Sec. I-H-4, a partially demagnetized state of this sort is characterized by a soft threshold. Switching from this state is much easier and there is no well-defined sharp threshold to be overcome before switching can start. For some circuit applications this is a serious drawback. In order to minimize this problem, the cross-sectional areas of the two legs should be equal. Assuming that the height  $h$  is common to all legs, this amounts to making  $w_1 = w_2$ .

One should distinguish between the poles in Fig. 95(a), which hold the legs in the stressed state, and the poles on the surface of the domains, which cause the state of soft threshold, Fig. 28. Soft threshold may exist even if the legs are not in a stressed state.

Consider now a three-leg core, Fig. 96(a). After CLEAR MMF  $N_C I_C$  is removed, Leg  $m$  is not saturated because  $w_m > w_3 + w_4$ . The resulting soft threshold of Leg  $m$  is undesirable if the use is such that spurious setting may occur. For example, referring back to the resistance flux-transfer scheme, Sec. II-B-3, it can be seen from Eq. (78) that a lower value of  $d_m^{\min}$  (due to a state of soft threshold) will decrease  $I_p^{\max}$ , and will thus cut down the range of bistable operation. In order to overcome this problem, Leg 4 is so shaped that  $w_m = w_3 + w_4$ , as shown in Fig. 96(b).

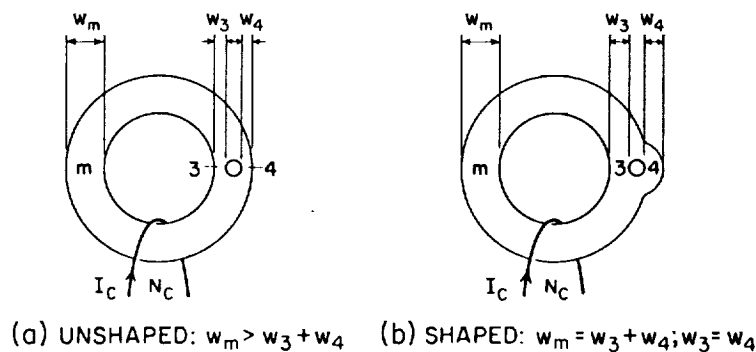
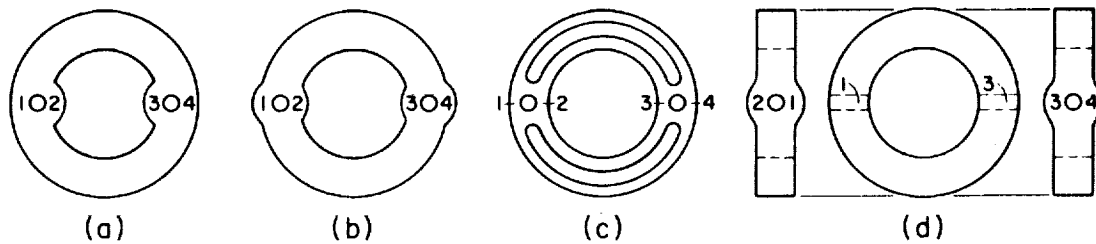


FIG. 96 CLEARING A THREE-LEG CIRCULAR CORE

There are other ways to shape a circular multipath core.<sup>38</sup> Four alternative ways for shaping a circular core with two minor apertures and one major aperture are illustrated in Fig. 97. In Fig. 97(a), Legs 2 and 3 are shaped; in Fig. 97(b), Legs 1, 2, 3, and 4 are shaped. An interesting shaping is shown in Fig. 97(c), where two slots are made in the upper and lower parts of Leg  $m$ . In Fig. 97(d), the axes of the major and minor apertures are perpendicular, and Legs 1, 2, 3, and 4 are shaped.



SOURCE: Ref. 38

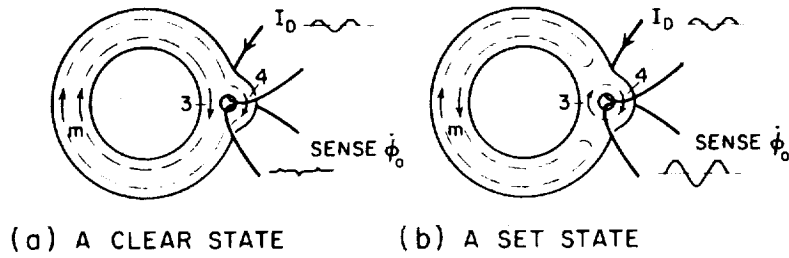
NA-3698-96

FIG. 97 ALTERNATIVE METHODS OF SHAPING A CIRCULAR MULTIPATH CORE

There are several examples in the literature in which multipath cores with soft threshold are used. In Refs. 19, 39, and 40,  $w_m > w_3 + w_4$ , hence one should expect some "mushy" area of soft threshold in Leg  $m$  of these cores. There are also regions of soft state in the Laddic, Ref. 32. This is especially true for a modified Laddic structure, similar to the multihole structure in Fig. 79.

## 2. EFFECT OF SHAPING ON READ-OUT

A flux state of a multipath core may be detected nondestructively by applying an ac drive to a minor aperture, and observing the voltage across a sense winding which is threaded through the same minor aperture. Consider an alternating current drive applied to Leg 4, Fig. 98. In Fig. 98(a) the core is in the CLEAR state. The amplitude of  $I_d$  is so adjusted that no spurious setting around the major aperture is possible. The read-out  $\dot{\phi}_o$  is low because at any half cycle, one of the legs is driven into negative saturation by a comparatively low current, resulting in low elastic  $\dot{\phi}$ . If a core is in a SET state, Fig. 98(b),  $\dot{\phi}_o$  is high because both legs are switched inelastically (and elastically). Note that nondestructive read-out is an inherent feature of a multipath core.



RA-3696-97

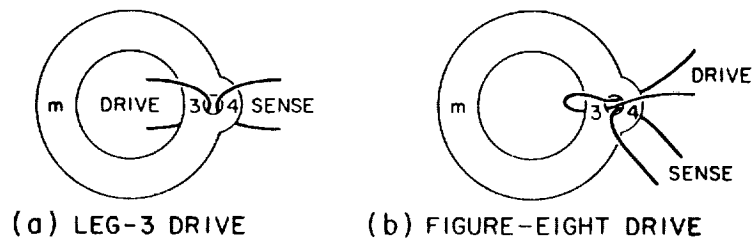
FIG. 98 FLUX-STATE READ-OUT

Other waveshapes of DRIVE current may be used, *e.g.*, square-wave or pulse train plus dc PRIME MMF.

Alternative arrangements for the DRIVE winding are shown in Fig. 99. In Fig. 99(a) the DRIVE winding is on Leg 3. In Fig. 99(b), the two arrangements of driving Legs 3 and 4 are combined into a figure-eight DRIVE.

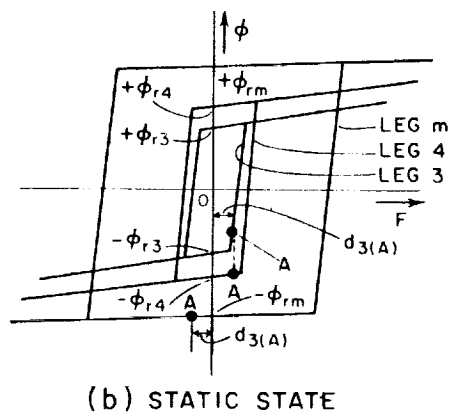
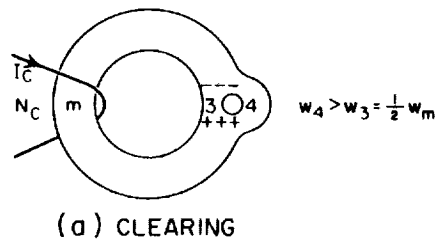
Our objective now is to examine how read-out voltage (or flux) is influenced by having  $w_3 + w_4 \neq w_m$ . First, consider the case of a core with  $w_4 > w_3 = 1/2 w_m$ . An MMF,  $N_C I_C$ , large enough to saturate all legs is applied in the CLEAR direction to Leg  $m$ , Fig. 100(a). As  $I_C$  is released, a static state, Point A in Fig. 100(b), is reached. This state is sustained by a pole distribution, Fig. 100(a). The higher  $N_C I_C$  is, the higher is  $\phi_3$  at Point A. We notice that in spite of the fact that  $w_3 = 1/2 w_m$ , it is Leg 3 that is partially set; and conversely,  $\phi_4 \approx -\phi_r$ , despite the fact that  $w_4 > 1/2 w_m$ . This condition stems from the fact that Leg 3 is the shortest leg and that  $F_3 = F_4$ . Note that  $-F_m = F_4 = d_{3(A)}$  at the stressed CLEAR state also when  $w_3 > w_4 = 1/2 w_m$  or when  $w_3 = w_4 > 1/2 w_m$ .

An ac drive is now applied through the minor aperture of a cleared core whose  $w_4 > w_3 = 1/2 w_m$ , Fig. 101(a). The resulting variations in  $F$  and  $\phi$  of Legs 3 and 4 are shown in Fig. 101(b). Path A-B-C-D corresponds to a positive half cycle, and Path D-E-F-G corresponds to a negative half cycle. Note that  $F_m^{\max} = -|F_3^{\max}| = -|F_{3(C)}|$ ; hence, by limiting  $N_C I_C$  so that  $|F_{3(C)}| < d_m^{\min}$ ,  $\Delta\phi_m \approx 0$ . The read-out  $\dot{\phi}$ , which is  $\dot{\phi}_0$ , is composed of an inelastic component, in addition to the elastic component  $\dot{\phi}_{e0}$ , because Leg 3 is partially set before the ac drive is applied. This shows how  $\dot{\phi}_0$  of a CLEAR state (noise) is increased by making  $w_3 + w_4 > w_m$ . This noise is independent of the ratio  $w_3/w_4$ .



RA-3696-98

FIG. 99 ALTERNATIVE DRIVES FOR READ-OUT



RA-3696-99

FIG. 100 STATIC CLEAR STATE WHEN  $w_4 > w_3 = 1/2 w_m$

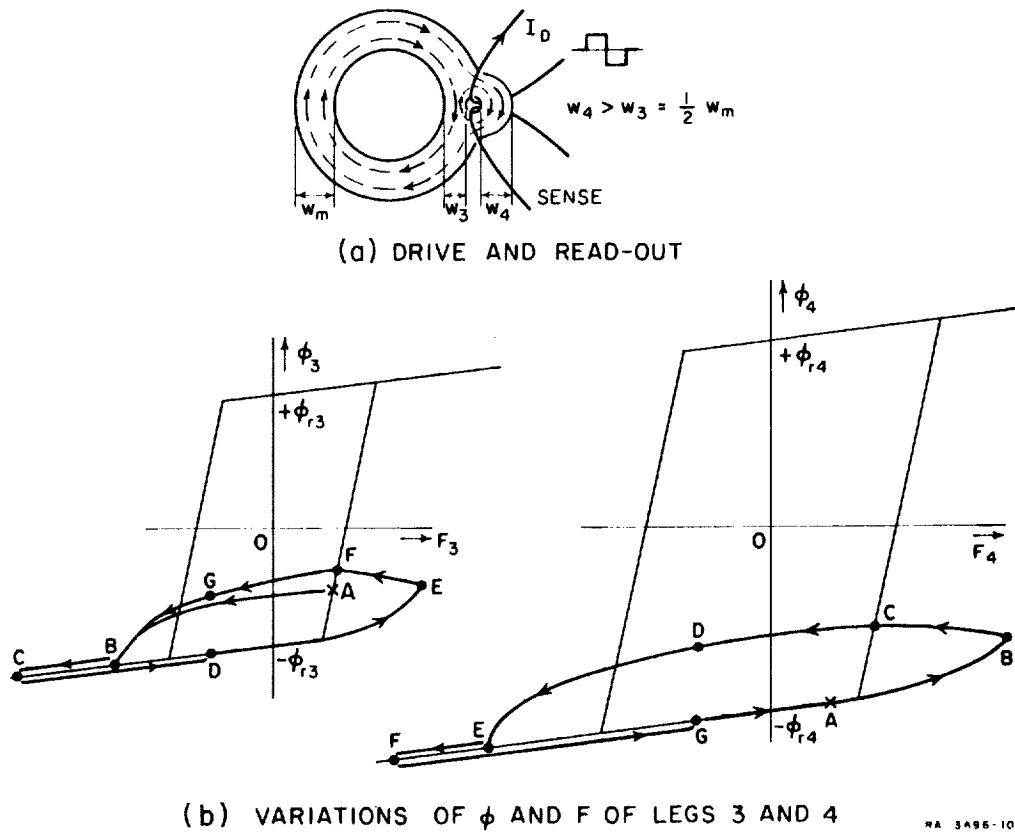


FIG. 101 EFFECT OF EXTRA LEG WIDTH ON CLEAR-STATE READ-OUT

Now consider read-out of a SET state, Fig. 98(b). If  $w_4 > w_3 = 1/2 w_m$ , or if  $w_3 > w_4 = 1/2 w_m$ , then  $\phi_{\rho_o}$  will be the same as when  $w_3 = w_4 = 1/2 w_m$  (provided  $\Delta\phi_3 \leq \phi_{r_m}$ ). In other words,  $\phi_{\rho_o}$  depends on the smaller of the values of  $w$  of Legs 3 and 4. On the other hand, for the same  $w_m$ , if  $w_4 = w_3 > 1/2 w_m$ ,  $\phi_{\rho_o}$  of the SET state will be higher. However, this increase in signal is not sufficient to offset the relative increase in noise that results from making  $w_3 + w_4 > w_m$ , so that the signal-to-noise ratio is lower than the one corresponding to  $w_3 = w_4 = 1/2 w_m$ .

In conclusion, by making  $w_3 + w_4 > w_m$  instead of  $w_3 + w_4 = w_m$ , the signal-to-noise ratio decreases. This is especially true if  $w_3 \neq w_4$ .

In discussing the signal and noise we have assumed so far that  $w_3 + w_4 > w_m$ . If  $w_3 + w_4 < w_m$ , then the polarity of the poles in the

CLEAR state, Fig. 100(a), is reversed, and  $-F_m = F_{3(A)} = F_{4(A)} < 0$ . However, since  $d_m \gg d_4 (>d_3)$ , then, assuming that  $(w_3 + w_4)/w_m$  is only slightly less than unity, Point A of Leg  $m$ , Fig. 100(b), will not rest above the knee. In this case all legs are in a hard CLEAR state. As a result, the noise is slightly smaller than in the case of  $w_3 + w_4 = w_m$ , and the signal is about the same. In conclusion, by making  $w_3 + w_4$  a small amount below  $w_m$ , the signal-to-noise ratio is slightly improved compared with the case of  $w_3 + w_4 = w_m$ .

The effect of leg length on noise is now considered, assuming that  $w_3 = w_4 = 1/2 w_m$  (the effect on signal is negligible). It is noticed that the noise stems from  $\Delta\phi_e$  of the leg which is driven further into negative saturation (while the other leg involved serves as a short circuiting path). During one half-cycle, Leg 4 is driven into negative saturation; during the following half-cycle, Leg 3 is driven into negative saturation. It is, therefore, concluded that in order to minimize  $\Delta\phi_e$  in both half cycles, Legs 3 and 4 should be as long as possible, preferably equal to each other. This is achieved by shaping Legs 3 and 4 as shown in Fig. 97(b). If in addition,  $w_3 = w_4 = 1/2 w_m$ , such a read-out aperture fulfills the requirement for a high signal-to-noise ratio.

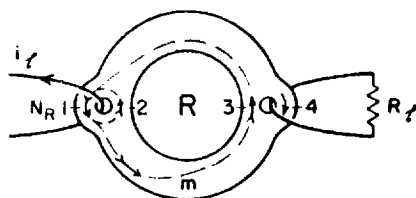
### 3. MINOR-APERTURE FLUX CLIPPING

It is shown in Sec. II-B-4, in connection with Fig. 67, that a bistable flux gain curve may be obtained by using a small toroid as a flux clipper. A contribution to flux clipping may also come from setting a receiver via Leg 1<sup>41</sup> or Leg 2. This mechanism is explained as follows.

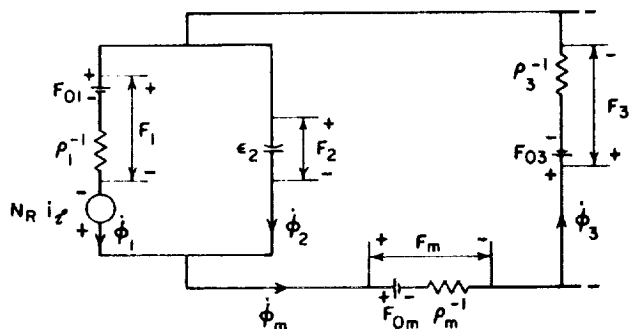
A SET MMF,  $N_R i_\ell$ , is applied to Leg 1, Fig. 102(a), and sets the receiver via Legs 1,  $m$ , and 3. Flux division into Leg 4 is made negligible by means of a low resistance,  $R_\ell$ . A simplified electrical-circuit analogue for the switching legs is shown in Fig. 102(b). By inspection,

$$F_2 = F_{01} + \dot{\phi}_1 \rho_1^{-1} - N_R i_\ell = - [F_{0m} + F_{03} + \dot{\phi}_m (\rho_m^{-1} + \rho_3^{-1})] . \quad (95)$$

Since  $\dot{\phi}_m > 0$ , then  $F_2 < 0$ , and hence the resulting  $\dot{\phi}_2$  is elastic and negative. Thus,  $\dot{\phi}_1 = \dot{\phi}_m + |\dot{\phi}_2|$ , and when integrated over switching time  $\tau$ ,  $\Delta\phi_m = \Delta\phi_1 - |\Delta\phi_2|$ . Recalling that  $\Delta\phi_m$  is the effective received flux,  $\Delta\phi_R$ , it is apparent that Leg 2 acts like a non-constant flux clipper. The clipped flux in Leg 2 is shown in Fig. 103 for the case of transferring a CLEAR state and for the case of transferring a SET state.



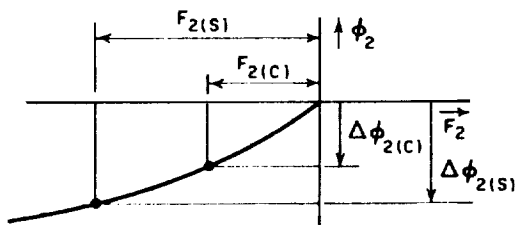
(a) CIRCUIT



(b) APPROXIMATE ELECTRICAL-CIRCUIT ANALOGUE FOR SWITCHING LEGS

RA-3896-101

FIG. 102 SETTING A RECEIVER VIA LEG 1



RA-3896-102

FIG. 103 LEG-2 FLUX CLIPPING IN FIG. 102(a)

For a given switching rate  $\dot{\phi}_m$ , there is a fixed  $F_2$ , given by Eq. (95). If  $w_1 = w_2 = 1/2 w_m$  then, for a given  $F_2$ , the shorter the leg is, the larger is the clipped elastic flux  $\Delta\phi_2$ , Eq. (30). If a core is set via Leg 2 instead of Leg 1, there will be little difference in  $\dot{\phi}_m$ , but since Leg 1 is longer than Leg 2, the resulting clipped flux  $\Delta\phi_1$  will be smaller by approximately the ratio of leg lengths. It is therefore concluded that, in order to get more flux clipping, SET MMF should be applied to the longer of the two small legs by an input minor aperture.

By making  $w_1 + w_2 > w_m$ , the CLEAR states of Legs  $m$ , 1, and 2 are the same as the CLEAR states of Legs  $m$ , 4, and 3, respectively, in Fig. 100. Hence, if the CLEAR MMF is high enough, Legs  $m$  and 1 are in a hard CLEAR state and Leg 2 is partially demagnetized by a fixed amount of flux which depends on  $N_c I_c$  but not on the transferred state. The flux level of Leg 2 is above  $-\phi_r$ , hence an additional amount of flux clipping is available for the following transfer time, as compared with the case of  $w_1 = w_2 = 1/2 w_m$ . Most of this additional flux change is inelastic, hence can be switched by the relatively low  $i_\ell$  in the case of transferring a CLEAR state, and hence the amount of the clipped flux is more nearly constant as a function of the transferred flux. Because of difference in path lengths, the relatively low MMF drop across Leg 2 minimizes any spurious flux that may be set into Legs  $m$  and 3.

In conclusion, more flux clipping may be achieved by Leg 1 input if the length of Leg 1 is longer than Leg 2 and if  $w_1 + w_2 > w_m$ , Fig. 104.

Incidentally, in Fig. 1(c) of Ref. 41, Leg 2 is shown in a CLEAR state and Leg 1 in a demagnetized state, despite the fact that Leg 1 is longer. Such a state can be reached if the CLEAR MMF is applied to

Leg 2 or to both Leg  $m$  and Leg 2, but not by applying a CLEAR MMF to Leg  $m$  alone.

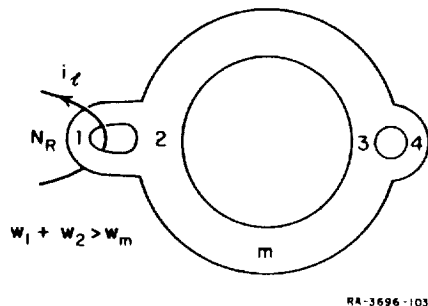
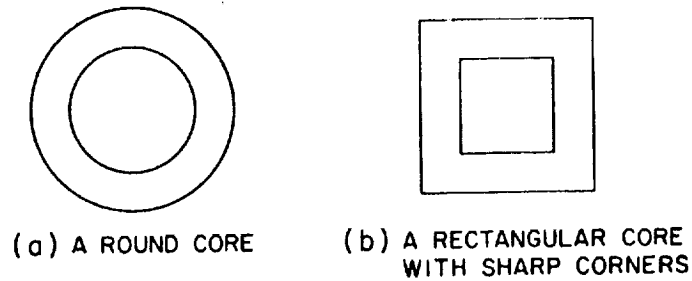


FIG. 104 SHAPING LEGS 1 AND 2 FOR FLUX CLIPPING

#### 4. EFFECT OF FLUX LEAKAGE

Consider two cores, Fig. 105. The circular core in Fig. 105(a) has no sharp corners; the rectangular core in Fig. 105(b) has four sharp corners, and the flux leakage due to surface poles is larger near the corners than in the circular core.





NA-3696-104

FIG. 105 ROUND AND RECTANGULAR CORES

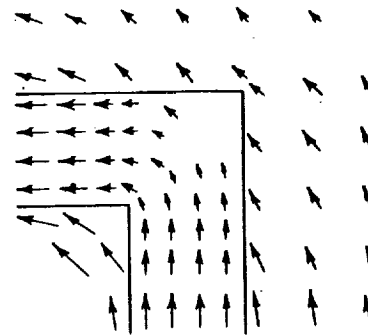
A two-dimensional wire mesh, composed of different gauges of wire, is used in Ref. 42 as an analogue for plotting the field distribution around a corner, Fig. 106, due to applied  $F$ . This problem is analyzed in Ref. 43.

The effect of flux leakage is to damage the squareness of the  $\phi$ - $F$  loop because part of the flux closes via the surrounding air. We would, therefore, expect the circular core, Fig. 105(a), to have better switching characteristics than those of the rectangular core, Fig. 105(b). The same conclusion is drawn with regards to the effect of sharp corners in multipath cores. Further investigation of the effect of sharp corners on switching characteristics is needed.

#### D. LEGS IN SERIES AND PARALLEL

##### 1. LEGS IN SERIES

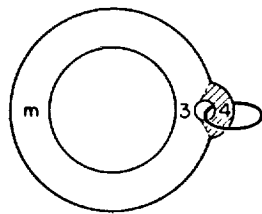
Consider the multipath core in Fig. 107(a) and assume that the winding on Leg 4 is essentially short-circuited. Leg 4 constitutes a flux-closure path, but not a switching path. A similar situation arises when Leg 4 is held in negative saturation by external HOLD MMF. During switching



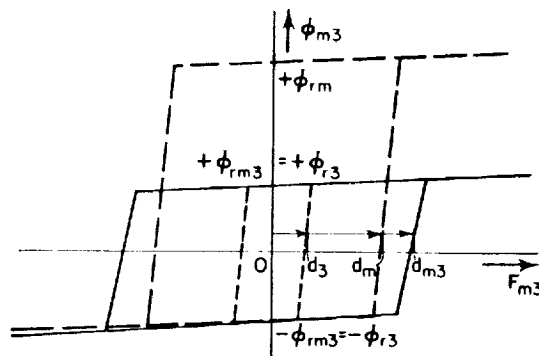
SOURCE: Ref. 42

NA-3696-105

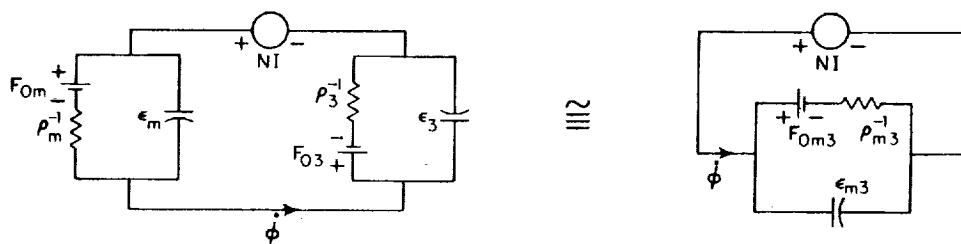
FIG. 106 FIELD DISTRIBUTION DETERMINED FROM A WIRE-MESH ANALOGUE



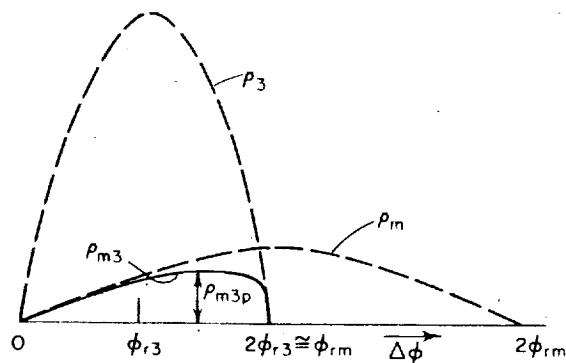
(a) LEGS m AND 3 IN SERIES



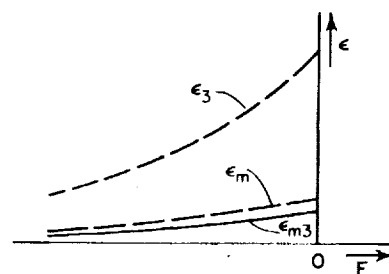
(b) STATIC  $\phi$ -F LOOP OF LEG m3



(c) ELECTRICAL-CIRCUIT ANALOGUES



(d)  $\rho_m$ ,  $\rho_3$  AND  $\rho_{m3}$  vs.  $\Delta\phi$



(e)  $\epsilon_m$ ,  $\epsilon_3$  AND  $\epsilon_{m3}$  vs. F

RB-3696-106

FIG. 107 EQUIVALENT LEG FOR TWO LEGS IN SERIES

time the core is composed essentially of Legs  $m$  and 3 in series, hence Leg 4 may be ignored. Our objective now is to represent this two-leg core by an equivalent single leg, to be called Leg  $m3$ , assuming that Leg 4 is held at negative saturation. In order to do this, we have to determine the static  $\phi$ - $F$  loop and the switching parameters  $F_0$ ,  $\rho$  and  $\epsilon$  of Leg  $m3$ .

The flux capacity of Leg  $m3$  is determined by the narrower leg, Leg 3. Overlapping the bottoms of the static  $\phi$ - $F$  loops of Legs  $m$  and 3,  $d_{m3}$  is simply

$$d_{m3} = d_m + d_3 \quad . \quad (96)$$

The construction of the static  $\phi$ - $F$  loop of Leg  $m3$  is shown in Fig. 107(b).

Let a positive MMF,  $NI$ , set the core. The electrical-circuit analogue for Legs  $m$  and 3 and an approximate analogue for Leg  $m3$  are shown in Fig. 107(c). To a good approximation,

$$F_{0m3} = F_{0m} + F_{03} \quad , \quad (97)$$

$$\rho_{m3}^{-1} = \rho_m^{-1} + \rho_3^{-1} \quad , \quad (98)$$

and

$$\epsilon_{m3}^{-1} = \epsilon_m^{-1} + \epsilon_3^{-1} \quad . \quad (99)$$

Both  $\rho_m$  and  $\rho_3$  are functions of  $\phi$ , Eq. (39), and in determining  $\rho_{m3}$ , proper values of  $\phi$  should be taken. If we assume that both Leg  $m$  and Leg 3 start from their CLEAR states, variations of  $\rho_m$  and  $\rho_3$  with  $\Delta\phi$  are as shown in Fig. 107(d). Substituting  $\phi_m = \Delta\phi - \phi_{rm}$  and  $\phi_3 = \Delta\phi - \phi_{r3}$  into Eq. (39) gives  $\rho_m$  and  $\rho_3$  as functions of  $\Delta\phi$ , and when these are applied to Eq. (98) we get

$$\rho_{m3} = \frac{\rho_{mp} \left[ 1 - \left( 1 - \frac{\Delta\phi}{\phi_{rm}} \right)^2 \right]}{1 + \frac{\rho_{mp}}{\rho_{3p}} \frac{1 - \left( 1 - \frac{\Delta\phi}{\phi_{rm}} \right)^2}{1 - \left( 1 - \frac{\Delta\phi}{\phi_{r3}} \right)^2}} \quad (100)$$

The plot of  $\rho_{\mathbf{m}3}$  versus  $\Delta\phi$  is shown in Fig. 107(d). Note that  $\rho_{\mathbf{m}3}(\Delta\phi)$  is not a symmetrical function, and that its peak,  $\rho_{\mathbf{m}3p}$ , occurs at a value of  $\Delta\phi$  between  $\phi_{r3}$  and  $\phi_{r\mathbf{m}}$ .

The values of  $\epsilon_{\mathbf{m}}$  and  $\epsilon_3$  in negative saturation may be obtained by substituting  $l_0$  and  $l_i$  of Legs  $\mathbf{m}$  and 3 into Eq. (34). For a given  $F$ , we have first to determine its components  $F_{\mathbf{m}}$  and  $F_3$ , then find the corresponding values of  $\epsilon_{\mathbf{m}}$  and  $\epsilon_3$ , from which  $\epsilon_{\mathbf{m}3}$  is calculated. A cut-and-try method may be needed to determine  $\epsilon_{\mathbf{m}}$  and  $\epsilon_3$ . Rough plots of  $\epsilon_{\mathbf{m}}$ ,  $\epsilon_3$  (cf., Fig. 27) and the resulting  $\epsilon_{\mathbf{m}3}$  in negative saturation are shown schematically in Fig. 107(e).

A similar procedure may be used when the equivalence for more than two legs in series is sought.

## 2. LEGS IN PARALLEL

Consider two legs, Legs 3 and 4, in parallel, Fig. 108(a). Let an equivalent leg be denoted by Leg 3||4. We are now looking for the static  $\phi$ - $F$  loop and the switching parameters  $F_0$ ,  $\rho$ , and  $\epsilon$  of Leg 3||4.

The  $\phi$ - $F$  loop of Leg 3||4 is obtained by superposing the  $\phi$ - $F$  loop of the longer leg (Leg 4) on top of the shorter leg (Leg 3), as shown in Fig. 108(b). Thus,

$$\phi_{r\ 3||4} = \phi_{r3} + \phi_{r4} \quad . \quad (101)$$

Assuming positive  $\dot{\phi}$  flowing into the junctions of Legs 3 and 4, Fig. 108(a), the electrical-circuit analogue for these legs and the one for Leg 3||4 are shown in Fig. 108(c). By imposing the conditions that  $\dot{\phi}$  and  $F$  are the same in the two analogues, and that  $|\dot{\phi}| > 0$  in both legs, we get

$$\dot{\phi} = \rho_{3||4}(F - F_{0\ 3||4}) = \rho_3(F - F_{03}) + \rho_4(F - F_{04}) \quad .$$

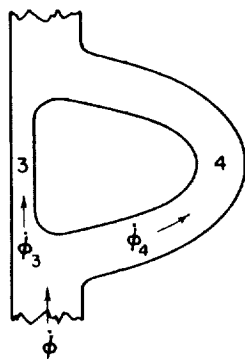
Hence

$$F_{0\ 3||4} = \frac{\rho_3 F_{03} + \rho_4 F_{04}}{\rho_3 + \rho_4} \approx F_{03} \frac{(A_3 + A_4) l_4^{\mathbf{a}\mathbf{v}}}{A_3 l_4^{\mathbf{a}\mathbf{v}} + A_4 l_3^{\mathbf{a}\mathbf{v}}} \quad , \quad (102)$$

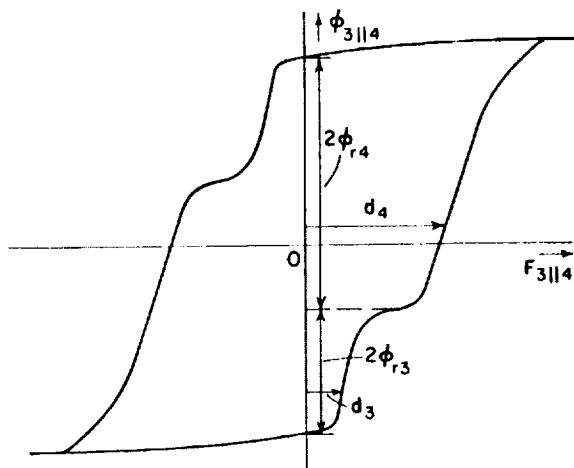
$$\rho_{3||4} = \rho_3 + \rho_4 \quad , \quad (103)$$

and

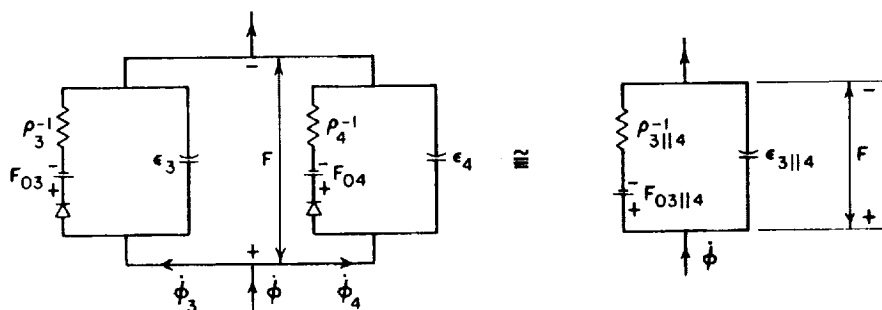
$$\epsilon_{3||4} = \epsilon_3 + \epsilon_4 \quad . \quad (104)$$



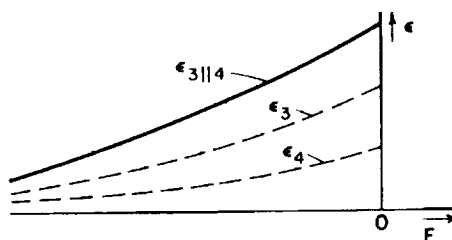
(a) LEGS 3 AND 4 IN PARALLEL



(b) STATIC  $\phi$ -F LOOP OF LEG 3||4



(c) ELECTRICAL-CIRCUIT ANALOGUES



(d)  $\epsilon_3$ ,  $\epsilon_4$  AND  $\epsilon_{3||4}$  vs. F

RB-3696-107

FIG. 108 EQUIVALENT LEG FOR TWO LEGS IN PARALLEL

Evaluation of  $\rho_{3\parallel 4}$  is a complex process, since  $\rho_3$  and  $\rho_4$  vary with flux, and we do not have the tools to determine how  $\dot{\phi}$  is divided into  $\dot{\phi}_3$  and  $\dot{\phi}_4$ . Further investigation is needed.

Determination of  $\epsilon_{3\parallel 4}$  is much simpler, since the same  $F$  appears across Legs 3, 4, and  $3\parallel 4$ . The plot of  $\epsilon_3$ ,  $\epsilon_4$ , and  $\epsilon_{3\parallel 4}$  versus  $F$  in negative saturation, based on Eq. (104), is shown in Fig. 108(d).

## E. CONCLUSIONS

This section deals with various switching effects that are caused by the geometry of a multipath core. The term *geometry* stands for the geometry of each individual leg as well as the topology of the legs that constitute the multipath core. Although the title of this section is "Geometry Effects," it should be emphasized that these effects depend not only on the relations among the geometries of the legs and on the way the legs are assembled together, but also on the flux state of each leg. The flux state of the individual leg, on the other hand, is a function of the material properties, the geometry, and the duration and amplitude of the MMF drive.

The material in this section is relatively new. A large portion of it needs further experimental verification. In addition, these phenomena have been treated qualitatively, in the main, because of the complexity involved. Wherever possible, this treatment should be supplemented by quantitative analysis in the future. Further investigation is thus needed in the following areas:

- (1) Flux-division effect
- (2) Stress effects
- (3) Supersetting and unsetting effects
- (4) Flux leakage and effect of a sharp corner on flux switching.

## IV FLUX PATTERNS

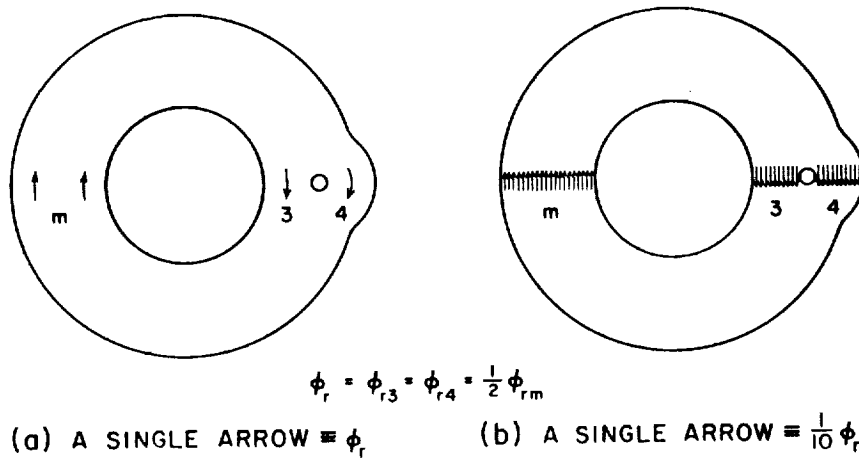
### A. ARROW MODEL

A simplified description of a flux pattern in a multipath core may be achieved by means of an arrow model. We have used this model in the previous sections; for example, four different flux states are distinguished in Fig. 61(b) by different arrangements of arrows.

#### 1. RULES

The use of this model is based on several simple rules, which are described as follows:

- (1) *Scaling*—Each arrow represents a predetermined amount of flux. The relative magnitude of this amount depends on the number of flux states that have to be distinguished. Consider the multipath core in Fig. 109, assuming that  $w_3 = w_4 = \frac{1}{2}w_m$ , and hence  $\phi_{r3} = \phi_{r4} = \frac{1}{2}\phi_{rm} \equiv \phi_r$ . In logic applications of a multipath core (Sec. II-B), flux states are differentiated in a discrete manner. The flux level of Leg 3 or Leg 4 is either near  $-\phi_r$  (CLEAR state) or

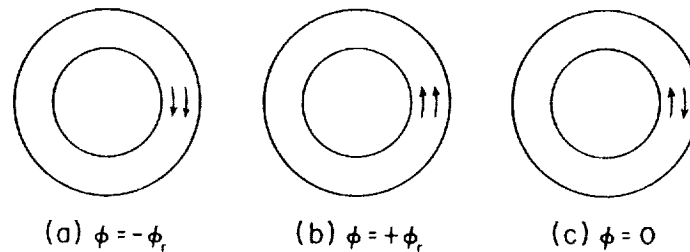


RA-5896-108

FIG. 109 ARROW-MODEL SCALING

near  $+\phi_r$  (SET state). In this case, it is sufficient to represent  $\phi_r$  by a single arrow, as in Fig. 109(a). On the other hand, when continuous variations of flux take place (Sec. II-A), a single arrow may be insufficient to represent  $\phi_r$ . In this case, the continuous variation in  $\phi$  is approximated by several small variations in  $\phi$ , Fig. 109(b). The number of arrows representing  $\phi_r$  depends on the smallest amount of  $\Delta\phi$  referred to in a discussion. For example, in analyzing the Setting characteristics in Appendix D,  $\phi_r$  may in some cases be represented by four arrows, yet in other cases ten arrows are needed. An alternative way of arrow scaling may be achieved by labeling the flux contents of each arrow. A third type of arrow scaling may be achieved by scaling the *length* of an arrow. In this way any continuous amount of flux may be described and arrows of different lengths may be combined. Unless carefully drawn and carefully read, graphical scaling is less accurate than the method where each arrow corresponds to fixed or labeled amount of flux.

- (2) *Polarity*—The arrowhead represents the direction of magnetization. It is assumed that an arrowhead in a clockwise direction around a major aperture represents a negatively saturated flux. In Fig. 110, the flux capacity of a toroid is represented by two arrows. In Fig. 110(a),  $\phi = -\phi_r$ ; in Fig. 110(b),  $\phi = +\phi_r$ ; and in Fig. 110(c),  $\phi = 0$ . Note that if  $\phi_r$  is represented by a single arrow, the state of  $\phi = 0$  will be represented by no arrow. In this case the flux change  $\Delta\phi = \phi_r$  is represented by erasing the initial arrow, and the flux change  $\Delta\phi = 2\phi_r$  is represented by reversing that arrow. This explains how the two arrows that represent elastic flux in Leg 1, Fig. 88(c), are annihilated in Fig. 88(d), causing the single arrow representing  $\phi_2$  to reverse.

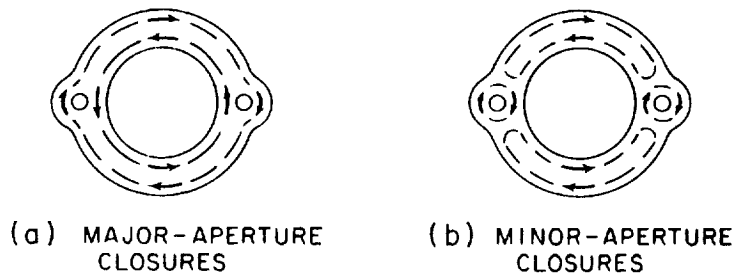


SA 5696 109

FIG. 110 ARROW-MODEL POLARITY



- (3) *Flux Continuity*—The most important rule to remember is that at any leg junction, the number of arrows pointing into the junction must always be equal to the number of arrows pointing out of the junction. This is simply a manifestation of the law of flux continuity, Eq. (88). This requirement should be satisfied in both static and dynamic flux states. When poles are distributed in the junction, an air-flux term, represented by the air-flux arrow [cf. Fig. 95(a)], should be added to Eq. (88).
- (4) *Flux Closure*—As a result of different drive sequences, two flux states represented by identical arrows may have different flux patterns because of different paths of flux closure, Fig. 111. The path of flux closure is represented by a dotted line. Note that the path of flux closure does not necessarily follow the path of flux switching.



RA 3696-110

FIG. 111 DIFFERENT FLUX CLOSURES

- (5) *Reversed Flux*—In order to designate a flux state established during the previous switching time, tails are added to the arrows representing such a state (cf. Fig. 88). The right-hand rule may be used as a guide for examining a possible flux-switching path, and arrows are reversed if the corresponding MMF threshold is exceeded.

## 2. APPLICATION

The arrow model is used extensively in the literature. Its use in Ref. 11 results in referring to the flux pattern of SET-R, SET-T and SET-P states, Figs. 61(b) and 63(b), as "kidney-shaped" flux distributions. Flux transfer in all-magnetic shift registers is very clearly described by means of the arrow model in Refs. 11, 17, 24, and 25. The arrow model facilitates the description of flux switching in multipath cores which are employed in shift register and logic circuitry<sup>11,14,15,17,25,29,32,34,40,41,44,45,46</sup> and in memory.<sup>15,47,48,49,50</sup> Unfortunately, in some cases the arrow model results in erroneous conclusions. We would like to call the attention of the reader to two of these cases.

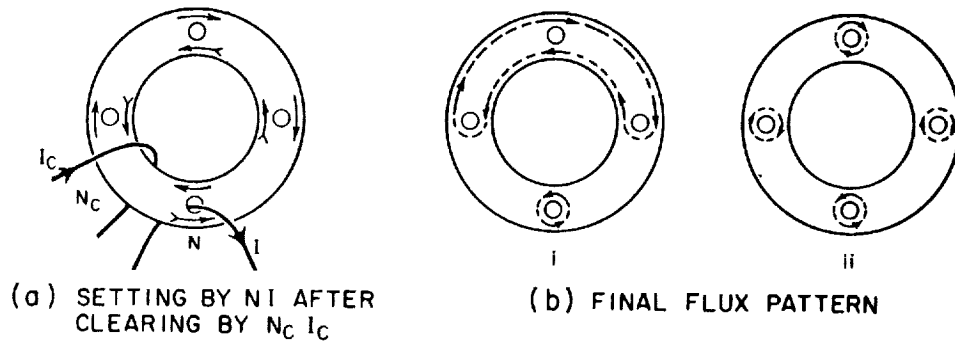


FIG. 112 FLUX PATTERN IN A SET CORE

A five-hole core is first cleared and then set, as shown in Fig. 112(a). It is claimed in Ref. 28 that the two flux patterns in Fig. 112(b) are equally valid on the basis of measurements of  $\Delta\phi$  in all legs, but since no coupling seems to occur later among the minor apertures, Pattern ii is preferred. There are two fallacies about this claim. First, no coupling among minor apertures occurs in either Pattern i or Pattern ii. (This feature enables us to obtain nondestructive read-out in multipath cores.) Second, the preferred Pattern ii seems to violate the principle of minimum energy, because this pattern calls for a large over-all domain-wall area (see Part B-2), which results in a higher domain-wall energy.

An erroneous explanation for flux switching in multipath cores is given in Ref. 7, where a five-hole core is driven as shown in Fig. 113(a). After the core is cleared by  $N_c I_c$ , SET MMF  $N_s I_s$ , sets the core. By means of a bias HOLD MMF,  $N_H I_H$ , Leg 3 is held and the core is set via Leg 4. Using

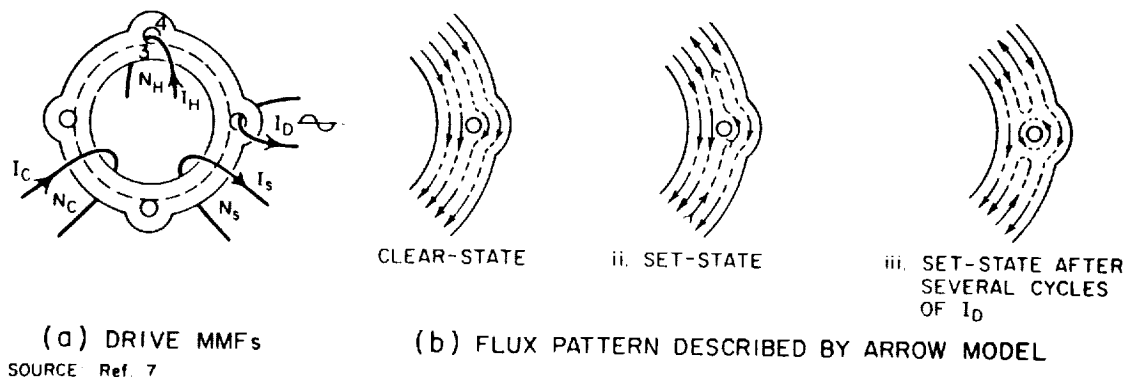


FIG. 113 ERRONEOUS DESCRIPTION OF FLUX SWITCHING

the erroneous toroidal model in Fig. 3, it is first incorrectly stated that the bias HOLD MMF prevents switching in the core material within the dotted circle, Fig. 113(a), and that hence  $N_s I_s$  switches some or all of the flux in the material outside the dotted circle, Figs. 113(b)i and ii. Second, it is stated that several cycles of  $I_D$  may be required before the "unstable" state in Fig. 113(b)ii reverts to the one in Fig. 113(b)iii around the minor aperture where  $I_D$  is applied. If the state in Fig. 113(b)ii were obtained, then it would be stable and it would switch to the state of Fig. 113(b)iii in only one cycle of  $I_D$ .

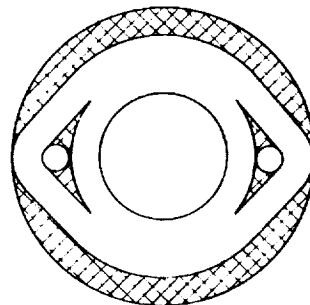
### 3. EVALUATION

There is no doubt that the arrow model for describing flux distribution has its merits. This is a simple model which is easily used and easily understood. Rather complex flux changes in multipath cores can be explained by using this simple model without sacrificing too much accuracy. However, this model does not provide enough information about the exact pattern of the distributed flux. In the following parts, such information is sought. In Part B, flux closure is analyzed in terms of domain-like patterns, and in Part C, theoretical calculations of static flux patterns, based on Laplace's equation, are described.

### B. ZONE CONFIGURATIONS

Some uncertainty about flux pattern arises when one tries to fulfill the requirement for flux continuity in a multipath core where there are variations in cross-section. In Ref. 20 this question is settled by cross-hatching a portion of the multipath core, Fig. 114, thus obtaining a constant cross-section in the rest of the core. The shaded area is treated as a "mushy" region, where domains close on themselves locally.

Our objective here is to look for an alternative, more specific, picture of flux patterns, based on the theory of domains. For the sake of simplicity, we shall assume that flux states are reached by slow switching.



SOURCE: Ref. 20 RA-3696-113

FIG. 114 MUSHY REGIONS

## 1. ZONE BOUNDARY

The pattern of a domain follows the principle of minimizing the total energy associated with a wall. The latter consists of exchange, anisotropy, magnetoelastic, and magnetostatic energies.<sup>51</sup> Domain patterns are much more clear cut in a bulk crystalline material than in a bulk polycrystalline material. Consider the magnetization pattern in a bulk region

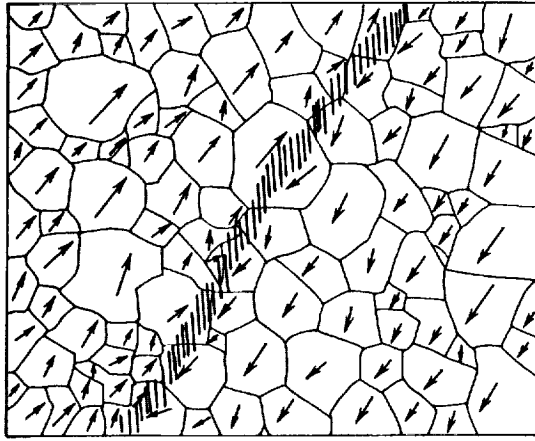


FIG. 115 ZONE BOUNDARY IN A BULK FERRITE

of polycrystalline ferrite, Fig. 115. A single crystallite may include unaligned magnetization, or even several domains, such as small spiky domains on the crystallite edges. For simplicity, each crystallite is shown as a single domain by means of an arrow which represents the resultant magnetization vector of the crystallite. We observe two regions, the upper left and lower right portions, whose resultant magnetizations are opposite in direction, although the magneti-

zation vectors of the individual crystallites in each region are not necessarily aligned. Each region will be called *zone* in order to differentiate it from the common term *domain*. A zone may be regarded as a gross domain, *i.e.*, an aggregate of individual domains that deviate only slightly from a certain average direction. This direction is identified with the zone orientation. The narrow transition region between two zones will be referred to as a *zone boundary* in order to differentiate such a boundary from a well-defined domain wall. The zone boundary is marked schematically by a shaded area in Fig. 115.

We are now attempting to predict roughly the shapes of zone boundaries in a multipath core. We shall start with a SET state because the plot of zone boundaries in this state is less complicated than it is in a CLEAR state.

## 2. ZONE PATTERN OF A SET CORE

Consider a shaped multipath core, Fig. 116, with  $w_3 = w_4 = \frac{1}{2}w_m$ . A circle of radius  $R = R_i + w_3$  is drawn concentric with the major aperture.

This circle and the circumference of the minor aperture are tangent at Point C. Two curves, A-B and D-E, are drawn at a fixed distance of magnitude  $w_4$  from the outer edge of the core. This results in two constant-width bands where flux is continuous, and two shaded regions, ABC and CDE.

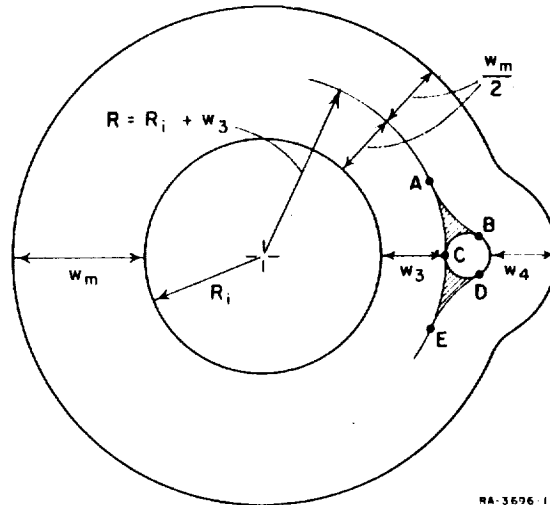


FIG. 116 A SHAPED MULTIPATH CORE

Let us assume that the core is set via Leg 3, and examine possible zone boundaries in the shaded areas. We know that these zones have a structure that tends to minimize the total energy. Theoretically, the total energy should include all four kinds of energy, but practically the demagnetizing energy due to poles is predominant by several orders of magnitude.<sup>51</sup> In figuring out zone patterns, we shall therefore try to minimize pole distribution by employing zones of closure.

A zone pattern with minimum pole distribution is proposed<sup>52</sup> in Fig. 117. Region ABC is divided into three portions: AFB, AFC, and BFC. The

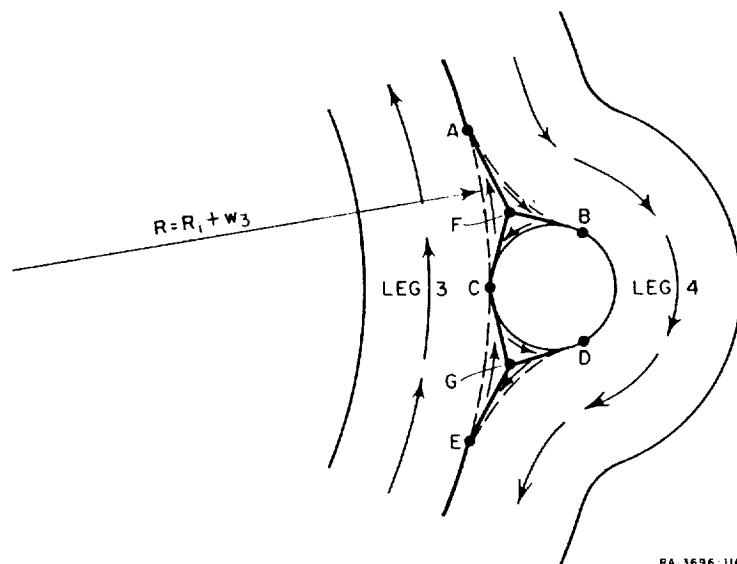


FIG. 117 ZONE BOUNDARIES FOR A CORE SET VIA LEG 3

distances between Point F and Arcs A-B, A-C, and B-C are the same. The flux in Region AFC has the same direction as the flux closing via Leg 3; hence Arc A-C, marked by a dashed line, does not constitute a zone boundary. Similarly, there is no zone boundary along the dashed line of Arc A-B. However, zone boundaries exist along Paths A-F, F-C, and F-B, which are determined by minimizing the pole density along these boundaries.

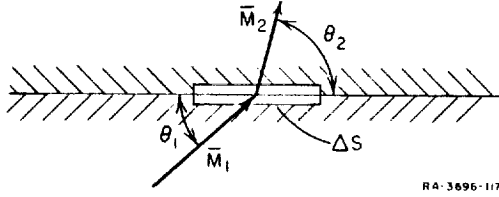


FIG. 118 MAGNETIZATION VECTORS  
ACROSS A BOUNDARY

Consider a small pill box of cross-sectional area  $\Delta s$  along a boundary between two nonlinear materials whose magnetization vectors,  $\bar{M}_1$  and  $\bar{M}_2$ , are shown in Fig. 118. Using the large-scale form of Maxwell's equation  $\nabla \cdot \bar{B} = 0$ ,

$$\oint_S \bar{B} \cdot d\bar{S} = \mu_0 \oint_S (\bar{H} + \bar{M}) \cdot d\bar{S} = 0 \quad (105)$$

Hence, the surface pole density at  $\Delta S$  is

$$\begin{aligned} \sigma &= \frac{1}{\Delta S} \oint_S \bar{H} \cdot d\bar{S} = -\frac{1}{\Delta S} \oint_S \bar{M} \cdot d\bar{S} \\ &= M_1 \sin \theta_1 - M_2 \sin \theta_2 \end{aligned} \quad (106)$$

For no poles to exist, the condition

$$M_1 \sin \theta_1 = M_2 \sin \theta_2 \quad (107)$$

must be satisfied, i.e., the normal components of  $M_1$  and  $M_2$  must be equal. In the case of a single material,  $M_1 = M_2 = M$ ; in order for no poles to exist, Condition (107) is thus reduced to

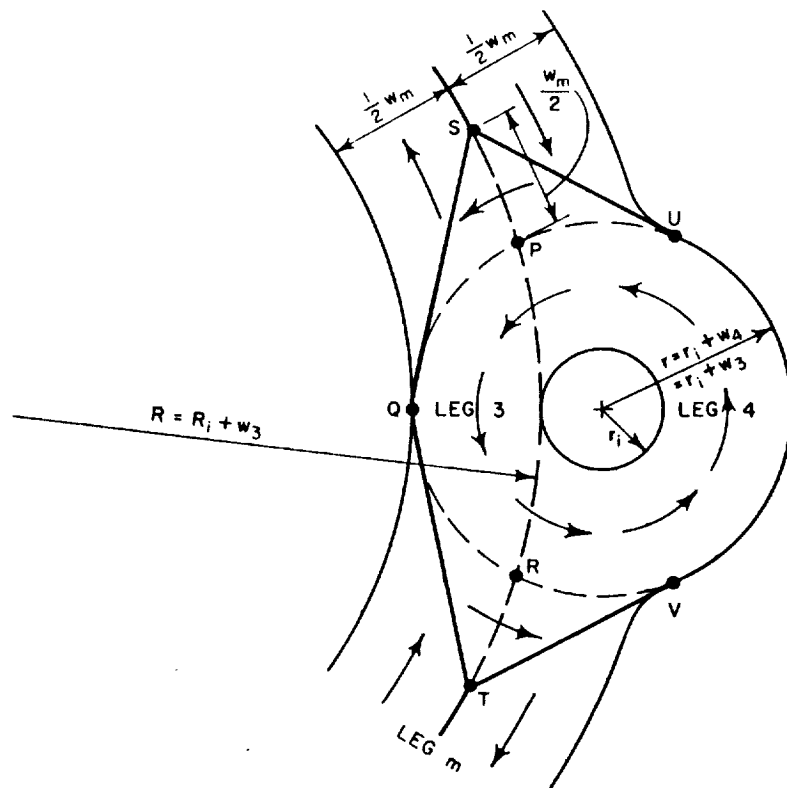
$$\sin \theta_1 = \sin \theta_2 \quad (108)$$

We conclude from Eq. (108) that no poles exist if there is no domain boundary ( $\theta_1 = \theta_2$ ) or if the domain boundary bisects the angle between the two magnetization vectors ( $\theta_1 = \pi - \theta_2$ ). The latter case is particularly important in determining the position of a domain wall without poles.

Let us refer back to Fig. 117. Zone Boundaries A-F, B-F, and C-F are determined by bisecting the angles between respective pairs of

magnetization vectors along each boundary. In this way no poles exist along these boundaries. Zone Boundaries C-G, D-G, and E-G are symmetrical to Zone Boundaries C-F, B-F, and A-F, respectively. In accordance with the assumption of slow switching, there is also a zone boundary from Point A to Point E around the major aperture along the middle circle of radius  $R = R_i + w_3$ .

The flux in Legs 3 and 4 of Fig. 117 is now switched by applying counterclockwise MMF through the minor aperture. The resulting zone pattern is suggested in Fig. 119. We notice that no flux switching has taken



RA-3696-118

FIG. 119 ZONE BOUNDARIES FOR A CORE SET VIA LEG 4

place in Regions BCF and CDG, Fig. 117; pictorially, these regions have, during switching, grown by zone-boundary motion from the pattern in Fig. 117 to the pattern in Fig. 119. Points P and R are the intersection points of two circles: a small circle, concentric with the minor aperture, of radius  $r = r_i + w_3 = r_i + w_4$ , and the large circle, concentric with the major aperture, of radius  $R = R_i + w_3$ . Points S and T lie on the circumference

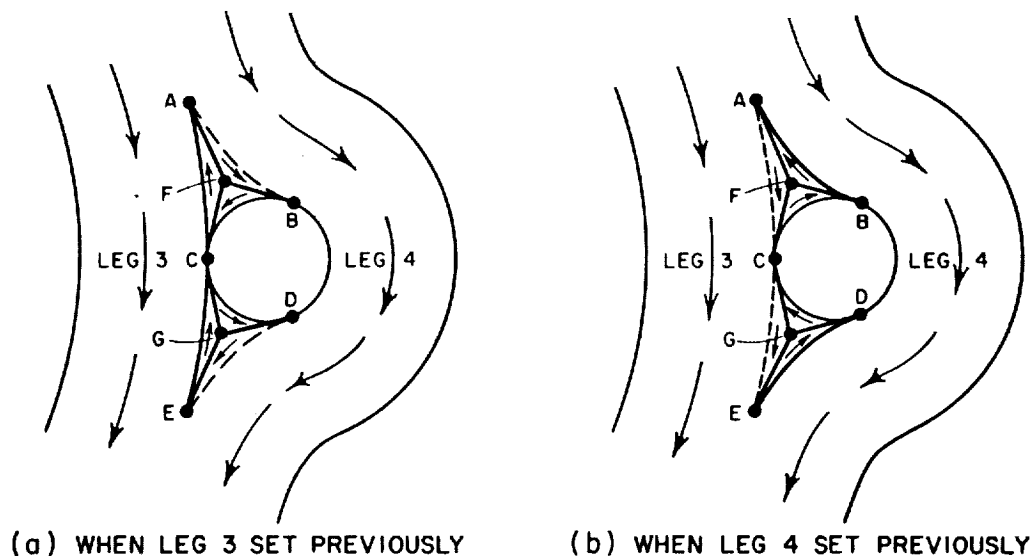
of the large circle, and the distance between Points S and P (or T and R) is equal to  $\frac{1}{2}w_m$ . Note that zone boundaries exist only along Path U-S-Q-T-V and from Point S to Point T around the major aperture along the circle of radius  $R = R_i + w_3$ .

The zone pattern in Fig. 119 holds also for the case where the core is set via Leg 4 from an initial CLEAR state. This is so because flux will tend to switch mainly around the inner ring of Leg  $m$ .

### 3. ZONE PATTERN OF A CLEARED CORE

Refer back to a set core, Fig. 117, where Leg 3 is in a SET state and Leg 4 is in a CLEAR state. A CLEAR MMF is now applied, causing the flux of Leg 3 to switch clockwise around the major aperture. The question is what the zone pattern would look like.

The simplest configuration of a zone boundary is shown in Fig. 120(a). Comparing this configuration with the initial one in Fig. 117, we observe that no flux has switched in Regions ABC and CDE. Flux switching has occurred only in the inner half of Leg  $m$  and in Leg 3. As a result, the zone boundary from Point A to Point E around the major aperture, Fig. 117, has been erased; in its stead, a new, shorter zone boundary has been formed along Arc A-C-E. As in the previous cases, poles are eliminated (or at least minimized) by this pattern.



WA-3896-119

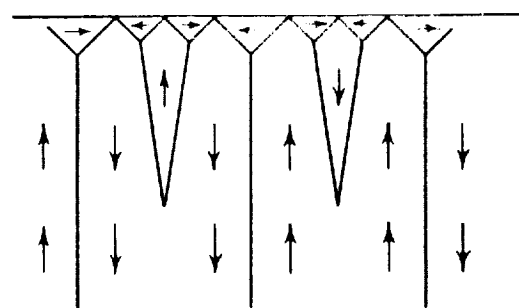
FIG. 120 POSSIBLE ZONE BOUNDARIES FOR A CLEARED CORE



Consider now the case where the multipath core is set via Leg 4 and via the *outer* half of Leg  $m$ . This state can be reached by setting the whole core first, and then applying CLEAR MMF to Leg 3. In this case, the zone pattern is identical with the one in Fig. 117, except that *all* of the magnetization vectors are reversed. If this is the initial state, clearing the core will result in the zone pattern shown in Fig. 120(b). In comparison with the pattern in Fig. 120(a), the directions of magnetization vectors in the zones of closure are reversed, and zone boundaries exist along Paths A-B and D-E rather than along Path A-C-E. If the models in Fig. 120 are valid, this means that a CLEAR state reached by driving on Leg  $m$  may have either of two possible internal zone structures, depending on its past state.

Suppose that the zone pattern is initially as shown in Fig. 120(b). Leg 3 is now set, and the final zone pattern should be as shown in Fig. 117. This calls for reversing the flux in the zones of closure. A possible mechanism by which this reversal can be achieved is as follows: During switching time, under the effect of applied  $H$ , Zone ABF grows to the left and Zones ACF and BCF are annihilated. In order to prevent the creation of surface poles, a new zone, whose magnetization vector points to the left, is formed near Point B, and the portion of Boundary A-B near Point B moves to the left of Point B, thereby gradually reversing the magnetization in Region ABF. This process of zone growth continues until, finally, the pattern in Fig. 117 is reached. Zones in Region CDE reverse in a similar manner.

It is suggested<sup>51</sup> that when anisotropy is high, the domains may branch near the crystal surface, as shown in Fig. 121. The magnetization in the vicinity of the minor aperture may induce stress in Regions ABC and CDE, Fig. 120, causing anisotropy to arise.<sup>53</sup> It is possible, therefore, that the zone pattern in the CLEAR state<sup>52</sup> is similar to the pattern in Fig. 121, as shown in Fig. 122. Each zone boundary is as close as possible to a position that bisects the angle between the corresponding magnetization vectors in order to



SOURCE: Ref. 51

RA-3696-120

FIG. 121 POSSIBLE DOMAINS NEAR CRYSTAL SURFACE

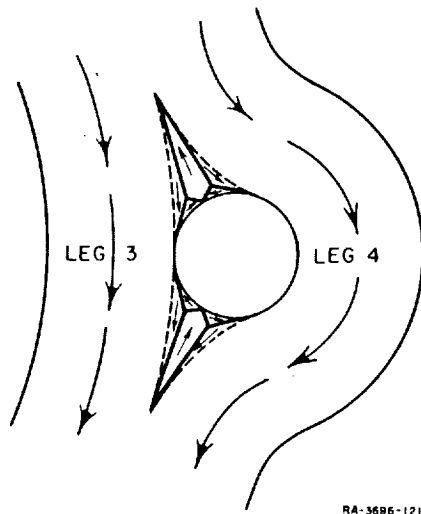


FIG. 122 ALTERNATIVE ZONE BOUNDARIES  
IN A CLEAR STATE

minimize pole density. Note that this pattern is not affected by whether it is Leg 3 or Leg 4 that is set before the core is cleared via Leg  $m$ .

#### 4. ZONE PATTERN OF AN UNSHAPED CORE

Zone patterns of an unshaped core are more complex because Leg  $m$  is not completely cleared. This case is treated in Ref. 20, and is summarized and evaluated as follows.

The flux pattern for a CLEAR state is shown in Fig. 123. Note that  $w_m$  varies and that its minimum value is equal to  $w_3 + w_4$ . The shaded area indicates regions of local flux closure. No experimental verification for this model is given.

A zone pattern for a core set via Leg 3 is shown in Fig. 124(a). It is not clear how the flux in the shaded region on the periphery of Leg  $m$ , Fig. 123, has switched clockwise. Furthermore, since the shaded region may have a soft threshold, flux may switch in this region in the counter-clockwise direction before Leg 3 is completely set. Next, the minor

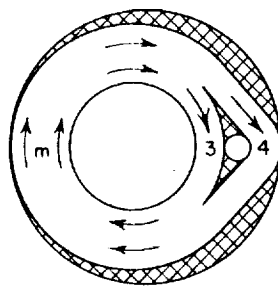
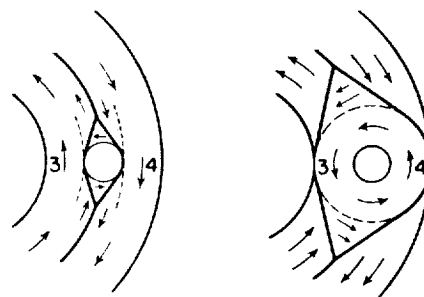


FIG. 123 ZONE PATTERN FOR  
A CLEAR STATE



(a) SET-U STATE (b) SET-P STATE  
SOURCE: Ref. 20

FIG. 124 ZONE PATTERN FOR  
A SET CORE

aperture is primed. The resulting zone pattern is shown in Fig. 124(b). This state is to be expected if the pattern of the SET- $U$  state in Fig. 124(a) is valid.

Zone patterns for partial SET and primed states are also given in Ref. 20. In this case, the shaded region on the periphery of Leg  $m$  is included. Figure 125 shows zone patterns for three states: initial partial SET state; intermediate state during priming; and final primed state.

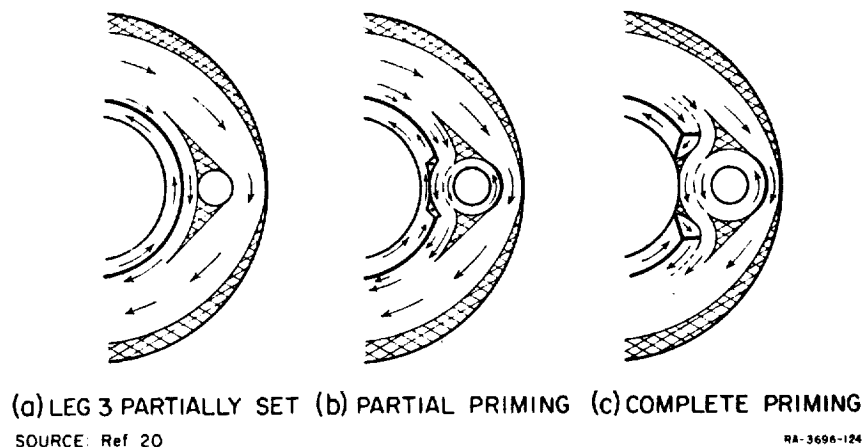


FIG. 125 ZONE PATTERN FOR A PARTIALLY SET AND PRIMED CORE

An effort is made in Ref. 20 to correlate between this model of flux pattern and various setting characteristics (cf. Figs. 57 through 60). The most significant experimental verification is that shown in Fig. 126. Output flux,  $\Delta\phi_o$ , is plotted versus increasing DRIVE MMF,  $F_d$ , and versus decreasing  $F_d$ , using a fixed value of  $F_s$ , which sets Leg 3 almost completely. It can be seen in Fig. 124(a) that the first pulse of  $F_d$  in the counterclockwise direction has to switch flux around the zones of closure. This amount of flux remains unchanged during the succeeding DRIVE cycles, despite a shorter switching path in the inner ring around the minor aperture. As  $F_d$  is increased,  $\Delta\phi_o$  is increased as well (if enough flux has been set into Leg 3). However, when  $F_d$  is decreased,  $\Delta\phi_o$  tapers off to a value higher than for same  $F_d$  when  $F_d$  is increased. This occurs because the same  $\Delta\phi_o$  that requires a relatively high  $F_d$  to switch flux around the zone of closure during the first cycle can now

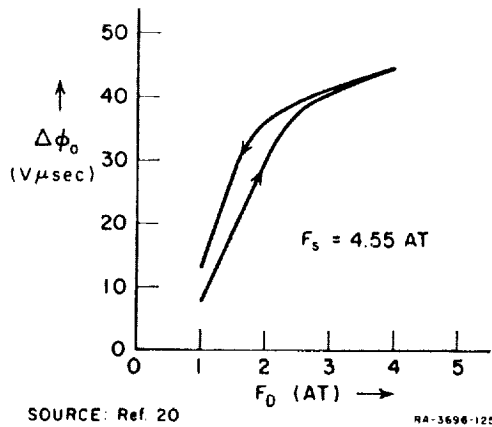


FIG. 126  $\Delta\phi_0$  vs. INCREASING AND DECREASING  $F_D$

be switched by a smaller  $F_D$  along a shorter path around the minor aperture, and because the switchable flux in the zones of closure is now larger than  $\Delta\phi_0$ .

Before we leave the subject of zone patterns, let us emphasize that what we have presented regarding zone boundaries is far from complete. Further theoretical and experimental study is needed.

## C. ANALYSIS OF FLUX PATTERNS

### 1. EFFECT OF POLES ON $H$ EQUALIZATION

An interesting physical interpretation for the function of magnetic poles in distributing  $H$  along a ferromagnetic toroid is given in Ref. 36. Consider a coil of  $N$  turns, Fig. 127(a), that carries a direct current  $I$ . Refer to two points: Point A in the middle of the coil, and Point B far from the coil. The magnetic field at Point A,  $H_A$ , is much larger than the magnetic field at Point B,  $H_B$ . Suppose that the same coil is now wrapped around a ferromagnetic core, Fig. 127(b). When  $I$  is applied,

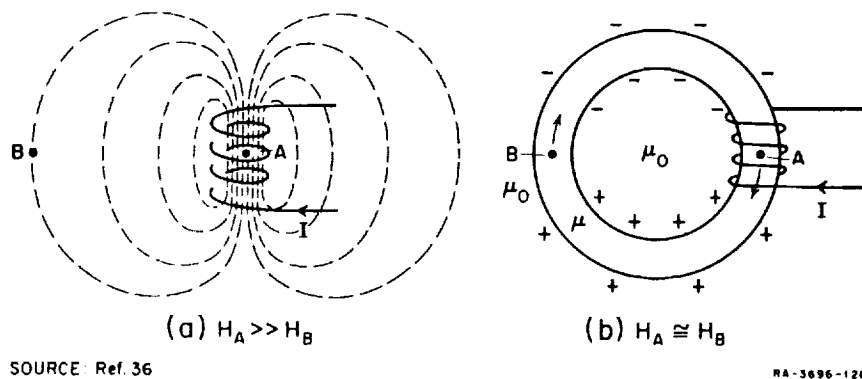


FIG. 127 EFFECT OF POLES ON  $H$  DISTRIBUTION

$H_A$  is about the same as  $H_B$ , or perhaps slightly larger. In other words, the presence of the ferromagnetic material tends to equalize  $H$  around the core by increasing  $H_B$  and decreasing  $H_A$ .

The physical explanation<sup>36</sup> for the effect of the ferromagnetic material is as follows. As  $I$  is applied,  $H_A \gg H_B$  as in Fig. 127(a), and as a result, Magnetization  $M$  at Point A switches more than Magnetization  $M$  at Point B. This results in a build-up of nonzero  $\nabla \cdot \bar{M}$ , or volume pole density, throughout the core material, but mainly near the core surface, resulting in surface pole density as shown in Fig. 127(b). These poles generate an  $H$  component of their own, which subtracts from  $H$  due to  $I$  at Point A and adds to  $H$  due to  $I$  at Point B, thus causing  $H_A \cong H_B$ .

## 2. CALCULATION OF FLUX LEAKAGE

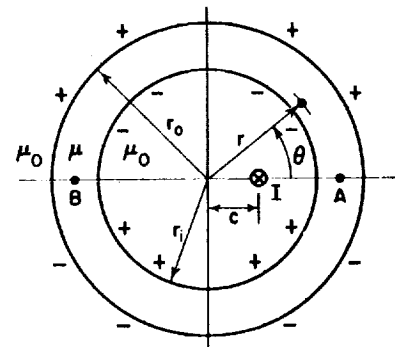
Calculation of flux leakage in a cylindrical core is performed in Ref. 36. In order to simplify the mathematics, the problem is reduced to two dimensions by assuming a very high cylinder, or tube. The calculations and the results are summarized as follows:

Consider a toroidal core driven by direct current  $I$ , Fig. 128, flowing in a conductor located at a distance  $c$  from the center of the core. The resultant field  $H$  due to  $I$  and the distributed poles may be expressed as a gradient of a magnetic scalar potential,  $V$ . In a static state,  $V$  satisfies Laplace's equation, which is written as follows in terms of the cylindrical coordinates  $r$  and  $\theta$ :

$$\nabla^2 V = \frac{\partial^2 V}{\partial r^2} + \frac{1}{r} \frac{\partial V}{\partial r} + \frac{1}{r^2} \frac{\partial^2 V}{\partial \theta^2} = 0 \quad (109)$$

The two components of  $H$  are

$$H_\theta = -\frac{1}{r} \frac{\partial V}{\partial \theta} \quad (110)$$



SOURCE: Ref. 36

NA-3698-127

FIG. 128 DIRECT CURRENT  $I$   
INSIDE A TUBE

and

$$H_r = -\frac{\partial V}{\partial r} \quad (111)$$

The magnetic scalar potential in mks units due to Current  $I$  alone inside the circle of radius  $c$  is

$$V_{ci} = -\sum_{n=1}^{\infty} \frac{I}{2\pi n} \frac{r^n}{c^n} \sin n\theta \quad (112)$$

and outside of the circle is

$$V_{co} = \frac{I\theta}{2\pi} + \sum_{n=1}^{\infty} \frac{I}{2\pi n} \frac{c^n}{r^n} \sin n\theta \quad (113)$$

Let the surface pole density  $\sigma$  on the outside surface be denoted by  $\sigma_{r_o}$  and on the inside surface be denoted by  $\sigma_{r_i}$ . Assuming that  $\sigma$  is symmetrical with respect to  $\theta = 0$ ,  $\sigma$  is expressed by an infinite Fourier series. Thus,  $V$  due to  $\sigma_{r_o}$ , for  $r < r_o$ , is

$$V_{r_o i} = \sum_{n=1}^{\infty} \frac{r^n}{2nr_o^{n-1}} \sigma_{r_o n} \sin n\theta \quad (114)$$

and for  $r > r_o$ ,

$$V_{r_o o} = \sum_{n=1}^{\infty} \frac{r_o^{n+1}}{2nr^n} \sigma_{r_o n} \sin n\theta \quad (115)$$

The expressions for  $V_{r_i i}$  and  $V_{r_i o}$  are similar, except that they are negative and  $r_i$  replaces  $r_o$ .

It is now assumed that the core material has a constant permeability. Satisfying the requirement for flux continuity at the boundary on the outside surface,

$$\mu_0 H_{r(r_o^+)} = \mu H_{r(r_o^-)} \quad (116)$$

where  $r_o^+$  refers to air and  $r_o^-$  to the core material. Note that Eq. (116)

is valid only for *linear* core material, which has constant  $\mu$  and no hysteresis. In Ref. 36 only the condition of constant  $\mu$  is stated; the condition for no hysteresis is implied later, when  $\phi$  is calculated to be proportional to Current  $I$ .

Following Eq. (111), Eq. (116) becomes

$$\mu_0 \frac{\partial}{\partial r} (V_{c_0} + V_{r_{i_0}} + V_{r_{o_0}}) \Big|_{\theta=r=r_0} = \mu \frac{\partial}{\partial r} (V_{c_0} + V_{r_{i_0}} + V_{r_{o_0}}) \Big|_{\theta=r=r_0} \quad (117)$$

An additional boundary condition, similar to Eq. (117), is written for  $r = r_i$ . Considering the  $n$ th term of the infinite series, two equations with two unknowns,  $\sigma_{r_{o_n}}$  and  $\sigma_{r_{i_n}}$ , are solved. The resulting expressions are substituted back into Eqs. (112) through (115) in order to calculate  $V = V_{c_0} + V_{r_{i_0}} + V_{r_{o_0}}$ , from which  $H_\theta$  and  $H_r$  inside the core [Eqs. (110) and (111)] are calculated. Substituting numerical values into the expressions for  $H_\theta$  and  $H_r$ , one can plot a map of  $H$  inside the core. Assuming that the core material is linear, the flux in the core is

$$\phi = - \int_{r_i}^{r_o} \mu H_\theta dr \quad (118)$$

Substituting the expression for  $H_\theta$  into Eq. (118), and assuming that  $\mu \gg \mu_0$ , it is found that

$$\phi = \frac{I}{2\pi} \left[ \mu \ln \frac{r_o}{r_i} - \mu_0 \ln \left( 1 + \frac{c^2}{r_i^2} - 2 \frac{c}{r_i} \cos \theta \right) \right] \quad (119)$$

With reference to Fig. 128,  $\theta_A = 0$  and  $\theta_B = \pi$ , hence

$$\frac{\phi_A}{\phi_B} = \frac{\mu \ln \frac{r_o}{r_i} - 2 \ln \left( 1 - \frac{c}{r_i} \right)}{\mu \ln \frac{r_o}{r_i} - 2 \ln \left( 1 + \frac{c}{r_i} \right)} \quad (120)$$

It is shown in Ref. 36 that as  $\mu \rightarrow \infty$ , the  $n$ th term of the external surface polarity,  $\sigma_{r_{o_n}}$ , approaches zero and the  $n$ th term of the internal

surface polarity,  $\sigma_{r_i n}$ , approaches a constant value which is independent of radius  $r_o$ . It is also shown that for  $r > r_i$  (inside the core material and outside of the core), as  $\mu \rightarrow \infty$ ,  $H_r \rightarrow 0$  and  $H_\theta \rightarrow I/2\pi r$ ; i.e., the core reacts as if the current conductor were at the center of the core. Thus, for  $r > r_i$  the material constitutes a perfect shield as far as  $H_r$  is concerned, but not as far as  $H_\theta$  is concerned. Note that, following Eq. (120), as  $\mu \rightarrow \infty$ ,  $\phi_A/\phi_B \rightarrow 1$ , but that the absolute value of the flux leakage will not tend to zero because the internal surface polarity  $\sigma_{r_i n}$  is not zero. It is concluded that for large  $\mu$ , the flux leakage is predominantly caused by internal surface polarity,  $\sigma_{r_i n}$ , as opposed to external surface polarity,  $\sigma_{r_o n}$ .

The same calculation procedure is repeated for the case where the current conductor is outside of the tube at a distance  $d$  from the center of the tube, as shown in Fig. 129. As expected, it is found that if  $\mu \rightarrow \infty$ ,  $\sigma_{r_i n} \rightarrow 0$  and  $\sigma_{r_o n} \rightarrow \text{constant}$ . Also, as  $\mu \rightarrow \infty$ ,  $H_\theta \rightarrow 0$  and  $H_r \rightarrow 0$  for  $r < r_o$  (inside the tube). It is concluded that perfect magnetic screening can be achieved if the current is outside of a tubular shield (but not if the current is inside such a shield). It is found that for  $\mu \rightarrow \infty$

$$\frac{\phi_A}{\phi_B} = \frac{\ln \left( 1 - \frac{r_o}{d} \right)}{\ln \left( 1 + \frac{r_o}{d} \right)} \quad (121)$$

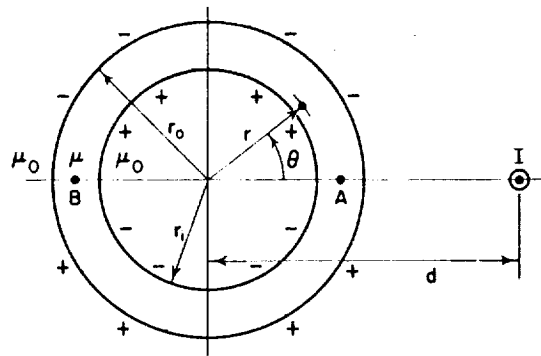
Note that although  $H \rightarrow 0$ ,  $\phi \neq 0$  since  $\mu \rightarrow \infty$ .

The two previous cases are combined as shown in Fig. 130, and

$$\frac{\phi_A}{\phi_B} = \frac{\mu \ln \frac{r_o}{r_i} - 2 \ln \left( 1 - \frac{c}{r_i} \right) - 2 \ln \left( 1 - \frac{r_o}{d} \right)}{\mu \ln \frac{r_o}{r_i} - 2 \ln \left( 1 + \frac{c}{r_i} \right) - 2 \ln \left( 1 + \frac{r_o}{d} \right)} \quad (122)$$

A plot of percentage flux leakage versus  $c/r_i (= r_o/d)$ , assuming that  $r_o/r_i = 3/2$ , is shown in Fig. 131. Experimental verification shows good agreement with the calculated flux leakage.

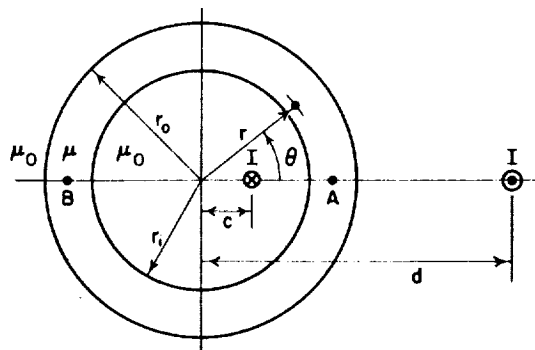




SOURCE: Ref. 36

RA-3698-128

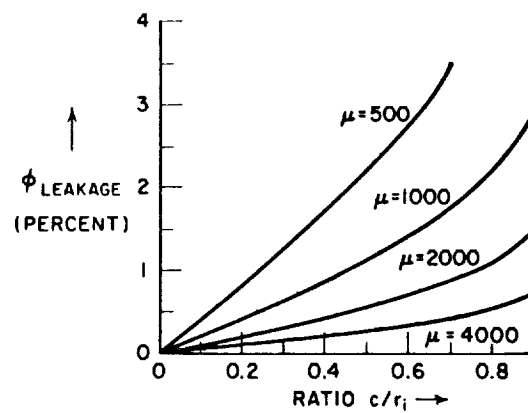
FIG. 129 DIRECT CURRENT I OUTSIDE A TUBE



SOURCE: Ref. 36

RA-3698-129

FIG. 130 DIRECT CURRENT I INSIDE AND OUTSIDE A TUBE



SOURCE: Ref. 36

RA-3698-130

FIG. 131 CALCULATED LEAKAGE FLUX

### 3. ANALYSIS OF FLUX PATTERN IN A MULTIPATH CORE

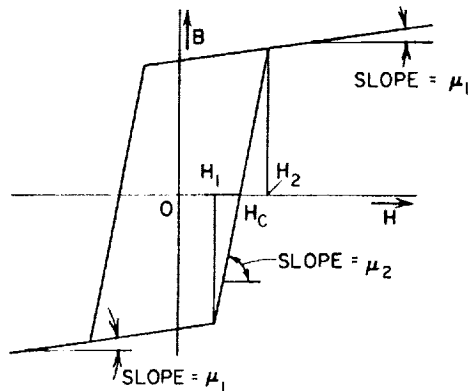
Analytical calculations of static flux pattern in a multipath core can be found on pp. 6-42 and 252-299 of Ref. 11. This piece of work is essentially a direct copy of Ref. 54. A summary of the basic assumptions and the most important results of this analysis may be found in Ref. 55 (the summary includes very little about the method of attack and the procedure of the analysis). The problem is reduced to two dimensions by assuming a tubular core.

The first part of the analysis deals with a toroidal core driven by a straight conductor, carrying direct current, which is located inside or outside the core. This part is essentially identical with the material in Ref. 36. There is, however, one important difference between the assumptions made in Ref. 54 and those made in Ref. 36.

Let  $\mu$  be the differential permeability, i.e., the slope of the static  $B$ - $H$  loop. It is assumed in Ref. 36 that the core material is linear, i.e.,  $B = \mu H$ , where  $\mu$  is constant. Under this assumption,  $\nabla \cdot \bar{B} = \mu \nabla \cdot \bar{H}$ , hence it is valid to replace Maxwell's equation  $\nabla \cdot \bar{B} = 0$  across a boundary of

Materials 1 and 2 by  $\mu_1 H_1 = \mu_2 H_2$ .

In Ref. 54 this boundary condition is applied to a *nonlinear* ferrite material whose idealized  $B$ - $H$  loop is shown in Fig. 132.



SOURCE: Ref. 54

RA-3696-131

FIG. 132 ASSUMED  $B$  vs.  $H$

It is shown in Ref. 54 that Laplace's equation,  $\nabla^2 V = 0$ , is applicable to linear material, but for nonlinear material, Poisson's equation,  $\nabla^2 V = \nabla \cdot \bar{M}$ , must be used. (Note that for nonlinear material in a region where  $B(H)$  is linear,  $\nabla \cdot \bar{M} = 0$ ; hence Laplace's equation is still

satisfied.) The physical difference between the two cases is that when  $\nabla \cdot \bar{M} = 0$ , poles are distributed only on the surface, whereas when  $\nabla \cdot \bar{M} \neq 0$ , poles are distributed both on the surface and throughout the volume. In order to be able to use Laplace's equation instead of Poisson's equation, the idealized  $B$ - $H$  loop of Fig. 132 is assumed. The author also assumes that  $H_1 \approx H_2 \approx H_c$ ; as a result of this assumption, the region of

high  $\mu$ , Region II in Fig. 24, degenerates to a thin band. There are, therefore, three regions, each with constant  $\mu$ : air with  $\mu = \mu_0$ ; saturated region with  $\mu = \mu_1$ , and a thin high- $\mu$  region with  $\mu = \mu_2$ . It is assumed that  $\mu_0 \ll \mu_1 \ll \mu_2$ . It appears as though an assumption is made in Ref. 54 that these conditions are sufficient to validate the use of the boundary condition  $\mu_1 H_1 = \mu_2 H_2$ . This basic assumption is erroneous despite the hypothesis of constant values of  $\mu$  because the straight line  $B$  versus  $H$  does not pass through the origin (i.e.,  $B \neq \mu H$ ).

Bearing in mind that the derivations in Ref. 54 are valid only for linear materials, let us briefly describe the analysis procedure. Skipping the part that can be found in Ref. 36 (for which, incidentally, no credit is given in Ref. 54), Laplace's equation is solved for a multipath core of constant  $\mu$ , driven by a direct current in a straight conductor that passes through the minor aperture, Fig. 133.

In the next step, a thin band of high  $\mu$  is added. For partial setting of Leg 4, experimental measurements of switched flux indicate that the shape of the high- $\mu$  band and the pole distribution are as shown in Fig. 134. A cut-and-try method is assumed in Ref. 54 for the shape of the high- $\mu$  band. Since no amenable function is found to describe this shape, a circle is assumed. The circle is assumed to be concentric with the core first

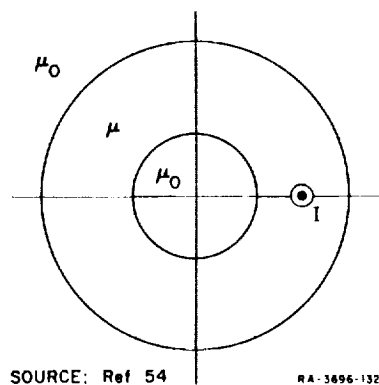


FIG. 133 A MULTIPATH CORE OF CONSTANT  $\mu$  DRIVEN BY DIRECT CURRENT

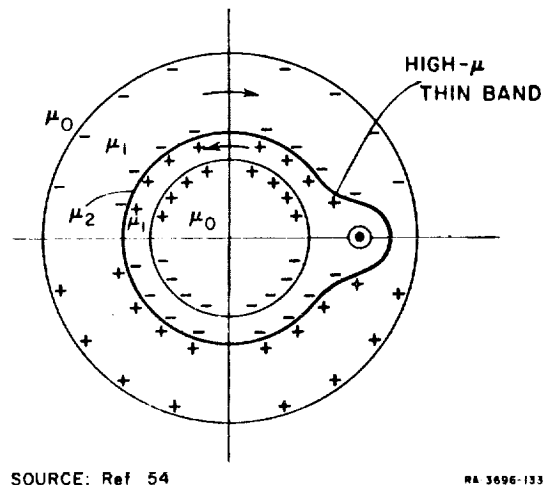


FIG. 134 HIGH- $\mu$  THIN BAND AND POLE DISTRIBUTION

and then eccentric. In the latter case a conformal mapping is used in order to simplify the calculations.

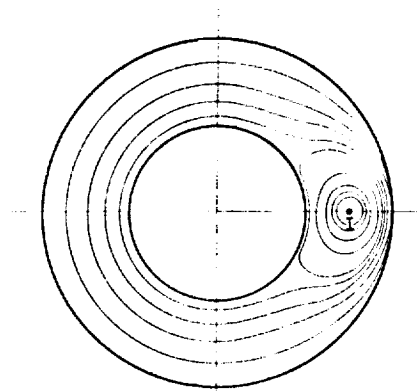
Numerical calculations for the magnetic field are performed on an IBM 650 computer for the above three cases. The resulting plots, as presented in Ref. 54, are shown in Fig. 135. The fact that the final plot resembles a "kidney shape" justifies the effort put into this work in the sense that the *mechanism* of producing a "kidney shape" is demonstrated. This mechanism is perhaps similar for nonlinear materials. However, it should be borne in mind that the derivations and the resulting "kidney-shaped" field plot in Ref. 54 have been shown to be valid only for the case where each  $B(H)$  characteristic is a straight line passing through the origin.

#### D. CONCLUSIONS

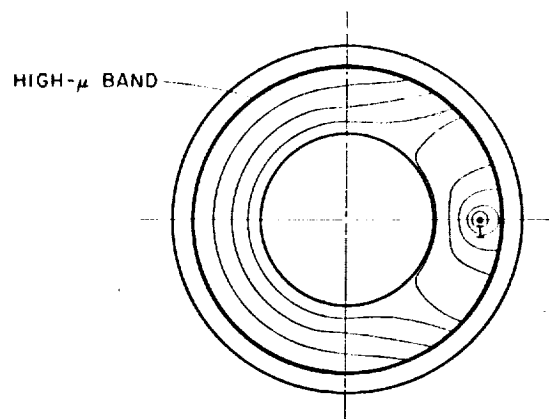
Three models for describing the flux pattern in a multipath core are discussed in this section. These models are presented in the order of increasing detail as well as increasing complexity.

From a practical point of view, the arrow model is completely adequate. In fact, due to its simplicity, this model should be used in engineering problems. On the other hand, from an academic point of view, physical models that describe the flux pattern in greater detail are needed. The zone-boundary model is an extension of the domain-wall concept in crystalline materials to a polycrystalline ferrite. The justification for such a model may, perhaps, lie in the fact that domain walls have been observed in polycrystalline grain-oriented silicon iron.<sup>51</sup> The zone-boundary model may be verified experimentally by indirect methods, but only a limited number of such experiments have been done so far. A further investigation is needed.

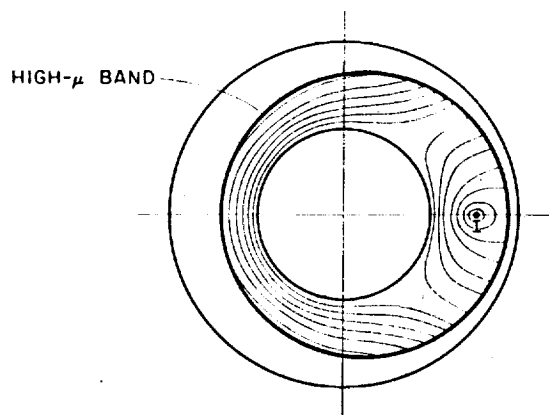
An attempt to determine the flux pattern of a multipath core by analytical calculation can be found in Ref. 54 (which later is copied into Ref. 11). We have criticized this work not because the nonlinearity of the ferrite core should have been included, but rather because claims are made that the analysis is applicable to a nonlinear material whose  $B(H)$  is a straight line not passing through the origin. We conclude that this analytical procedure is not practical for general determination of flux patterns in ferrite multipath cores for the following reasons:



(a) CONSTANT  $\mu$  THROUGHOUT THE TUBE



(b) HIGH- $\mu$  BAND CONCENTRIC WITH TUBE



(c) HIGH- $\mu$  BAND ECCENTRIC WITH TUBE

SOURCE Ref 54

RB-3696 (3)

FIG. 135 COMPUTED MAGNETIC FIELD IN A TUBE

- (1) The analysis is valid only for linear materials.
- (2) The procedure of this analysis is too complex for three dimensional problems.
- (3) The shape of high- $\mu$  region is assumed, rather than solved for. The resulting kidney-shaped flux pattern is not a proof for the validity of the assumed shape of the high- $\mu$  region; there may be other shapes of high- $\mu$  regions that result in a kidney-shaped flux pattern.

## V LITERATURE SURVEY

A number of literature sources have been referred to so far in connection with flux switching in multipath cores. In the majority of these references, additional topics are discussed, *e.g.*, a general theory on flux switching or the application of multipath cores in logic circuitry. In addition, there are other literature sources that deal with multipath cores which are not referred to in the Secs. I through IV of this report; these are included in the bibliography list.

The objective of this section is to provide the reader with some information about these literature sources. We shall organize the material as follows. The references quoted in this report are listed first, and, in most cases, brief annotations are added after each reference. The same procedure is then repeated for the bibliography list. In the third part of this section, all sources are classified according to topic and according to alphabetical order of authors' names.

### A. REFERENCES

1. J. A. Rajchman and A. W. Lo, "The Transfluxor--A Magnetic Gate with Stored Variable Setting," *RCA Rev.* **16**, pp. 303-311 (June 1955).

This is the first published paper found on a multipath core (Transfluxor). Partial setting, priming, and read-out driving are explained qualitatively. Experimental data of the  $B$ - $H$  loops around the output aperture are presented for different amounts of set flux.

2. U. F. Gianola, "Integrated Magnetic Circuits for Synchronous Sequential Logic Machines," *Bell Syst. Tech J.* **39**, pp. 295-332 (March 1960).

The leg model and its restrictions are discussed [*cf.* pp. 1-3].\* The mirror notation is used to portray windings on each leg of a complete shift-register circuit. Most of the paper deals with resistance-type shift registers [*cf.* pp. 64-67] and logic circuits. The material is well organized and written in a clear and simple manner.

\* Page numbers in brackets refer to this report, not to the sources themselves.

3. D. Nitzan, "Analysis of MAD-R Shift Register and Driver," pp. 113-133, Proc. Special Tech. Conf. on Nonlinear Magnetics and Magnetic Amplifiers, Philadelphia, Pa., October 26-28, 1960, Published by AIEE, New York, N.Y., (1960).

Electrical-circuit analogues [cf. pp. 31-35] are used to analyze a resistance-type shift register, and computation procedure is outlined [cf. pp. 35-36]. The priming phase of operation is analyzed and verified experimentally.

4. D. C. Engelbart, "High Speed Components for Digital Computers," Quarterly Rept. 2, Contract AF 33(616)-5804 Stanford Research Institute, Menlo Park, California (Feb. 1959).

The basic operation of nonresistance flux transfer using multipath cores is explained physically. An equivalent scheme, using only toroidal cores, is synthesized and its operation is described for positive and negative flux transfers.

5. D. C. Engelbart, "A New All-Magnetic Logic System Using Simple Cores," pp. 66-67 Digest of Tech Papers, 1959 Solid-State Circuits Conf., Phil., Pa., (Feb. 12-13, 1959).

The toroidal equivalence of multipath cores is used to synthesize all-magnetic circuits by means of toroidal cores instead of multipath cores.

6. G. D. Kozlov, "Effect of Magnetization Irregularity on the Static Characteristics of Cores. II" (Moscow) Translated from *Avtomatika i Telemekhanika*, 21, 7, pp. 1057-1072 (July 1960):

This is the only Russian reference on multipath cores that we have been able to reach. In the first part of the paper, calculations of the static  $\phi$ - $F$  loop of a toroid from an earlier paper, Ref. 16, are repeated, except for the addition of a constant slope to the  $B$ - $H$  loop in saturation. An erroneous toroidal model is assumed for a multipath core [cf. pp. 3-4], and wrong conclusions are drawn with regards to spurious flux setting into the output leg [cf. pp. 44-45].



7. A. Brain, "The Simulation of Neural Elements by Electrical Networks Based on Multiaperture Magnetic Cores," *Proc. IRE* **49**, 1, pp. 49-52 (January 1961).

An erroneous toroidal model, similar to the one in Ref. 6, is assumed [cf. pp. 3-4], and wrong statements are made with regards to the effect of HOLD MMF on the location of flux switching and the effect of DRIVE MMF on the flux pattern [cf. pp. 118-119]. Most of the paper deals with the application of a multiaperture core in neuron simulation.

8. N. Menyuk and J. B. Goodenough, "Magnetic Materials for Digital Computers—I. A Theory of Flux Reversal in Polycrystalline Ferromagnetics," *J. Appl. Phys.* **6**, pp. 8-18 (January 1955).

This paper is an important contribution to the theory of flux switching in ferrites.

9. D. R. Bennion, "Research on Multiaperture Magnetic Logic Devices," Tech. Rept. 1, Contract Nonr. 2712(00) Stanford Research Institute, Menlo Park, California (May 1960).

Methods for describing the properties of material, cores, and circuits are presented. Static  $\phi$ - $F$  loops are calculated for a general leg shape [cf. p. 39], and mathematical flux-switching models are developed, assuming planar and cylindrical domain walls. Logic devices for OR-NOR functions and Positive and Negative transfers are developed.

10. V. W. Hesterman, "Evaluation of Flux-Switching Models for Magnetic Devices," pp. 265-292 Special Technical Conference on Nonlinear Magnetics, Los Angeles (November 1961).

An extensive study is made in order to evaluate different switching models that have appeared in the literature. These models are brought into common terminology and then compared with measured data [cf. p. 27].

11. "Final Report on the Development and Use of Multiaperture Core Flux Logic Devices to Perform Logical Functions in Digital Data Processing," Vols. I and II, Contract AF 33(600)-31315, IBM Corp. Federal Systems Div., Owego, N.Y. (Dec. 1959).

This is a final report by IBM on the use of multipath cores as logic devices. Volume I describes mainly hardware and circuitry. Volume II, referred to as Appendixes A and B for Volume I, can stand by itself. Appendix A, "Magnetic Logical Element and Circuit Study Program," includes 316 pages of important but poorly organized material, written by the following fourteen members of the IBM staff in Poughkeepsie, N.Y.: S. A. Abbas, E. W. Bauer, J. M. Berger, E. J. Breitenbach, E. F. Brosseau, S. A. Butler, D. L. Critchlow, M. E. Kane, R. T. Kikoshima, G. J. Lasher, J. Petersen, V. Skwiercz, R. Turnbull, and R. L. Ward. Perhaps because of the large number of authors, the material lacks continuity and varies considerably in depth. Most of an earlier report by Abbas (Ref. 54) on work supported by IBM appears in this report with essentially no change. The validity of Abbas's application of his analysis to problems involving nonlinear ferrite material [cf. pp. 134-137] should have been better checked. In addition, the mathematical manipulations given in the appendixes of Appendix A are unduly detailed and contain a number of misprints.

Appendix B, "Ferrite Toroid Core Circuit Analysis," covers only 28 pages written by IBM Advance Systems Research group in Owego, N.Y. No mention is made of multipath cores in this Appendix.

Despite all these drawbacks, Vol. II of Ref. 11 includes a large amount of pertinent information on flux switching in multipath cores. This is evident from the large number of times we have referred to Ref. 11 in this report. Had it been better edited, it could have been the most useful single source available on flux switching in multipath cores.

12. R. W. McKay, "The Reversible Component of Magnetization," *J. Appl. Phys.*, Supplement to vol. 30.4, pp. 56S-57S (April 1959).

Experimental data on elastic-flux switching between negative and positive saturation are presented [cf. p. 21].

13. E. P. Stabler, "Square-Loop Magnetic Logic Circuits," pp. 47-53 *Proc. Western Joint Computer Conference*, San Francisco, Calif. (March 3-5, 1959).

An electrical-circuit analogue for a leg or a toroid is introduced [cf. p. 32]. The largest portion of the paper deals with logic circuits described by graphical diagrams.

14. M. K. Haynes, L. A. Russell, J. J. Coughlin, W. A. Crapo, J. A. Kauffmann, N. F. Lockhart, R. F. Rutz, R. M. Tomasulo, and J. N. Cole, "Improvement Program for Magnetic Logical Circuits, Physical Research Effort," Terminal Rept. IBM Corp. Res. Lab., Poughkeepsie, N.Y. KMPD P.O. No. AL7715D, (May 24, 1956).

Only a small portion of this 231-page report deals directly with flux switching in multipath core. This portion includes experimental data on supersetting effect [cf. p. 94], loading effect [cf. p. 84] and flux steering into Leg 3 or Leg 4, depending on the polarity of a steering MMF drive on Leg 4. Machine computation of an all-magnetic shift register, using toroidal cores, is described in great detail, and computed flux-gain curves are compared with experimental curves. A large portion of Ref. 14 is devoted to realization of logic functions by multipath cores.

15. H. D. Crane, "Multi-Aperture Magnetic Devices for Computer Systems," Special Rept. to Burroughs Corp. (Paoli, Pa.), Stanford Research Institute, Menlo Park, Calif. (February 1957).

A possibility is mentioned for stacking punched metallic foils in order to make a multipath core. Several ways are shown for overcoming flux division to the output leg [cf. p. 84].

16. G. D. Kozlov, "The Effect of Nonuniformity of Magnetization on the Static Characteristics of Cores, I," (Moscow) Translated from *Avtomatika i Telemekhanika*, **21**, 1, pp. 119-134 (January 1960).

Static  $\phi$ - $F$  loops for a toroid are calculated [cf. pp. 37-39] for complete switching (without and with bias MMF) and for partial switching around the origin.

17. H. D. Crane and D. R. Bennion, "Design and Analysis of MAD Transfer Circuitry," pp. 21-36 Proc. Western Joint Computer Conference, San Francisco, Calif. (March 3-5, 1959).

A nonresistance scheme employing multipath cores is discussed in detail [cf. pp. 61-63], especially the required flux gain characteristics [cf. pp. 67-70]. Various circuit modifications are proposed in order to improve the range of operation. Basic flux switching in a toroid is discussed, and calculated curves of  $\phi(t)$  are compared with experimental curves [cf. p. 42]. Effect of pulse width on  $\phi$ - $F$  curve is demonstrated

by experimental curves [cf. pp. 46-47], including soft threshold due to preset drive [cf. pp. 48-50]. A method to obtain flux gain (not mentioned in our report) is introduced and denoted by " $\phi^*$  mechanism." In this scheme, when ADVANCE current is applied to a transmitter in a SET state,  $\Delta\phi_T$  is larger by the amount of flux  $\Delta\phi^*$  that switches around the major aperture because of soft threshold. In this way a higher flux gain may be achieved.

18. U. F. Gianola, "Switching in Rectangular Loop Ferrites Containing Air Gaps," *J. Appl. Phys.* **29**, pp. 1122-1124 (July 1958).

The effect of an air gap on flux switching in a toroid is analyzed [cf. p. 52], and it is shown that the resulting  $\phi$  is of the form  $C_1 e^{-C_2 t} - C_0$ . No mention is made of the fact that a similar waveform may result from a nonrectangular  $R$ - $H$  loop or a relatively high ratio of outside to inside diameter. Hence, when the oscillograms of  $\phi$  in Ref. 18 are analyzed, these material and geometrical factors should be considered as well.

19. J. A. Rajchman and A. W. Lo, "The Transfluxor," *Proc. IRE* **44**, pp. 321-332 (March 1956).

The first portion is spent on repeating the material of Ref. 1. The new material includes experimental data on setting characteristics [cf. pp. 55-59] that are explained qualitatively, but no analysis is carried out. The data on the setting characteristics are then redrawn as driving characteristics by plotting  $\Delta\phi_o$  versus  $F_d$  with  $F_s$  as a parameter. The driving characteristics resemble the characteristics of a pentode tube for  $F_s$  varying from zero to the value corresponding to full setting of Leg 3. The curves shown in Ref. 19 are limited to this region of  $F_s$ , but this is not the complete picture. As  $F_s$  is increased further,  $\Delta\phi_o$  starts to drop and the driving characteristics are inferior to the ones shown.

20. I. H. Rowe and G. R. Slemon, "On the Process of Flux Reversal in Multiaperture Ferrite Cores," *Communication and Electronics* **56**, pp. 431-438, (September 1961).

Experimental setting characteristics under various drives are presented as a verification for a proposed flux-pattern model (what we call

"zone pattern") in an unshaped multipath core [cf. pp. 126-128]. It seems that simpler experiments should be carried out first in order to establish this model.

21. D. R. Bennion, H. D. Crane, and D. C. Engelbart, "A Bibliographical Sketch of All-Magnetic Logic Schemes," IRE Trans. of the Professional Group on Electronic Computers, Vol. *PGEC-10*, 2, pp. 203-207 (June 1961).

The difference between resistance and nonresistance all-magnetic schemes is clarified. Two bibliographies, one on resistance schemes and the other on nonresistance schemes, are listed, and short annotations are added.

22. D. I. Gordon, "Magnetic Cores and Permanent Magnets in Hyper-Environments," pp. 205-228, 1960 Proceedings of the Institute of Environmental Sciences National Meeting, Los Angeles, (April 6,7,8, 1960), (Inst. Environmental Sciences, Mt. Prospect, Ill.)

The paper includes a large amount of experimental data on the effect of radiation on the switching characteristics of different ferromagnetic materials during and after radiation. As an example, it is shown that ferrites are much less influenced by radiation than the 50% Fe, 50% Ni alloy which is so commonly used in magnetic amplifiers.

23. J. L. Haynes, "Logic Circuits Using Square-Loop Magnetic Devices: A Survey," IRE Trans. of the Professional Group on Electronic Computers, Vol. *PGEC-10*, 2, pp. 191-203 (June 1961).

The literature on magnetic devices in logic circuits is classified and condensed into a twelve-page paper.

24. H. D. Crane, "A High-Speed Logic System Using Magnetic Elements and Connecting Wire Only," *Proc. IRE* **47**, pp. 63-73 (January 1959). See also Proc. Tech. Conf. on Nonlinear Magnetics and Magnetic Amplifiers, Los Angeles, Calif., pp. 465-482 (August 1958).

This is an earlier paper which describes the nonresistance scheme that is treated later in more detail in Ref. 17.

25. N. S. Prywes, "Diodeless Magnetic Shift Registers Utilizing Transfluxors," IRE Trans. of the Professional Group on Electronic Computers, Vol. *PGEC-7*, pp. 316-324 (December 1958).

This is an independent paper that describes basically the same non-resistance scheme as Ref. 17, using the arrow model rather generously. The paper includes schemes for continuous-structure shift register.

26. H. D. Crane and E. K. Van De Riet, "Design of an All-Magnetic Computing System, Part I--Circuit Design," IRE Trans. of the Professional Group on Electronic Computers, Vol. *PGEC-10*, 2, pp. 207-220 (June 1961).

A detailed description is presented of the construction of an all-magnetic arithmetic unit that adds, subtracts, and multiplies. The machine, designed and built at Stanford Research Institute, employs a nonresistance type of all-magnetic logic.

27. G. R. Briggs and A. W. Lo, U.S. Patent No. 2,968,795; January 17, 1961 (filed May 1, 1957).

This patent covers a resistance-type shift register using Transfluxor cores.

28. L. S. Onyshkevych, "Analysis of Circuits with Multiple-Hole Magnetic Circuits," Technical Report 329, MIT Research Laboratory of Electronics, Cambridge, Mass. (July 9, 1957).

A large amount of material is condensed into a relatively short paper, written in a simple manner. The paper covers the flux-division phenomenon [cf. pp. 80-81], touches on the subject of flux closure [cf. p. 118] and reports on the "Near Leg Effect," which is merely elastic switching via an outer leg. Unfortunately the interpretations for these three phenomena are doubtful. The author then introduces a complex symbolic diagram for multipath cores and the associated windings. Perhaps the most significant contribution of the paper is the development of a resistance-type shift register. The circuit is analyzed, using an equivalent circuit in which  $\bar{\rho}$  of the core is included.

29. H. P. Zeiger, "Diodeless Magnetic-Core Logic Circuits," M.S. Thesis, Massachusetts Institute of Technology, Cambridge, Mass. (June 1960).

The first part deals with logic realization by means of toroidal cores. The second part deals with switching in multipath cores, their use in resistance-type shift registers, and the capabilities of multipath cores as logic elements. The use of a Laddic to perform logic functions is treated and an example is given.

30. D. R. Bennion, "A Note on Magnetic Shift Registers," IRE Trans. of the Professional Group on Electronic Computers, Vol. *PGEC-9*, p. 262 (June 1960).

This is a letter to the editor in which an error in Ref. 2 is pointed out. In addition, it is shown that the turns ratio  $N_T/N_R = 2$  in the resistance-type shift register [Fig. 63] is mathematically an optimum value.

31. D. R. Bennion, "MAD Resistance-Type Magnetic Shift Registers," pp. 96-112 Proc. Special Tech. Conf. on Nonlinear Magnetics and Magnetic Amplifiers, Philadelphia, Pa., Oct. 26-28, 1960, published by AIEE, New York, N.Y. (1960).

A detailed explanation for the resistance scheme is presented [cf. pp. 64-67] and compared with the nonresistance scheme [cf. pp. 72-73]. Simplified analysis is developed in order to predict the range of bistable operation. Unfortunately, the symbols chosen to represent multipath cores are not easily followed.

32. U. F. Gianola and T. H. Crowley, "The Laddic, a Magnetic Device for Performing Logic," *Bell Syst. Tech. J.* **38**, pp. 45-72 (January 1959).

The Laddic is introduced and experimental data on flux division are presented [cf. pp. 75-76]. Most of the paper deals with realization of logic functions by means of a Laddic.

33. U. F. Gianola, "Lesser-Known Properties of Ferrite Multi-Apertured Cores," pp. 111-115 Proc. of the 1960 Electronic Components Conference, Washington, D.C. (May 1960).

Four switching phenomena are discussed. First, the initial sharp spike in a  $\phi$  waveshape due to a step  $I$  is explained. The phenomenon is well known, and the explanation adds little to our understanding of it.

Second, slightly different ac  $B$ - $H$  loops are recorded by driving a three-rung Laddic on an outer rung from those recorded by driving on the central rung. In explaining the difference between the two  $B$ - $H$  loops it is stated that the Laddic behaves as a toroid when driven on the outer rung and as a two-leg core [cf. Fig. 95(a)] when driven on the central rung. This explanation is incomplete. The main difference stems from a deeper swing into saturation of the central leg when the drive is applied on this leg (the  $F$ 's of the side legs are essentially clamped to their soft threshold value). The third effect is the flux division [cf. pp. 75-80], and the fourth effect is the "walk-down effect," or what we call "unsettling effect" [cf. pp. 96-99].

34. J. A. Rajchman, "Principles of Transfluxor and Core Circuits," RCA Labs. Div., Princeton, N.J., RCA Industry Service Lab. Bull. RB-120 (September 10, 1957).

The paper covers material that appears also in more widely available publications. Included are the following subjects: the ferrite memory plate; the use of the Transfluxor in a memory array and in a coded channel selector; a current-steering technique; a magnetic shift register using internal flux transfer and assuming that flux switches in the shortest path [cf. p. 82]; and the setting of a Transfluxor by short pulses.

35. S. Duinker and B. van Ommen, "The Scansor, A New Multi-Aperture Rectangular-Loop Ferrite Device," *Solid-State Electronics*, Vol. 1, pp. 176-182 (Pergamon Press, London, 1960).

This is one of the few articles on multipath cores from Europe. A multihole structure is driven by a ramp MMF in order to generate voltage pulses that are displaced in time [cf. Fig. 80].

36. P. Hammond, M. A. Associate Member, "Leakage Flux and Surface Polarity in Iron Ring Stampings," *Proc. IEE (London)*, Vol. 102, Part C, pp. 138-147, (January 1955).

Flux leakage in an iron core is calculated by solving Laplace's equations in two dimensions, assuming that the material is linear and that the height of the core is very large [cf. pp. 128-133]. The paper is very well written.



37. E. K. Van De Riet, "Stress Effects in Multipath Cores," Magnetics Seminar, Stanford Research Institute, Menlo Park, California (February 1961).

38. H. D. Crane, D. R. Bennion, and F. C. Heinzman, "Multi-Aperture Core Element Design For Magnetic Circuits," U.S. Patent No. 2,958,854, Nov. 1, 1960 (filed Nov. 25, 1957).

This patent covers various ways of shaping a multipath core [cf. p. 102].

39. H. W. Abbott and J. J. Suran, "Temperature Characteristics of the Transfluxor," IRE Trans. of the Professional Group on Electron Devices, Vol. PGED-4, pp. 113-119 (April 1957).

This paper may be very misleading. It describes the operation of a Transfluxor, using a core with  $w_m/(w_3 + w_4) = 7/5$  [cf. p. 102]. An erroneous statement is made with regard to the range of operation of the SET current. Vertical (instead of diagonal)  $\phi$ - $F$  loops are drawn for a path around Legs  $m$  and 3 and a path around Legs  $m$  and 4, and the region  $d_{m3} \leq F_s \leq d_{m4}$  is stated to be the range of operation for  $F_s$ , based on prevention of flux division into Leg 4. Any one of the first three methods in Fig. 81 would minimize this problem (such a possibility is realized by the same authors in a later paper, Ref. 40). Note that had the correct diagonal  $\phi$ - $F$  loop been assumed, the claimed range of operation might shrink to nothing. Distorted oscillograms of 60-cycle  $B$ - $H$  loops are shown (the authors do not bother to minimize phase shift in the resulting Lissajous figures) in connection with ac characteristics which are plotted in terms of output voltage versus SET current. The effect of temperature on the ac characteristics is determined experimentally; the explanation for the results is incomplete.

40. H. W. Abbott and J. J. Suran, "Multihole Ferrite Core Configurations and Applications," *Proc. IRE* 45, pp. 1081-1093 (August 1957).

The authors first repeat the material, including the errors, of their previous paper, Ref. 39. A useful arrangement is then shown for a digital-to-analogue converter in which the weighting of the significant figures is obtained by multiplying the sense turns of the read-out windings that are connected in series on the digit cores. Read-out problems are caused

by variation in temperature, spurious setting or clearing, and unsquareness of the hysteresis loop. In order to improve the range of operation, a four-hole multipath core is introduced and the SET MMF is applied on the outside legs of two of the apertures. This modification will certainly increase the range, but simpler methods [such as are shown in Fig. 81] would do a better job. A useful scheme for a voltage read-out is shown where the drive winding threads an additional small toroid. A comparison between voltage drive and current drive for read-out purposes shows that a higher ratio of signal to noise is obtained with voltage drive over a temperature range of  $-40^{\circ}\text{C}$  to  $100^{\circ}\text{C}$ . A further increase in this ratio is obtained by linking the output winding with another leg. The last portion of the paper deals with application of multipath cores to logic circuits. Schemes are shown for realizing OR and EXCLUSIVE-OR functions, an odd-parity checker and a half-adder, each by a single multipath core. No range maps are provided.

41. D. R. Bennion, "A New Multiaperture Magnetic Logic Element," *J. Appl. Phys.* Supplement to Vol. 31, pp. 129S-130S (May 1960).

A positive-transfer element and a negative-transfer element, both of the nonresistance type, are combined into a single multipath core. Problems due to soft threshold, partial switching instead of full switching, and poor clipping are partially solved by proper core shaping [cf p. 108].

42. P. F. Davis, "An Electrical Analogue of Magnetic Domains," *British Journal of Applied Physics*, Vol. 8, pp. 19-20 (January 1957).

Mapping a magnetic field around sharp corners is done by a square-mesh network of resistance wires composed of different gauges of wire.

43. David S. Robertson, and David Elliott, "Magnetic Losses in Cores of Various Shapes," *Nuclear Instruments and Methods*, Vol. 5 pp. 133-141 (North-Holland Publishing Co., Amsterdam, 1959).

44. N. F. Lockhart, "Logic by Ordered Flux Changes in Multipath Ferrite Cores," 1958 IRE National Convention Record, Part 4, pp. 268-278 (1958).

A multipath core that looks like a Laddic, except that the windows are narrower, is used to realize logic functions. The device is based on the optimistic assumption that flux switches only in the shortest available path. For proper operation, the following requirements should be fulfilled: large enough input pulses (true for any magnetic circuits); simultaneous input pulse (to prevent switching in the wrong leg); rectifiers in the output line (to prevent loading); read-out during CLEAR time (since extreme legs are late to switch during SET time); and distribution of the CLEAR winding along the core (to achieve simultaneous switching in all legs, a condition required for logic functions realized by sensing more than one leg in series--such as EXCLUSIVE OR). The main drawback of this circuit is the fact that a portion of the flux switches in a remote leg, especially when the input pulses are high in magnitude.

45. W. L. Morgan, "Transfluxor Design Considerations," IRE Trans. of the Professional Group on Elec. Devices, Vol. *PGED* **10**, 1, pp. 155-162 (1961).

Considering the amount of information included, the whole paper could have been condensed to two or three pages. This paper might be a good starting point for beginners in the field. Although the author does not state it, his assumptions are valid for slow switching only. The author describes the CLEAR, SET, PRIME, and DRIVE operations and calculates the relation  $\Delta\phi = 2hB_s[(NI/2\pi H_c) - r_i]$ , which is nothing more than the static  $\phi$ - $F$  loop of a toroid [Fig. 9] assuming rectangular  $B$ - $H$  loop, [Fig. 4(b)iv] and a ring model, [Eq. (54)]. The paper terminates with a list of design tips, some of which are superfluous, and with a numerical design example.

46. K. V. Mina and E. E. Newhall, "A Straightforward Way of Generating All Boolean Functions of  $N$  Variables Using a Single Magnetic Circuit," IRE Trans. of the Professional Group on Electronic Computers, Vol. *PGEC*-**10**, 2, pp. 151-156 (June 1961).

Two methods are shown for operating a multipath core as a relay contact by controlling flux switching. The first method utilizes a single aperture and a HOLD MMF on one of the two legs in order to prevent flux from switching. In the second method, flux switching is prevented by utilizing two small apertures and a HOLD MMF on the leg between the two

apertures. The authors point out that the first method is inferior because if many such gates are in parallel, the over-all elastic  $\phi$  may generate a current high enough to switch an unheld leg spuriously. The second version may be looked at as two gates of the first version connected in series.

47. L. P. Hunter and E. W. Bauer, "High Speed Coincident Flux Storage Principles," *J. Appl. Phys.* **27**, pp. 1257-1261 (November 1956).

The speed limitation in a toroidal memory core due to half-select is overcome by using a three-hole core.

48. W. W. Lawrence, Jr., "Recent Developments in Very-High-Speed Magnetic Storage Techniques," Proc. Eastern Joint Computer Conference, pp. 101-103 (December 1956)

High speed and low half-select noise can be obtained by biasing a toroidal memory core, but upon removal of the WRITE current, the core is cleared to the bias point and the information is erased. The use of a multipath core instead of a toroid overcomes this drawback and the information is retained. A figure-eight BIAS MMF on an input aperture of a three-aperture core switches the output minor aperture to a ONE or ZERO state, depending on the initial state of the core (fully saturated positively or negatively). This is a clever scheme, but compared with toroids, the cost is high due to the extra costs of individual cores, wiring and testing.

49. J. A. Baldwin, Jr. and J. I. Rogers, "Inhibited Flux--A New Mode of Operation of Three-Hole Memory Core," *J. Appl. Phys. Suppl.* to Vol. 30.4, pp. 58S-59S (April 1959).

A three-hole core is used as a memory core. The word-oriented drive is applied to the central aperture and the bit-oriented drive is applied to one of the side apertures. In this way fast switching (READ and WRITE time of 0.75 to 1  $\mu$ sec) and low half-select noise are obtained.

50. B. R. Eichbaum, "An Evaluation of a New High Speed Magnetic Ferrite System for Use in Computer Components," *J. Appl. Phys. Suppl.* to Vol. 30.4, pp. 49S-52S (April 1959).

The use of a multipath core for memory application similar to that of Ref. 48 is described.

51. C. Kittel, "Physical Theory of Ferromagnetic Domains," *Rev. of Modern Physics*, **21**, 4, pp. 541-583 (October 1949).

This is a classical paper on domain wall theory.

52. V. W. Hesterman and D. Nitzan, "Possible Domain Structure in a MAD," Magnetism Seminar, Stanford Research Institute, Menlo Park, California (February 2, 1961).

53. J. Smit, and H. P. J. Wijn, *Ferrites* (John Wiley & Sons, Inc., New York City, 1959).

The book includes a large amount of information. Sometimes it is not clear whether the discussion applies to crystalline or polycrystalline material.

54. S. A. Abbas, "Methods of Analysis of Flux Patterns in Ferrite Multipath Cores," Carnegie Institute of Technology, Department of Electrical Engineering, Pittsburgh, Pennsylvania (June 1958).

See Sec. IV-C-3, pp. 134-137, for a discussion of this work.

55. S. A. Abbas and D. L. Critchlow, "Calculation of Flux Patterns in Ferrite Multipath Structures," 1958 IRE National Convention Record, Part 4, pp. 263-267 (March 1958).

This is a summary of the basic assumptions and final results of Ref. 54. Not a single equation is given in this summary.

56. E. U. Cohler and T. E. Baker, "Geometric Factors in Multi-aperture Ferrite Devices," pp. 215-249, Special Technical Conference on Nonlinear Magnetism, Los Angeles (November 1961).

This paper deals with flux switching in multipath cores and the design of nonresistance schemes for flux transfer, including biasing

techniques. A square-root parabolic model for  $\rho/\rho_p$  is used in order to analyze the division of flux between Legs 3 and 4\* of a shaped MAD that is driven via Leg 1 [as in Fig. 76(a)]. For a constant MMF drive  $NI$ , calculation based on the assumption that  $H_3$  and  $H_4$  are constant during the entire switching time yields flux division ratio

$$\frac{\Delta\phi_3}{\Delta\phi_4} = \tan^2 \left( \frac{\pi}{2} \frac{1}{1 + \frac{H_4 - H_0}{H_3 - H_0}} \right) \quad (123)$$

If no winding links Leg 4, then  $H_3 l_3 = H_4 l_4$ . Calculations are carried out in order to determine  $H_3$  and  $H_4$  when a coupling loop of negligible impedance links Leg 4 with  $n$  turns and a second core of length  $l$  with a single turn. It is shown that for the case of  $n = 1$ ,  $H_3 l_3 = H_4 (l_4 + l)$ ; thus, adding the loading core is equivalent to opening the coupling loop and lengthening Leg 4 by  $l$ , thereby decreasing  $\Delta\phi_4$ . Having  $n > 1$  is equivalent to lengthening Leg 4 by more than  $nl$ .

The calculation of  $\Delta\phi_3/\Delta\phi_4$  is straightforward. However, it is not clear what is the justification for assuming that  $H_3$  and  $H_4$  are constant during the switching time. Suppose, for example, that  $n$  is large enough to justify neglecting  $\phi_4$ , thus  $\phi_m \approx \phi_3$ . Hence, assuming that  $(1/2) \phi_{r_m} = \phi_{r_3} = \phi_{r_4} = \phi_r$ ,  $\phi_m$  varies from  $-2\phi_r$  to 0,  $\phi_3$  varies from  $-\phi_r$  to  $\phi_r$ , and  $\phi_4$  stays at  $-\phi_r$ . In the beginning of the switching time,  $H_3 = H_m$ . As switching proceeds,  $\rho_3/\rho_{3p} > \rho_m/\rho_{mp}$  [cf. Fig. 107(d)], and since  $\phi_m = \phi_3$ ,  $H_3 < H_m$ . While  $\rho_m/\rho_{mp}$  keeps increasing,  $\rho_3/\rho_{3p}$  increases to a peak value of 1 (at  $\phi_3 = 0$ ), then decreases, until  $\rho_3/\rho_{3p} = \rho_m/\rho_{mp}$  and then  $H_3 = H_m$ . Beyond this time  $\rho_m/\rho_{mp} > \rho_3/\rho_{3p}$ , hence  $H_m < H_3$ . Finally, as Leg 3 reaches saturation,  $\dot{\phi}_m = \dot{\phi}_3 = 0$ , and Leg  $m$  is clamped to the static loop, hence,  $H_m = H_c$  and  $H_3 = (NI - H_c l_m)/l_3$ . It is, therefore, concluded that, unlike the assumption in the paper,  $H_3$  varies during switching time. Similar arguments may be applied to  $H_4$ . Needless to say, variation of  $H_3$  and  $H_4$  with time would complicate the calculation of  $\Delta\phi_3/\Delta\phi_4$  [Eq. (123)] considerably.

The rest of the paper deals with flux transfer between a transmitter and a receiver. Curves of  $\Delta\phi_R$  versus  $\Delta\phi_T$  [cf. Fig. 66(a)i] are photographed directly from an oscilloscope screen. Analytical derivation shows that a wider range of operation is obtained by biasing the receiver through the input minor aperture.

\* Symbols and leg designation here are different than in the paper.

## B. BIBLIOGRAPHY

57. AMP Inc. Bulletins 610A, 610B and 610C, Harrisburg, Pa. (1960).

These catalogs provide qualitative and quantitative information about a resistance-type shift register and sequence detector and the associated drivers. The typical shape of an ADVANCE pulse and the range of operation at different temperatures are presented. The clock pulse system and read-out arrangements are described briefly.

58. D. R. Bennion, H. D. Crane, and F. Heinzmann, "Multi-Aperture Magnetic Devices for Computer Systems," Tech. Report 2 to Burroughs Corp. (Paoli, Pa.) Stanford Research Institute, Menlo Park, California (October 1957).

Problems of core shaping arise in the development of a NEGATION element. It is found experimentally that by constricting the legs around the output aperture, better  $\phi$ - $F$  curves are obtained. It is then shown that for better operation as a logic device, a multipath core should have, first,  $\phi$ - $F$  curves with high  $F_A/F_B$  ratio [cf. Fig. 49], sharp corners, flat top and bottom regions and high slope between the two regions; and second, delayed peaking time of  $\phi(t)$  waveform when a CLEAR state is transferred, compared with the transfer of a SET state. In order to achieve these features, regions of soft threshold are minimized by shaping the core in different ways [Fig. 97]. The selected shape [Fig. 96(b)] has the fewest sharp corners.

59. D. R. Bennion, H. D. Crane, and F. Heinzmann, "Multi-Aperture Magnetic Devices for Computer Systems," Final Rept. to Burroughs Corp. (Paoli, Pa.), Stanford Research Institute, Menlo Park, Calif. (January 1958).

A large portion of the material in this report can be found in Ref. 17. The effects of bias on the range of operation of a nonresistance scheme are discussed and possible ways of achieving the effect of fractional turns are proposed. Several drive modifications are shown and design problems are discussed. Multipath structures that perform EXCLUSIVE-OR and AND functions are presented. The main disadvantage of these elements is their complexity and, hence, high cost. Flow diagrams for a binary counter and a decimal counter are included at the end of the report.

60. D. A. Buck and W. I. Frank, "Nondestructive Sensing of Magnetic Cores," Trans. AIEE, pt. I, Vol. 72, pp. 822-830 (January 1954).

Nondestructive sensing is obtained by an  $H$  pulse applied at a right angle to the original easy direction of magnetization. The polarity of the induced voltage depends on the initial polarity of the magnetization. Methods are shown for generating the transverse field externally and internally. A transverse field is also generated internally by drilling three perpendicular holes in a ferrite cube. These devices were built and tested. The authors provide experimental data and explain them theoretically.

61. H. D. Crane, "Research on the Realizability of an All-Magnetic Computing System," Scientific Report 1, Contract AF19(604)-5909, Stanford Research Institute, Menlo Park, California (October 1959).

Basic schemes and basic design of the all-magnetic arithmetic unit, which is described in Ref. 26, are developed.

62. H. D. Crane, "Sequence Detection Using All-Magnetic Circuits," IRE Trans. of the Professional Group on Electronic Computers, Vol. PGEC-9, pp. 155-160 (June 1960).

The author shows three types of sequence detector that employ multipath cores. A special pen is used to encode handwriting symbols into different sequences of five pulses that are generated by a commutator contact sensitive to the direction of writing. These pulse sequences can be decoded by an array of sequence detectors, each of which responds to a particular sequence.

63. H. D. Crane, "Design of an All-Magnetic Computing System—Part II: Logical Design," IRE Trans. of the Professional Group on Electronic Computers, PGEC-10 (June 1961).

The paper summarizes the logical design for the all-magnetic arithmetic unit described in Ref. 26.



64. H. D. Crane and E. K. Van De Riet, "Circuit Approach for an All-Magnetic Computing System," Digest of Tech Papers, 1961 Solid-State Circuits Conf., Philadelphia Pa. (February 1961).

This paper summarizes the material in Ref. 26.

65. D. C. Engelbart and J. L. Haynes, "Research on the Philosophy of Logic Realization," Final Report, Contract AF33(616)-6303, Stanford Research Institute, Menlo Park, California (May 1960).

A vast amount of material on various schemes of digital-computer circuitry that is scattered throughout the literature is classified. Schemes employing multipath cores constitute a small portion of this report.

66. U. F. Gianola, "The Possibilities of All-Magnetic Logic Circuitry," presented at the Conf. on Magnetism and Magnetic Materials, New York, N.Y. (Nov. 14-17, 1960), see *J. Appl. Phys.*, Supplement to Vol. 32, pp. 27S-34S (March 1961).

Various known all-magnetic schemes are reviewed with emphasis on schemes that employ multipath cores.

67. D. G. Hammel, W. L. Morgan, and R. D. Sidnam, "A Multiload Transfluxor Memory," Proc. Western Joint Computer Conference (March 1959).

68. P. T. Harper, "Magnetic Logic Elements Using a Single MAD Device and Wire Interconnections Only," pp. 169-200, Special Technical Conference on Nonlinear Magnetics, Los Angeles, (November 1961).

A third clock phase is added to a two-phase clock (plus dc PRIME) resistance scheme [cf. Sec. II-B-3, pp. 64-67] in order to build various logic circuits. These circuits include NOR, flip-flop, and NOR-OR gates as well as a serial binary adder.

69. V. W. Hesterman, "Evaluation of Flux-Switching Models for Magnetic Devices," Technical Report 2, Contract Nonr. 2712(00), Stanford Research Institute, Menlo Park, California (September 1961).

The text of Ref. 10, as well as additional material on experimentation and calculation of  $\phi$ , are included in the report.

70. "Magnetic Logic Core Improvement Program Final Report," Contract AF 30(635)-3130 IBM Corp., Kingston, N.Y. (January 1, 1958).

Only a small portion of this 48-page report deals with the use of multipath cores in performing logic functions. The technique used is based on flux summation and flux steering.

71. W. R. Johnston, "Poly-Aperture Cores Used in Non-Destructive Readout Counter," pp. 68-73, Proc. of the Special Technical Conference on Nonlinear Magnetics and Magnetic Amplifiers, Philadelphia, Pa., (October 26-28, 1960).

72. D. H. Looney, "New Magnetic Devices For Digital Computers," pp. 96-104, Proc. of the 1960 Electronic Components Conference, Washington, D.C., (May 1960).

The paper reviews known magnetic devices in digital applications, including multipath cores. Among the reviewed devices for memory application are a ferrite sheet, a three-hole core (called "fluxor"), the Transfluxor, and the BIAX. Among the reviewed devices for logic application are the parametron, the MAD and the Laddic.

73. W. Matthews, "Telemetering in Earth Satellites," *Electrical Engr.* **76**, pp. 976-981 (November 1957).

A multipath core is employed as a storage device with nondestructive read-out in a counter used in earth-satellites.

74. A. J. Meyerhoff *et al*, *Digital Applications of Magnetic Devices* (John Wiley & Sons, Inc., New York City 1960).

The first part of this book summarizes briefly some basic concepts in magnetism, ferromagnetism, and flux switching in magnetic cores.

A small section (written by H. D. Crane of Stanford Research Institute) at the end of the book is devoted to multipath cores and their use in nonresistance schemes of shift registers and logic circuits. The largest portion of the book deals with the use of magnetic devices in conjunction with semiconductor elements for digital applications.

75. A. Papoulis, "The Nondestructive Readout of Magnetic Cores," *Proc. IRE* **42**, pp. 1283-1288 (August 1954).

For the case of a magnetic-tape core, the author analyzes the flux vector rotation described in Ref. [60]. He calculates the stable angles to which a magnetization vector may fall when an external field is applied perpendicular to the direction of the residual magnetization. His calculations are based on minimizing the anisotropy and magnetostatic energy, assuming that the magnetostrictive energy is negligible. The article is well written and instructive.

76. J. A. Rajchman, "Ferrite Apertured Plate for Random Access Memory," pp. 325-334, *Proc. IRE* (March 1957).

77. J. A. Rajchman, "A Survey of Magnetic and Other Solid-State Devices for the Manipulation of Information," *IRE Trans. of the Professional Group on Circuit Theory*, Vol. *PGCT-4*, pp. 210-225 (September 1957).

Among other topics, the author reviews the operation of the Transfluxor, its setting characteristics [cf. Sec. II-A, pp. 55-59] and its application in a memory array and decoder switch. An analogy is drawn between the Transfluxor and a ferroelectric circuit.

78. J. A. Rajchman, G. R. Briggs, and A. W. Lo, "Transfluxor Controlled Electroluminescent Display Panels," *Proc. IRE* **46**, pp. 1808-1824 (November 1958).

An array of Transfluxors is used to illuminate electroluminescent cells. A continuous amount of flux is set into each core and a fixed DRIVE MMF is applied to each minor aperture, resulting in different  $\phi$  values. A sense winding linking the output leg is applied across its own electroluminescent cell, whose light brightness is a function of the applied voltage.

79. J. A. Rajchman and H. D. Crane, "Current Steering in Magnetic Circuits," IRE Trans. of the Professional Group on Electronic Computers, Vol. PGEC-6, pp. 21-30 (March 1957).

Current steering by the use of a pair of Transfluxors is described. In order to divide flux equally between the legs around the minor output aperture, the minor aperture is perpendicular to the major aperture. The current steering is applied to build a decoder. By setting one of each pair of Transfluxors, one of each pair of conductors is made to carry most of the applied current that comes from a current source.

80. T. D. Rossing and S. M. Rubens, "Effects of a Transverse Field on Switching Rates of Magnetic Memory Cores," *J. Appl. Phys.* **29**, pp. 1245-1247 (August 1958).

The effect on switching characteristics of adding a quadrature field to the applied field is discussed. It is demonstrated that  $B$ - $H$  loops with a quadrature field present are lower in height and narrower than they are if the quadrature field is removed. The effect of the quadrature field is also to shift the curve of  $1/\tau$  versus  $H$  to the left without changing the slope.

81. D. H. Schaefer, "Magnetic Core Event Counter for Earth Satellite Memory," *Electrical Engineering* **77**, pp. 52-56 (January 1958).

A multipath core is used as a storage element for an earth satellite counter similar to the one in Ref. [73].

82. R. L. Snyder, "Magnistor Circuits," *Electronics Design* **3**, pp. 74-77, (August 1955).

The Magnistor operates as a magnetic amplifier, using no diodes. A distinction is made between a "transient" Magnistor that uses soft magnetic material and a "permanent" Magnistor that uses hard material, except around the small aperture [cf. Sec. III-A-6-f, p. 85]. Different read-out circuits are shown in which signal-to-noise ratio is increased. All the circuit diagrams and the associated short explanations are conveniently condensed on one page.

83. E. K. Van De Riet and C. H. Heckler, Jr., "Research on General Digital Logic Systems Utilizing Magnetic Elements and Wire Only," Final Engr. Rept., Contract AF 19(604)-5909, Air Force Cambridge Research Center, Bedford, Mass., Stanford Research Institute, Menlo Park, California (October 1960).

This report describes in more detail most of the material that is covered in Ref. 26.

84. A. W. Vinal, "The Development of a Multiaperture Reluctance Switch," Proc. Western Joint Computer Conference, Los Angeles, Calif., (May 9-11, 1961).

The paper is lengthy and written in an obscure manner. An attempt is made to explain switching mechanism in a two-hole core. The reader is referred to a review on this paper by D. R. Pennion in the *Proceedings of the Western Joint Computer Conference*, vol. 19, pp. 443-475 (May 1961).

85. C. L. Wanlass and S. D. Wanlass, "BIAX High Speed Magnetic Computer Element," WESCON, 1959, Pt. 4, pp. 40-54.

The BIAx element is very similar to the element proposed by D. A. Buck and W. I. Frank in Ref. [60]. A BIAx element is a ferrite cube with two non-intersecting perpendicular square holes. If the two holes are separated by a slab, the element is a memory BIAx; if no such slab exists, the element is a logic BIAx. In the memory element, the top hole contains the storage and sense windings and the bottom hole contains the INTERROGATE winding, [Fig. 136]. To write information, flux is switched to positive or negative saturation. To read information, the interrogate winding is energized, and voltage, the polarity of which depends on the polarity of the stored flux, appears across the sense winding. The authors interpret this operation in terms of orientation of magnetization in the slab, hence claim that the BIAx element is inherently a fast-switching element. However, let us examine this interpretation.

The width  $w$  of the slab is equal to the width of Leg S (for Storage) and Leg I (for Interrogation). Following the description of theory of operation in the paper, as Leg I is interrogated, flux change in Leg I must be accompanied by flux change in Leg S,  $\Delta\phi_s$ , which is proportional

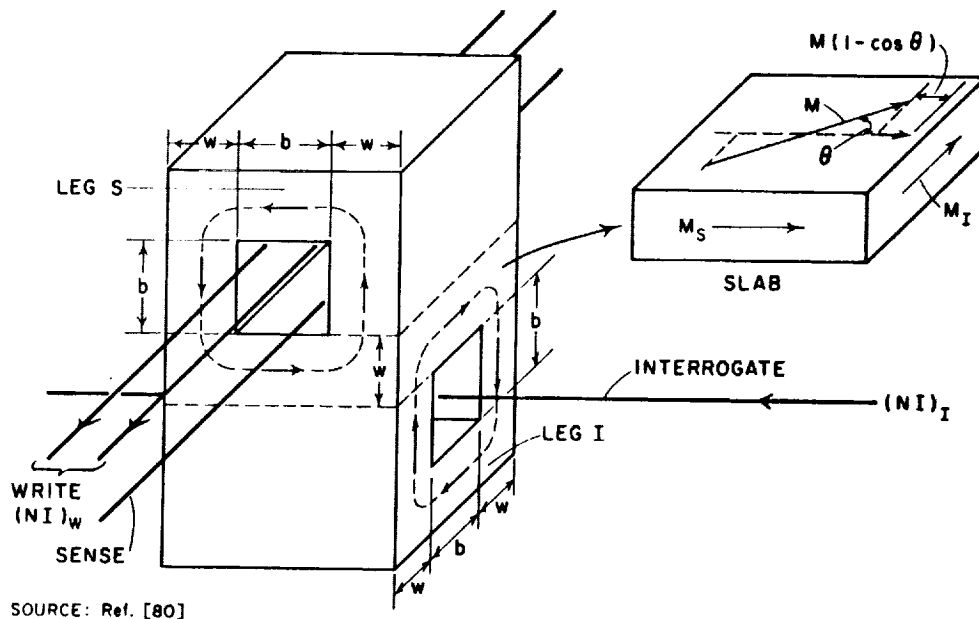
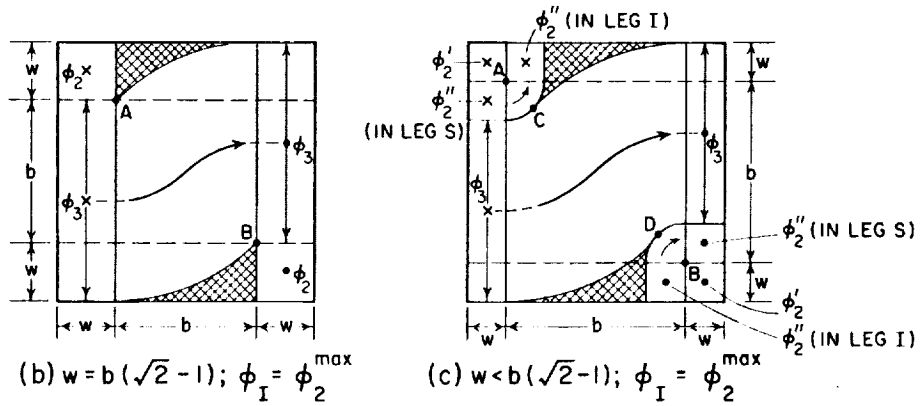
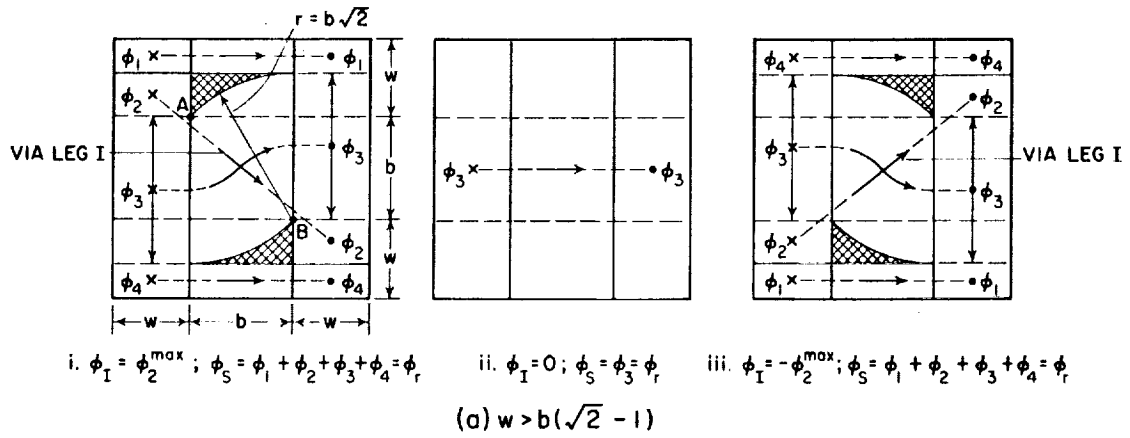


FIG. 136 BIAx MEMORY ELEMENT

to  $(1 - \cos \theta)$  [Fig. 136]. Based on this model, if Leg S is held saturated, Leg I must be demagnetized, i.e.,  $\phi_I = 0$ . We shall assume that Leg S is saturated, and examine if  $\phi_I$  is zero, assuming another switching model.

A different interpretation of the flux switching mechanism in the BIAx slab is based on motion of zone boundaries.\* Figure 137(a) shows three static flux states (in a top view of a BIAx element, broken above the slab) that result from varying the amplitude of INTERROGATE MMF,  $(NI)_I$ , that is applied simultaneously with a fixed, positive and high WRITE MMF,  $(NI)_W$ . At and below some maximum magnitude of  $(NI)_I$ ,  $(NI)_I^{\text{max}}$ , Leg S is maintained saturated by  $(NI)_W$ . By varying  $(NI)_I$  between  $(NI)_I^{\text{max}}$  and  $-(NI)_I^{\text{max}}$ ,  $\phi_I$  varies between  $\phi_I^{\text{max}}$  and  $-\phi_I^{\text{max}}$ , but  $\phi_S = \phi_r$ , where  $\phi_r$  is the saturation flux level of Leg S or of Leg I. Note that  $(NI)_I^{\text{max}}$  is a function of  $(NI)_W$ . In order to explain the mechanism of flux switching by the motion of zone boundaries, let us divide  $\phi_S$  into four components:  $\phi_1$  and  $\phi_4$ , which close via the slab edges (due to symmetry,  $\phi_1 = \phi_4$ );  $\phi_2$ , which closes via Leg I (hence,  $\phi_I = \phi_2$ ); and  $\phi_3$ , which closes via the middle part of the slab. For  $(NI)_I = (NI)_I^{\text{max}}$  [Fig. 137(a)i],  $\phi_2 = \phi_2^{\text{max}}$ , hence  $\phi_I = \phi_2^{\text{max}}$ . All of  $\phi_S$ , except  $\phi_2$ , closes via the slab, and the remaining shaded areas

\* This interpretation is in part due to E. K. Van De Riet, Stanford Research Institute, Menlo Park, California.



RB-3696-136

FIG. 137 FLUX SWITCHING IN A BIAx MEMORY ELEMENT BY ZONE GROWTH

correspond to demagnetized regions ( $\phi = 0$ ). As  $(NI)_I$  is decreased,  $\phi_2$  changes by only a small amount, until at some threshold value of a negative  $(NI)_I$ ,  $\phi_2$  starts to reverse along the shortest path. Although the closure of  $\phi_2$  is via Leg S, the switching path in Leg I is completed along the diagonal of the slab. Since this path connects Points A and B via the diagonal in the BIAx floor, the magnitude of this threshold MMF is equal to  $H_{th}b(\sqrt{10} + \sqrt{2})$ . A further decrease in  $(NI)_I$  causes the reversed  $\phi_2$  to expand radially around Points A and B and the demagnetized areas shrink until at some negative value of  $(NI)_I$ ,  $\phi_2 = 0$  [Fig. 137(a)ii], and  $\phi_3 = \phi_S = \phi_r$ . The magnitude of the negative  $(NI)_I$  is increased, until at  $(NI)_I = -(NI)_I^{max}$ ,  $\phi_I = -\phi_2^{max}$  [Fig. 137(a)iii]. The plot  $\phi_I$  versus  $(NI)_I$ , where  $-\phi_2^{max} \leq \phi_I \leq \phi_2^{max}$  and  $-(NI)_I^{max} \leq (NI)_I \leq (NI)_I^{max}$ , will have the shape of a typical dc  $\phi$ - $F$  loop, while  $\phi_S$  is maintained at a constant level of  $\phi_r$ . This mechanism of flux switching is typical for multipath cores where the path of flux closure is not necessarily the path of flux switching [cf. Figs. 61 and 63].

Let us briefly analyze this switching model. It can be shown by simple calculation that for the case of  $\phi_2 = \phi_2^{max}$ ,

$$\phi_1 = \phi_4 = \phi_r \frac{w - b(\sqrt{2} - 1)}{2w + b}, \quad (124)$$

$$\phi_2 = \phi_I^{max} = \phi_r \frac{b(\sqrt{2} - 1)}{2w + b}, \quad (125)$$

and

$$\phi_3 = \phi_r \frac{b\sqrt{2}}{2w + b}. \quad (126)$$

These equations are based on the situation shown [Fig. 137], hence hold as long as  $b\sqrt{2} \leq b + w$ , or  $w \geq b(\sqrt{2} - 1)$ . When  $b \rightarrow 0$  (infinitesimal holes),  $\phi_1 = \phi_4 \rightarrow \phi_r/2$ ,  $\phi_I^{max} \rightarrow 0$ , and  $\phi_3 \rightarrow 0$ . When  $w = b(\sqrt{2} - 1)$  [Fig. 137(b)],  $\phi_1 = \phi_4 = 0$ ,  $\phi_I^{max} = \phi_r(\sqrt{2} - 1)/(2\sqrt{2} - 1) = 0.225 \phi_r$ , and  $\phi_3 = \phi_r\sqrt{2}/(2\sqrt{2} - 1) = 0.775 \phi_r$ .

Suppose that the hole size  $b$  is increased beyond  $w/(\sqrt{2} - 1)$ , while the over-all dimension  $2w + b$  is maintained constant. Flux  $\phi_2$  is now composed of two components,  $\phi_2'$  and  $\phi_2''$ .



These components are shown [Fig. 137(c)] for maximum value of  $\phi_2$ . In order to explain how this state has been reached, assume that  $\phi_I = 0$  and  $\phi_S = \phi_3 = \phi_r$ , [Fig. 137(a)ii]. MMF  $(NI)_I$  is now gradually increased. When  $(NI)_I$  reaches the value of  $H_{th}b(\sqrt{10} + \sqrt{2})$ , flux starts to switch along the shortest path in Leg I, i.e., the path that connects Points A and B via the diagonal of developed Leg I. A further increase in  $(NI)_I$  completes the switching of  $\phi'_2$  in Leg I in a way similar to that shown for  $\phi_2$  [Fig. 137(b)], except that now Diagonal A-B is longer than  $b + w$ , hence  $\phi''_2$  switches as well until  $\phi_3$  is constricted by Diagonal C-D in the slab. Pictorially,  $\phi'_2$  and  $\phi''_2$  expand radially around Points A and B ( $\phi'_2$  switches faster than  $\phi''_2$ ). From the geometry [Fig. 137(c)], it can be shown that

$$\phi'_2 = \phi_r \frac{w}{2w + b}, \quad (127)$$

$$\phi''_2 = \phi_r \frac{b(\sqrt{2} - 1) - w}{2w + b}, \quad (128)$$

and

$$\phi_3 = \phi_r \frac{b(2 - \sqrt{2}) + 2w}{2w + b}. \quad (129)$$

However, since  $\phi_2 = \phi'_2 + \phi''_2$ , adding the expressions in Eqs. (127) and (128) yields the same expression as in Eq. (125). We, therefore, conclude that  $\phi_I^{max}$ , expressed by Eq. (125), holds for all values of  $w/b$ . When  $w = b(\sqrt{2} - 1)$ , Eqs. (129) and (126) yield the same expression for  $\phi_3$ , as expected. When  $w \rightarrow 0$  (thin legs and thin slab),  $\phi_I^{max} \rightarrow \phi_r(\sqrt{2} - 1)$ .

There is an additional component of  $\phi_I$  that has not been considered so far. Assume that Leg I is completely demagnetized and  $\phi_S = \phi_3 = \phi_r$ , [Fig. 137 (a)ii]. In each of two places where the walls of Leg S meet with the slab,  $\phi_S$  rotates by 90 degrees, leaving a fillet in a demagnetized state. The cross section of this fillet is what is left over after subtracting a quadrant of radius  $w$  from a square of side  $w$ , hence its area is equal to  $w^2[1 - (\pi/4)]$ . MMF  $(NI)_I$  is now increased from zero, and when it reaches the value of  $4bH_{th}$ , flux switching starts to take place around the INTERROGATE hole via the two fillets. Denoting this flux by  $\phi_{IF}$ , its maximum value is

$$\phi_{IF}^{max} = \phi_r \frac{2w \cdot \left(1 - \frac{\pi}{4}\right)}{2w + b} \quad (130)$$

Due to having a lower threshold,  $\phi_{IF}$  starts switching before  $\phi_2$ . If effects of soft threshold are neglected and  $w < b(\sqrt{10} + \sqrt{2} - 4)/2\pi$ ,  $\phi_{IF}$  will complete switching before  $\phi_2$  starts switching, otherwise both will overlap partially in time. It appears that in the latter case,  $\phi_2$  and  $\phi_{IF}$  may have a conflict concerning the path of switching, hence  $\phi_2$  may not be able to reach  $\phi_2^{max}$ . There is, however, some additional path for  $\phi_2$  to sneak via the demagnetized volume in the slab.

In the paper under discussion,  $w = 15$  mils and  $b = 20$  mils, hence, following Eqs. (125) and (130).

$$\phi_I^{max} = \phi_r \frac{20(\sqrt{2} - 1)}{2 \cdot 15 + 20} = 0.165 \phi_r$$

and

$$\phi_{IF}^{max} = \phi_r \frac{2 \cdot 15 \left(1 - \frac{\pi}{4}\right)}{2 \cdot 15 + 20} = 0.129 \phi_r$$

We, therefore, conclude that based on the zone-growth model,  $\phi_I$  may vary between at least  $\pm 0.165 \phi_r$  while  $\phi_S$  is held at  $\phi_r$ . On the other hand, the model presented in the paper calls for  $\phi_I$  to be fixed at a zero level while  $\phi_S$  is held at  $\phi_r$ . We thus see that two models are not in agreement. The experimental evidence of fast switching, which is attributed in the paper to rotation of magnetization, may be interpreted as elastic switching caused by very narrow interrogation drive pulse. No data are given in the paper for longer drive pulses. Further investigation is needed. One way to test which model to accept is to hold Leg S, interrogate Leg I, and sense  $\phi_I$ . If  $|\Delta\phi_I| \approx 2\phi_I^{max}$  while  $\Delta\phi_S = 0$ , the model presented in the paper is not valid.

The rest of the paper deals with assembly of BIAx cores and the use of the BIAx element for logic applications.

The following four sources are German papers on multipath cores that have not yet been translated. Although most of the material appears to be

a review of the literature on multipath cores in this country, these papers include new ideas that justify their translation.

86. A. Darre, "Abfragen magnetischer Speicher ohne Informationsverlust," *Frequenz* **11**, 1 (January 1957).

87. A. Darre, "Abfragen magnetischer Speicher ohne Informationsverlust," *Frequenz* **11**, 2 (February 1957).

88. F. Schreiber, "Der Transfluxor Als Verstärker," *Nachr.-tech. Fachber.* **21**, S76-S-86 (1960).

89. F. Schreiber, "Anwendung der Karnaughschen Spiegelsymbolik auf Transfluxoren," *Frequenz* **15**, 2 (February 1961).

The following list includes U.S. patents that involve multipath cores (Refs. 27 and 38 are not included in this list).

90. H. W. Abbot *et al.*, "Signal Translating Device," U.S. Patent 2,863,136, Dec. 2, 1958 (Filed Jan 3, 1957).

91. W. R. Arsenault *et al.*, "Magnetic Flip-Flop," U.S. Patent 2,802,953, Aug. 13, 1957 (Filed April 25, 1955).

92. R. L. Ashenurst *et al.*, "Electrical Circuits Employing Sensing Wires Threading Magnetic Core Memory Elements," U.S. Patent 2,912,677, Nov. 10, 1959 (Filed Dec. 31, 1953).

93. E. W. Bauer, "Non-Destructive Sensing of Magnetic Cores," U.S. Patent 2,814,794, Nov. 26, 1957 (Filed Aug. 17, 1955).

94. E. W. Bauer, "Magnetic Half Adder," U.S. Patent 2,868,451, Jan. 13, 1959 (Filed May 22, 1956).

95. D. R. Bennion *et al.*, "Multiple-Setting Magnetic Core Circuits," U.S. Patent 2,936,445, May 10, 1960 (Filed June 12, 1958).

96. D. R. Bennion, "Bidirectional Shift Register," U.S. Patent 2,969,524, Jan. 24, 1961 (Filed Nov. 25, 1957).

97. G. R. Briggs *et al.*, "Magnetic Systems," U.S. Patent 2,911,628, Nov. 3, 1959 (Filed May 1, 1957).

98. K. D. Broadbent, "Magnetic Device," U.S. Patent 2,993,197, July 18, 1961 (Filed Aug. 2, 1957).

99. E. A. Brown, "Magnetic Core Logical Device," U.S. Patent 2,855,586, Oct. 7, 1958 (Filed June 26, 1956).

100. Tung C. Chen *et al.*, "Nondestructive Read-Out of Magnetic Cores," U.S. Patent 2,918,660, Dec. 22, 1959 (Filed May 25, 1956).

101. Wayne H. Chen, "Connector and Selector Circuits," U.S. Patent 2,733,424, Jan. 31, 1956 (Filed Sept. 15, 1954).

102. S. B. Cohen *et al.*, "Magnetic Amplifier," U.S. Patent 2,745,908, May 15, 1956 (Filed Jan. 10, 1951).

103. H. L. Cooke, "Transfluxor System," U.S. Patent 2,921,136, Jan. 12, 1960 (Filed Oct. 31, 1955).

104. H. D. Crane, "Magnetic Logic Systems," U.S. Patent 2,810,901, Oct. 22, 1957 (Filed Feb. 29, 1956).

105. H. D. Crane, "Magnetic Switching Systems," U.S. Patent 2,896,194, July 21, 1959 (Filed May 7, 1956).

106. H. D. Crane, "Magnetic Core Logic Element," U.S. Patent 2,935,622, May 3, 1960 (Filed June 12, 1958).
107. H. D. Crane, "Multi-Aperture Core Storage Circuit," U.S. Patent 2,935,739, May 3, 1960 (Filed June 12, 1958).
108. H. D. Crane, "Magnetic Core Flip-Flop Circuit," U.S. Patent 2,968,030, Jan. 10, 1961 (Filed June 12, 1958).
109. H. D. Crane, "Magnetic Switching Systems," U.S. Patent 2,980,892, April 18, 1961 (Filed June 27, 1956).
110. H. D. Crane, "Magnetic Systems," U.S. Patent 2,983,906, May 9, 1961 (Filed May 7, 1956).
111. H. D. Crane, "Magnetic Core Binary Counter Circuit," U.S. Patent 2,995,663, Aug. 8, 1961 (Filed June 12, 1958).
112. H. D. Crane, "Magnetic Core Negation Circuit," U.S. Patent 3,003,140, Oct. 3, 1961 (Filed Dec. 16, 1957).
113. H. D. Crane, "Digital Circuit Using Core Elements," U.S. Patent 3,004,244, Oct. 10, 1961 (Filed Dec. 23, 1957).
114. H. D. Crane *et al.*, "Magnetic Control System," U.S. Patent 2,962,601, Nov. 29, 1960 (Filed Aug. 10, 1955).
115. H. D. Crane *et al.*, "Magnetic Core Digital Circuit," U.S. Patent 3,004,245, Oct. 10, 1961 (Filed Dec. 30, 1957).
116. T. H. Crowley *et al.*, "Magnetic Control Circuits," U.S. Patent 2,963,591.

117. S. Duinker, "Magnetic Memory Device," U.S. Patent 2,907,988, Oct. 6, 1959 (Filed Sept. 28, 1955).
118. R. B. Goldner *et al.*, "Magnetic Coincidence Gating Register," U.S. Patent 2,889,542, June 2, 1959 (Filed March 22, 1957).
119. D. W. Grant, "Alternating Current Control Device," U.S. Patent 2,519,426, Aug. 22, 1950 (Filed Feb. 26, 1948).
120. C. B. House, "Variable Frequency Magnetic Multivibrator," U.S. Patent 2,938,129, May 24, 1960 (Filed Jan. 21, 1958).
121. L. P. Hunter, "Coincidence Flux Memory System," U.S. Patent 2,869,112, Jan 13, 1959 (Filed Nov. 10, 1955).
122. H. Kihn, "Electrical Circuits," U.S. Patent 2,951,245, Aug. 30, 1960 (Filed March 12, 1957).
123. W. F. Kosonocky, "Magnetic Switching Systems," U.S. Patent 2,902,678, Sept. 1, 1959 (Filed Aug. 31, 1956).
124. R. C. Lamy, "Ternary Magnetic Storage Device," U.S. Patent 2,842,755, July 8, 1958 (Filed Aug. 25, 1955).
125. Kam Li, "Memory System," U.S. Patent 2,988,731, June 13, 1961 (Filed June 25, 1958).
126. Arthur W. Lo, "Magnetic Control Systems," U.S. Patent 2,818,555, Dec. 31, 1957 (Filed July 27, 1955).
127. Arthur W. Lo, "Magnetic System," U.S. Patent 2,818,556, Dec. 31, 1957 (Filed July 27, 1955).

128. Arthur W. Lo *et al.*, "Magnetic Circuits," U.S. Patent 3,014,204, Dec. 19, 1961 (Filed Dec. 11, 1956).
129. N. F. Lockhart, "Multipath Logical Core Circuits," U.S. Patent 2,978,176, April 4, 1961 (Filed Sept. 20, 1957).
130. E. E. Newhall *et al.*, "Magnetic Control Circuits," U.S. Patent 2,976,472, March 21, 1961 (Filed Jan. 4, 1960).
131. L. W. Orr *et al.*, "Gate Circuit," U.S. Patent 2,685,653, Aug. 3, 1954 (Filed Jan. 31, 1952).
132. F. L. Post, "Multipath Magnetic Core Memory Devices," U.S. Patent 2,898,581, Aug. 4, 1959 (Filed Nov. 19, 1956).
133. J. A. Rajchman *et al.*, "Electrical Control Systems," U.S. Patent 2,803,812, Aug. 20, 1957 (Filed May 31, 1955).
134. J. A. Rajchman, "Magnetic Switching Systems," U.S. Patent 2,884,622, April 28, 1959 (Filed June 27, 1956).
135. J. A. Rajchman, "Magnetic Switching System," U.S. Patent 2,919,430, Dec. 29, 1959 (Filed Nov. 1, 1954).
136. S. K. Raker, "Biased Magnetic Storage System," U.S. Patent 2,923,923, Feb. 2, 1960 (Filed Oct 31, 1956).
137. D. S. Ridler *et al.*, "Intelligence Storage Device," U.S. Patent 2,952,840, Sept. 13, 1960 (Filed March 8, 1955).
138. J. L. Rogers, "Magnetic Memory Device," U.S. Patent 2,926,342, Feb. 23, 1960, (Filed July 31, 1957).

139. A. G. Samusenko, "Transfluxor Counting Circuit," U.S. Patent 2,988,653, June 13, 1961 (Filed June 3, 1958).
140. A. G. Samusenko, "Magnetic Memory Systems," U.S. Patent 2,988,734, June 13, 1961 (Filed Feb. 24, 1959).
141. D. H. Schaefer, "Counting Circuit," U.S. Patent 2,934,750, April 26, 1960 (Filed Jan. 21, 1958).
142. A. W. Simpson, "Storage Devices," U.S. Patent 2,870,433, Jan. 20, 1959 (Filed July 20, 1955).
143. J. C. Slonczewski, "Magnetic Core," U.S. Patent 2,934,747, April 26, 1960 (Filed Dec. 21, 1956).
144. A. T. Starr *et al.*, "Pulse Coding Arrangements for Electric Communication Systems," U.S. Patent 2,954,550, Sept. 27, 1960 (Filed Jan 10, 1958).
145. I. H. Sublette *et al.*, "Control Systems," U.S. Patent 2,990,540, June 27, 1961 (Filed July 30, 1957).
146. R. L. Thompson, "Binary Counting Circuit," U.S. Patent 2,519,513, Aug. 22, 1950 (Filed Sept. 9, 1948).
147. A. W. Vinal, "Binary Memory System," U.S. Patent 2,988,732, June 13, 1961 (Filed Oct. 30, 1958).
148. J. L. Valentine *et al.*, "Magnetic Device," U.S. Patent 2,882,519, April 4, 1959 (Filed July 2, 1956).
149. C. L. Wanlass, "Flip-Flop Circuit," U.S. Patent 2,983,829, May 9, 1961 (Filed July 31, 1959).



150. C. S. Warren, "Magnetic Memory Systems," U.S. Patent 2,911,631, Nov. 3, 1959 (Filed June 27, 1958).

151. H. J. Wetzstein *et al.*, "Magnetic Storage Systems," U.S. Patent 2,911,629, Nov. 3, 1959 (Filed June 25, 1958).

## C. LITERATURE CLASSIFICATION

The sources listed as references and bibliography will now be classified: first according to subjects and second according to author.

### 1. SUBJECT CLASSIFICATION

In the following lists, sources are classified into nine subjects. When a Reference source is listed, the parentheses that follow include the page numbers in Secs. I through IV where the source is referred to. A Reference source is inclosed in parentheses and a Bibliography source is inclosed in brackets.

#### (a) GENERAL FLUX SWITCHING

- |  |                                      |
|--|--------------------------------------|
| (6), July 60 (pp. 3,44,45,81)                        | (17), March 59 (pp. 43,46-47, 48-50) |
| (8), Jan 55 (p. 4)                                   | (18), Apr. 59 (p. 52)                |
| (9), May 60 (pp. 7,39,50)                            | (36), Jan. 55 (pp. 88,128-133)       |
| (10), Nov. 61 (pp. 17,27)                            | (42), Jan. 57 (p. 109)               |
| (11), Dec. 59 (pp. 19,37,40-44, 45,64,80-85,117,134) | (43), Sept. 59 (p. 109)              |
| (12), Apr. 59 (p. 21)                                | (51), Oct. 49 (pp. 120,121,125)      |
| (13), March 59 (p. 32)                               | (53), 59 (p. 125)                    |
| (14), May 57 (pp. 36,84,94,117)                      | [59], Jan. 58                        |
| (15), Feb. 57 (pp. 37,45)                            | [69], Sept. 61                       |
| (16), Jan. 60 (p. 37)                                | [77], Sept. 57                       |

#### (b) FLUX SWITCHING IN MULTIPATH CORES

- |                               |   |
|-------------------------------|---|
| (1), June 55 (p. 1)           | (11), Dec. 59 (pp. 19,37,40-44 45,64,80-85,117,134) |
| (3), Oct. 60 (pp. 1,32,35,36) | (14), May 57 (pp. 36,84,94,117)                     |
| (6), July 60 (pp. 3,44,45,81) | (15), Feb. 57 (pp. 37,45,84)                        |
| (7), Jan. 61 (pp. 3,81,118)   | (17), March 59 (pp. 46-47,48-50)                    |
| (9), May 60 (pp. 7,39,50)     |   |

- |  |                             |
|--|-----------------------------|
| (19), Feb. 56 (pp. 55-59)              | (37), Feb. 61 (p. 88)       |
| (20), Sept. 61 (pp. 59,119,126-128)    | (39), April 57 (p.102)      |
| (24), Jan. 59 (p. 61)                  | (40), Aug. 57 (p. 102)      |
| (28), July 57 (pp. 64,80,81,82,84,118) | (45), March 61 (p.117)      |
| (29), June 60 (pp. 64,117)             | (52), Feb. 61 (pp. 121,125) |
| (32), Jan. 59 (pp. 75,76,102)          | (54), June 58 (pp. 134-137) |
| (33), May 60 (pp. 75-77,79,99)         | (55), March 58 (p. 134)     |
|  | (56), Nov. 61 (p. 81)       |
|  | [84], May 61                |

(c) MULTIPATH CORE SHAPING

- |                            |                |
|----------------------------|----------------|
| (38), Nov. 60 (p. 102)     | [106], May 60  |
| (41), May 60 (pp. 108,117) | [111], Aug. 61 |
| (45), March 61 (p. 117)    | [112], Oct. 61 |
| [58], Oct. 57              |                |

(d) SHIFT REGISTER APPLICATION

- |                                  |                |
|----------------------------------|----------------|
| (2), March 60 (p. 64)            | [59], Jan. 58  |
| (3), Oct. 60 (p. 35)             | [61], Oct. 59  |
| (4), Feb. 59 (p. 61)             | [64], Feb. 61  |
| (11), Dec. 59 (pp. 64,117)       | [65], May 60   |
| (17), March 59 (pp. 61,70,117)   | [74], 1960     |
| (21), June 61 (p. 60)            | [77], Sept. 57 |
| (24), Jan. 59 (pp. 61,117)       | [95], May 60   |
| (25), Dec. 58 (pp. 61,117)       | [96], Jan. 61  |
| (26), June 61 (p. 61)            | [97], Nov. 59  |
| (27), Jan. 61 (p. 64)            | [98], July 61  |
| (28), July 57 (pp. 64,82,84,117) | [107], May 60  |
| (29), June 60 (pp. 64,117)       | [112], Oct. 61 |
| (30), June 60 (p. 64)            | [113], Oct. 61 |
| (31), Oct. 60 (pp. 64,72)        | [115], Oct. 61 |
| [57], 1960                       | [118], June 59 |
| [58], Oct. 57                    | [133], Aug. 57 |

(e) CONTINUOUS-FLUX APPLICATION

- |                            |                |
|----------------------------|----------------|
| (1), June 55 (p. 1)        | [92], Nov. 59  |
| (19), March 56 (pp. 55-59) | [117], Oct. 59 |
| (20), Sept. 61 (p. 59)     | [118], June 59 |

[122], Aug. 60	[142], Jan. 59
[123], Sept. 59	[144], Sept. 60
[129], April 61	[147], June 61
[130], March 61	[148], April 59
[137], Sept. 60	[150], Nov. 59

(f) LOGIC CIRCUITRY APPLICATION

(11), Dec. 59 (pp. 64,117)	[74], 1960
(14), May 57 (pp. 36,117)	[75], Aug. 54
(15), Feb. 57 (pp. 84,117)	[76], March 57
(23), June 61 (p. 60)	[77], Sept. 57
(26), June 61 (p. 61)	[83], Oct. 60
(29), June 60 (pp. 64,117)	[90], Dec. 58
(32), Jan. 59 (pp. 102,117)	[91], Aug. 57
(34), Sept. 57 (pp. 82,117)	[94], Jan. 59
(41), May 60 (pp. 108,117)	[95], May 60
(44), 1958 (p. 117)	[99], Oct. 58
(46), June 61 (p. 117)	[104], Oct. 57
[58], Oct. 57	[106], May 60
[59], Jan. 58	[108] Jan. 61
[61], Oct. 59	[111], Aug. 61
[62], June 60	[112], Oct. 61
[63], Feb. 61	[128], Dec. 61
[64], Feb. 61	[129], April 61
[65], May 60	[139], June 61
[66], March 61	[141], April 60
[70], Jan. 58	[142], Jan. 59
[71], Oct. 60	[146], Aug. 50
[72], May 60	[149], May 61

(g) MEMORY APPLICATION

(34), Sept. 57 (pp. 82,117)	[67], March 59
(40), Aug. 57 (pp. 102,117)	[72], May 60
(47), Nov. 56 (p. 117)	[74], 1960
(48), Dec. 56 (p.117)	[77], Sept. 57
(49), April 59 (p. 117)	[84], May 61
(50), April 59 (p. 117)	[92], Nov. 59
[65], May 60	[93], Nov. 57
[66], March 61	[101], Jan. 56

- |                |                 |
|----------------|-----------------|
| [117], Oct. 59 | [137], Sept. 60 |
| [121], Jan. 59 | [138], Feb. 60  |
| [124], July 58 | [143], April 60 |
| [125], June 61 | [147], June 61  |
| [132], Aug. 59 | [148], April 59 |
| [136], Feb. 60 | [150], Nov. 59  |

(h) MISCELLANEOUS CIRCUITRY APPLICATION

- |                        |                 |
|------------------------|-----------------|
| (22), April 60 (p. 60) | [114], Nov. 60  |
| (35), 1960 (p. 82)     | [119], Aug. 50  |
| [57], 1960             | [120], May 60   |
| [62], June 60          | [122], Aug. 60  |
| [71], Oct. 60          | [123], Sept. 59 |
| [73], Nov. 60          | [126], Dec. 57  |
| [78], Nov. 58          | [127], Dec. 57  |
| [79], March 57         | [130], March 61 |
| [81], Jan. 58          | [131], Aug. 54  |
| [82], Aug. 58          | [134], April 59 |
| [101], Jan. 56         | [135], Dec. 59  |
| [102], May 56          | [140], June 61  |
| [103], Jan. 60         | [144], Sept. 60 |
| [105], July 59         | [145], June 61  |
| [109], April 61        | [151], Nov. 59  |
| [110], May 61          |                 |

(i) TRANSVERSE FIELD

- |               |               |
|---------------|---------------|
| [58], Jan. 58 | [75], Aug. 58 |
| [65], May 60  | [80], Aug. 59 |
| [69], Nov. 57 | [149], May 61 |

2. ALPHABETICAL ORDER OF AUTHORS' NAMES

In the following list, each Reference source is enclosed in parentheses and each Bibliography source is enclosed in brackets.

- Abbas, (54)
- Abbas and Critchlow, (55)
- Abbot and Suran, (39)
- Abbot and Suran, (40)

Abbot *et al.*, [90]  
 Arsenault *et al.*, [91]  
 Ashenhurst *et al.*, [92]  
  
 Baldwin and Rogers, (49)  
 Bauer, [93]  
 Bauer, [94]  
 Bennion, (9)  
 Bennion, (41)  
 Bennion, (30)  
 Bennion, (31)  
 Bennion, [96]  
 Bennion *et al.*, [95]  
 Bennion, Crane and Engelbart, (21)  
 Bennion, Crane and Heinzman, [58]  
 Bennion, Crane and Heinzman, [59]  
 Brain, (7)  
 Briggs *et al.*, [97]  
 Briggs and Lo, (27)  
 Broadbent, [98]  
 Brown, [99]  
 Buck and Frank, [60]  
  
 Chen T. C. *et al.*, [100]  
 Chen W. H, [101]  
 Cohen, [102]  
 Cohler and Baker, (56)  
 Cooke, [103]  
 Crane, (15)  
 Crane, (24)  
 Crane, [61]  
 Crane, [62]  
 Crane, [63]  
 Crane, [104]  
 Crane, [105]  
 Crane, [106]  
 Crane, [107]  
 Crane, [108]  
 Crane, [109]  
 Crane, [110]

Crane, [111]  
 Crane, [112]  
 Crane, [113]  
 Crane *et al.*, [114]  
 Crane *et al.*, [115]  
 Crane and Bennion, (17)  
 Crane, Bennion and Heinzman, (38)  
 Crane and Van De Riet, [64]  
 Crane and Van De Riet, (26)  
 Crowley, [116]  
  
 Darre, (86)  
 Darre, (87)  
 Davis, (42)  
 Duinker and van Ommen, (35)  
 Duinker, [117]  
  
 Eichbaum, (50)  
 Engelbart, (4)  
 Engelbart, (5)  
 Engelbart and Haynes, [65]  
  
 Gianola, (18)  
 Gianola, (2)  
 Gianola, (33)  
 Gianola, [66]  
 Gianola and Crowley, (32)  
 Goldner *et al.*, [118]  
 Gordon, (22)  
 Grant, [119]  
  
 Hammel, Morgan and Sidnana, [67]  
 Hammond, (36)  
 Harper, [68]  
 Hayner, (23)  
 Hesterman, (10)  
 Hesterman, [69]  
 House, [120]  
 Hunter and Bauer, (47)  
 Hunter, [121]

Johnston, [71]  
Kihn, [122]  
Kittel, (51)  
Kosonocky, [123]  
Kozlov, (16)  
Kozlov, (6)  
  
Lamy, [124]  
Lawrence, (48)  
Li, [125]  
Lo, [126]  
Lo, [127]  
Lo *et al.*, [128]  
Lockhart, (44)  
Lockhart, [129]  
Looney, [72]  
  
Matthews, [73]  
McKay, (12)  
Menyuk and Goodenough, (8)  
Meyerhoff *et al.*, [74]  
Mina and Newhall, (46)  
Morgan, (45)  
  
Newhall *et al.*, [130]  
Nitzan, (3)  
  
Onyshkevych, (28)  
Orr *et al.*, [131]  
  
Papoulis, [75]  
Post, [132]  
Prywes, (25)  
  
Rajchman, (34)  
Rajchman, [76]  
Rajchman, [77]  
Rajchman *et al.*, [133]  
Rajchman, [134]  
Rajchman, [135]  
Rajchman and Briggs, [78]

Rajchman and Crane, [79]  
Rajchman and Lo, (1)  
Rajchman and Lo, (19)  
Raker, [136]  
Ridler *et al.*, [137]  
Robertson, (43)  
Rogers, [138]  
Rossing and Rubens, [80]  
Rowe and Slemon, (20)  
  
Samusenko, [139]  
Samusenko, [140]  
Schaefer, [81]  
Schaefer, [141]  
Schreiber, [88]  
Schreiber, [89]  
Simpson, [142]  
Slonczewski, [143]  
Smit and Wijn, (53)  
Snyder, [82]  
Stabler, (13)  
Starr *et al.*, [144]  
Sublette *et al.*, [145]  
  
Thompson, [146]  
  
Van De Reit and Heckler, [83]  
Vinal, [84]  
Vinal, [147]  
  
Walentine *et al.*, [148]  
Wanlass and Wanlass, [85]  
Wanlass, [149]  
Warren, [150]  
Wetzstein *et al.*, [151]  
  
Zeiger, (29)



*APPENDIX A*

**GEOMETRICAL PROPERTIES OF A LEG**



## APPENDIX A

### GEOMETRICAL PROPERTIES OF A LEG

Consider a leg of constant width  $w$ , of inside-edge length  $l_i$  and outside-edge length  $l_o$ , and of angle  $\alpha$  formed between two planes that are perpendicular to the inner and the outer edges at the leg ends, Fig. A-1. A curve of length  $l$  is drawn at a distance  $x$  from  $l_i$ . Let  $R$  be the radius of curvature of  $l_i$  along the leg. Note that  $R$  is a variable quantity. A sector element of angle  $d\theta$  is drawn perpendicular to the leg edges. The difference between the two segment elements is

$$d(l - l_i) = (R + x)d\theta - Rd\theta = xd\theta \quad . \quad (A-1)$$

Integrating Eq. (A-1) along the whole leg gives

$$l - l_i = \int_{\text{leg}} xd\theta = x \int_{\text{leg}} d\theta = x\alpha \quad . \quad (A-2)$$

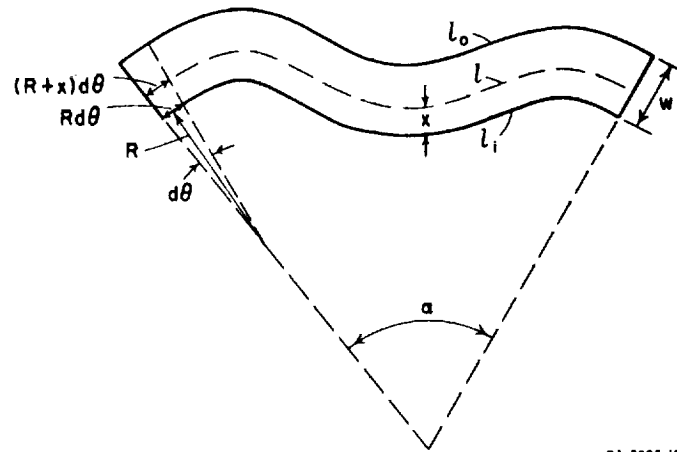


FIG. A-1 CONSTANT-WIDTH LEG

For  $x = w$ ,  $l = l_o$ , hence

$$\alpha = \frac{l_o - l_i}{w} \quad (A-3)$$

Combining Eqs. (A-2) and (A-3),

$$l = l_i + \alpha x = l_i + \frac{l_o - l_i}{w} x \quad (A-4)$$

which is identical with Eq. (26).

Note that if the two cross sections of the leg are parallel,  $\alpha = 0$  and  $l = l_i = l_o$ , as expected.

Another point that deserves comment is as follows. If the radius of curvature of  $l_i$  is relatively small and  $x$  relatively large, the plot of  $l$  may have "loops" in it, i.e., in certain portions of  $l$  three segments overlap each other. In such a case, the shortest distance should be considered, since a back and forth motion yields no change in  $\theta$ . However, this case does not constitute a physical constant width for the flux path.

*APPENDIX B*

**CALCULATION OF  $\Delta \phi_{\epsilon}$**



## APPENDIX B

### CALCULATION OF $\Delta \phi_{\epsilon_s}$

Referring to Fig. 19, assume that a leg is initially at a remanent state  $\phi = -\phi_r$ . A negative  $F$  is now applied, causing an elastic change of flux,  $\Delta \phi_{\epsilon_s}$ , in the cross section of area  $A$ .

Consider an element of length  $l$  and thickness  $dx$  at a distance  $x$  from  $l_i$ . Along  $l$ ,

$$H = \frac{F}{l} \quad . \quad (B-1)$$

Assuming that  $H$  causes an elastic change in  $B$ ,  $\Delta B_{\epsilon_s}$ , the elastic change in flux in the element of area  $hdx$  is

$$d\Delta \phi_{\epsilon_s} = \Delta B_{\epsilon_s} hdx \quad . \quad (B-2)$$

From Eq. (26),

$$dx = \frac{w}{l_o - l_i} dl \quad . \quad (B-3)$$

From Eqs. (B-2) and (B-3),

$$\Delta \phi_{\epsilon_s} = h \frac{w}{l_o - l_i} \int_{l_i}^{l_o} \Delta B_{\epsilon_s} dl \quad . \quad (B-4)$$

If  $\mu_s$  is constant, then

$$\Delta B_{\epsilon_s} = \mu_s \frac{F}{l} \quad . \quad (B-5)$$

Substituting Eq. (B-5) into Eq. (B-4) gives

$$\Delta \phi_{\epsilon_s} = h \frac{w}{l_o - l_i} \mu_s F \ln \frac{l_o}{l_i} \quad (B-6)$$

which is identical with Eq. (27).

If, however, the hyperbolic model for  $B(H)$ , Eq. (28), is assumed,

$$\Delta B_{\epsilon_s} = -\frac{B_s - B_r}{1 - \frac{a}{F} l} + \mu_0 \frac{F}{l} \quad (\text{B-7})$$

Substituting Eq. (B-7) into Eq. (B-4) and integrating results in

$$\Delta \phi_{\epsilon_s} = h \frac{w}{l_o - l_i} F \left[ \frac{B_s - B_r}{a} \ln \frac{F - al_o}{F - al_i} + \mu_0 \ln \frac{l_o}{l_i} \right] \quad (\text{B-8})$$

which is identical with Eq. (30).



*APPENDIX C*

**CALCULATION OF  $\dot{\phi}_\rho$ ,  $\bar{\rho}$  AND  $\rho_{\phi,uv}$**



## APPENDIX C

### CALCULATION OF $\dot{\phi}_p$ , $\bar{\rho}$ AND $\rho_{\phi,av}$

#### 1. CALCULATION OF $\dot{\phi}_p$

Substituting Eq. (39) into Eq. (38) gives

$$\frac{d\phi}{dt} = \rho_p (F - F_0) \left[ 1 - \left( \frac{\phi}{\phi_r} \right)^2 \right] \quad (C-1)$$

Hence,

$$\int_{-\phi_{r0}}^{\phi} \frac{d\phi}{1 - \left( \frac{\phi}{\phi_r} \right)^2} = \rho_p \int_0^t (F - F_0) dt' \quad (C-2)$$

where  $\phi = -\phi_{r0}$  is the initial flux level which is slightly above  $-\phi_r$ .

Assuming constant  $F$ , after integration we get

$$\phi = \phi_r \tanh \left[ \frac{\rho_p (F - F_0)}{\phi_r} t + \tanh^{-1} \left( -\frac{\phi_{r0}}{\phi_r} \right) \right] \quad (C-3)$$

Differentiating Eq. (C-3) with respect to time yields the inelastic  $\dot{\phi}$ ,

$$\dot{\phi}_p = \rho_p (F - F_0) \operatorname{sech}^2 \left[ \frac{\rho_p (F - F_0)}{\phi_r} t - \tanh^{-1} \left( \frac{\phi_{r0}}{\phi_r} \right) \right] \quad (C-4)$$

Let

$$\dot{\phi}_p = \rho_p (F - F_0) \quad (C-5)$$

Hence, Eq. (C-4) becomes

$$\dot{\phi}_p = \dot{\phi}_p \operatorname{sech}^2 \left[ \frac{\dot{\phi}_p}{\phi_r} t - \tanh^{-1} \left( \frac{\phi_{r0}}{\phi_r} \right) \right] \quad (C-6)$$

Equations (C-6) and (C-5) are identical with Eqs. (40) and (41) respectively.

## 2. CALCULATION OF $\bar{\rho}$

Let  $\bar{\rho}$  be the time-averaged  $\rho$  over the period  $2t_p$ , i.e.,

$$\bar{\rho} = \frac{1}{2t_p} \int_0^{2t_p} \rho dt \quad . \quad (C-7)$$

Referring to Fig. 30, we get

$$2\phi_{r0} = \int_0^{2t_p} \dot{\phi}_\rho dt = (F - F_0) \int_0^{2t_p} \rho dt = (F - F_0) 2t_p \bar{\rho} \quad . \quad (C-8)$$

Hence,

$$\bar{\rho} = \frac{\phi_{r0}}{(F - F_0) t_p} \quad . \quad (C-9)$$

Substituting the expression for  $t_p$ , Eq. (42), gives

$$\bar{\rho} = \rho_p \frac{\phi_{r0}/\phi_r}{\tanh^{-1}(\phi_{r0}/\phi_r)} \quad . \quad (C-10)$$

Equation (C-10) is identical with Eq. (43).

## 3. CALCULATION OF $\rho_{\phi,av}$

Let  $\rho_{\phi,av}$  be the flux-averaged  $\rho$  from  $\phi = -\phi_r$  to  $\phi = +\phi_r$ , i.e.,

$$\rho_{\phi,av} = \frac{1}{2\phi_r} \int_{-\phi_r}^{\phi_r} \rho d\phi \quad . \quad (C-11)$$

Substituting Eq. (39) into Eq. (C-11),

$$\rho_{\phi,av} = \frac{\rho_p}{2\phi_r} \int_{-\phi_r}^{\phi_r} \left[ 1 - \left( \frac{\phi}{\phi_r} \right)^2 \right] d\phi \quad . \quad (C-12)$$

Integrating Eq. (C-12) results in the following.

$$\rho_{\phi, \mathbf{a} \mathbf{v}} = \frac{2}{3} \rho_p \quad . \quad (\text{C-13})$$

Equation (C-13) is identical with Eq. (44).



*APPENDIX D*

**ANALYSIS OF SETTING CHARACTERISTICS**





## ANALYSIS OF SETTING CHARACTERISTICS

- (1)  $B$ - $H$  Loops are rectangular [cf. Fig. 4(b)iv], except that  $H_c$  is replaced by  $H_0$ , Eq. (65).
- (2) MMF pulses are long enough to complete the switching of available flux.
- (3) A ring model will be used.
- (4) The shortest path is preferred for complete flux switching.
- (5) The minor aperture diameter is very small.

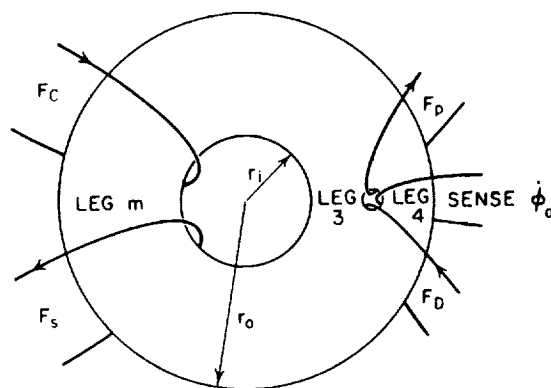
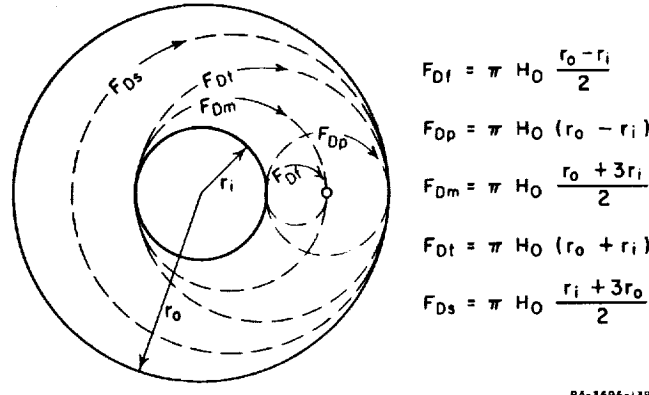
$$\Delta\phi_s = 2E_F h (r_s - r_i) \quad (\text{D-1})$$
$$r_s = F_s / 2\pi H_0 \quad (\text{D-2})$$


FIG. D-1 SETTING CHARACTERISTIC WINDINGS

From Eqs. (D-1) and (D-2),

$$\Delta\phi_s = \dot{B}_r h \left( \frac{F_s}{\pi H_0} - 2r_i \right) \quad (D-3)$$

Based on Assumptions (2) and (3), switching paths are assumed to be circular, with diameters depending on the DRIVE MMFs  $F_{Df}$ ,  $F_{Dp}$ ,  $F_{Dm}$ ,  $F_{Dt}$ , and  $F_{Ds}$ , as indicated in Fig. D-2.



RA-3696-139

FIG. D-2 SWITCHING PATHS CORRESPONDING TO VARIOUS  $F_D$  VALUES

Two cases are now distinguished: (1) asymmetrical characteristics, where  $F_p$  is fixed ( $F_{Dp} \leq F_p < F_{Dm}$ ) and  $F_D$  is variable; (2) symmetrical characteristics, where  $F_p = F_D$ , both variable.

#### 1. ASYMMETRICAL SETTING CHARACTERISTICS\*

The shape of  $\Delta\phi_o$  versus  $F_s$  depends on  $F_D$ . Five ranges of  $F_D$ , whose boundaries are  $F_{Dp}$ ,  $F_{Dm}$ ,  $F_{Dt}$  and  $F_{Ds}$ , Fig. D-2, are distinguished:

- (1)  $0 \leq F_D \leq F_{Dp}$ . The primed flux,  $\Delta\phi_p$ , depends on  $\Delta\phi_s$ , Eq. (D-3), as follows

$$\Delta\phi_p = \begin{cases} \Delta\phi_s & \text{if } \Delta\phi_s \leq 2\phi_r \\ 4\phi_r - \Delta\phi_s & \text{if } \Delta\phi_s \geq 2\phi_r \end{cases} \quad (D-4)$$

where  $2\phi_r$  is the flux capacity of Leg 3 or Leg 4, hence the flux capacity of Leg  $m$  is  $4\phi_r$ . Note

\* It is easier to follow the following derivations by referring to Fig. D-5, where the calculated asymmetrical setting characteristics are plotted.

that  $2\phi_r = B_r h(r_o - r_i)$ . The driven flux is

$$\Delta\phi_D = \frac{B_r h}{\pi H_0} F_D \quad (D-5)$$

Note that  $\Delta\phi_p$  is the available flux, and  $F_D$  determines what portion of  $\Delta\phi_p$  will be switched around, hence

$$\Delta\phi_o = \begin{cases} \Delta\phi_p & \text{if } \Delta\phi_D \geq \Delta\phi_p \\ \Delta\phi_D & \text{if } \Delta\phi_D \leq \Delta\phi_p \end{cases} \quad (D-6)$$

Four examples are furnished in Fig. D-3, using the arrow model, where an arrow without a tail indicates unchanged flux and an arrow with a tail indicates changed flux.

- (2)  $F_{Dp} \leq F_D \leq F_{Dm}$ .  $F_D$  is too small to switch flux around the major aperture, hence  $\Delta\phi_o$  versus  $F_s$  is identical with that of  $F_D = F_{Dp}$ , i.e., triangular in shape.
- (3)  $F_{Dm} \leq F_D \leq F_{Dt}$ . If  $\Delta\phi_s \leq 2\phi_r$ ,  $\Delta\phi_o$  is the same as in Range (2), thus  $\Delta\phi_o = \Delta\phi_s$  if  $F_s \leq \pi H_0(r_o + r_i)$ . If  $\Delta\phi_s \geq 2\phi_r$ ,  $\Delta\phi_o$  is composed of a primable flux and what is left in Leg 4 that  $F_D$  is capable of clearing around the major aperture, as shown in Fig. D-4. Using the ring model, zones of switching  $\delta_3$  and  $\delta_m$  are indicated in the figure, where

$$\delta_3 = r_o - \frac{F_s}{2\pi H_0} \quad (D-7)$$

and

$$\delta_m = \frac{2F_D + F_s}{4\pi H_0} - \frac{3}{4}(r_o + r_i) \quad (D-8)$$

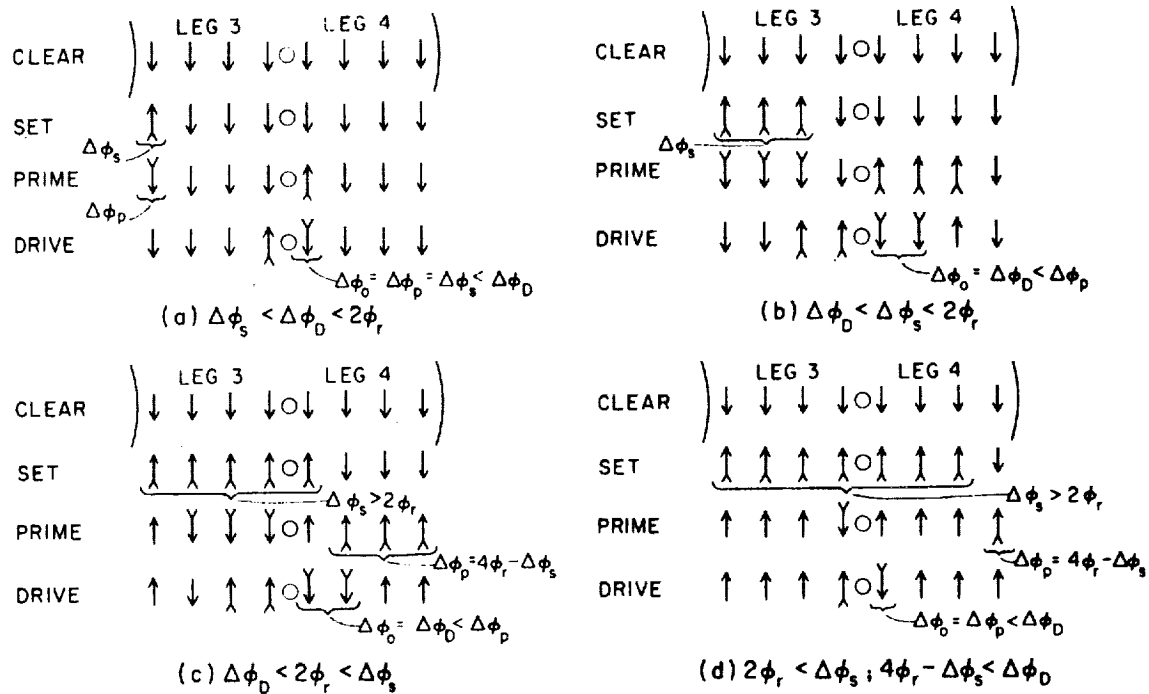
Let the switched flux be denoted by  $\Delta\phi'_D$ , where

$$\Delta\phi'_D = 2B_r h(\delta_3 + \delta_m) \quad (D-9)$$

Substituting Eqs. (D-7) and (D-8) into Eq. (D-9) gives

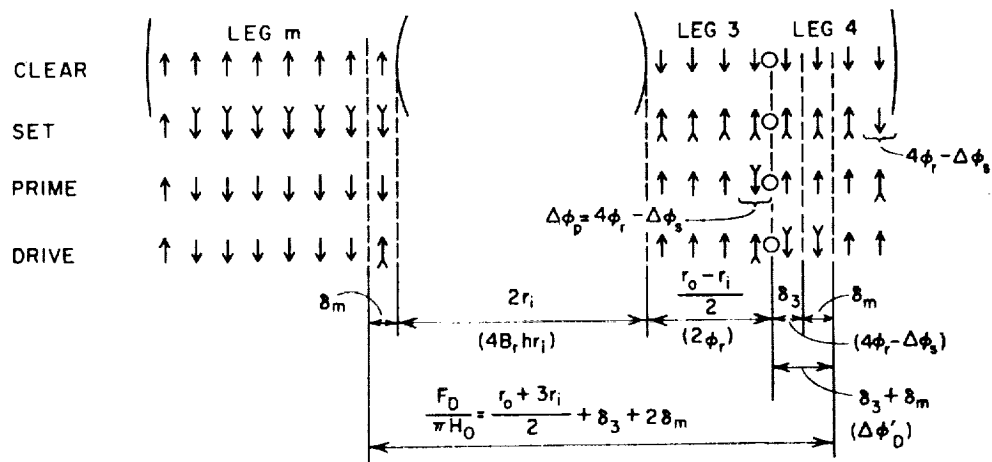
$$\Delta\phi'_D = \frac{B_r h}{2} \left( \frac{2F_D - F_s}{\pi H_0} + r_o - 3r_i \right) \quad (D-10)$$

This relation holds as long as  $\pi H_0(r_o + r_i) \leq F_s \leq 2\pi H_0 r_o$ . For  $F_s \geq 2\pi H_0 r_o$ , both Legs 3 and 4 are set,



RA-3696-140

FIG. D-3 FLUX SWITCHING IN LEGS 3 AND 4 FOR  $F_D = F_{Df}$  vs.  $\Delta\phi_D$



RA-3696-141

FIG. D-4 FLUX SWITCHING FOR  $F_D = F_{Dm} + 3/4 F_{Df}$  AND  $\Delta\phi_s = 7/2 \phi_r$

$\Delta\phi_p = 0$ ,  $\delta_3 = 0$  and  $\delta_n = (F_D - F_{Dn})/2\pi H_0$ , hence

$$\Delta\phi_D'' = \frac{B_r h}{\pi H_0} (F_D - F_{Dn}) \quad (D-11)$$

where  $\Delta\phi_D''$  is  $\Delta\phi_o$  due to  $F_D$  alone after both Legs 3 and 4 are set by  $F_s$ . In conclusion,  $\Delta\phi_o$  may have one of four expressions, depending on  $F_s$ , as follows:

$$\Delta\phi_o = \begin{cases} \Delta\phi_s & \text{if } 0 \leq F_s \leq \pi H_0 (r_o + r_i) \\ 4\phi_r - \Delta\phi_s & \text{if } \pi H_0 (r_o + r_i) \leq F_s \leq F_{ss} \\ \Delta\phi_D', \text{ Eq. (D-10)} & \text{if } F_{ss} \leq F_s \leq 2\pi H_0 r_o \\ \Delta\phi_D'', \text{ Eq. (D-11)} & \text{if } 2\pi H_0 r_o \leq F_s \end{cases} \quad (D-12)$$

where  $F_{ss}$  is the value of  $F_s$  at the intersection of  $\Delta\phi_o = \Delta\phi_D'$ , Eq. (D-10), and  $\Delta\phi_o = 4\phi_r - \Delta\phi_s$ , i.e., the value of  $F_s$  for which  $\delta_n = 0$ . Following Eq. (D-8),

$$F_{ss} = 3\pi H_0 (r_o + r_i) - 2F_D \quad (D-13)$$

Note that for  $F_D = F_{Dt}$ ,  $F_{ss} = \pi H_0 (r_o + r_i)$ .

- (4)  $F_{Dt} \leq F_D \leq F_{Ds}$ . Equations (D-12) still hold, except that  $\Delta\phi_D'$ , Eq. (D-10), is limited by  $2\phi_r$ . Let  $F_{sc}$  be the value of  $F_s$  for which  $\Delta\phi_D' = 2\phi_r$ , i.e.,

$$F_{sc} = 2F_D - \pi H_0 (r_o + r_i) \quad (D-14)$$

Let  $F_{Ds}$  be the value of  $F_D$  for which  $\Delta\phi_D''$ , Eq. (D-11), is equal to  $2\phi_r$ , i.e.,

$$F_{Ds} = \pi H_0 \frac{r_i + 3r_o}{2} \quad (D-15)$$

- (5)  $F_{Ds} \leq F_D$ . For  $\Delta\phi_s \geq 2\phi_r$ ,  $\Delta\phi_o = \Delta\phi_D'' = 2\phi_r$ . Hence,

$$\Delta\phi_o = \begin{cases} \Delta\phi_s & \text{if } 0 \leq F_s \leq \pi H_0 (r_o + r_i) \\ 2\phi_r & \text{if } \pi H_0 (r_o + r_i) \leq F_s \end{cases} \quad (D-16)$$

A summary of the expressions for  $\Delta\phi_o$  in the five ranges of  $F_D$  is performed graphically by plotting the setting characteristics in Fig. D-5. Note the resemblance to the experimental curves of Fig. 58.



202

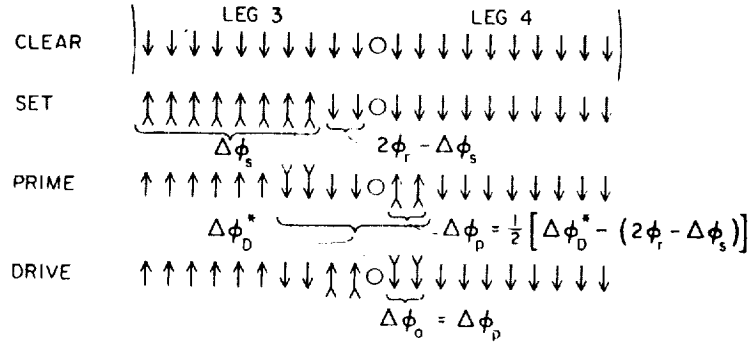


FIG. D-6 FLUX SWITCHING IN LEGS 3 AND 4 FOR  
 $F_D = F_P = 3/5 F_{Df}$

The second expression reaches zero at  $F_s = F_{s0}$ , where

$$F_{s0} = \pi H_0 (r_o + r_i) - 2F_D. \quad (D-20)$$

The peak of  $\Delta\phi_o$ ,  $\Delta\phi_{op}$ , is reached when Leg 3 is fully set, i.e., at  $F_s = \pi H_0 (r_o + r_i)$ , hence,

$$\Delta\phi_{op} = \frac{B_r h}{\pi H_0} F_D. \quad (D-21)$$

Note that  $\Delta\phi_{op} = \Delta\phi_D$ , Eq. (D-5), of the asymmetrical case.

If  $\Delta\phi_s \geq 2\phi_r$ ,  $\Delta\phi_o$  drops in a symmetrical fashion beyond  $F_s = \pi H_0 (r_o + r_i)$  because, for a fixed  $F_p (=F_D)$ ,  $\Delta\phi_o = \Delta\phi_p = (1/2)(\Delta\phi_D^* + 2\phi_r - \Delta\phi_s)$ .

- (2)  $F_{Df} \leq F_D \leq F_{Dp}$ . Consider the case where  $\Delta\phi_s \leq 2\phi_r$ . As long as  $\Delta\phi_D^* \leq 2\phi_r + \Delta\phi_s$ , Eq. (D-19) still holds. If  $\Delta\phi_D^* \geq (2\phi_r + \Delta\phi_s)$ , all the set flux will be primed and  $\Delta\phi_o = \Delta\phi_s$ , as shown in Fig. D-7. Hence,

$$\Delta\phi_o = \begin{cases} B_r h \left( \frac{F_s + 2F_D}{2\pi H_0} - \frac{r_o + r_i}{2} \right) & \text{if } 2\phi_r \leq \Delta\phi_D^* \leq 2\phi_r + \Delta\phi_s \\ \Delta\phi_s & \text{if } 2\phi_r + \Delta\phi_s \leq \Delta\phi_D^* \leq 4\phi_r \end{cases} \quad (D-22)$$

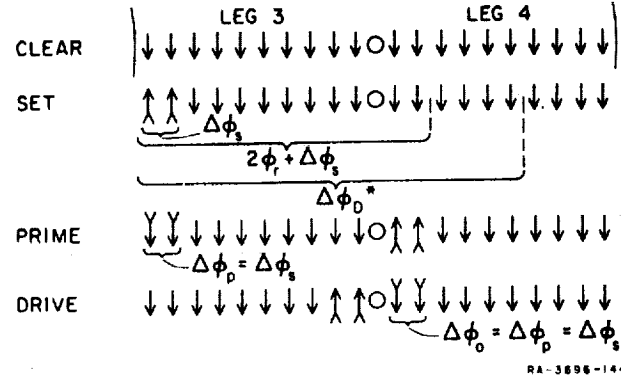


FIG. D-7 FLUX SWITCHING IN LEGS 3 AND 4 FOR  
 $2\phi_r + \Delta\phi_s < \Delta\phi_D^* < 4\phi_r$

At  $F_s = F_{s1}$ ,

$$\Delta\phi_s = B_r h \left( \frac{F_s + 2F_D}{2\pi H_0} - \frac{r_o + r_i}{2} \right)$$

Hence,

$$F_{s1} = 2F_D - \pi H_0 (r_o - 3r_i) \quad (D-23)$$

For  $F_{s1} = \pi H_0 (r_o + r_i)$ ,  $\Delta\phi_o = 2\phi_r$  and  $F_D = F_{Dp}$ ,  
 Fig. D-2.

Symmetrical characteristics about  $F_s = \pi H_0 (r_o + r_i)$  are obtained for  $\Delta\phi_s \geq 2\phi_r$ .

- (3)  $F_{Dp} \leq F_D \leq F_{Dm}$ .  $F_p$  and  $F_D$  are too small to switch flux around the major aperture, hence the setting characteristic is identical with that of  $F_D = F_{Dp}$ . Note that this characteristic is triangular in shape and is identical with the corresponding one in the asymmetrical case.

- (4)  $F_{Dm} \leq F_D \leq F_{Dt}$ . We distinguish between  $\Delta\phi_s \leq 2\phi_r$  and  $\Delta\phi_s \geq 2\phi_r$ .

- (a)  $\Delta\phi_s \leq 2\phi_r$ . Referring to Fig. D-8, note that since  $F_p > F_{Dm}$  the amount of flux ( $\Delta\phi_D'' - \Delta\phi_s$ ) switches around the major aperture along a path regardless of  $\Delta\phi_s$ , provided that  $\Delta\phi_s \leq \phi_D''$ . If  $2\phi_r \geq \Delta\phi_s \geq \Delta\phi_D''$ ,  $\Delta\phi_o = \Delta\phi_s$ , hence

$$\Delta\phi_o = \begin{cases} \Delta\phi_D'', \text{ Eq. (D-11)} & \text{if } \Delta\phi_D'' \geq \Delta\phi_s \\ \Delta\phi_s & \text{if } \Delta\phi_s \geq \Delta\phi_D'' \end{cases} \quad (D-24)$$



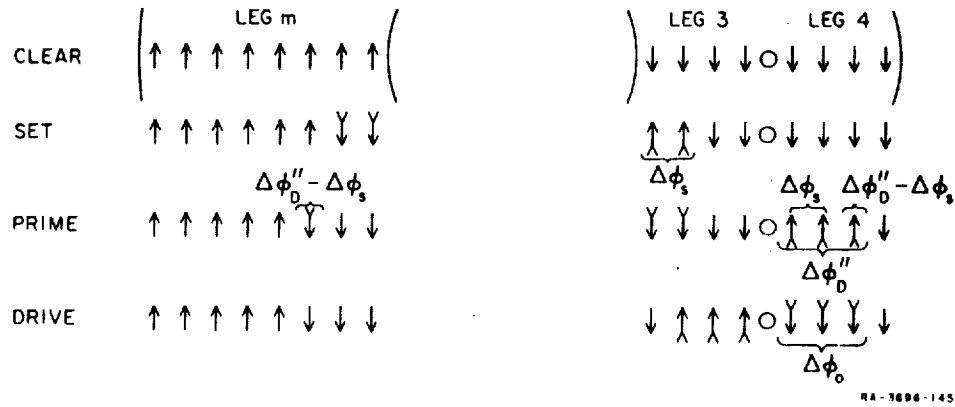


FIG. D-8 FLUX SWITCHING WHEN  $\Delta\phi_o'' > \Delta\phi_s$ .

$\Delta\phi_o''$ , Eq. (D-11), intersects  $\Delta\phi_s$ , Eq. (D-3), at

$$F_{s2} = F_D - F_{Df} \quad (D-25)$$

- (b)  $\Delta\phi_s \geq 2\phi_r$ . Since  $\Delta\phi_s \geq 2\phi_r$  (so that Leg 3 is fully set), and since  $F_p = F_D > F_{Dp}$  (i.e., high enough for full priming),  $\Delta\phi_p = 4\phi_r - \Delta\phi_s$ , and the effect of the magnitude of  $F_D$  on the setting characteristics is identical with that of the asymmetrical case. Note that for  $F_D = F_{Dt}$ ,  $\Delta\phi_o'' = \phi_r$ .
- (5)  $F_{Dt} \leq F_D \leq F_{Ds}$ . The behavior is the same as when  $F_{Ds} \leq F_D \leq F_{Dt}$ , hence the setting characteristics are the same as in the asymmetrical case, except that  $\Delta\phi_o = \Delta\phi_o''$ , Eq. (D-11) for  $0 \leq F_s \leq F_{s2}$ , Eq. (D-25). For  $F_D = F_{Ds}$ , following Eq. (D-25),  $F_{s2} = \pi H_0(r_o + r_i)$  and following Eq. (D-11),  $\Delta\phi_o'' = 2\phi_r$ . This amounts to full output for all values of  $F_s$ .
- (6)  $F_{Ds} \leq F_D$ . Since maximum output has been reached with  $F_D = F_{Ds}$ , increasing  $F_D$  further has no effect, and  $\Delta\phi_o = 2\phi_r$ . Following these derivations, the symmetrical setting characteristics are plotted in Fig. D-9. Note the resemblance to the experimental curves of Fig. 59.



## INDEX



# INDEX\*

- ADVANCE current, 62-64
- ADVANCE MMF, 61-64
- Air gap, *see* Cracked core
- ALL-magnetic schemes:
  - advantages, 60
  - definition, 59
  - nonresistance type, *see* Nonresistance schemes
  - resistance type, *see* Resistance schemes
- Analysis, pole distribution:
  - multipath core, 134-138
  - toroid, 128-132
- Analysis, shift register:
  - nonresistance, 143
  - resistance, 140
- Analogue, electrical circuit, *see* Electrical-circuit analogue
- Apertured plate, 159
- Arithmetic unit, all magnetic, 146, 156, 157, 161
- Arrow model, 115
  - application, 117-119
  - evaluation, 119
  - flux closure, 117
  - flux continuity, 117
  - polarity, 116
  - reversed flux, 117
  - scaling, 115
- BIAX, memory element, 161
  - effect of dimensions, 164
  - rotation model, 162
  - zone boundary model, 162-166
- Bistable transfer characteristic, 67
- CLEAR MMF, 55, 61
- CLEAR state, 61, 64
  - effect of shaping, 103
- Clipper, 70
- Clipping, flux, 67, 70, 106-108
- Computation procedure, 35-36, 143
- Continuous-structure shift register, 82, 146, 148
- Coupling loop:
  - nonresistance type, 62-63
  - resistance type, 147
- Cracked core, 50
  - static  $\phi$ - $F$  loop, 51-52
  - $\phi$ - $F$  curves, 52
  - $\dot{\phi}(t)$ , 144
- Current:
  - ADVANCE, 62-64
  - CLEAR, 55
  - DRIVE, 55, 64
  - PRIME, 55, 64-66
  - SET, 55
  - steering, 62, 160
- Curves,  $\phi$ - $F$ , 45-46
  - automatic plot of, 45-46
  - calculated, 47, 143
  - of cracked multipath core, 52-53
  - of cracked toroid, 52
  - effect of  $T$  on, 46
  - of multipath core, 49-50
  - of toroid, 47-48
  - presetting effect on, 48-49
  - soft threshold, 48-50
  - threshold, 46-47
  - uniformity test, 50
- Domains:
  - collisions, 7, 141
  - ellipsoidal, 4, 141
  - growth, 11
  - orientation, 5
  - static energy diagram of, 7, 11
  - theory, 153
- DRIVE MMF, 55
- Drive on outside leg:
  - negative, cleared core, 86-88
  - negative, set core, 96-99
  - positive, high, 89-94
  - positive, low, 92
  - stress effect, 88
  - stressed state, negative drive, 88
  - stressed state, positive drive, 91
  - supersetting effect, 93-94
  - unsettling effect, 99
  - winding position, 94-96
- Elastic permeability, 17
- Elastic switching:
  - of  $B$ , 12-13, 19
  - coefficient, 23
  - coefficient, average, 23-24
  - coefficients, multipath core, 24
  - by domain growth, 11, 16
  - during fast  $H$  fall, 14-15
  - history effect, 15
  - measurement problem, 25
  - near leg effect, 146
  - by rotation, 11, 16
  - relation to static energy, 11
  - time rate of change of, 16
  - of  $\phi$  in leg, 19, 187
  - of  $\phi$  in toroid, 21, 142

\* Page numbers 139-180 correspond to the literature survey, Sec. V.

# INDEX

- Electrical-circuit analogue:
  - leg, 32, 140, 142
  - legs in parallel, 112-114
  - legs in series, 109-112
  - multipath core, 34
- Energy diagram, static, 7, 11
  - relation to elastic switching, 11
  - relation to  $H$  threshold, 7
- Ferrite, 153
  - particle, 4
- Flux clipping, 67, 70
  - by minor aperture, 106-108
  - shaping, effect on, 108
- Flux continuity:
  - at boundary, 130
  - at leg junction, 85
- Flux density, 5
  - physical interpretation, 4
  - versus  $H$  and domain growth, 5, 7
- Flux density, change of:
  - elastic, 11-15, 19
  - inelastic, 13-14
  - elastic and inelastic, 14-15
  - at fast  $H$  fall, 14
- Flux density, time rate of change of, 15-17
  - elastic, 16
  - inelastic, 16
  - measurement problem, 25
  - near  $B = 0$ , 16
- Flux division:
  - calculation of, 153-154
  - in circular multipath core, 80-81
  - effect of  $dI/dt$  on, 81
  - in Laddic, 75-76
  - in Laddic,  $\dot{\phi}$  waveforms, 76-78
  - in Laddic,  $\phi$ - $F$  variation, 79-80
  - measures against, 82, 84, 143
  - in multihole structure, 82
- Flux gain, 67
- Flux leakage:
  - calculation, toroid, 131-132, 148
  - experimental verification, 132
  - effect of sharp corner, 108-109
- Flux spreading, 81
- Flux switching:
  - elastic,  $\Delta\phi$ , 19, 187
  - elastic  $\dot{\phi}$ , 21, 23, 142
  - inelastic,  $1/\tau$  vs.  $H$ , 29
  - inelastic  $\dot{\phi}$ , 25-28, 40-42, 191
  - inelastic,  $\dot{\phi}$  vs.  $F$ , 29
  - literature on, 173
  - time of, 30, 40
- Fourier series of pole distribution, 130
- Future investigation, 54, 114, 136
- Gain, flux, 67
- Geometry coefficient, 37
- Geometry, leg, 9, 18
- High- $\mu$  region, 21, 40-42
- Hyperbolic model for:
  - $B$ , 19
  - $\mu_s$ , 19
  - $\Delta\phi_{\epsilon_s}$ , 19, 187
- Inelastic switching:
  - of  $B$ , 13-14
  - dynamic threshold, 25-26
  - and elastic switching, 14-15
  - measurement problem, 25
  - peaking time, 28
  - plot of  $1/\tau$  vs.  $H$ , 29
  - plot of  $\dot{\phi}$  vs.  $F$ , 29
  - time of, 30, 40
  - $\dot{\phi}$ , 16
  - $\dot{\phi}$ , calculated, 27-28, 40-42, 191
- Inelastic-switching coefficient, 25-30
  - flux averaged, 29, 192
  - of multipath core legs, 30
  - parabolic model, 27
  - time averaged, 28-29, 192
  - vs.  $\phi$ , 27
- Kidney-shaped field plot, 136
- Laddic, 2, 147
  - flux division, 75-76, 147
  - flux division,  $\dot{\phi}$  waveforms, 76-78
  - flux division,  $\phi$ - $F$  variation, 79-80
  - logic application, 147
  - unsettling effect, 99
- Laplace's equation, 129
- Leakage, flux, *see* Flux leakage
- Leg model, 1
  - division into legs, 8
  - elastic switching, 19
  - electrical-circuit analogue, 32, 140, 142
  - geometry, 9, 18
  - geometrical properties, 18, 183
  - junction, flux continuity, 85
  - of legs in parallel, 112-114
  - of legs in series, 109-112
  - restriction on, 3
- Literature on multipath core:
  - authors' names, 176-180
  - continuous flux, 174
  - flux switching, 173
  - German, 167
  - logic, 175
  - memory, 175
  - Russian, 140
  - shaping, 174
  - shift register, 174
  - survey, 139-180
  - transverse field, 176

# INDEX

- Logic application, 141, 145, 147-151, 155, 157, 158, 175
- MAD, 2
- Magnetic field intensity:
  - distribution in multipath core, 134-138
  - effect on  $B$ , 5, 7
  - equalization by poles, 128-129
  - threshold, 7, 29
- Magnetic scalar potential, 129
- Magnetization:
  - orientation, 5
  - rotation, 11
- Magnistor, 160
- Material coefficient, 37
- Memory application, 148, 152, 161, 175
- Minor aperture input, 61, 63, 69, 106
  - flux clipping, 106-108
  - shaping effect, 108
- Multihole structure, 82
- Multipath core:
  - all magnetic schemes, 59-74
  - BIAX, 161-166
  - division into legs, 1, 8
  - drive on outside leg, 85-99
  - electrical-circuit analogue, 34-35
  - flux division, 75-85
  - flux pattern, analysis, 128-138
  - geometry, 8-9
  - literature on, 139-180
  - ring model, 44-45, 197
  - setting characteristics, 55-59
  - shaping, 99-108
  - static  $\phi$ - $F$  loops, 8-10
  - switching inductance, 24
  - switching resistance, 30-31
  - toroidal equivalence, 1-3, 140-141
  - zone boundaries, 119-128
- Near leg effect, 146
- Nonresistance schemes, 61, 62
  - ADVANCE current, maximum, 62
  - ADVANCE MMF, 61
  - alternative loop scheme, 63
  - CLEAR MMF, 61
  - CLEAR state, 61
  - comparison with resistance schemes, 72-73, 145
  - $\phi^*$  mechanism, 144
- Nonresistance type of:
  - arithmetic unit, 146, 156, 157, 161
  - logic application, 141, 149-150, 157, 158
  - sequence detector, 156
- Nonresistance-type shift register:
  - analysis, 143
  - application, 140, 143, 145-147, 155, 157
- Patents, U. S., multipath cores, 167-173
- Permeability, elastic, 17
  - hyperbolic model, 19
- Plate, apertured, 159
- Pole distribution:
  - calculation of, multipath core, 134-138
  - calculation of, toroid, 129-132
  - effect on  $H$  equalization, 128-129
  - elimination of, 122
  - Fourier series of, 130
  - in stressed state, 88, 91-92, 95, 100
- PRIME:
  - bias, 65
  - current, 64-66
  - MMF, 55-56, 65
  - range, 65-66
  - range, effect of soft threshold on, 101
- Quiescent state, 66
- Radiation effects, 145
- Range map, 70
  - of double monostable CLEAR state, 72
  - effect of soft threshold, 101
- Read-out, 102
  - effect of drive, 150
  - effect of shaping, 103-106
  - nondestructive, 102
- Receiver, 61, 64
- Resistance schemes, 64, 65
  - ADVANCE current, 64
  - CLEAR state, 64-66
  - comparison with nonresistance schemes, 72-73, 145
  - logic application, 139, 157
  - PRIME bias, 65
  - PRIME current, 64
  - PRIME range, 65-66, 101
  - SET- $P$  state, 64
  - SET- $U$  state, 64
- Resistance-type shift register:
  - analysis, 140, 146, 147
  - application, 139, 146, 147, 155
  - optimum turns ratio, 147
- Ring model:
  - dynamic state, 40
  - innermost band, 40
  - motion of high- $\mu$  region, 40-42
  - in multipath core, 44-45
  - static  $\phi$ - $F$  loop calculation, 37-38
  - static state, 36-37
  - $\phi_p$  calculation, 42
- Rotation, magnetization, 11
- Scanner, 82, 148
- Sequence detector, 156
- SET MMF, 55

# INDEX

- SET state:
  - SET-D, 61
  - SET-P, 64
  - SET-R, 61
  - SET-T, 61
  - SET-U, 64
- Setting characteristics:
  - analysis, 197-206
  - asymmetrical, 55-57, 198-202
  - MMFs, applied, 55-56
  - other kinds, 59, 144
  - read-out, 55
  - symmetrical, 58-59, 202-206
- Shaping, 99, 149
  - literature on, 174
- Shaping, effects on:
  - CLEAR state, 103
  - flux clipping, 108
  - read-out, 103-106
  - soft threshold, 100-101
- Sharp corner effect, 108-109, 150
- Shift register literature, 174
- Soft threshold, 26, 48-50
  - shaping effect, 100-102
  - range map, effect on, 101
- Stability, 67, 70
  - double monostable CLEAR state, 72
  - regions of, 70
- Static  $\phi$ - $F$  characteristics, 9-10
  - calculation, 37-38, 140, 141, 143
- Stress effect, 88
- Stressed state following drive:
  - negative, cleared core, 88
  - negative, set core, 98-99
  - positive, high, 91
  - positive, low, 92
- Supersetting effect, 93-94
- Switching:
  - coefficient, 29-30
  - elastic, *see* Elastic switching
  - flux, *see* Flux switching
  - inelastic, *see* Inelastic switching
  - models, 31-32, 141
  - time, 30, 40
- Switching inductance, 23
  - average, 23-24
  - of multipath-core legs, 24
- Switching resistance, 25-26
  - flux-averaged, 29, 192
  - time-averaged, 28-29, 192
  - of multipath-core legs, 30
  - vs.*  $\phi$ , 27-28
- Temperature effect, 149-150
- Threshold:
  - dynamic, 25-26
  - soft, 26, 48-50
  - static, 4, 7
  - of  $\phi$ - $F$  curve, 46-47
- Toroid, 7
- Toroidal equivalence, 1-3, 140-141
- Transfluxor, 1, 139, 144, 159
- Transmitter, 61, 64
- Transverse field, 156, 159-166
  - literature on, 176
- Unsetting effect, 99
  - in Laddic, 99
- Walk down effect, 148
- Winding position, 94-95
  - effect of, 95-96
- Zone boundary, 120
  - experimental verification, 127
  - motion of, 125
  - motion of, unshaped core, 127
  - mushy, 119
  - unshaped core, 126, 144-145
- Zone boundary in:
  - CLEAR state, 124-125
  - SET state, 121-123



STANFORD  
RESEARCH  
INSTITUTE

MENLO PARK  
CALIFORNIA

## Regional Offices and Laboratories

Southern California Laboratories  
820 Mission Street  
South Pasadena, California

Washington Office  
808 17th Street, N.W.  
Washington 5, D.C.

New York Office  
270 Park Avenue, Room 1770  
New York 17, New York

Detroit Office  
The Stevens Building  
1025 East Maple Road  
Birmingham, Michigan

European Office  
Pelikanstrasse 37  
Zurich 1, Switzerland

## Representatives

Honolulu, Hawaii  
Finance Factors Building  
195 South King Street  
Honolulu, Hawaii

London, Ontario, Canada  
85 Wychwood Park  
London 14, Ontario, Canada

London, England  
15 Abbotsbury Close  
London W. 14, England

Milan, Italy  
Via Macedonio Melloni 40  
Milano, Italy

Tokyo, Japan  
911 Iino Building  
22, 2-chome, Uchisaiwai-cho, Chiyoda-ku  
Tokyo, Japan

